Regional aerosol modeling in Europe: Evaluation with focus on vertical profiles and radiative effects

Von der Fakultät für Physik und Geowissenschaften
der Universität Leipzig
genehmigte

DISSERTATION
zur Erlangung des akademischen Grades

Doctor rerum naturalium
(Dr. rer. nat.)

vorgelegt
von Dipl.-Met. Jessica Meier
geboren am 08.03.1981 in Berlin

Gutachter: Prof. Dr. Ina Tegen
Prof. Dr. Peter Builtjes

Tag der Verleihung: 22. April 2013

Abstract

Jessica Meier

Regional aerosol modeling in Europe: Evaluation with focus on vertical profiles and radiative effects

Universität Leipzig, Dissertation, 2012
203 pages, 148 references, 52 figures, 22 tables

In this thesis the occurrence and the properties of atmospheric particles within Europe are studied by means of the regional transport model COSMO – MUSCAT (Consortium for Small-scale Modeling – MultiScale Atmospheric Transport Model). The model is used to perform calculations for a summer (19 – 26 July 2006) and a winter (16 – 26 February 2007) period.

Individual extinction coefficients are computed taking into account hygroscopic growth and mass extinction efficiencies of specific chemical compounds. The model study focuses on vertical backscatter profiles, aerosol optical depths, particle surface concentrations and radiative effects.

Different descriptions of the vertical distribution of chemical compounds at the lateral model boundaries are tested. The results show that for the tested model setup the influence of the aerosol distribution at the model boundaries on European aerosol is limited. Information from lidar profiles may improve the description at the lateral model boundaries. This may be more important for smaller model domains.

Space-based lidar (light detection and ranging) observations (CALIOP – Cloud-Aerosol Lidar with Orthogonal Polarization) observations are compared to the simulated backscatter profiles caused by the simulated anthropogenic aerosol. The model reproduces the shape and magnitude of the vertical backscatter profiles well for both time periods. Better agreements are found for night-time observations compared to day-time data. Satisfying agreements between the model results and experimental observations of ground-based vertical backscatter profiles, aerosol optical depths and particle surface concentrations are also found for the two time periods in Europe. Discrepancies between measurement and simulation highlight the difficulties to describe horizontal and vertical aerosol properties properly.

The direct and semi-direct radiative effects of the absorbing aerosol are studied for both summer and winter period. For both periods, an increase of the solar heating rate due to the aerosol forcing is determined. This heating leads to an average decrease of the total cloud cover of 1.0% (summer) and of 0.7% (winter). This semi-direct radiative effect causes a positive forcing at the surface and at the top-of-atmosphere in the European domain.

Contents

Chapter 1

Introduction

Atmospheric particles are of different origin e.g, marine, dust, urban or volcanic and thus are characterized by different physical and chemical properties. These properties are studied in various regions globally. For instance, in Europe long-term observations are performed at different locations (natural, rural, near-city, urban, and kerbside sites) and results are presented by e.g., Putaud et al. (2004, 2010) and Van Dingenen et al. (2004). Putaud et al. (2004, 2010) show measurement results of particulate matter up to 2.5 μm ($PM_{2.5}$) and 10 μm (PM_{10}) as well as of number concentrations. The authors found that organic matter (OM) is a major component of PM_{10} and $PM_{2.5}$, depending on the observation site. Further, a fraction of black carbon (BC) on $PM_{2.5}$ of $5-10\%$ is observed and is higher at kerbside regions ($15-20\%$). The main compounds of both PM_{10} and $PM_{2.5}$ are OM, sulfate and nitrate, whereas mineral dust is most important in PM_{10} and occurs mainly in southern Europe. Such data characterize the aerosol near the surface whereas information about the vertical profiles of specific aerosol properties, like their chemical composition, structure and size distribution, are rare. It is reported by Redemann et al. (2000) that the vertical structure of the aerosol-induced radiative flux changes modifies the atmospheric stabilities, the convective processes and the formation and the life cycle of clouds. Additionally, such information about the vertical distribution of specific aerosol properties is needed for model evaluations, also to describe transport processes correctly. So the information about the vertical distribution of chemical compounds is required.

Vertical profiles of aerosol properties

Morgan et al. (2009) presented results of airborne in-situ measurements which were performed in Europe with focus on air-mass from North-West Europe and the North-East Atlantic. By means of Quadrupole Aerosol Mass Spectrometer (Q-AMS) vertical profile of sub-micron aerosol chemical compositions is derived. OM as well as sulfate aerosol are found to be primarily characteristic for background sub-micron profiles. It is shown by the authors, that the vertical structure of sulfate and organic aerosol profiles is strongly dependent on large-scale dynamical processes whereas in case of nitrate distribution dynamic as well as thermodynamic processes are relevant. Further studies regarding the vertical distribution of sub-micron aerosol compositions were obtained during May 2008 at Cabauw (The Netherlands) at an airborne platform by Morgan et al. (2010). During that time period enhanced pollution loadings were observed pointing to an increase of ammonium nitrate and OM in the boundary layer with increasing altitude. Over the Paris Basin the vertical composition of aerosol was measured by an aircraft (Hodzic et al., 2006) during July 2000 with focus on pollution events. These data were used to test the ability of the chemistry-transport model CHIMERE to simulate location as well as vertical distribution of plume structures. Here, the aerosol composition is nearly reproduced, but the total mass is underestimated by the model by about 20%. Measurements based on aircrafts and airborne platforms are rarely performed and are often limited to specific loactions and time periods. Thus, no compact information about the vertical structure of the atmosphere as well as about the vertical distribution of aerosol properties is available.

Lidar observations

Information about the vertical distribution of atmospheric particles are determined based on their optical properties (Mattis et al., 2008; Müller et al., 2007) provided by lidar (light detection and ranging) observations. For the European region, ground-based observations are performed within EARLINET (European Aerosol Research Lidar Network; EARLINET (2012)). These observations are performed regularly three time a week at each station within Europe since several years and thus provide a large amount of vertical backscatter and extinction profiles.
One-year EARLINET lidar observations were used by Guibert et al. (2005) for model evaluation. The authors found only moderate agreements of aerosol extinction profiles when comparing individual lidar profiles with simulation results. After averaging over certain spatial and temporal scales these agreements are better, but differences between northern and southern European stations were found. An average bias of 22% was analyzed for northern stations and a bias of 29% for southern stations. The contribution of modeled individual atmospheric substances, like dust, seasalt, sulfate, BC and particulate organic matter (POM) on the aerosol extinction was analyzed. Thus, the presence of dust in the south of Europe was found to cause larger discrepancies between observation and simulation. Hodzic et al. (2004) used hourly lidar profiles of one day at Palaiseau (France) and found quite good agreements when comparing

data with model results. After averaging hourly data for a certain number of days the agreement becomes better. However, individual profiles as computed from regional models have rarely been comprehensively compared to lidar profiles in Europe.

In addition to ground-based lidar data, space-based observations as done by CALIOP (Cloud-Aerosol Lidar with Orthogonal Polarization) are available since 2006 (Winker et al., 2009) and provide extensive coverage of measurements which can be used to perform studies about cloud and aerosol properties. These are distinct structures and can be observed very well by CALIOP and therefore used for detailed analysis as it was shown by e.g., Liu et al. (2008) and Su and Toon (2011) in case of dust and by e.g., Hu et al. (2010) and Yoshida et al. (2010) in case of clouds. With focus on different aerosol types, Yu et al. (2010) and Koffi et al. (2012) performed comparisons between CALIOP observations and model results. They used one global model (Yu et al., 2010) and 12 global models from the AeroCom (Aerosol Comparisons between Observations and Models; AeroCom (2012)) (Koffi et al., 2012) to simulate mean extinction profiles and other parameters. Koffi et al. (2012) showed that the results of most models correlate quite well with the observed extinction mean height diagnostic, whereas most models overestimate the observed data over industrial and maritime regions. Additionally, Koffi et al. (2012) used annual and seasonal aerosol extinction profiles for comparisons with models. Yu et al. (2010) presented results from the GOCART (Goddard Chemistry Aerosol Radiation Transport) model compared with CALIOP profiles based on 17 month data. The authors found a general underestimation of the detected extinction over the Indian sub-continent but higher values over dust source regions. Comparisons representing smaller time and spatial scales are not presented by Koffi et al. (2012); Yu et al. (2010). Thus, due to the coverage and the large amount of data, CALIOP profiles contain necessary information which can be used for model studies on small time and spatial scales.

Radiative forcing

Lidar observations are useful to get information about the vertical aerosol distribution because measurements of chemical composition, mass and size distribution at different height levels are rare. The knowledge about the vertical distribution of aerosol is important in case of radiative transfer calculations. The radiative forcing[1] of aerosol is of major interest for climate change studies. In the previous IPCC (Intergovernmental Panel on Climate Change; IPCC (2007)) report several results on aerosol radiative

---

[1] The radiative forcing describes the change of the solar flux within the atmosphere due to aerosol particles (Kiehl and Rohde, 1995), whereas a positive forcing (more incoming than outgoing radiation) leads to a warming and a negative forcing (more outgoing than incoming radiation) a cooling of the atmosphere. The incoming and outgoing radiation is named as radiant flux density (F), which describes the energy which reaches a specific area within a specific time.

forcing based on observations and model simulations are summarized. Aerosol particles cause, due to scattering and absorption, the direct, indirect and semi-direct (influence of the change in radiative heating of added (absorbing) aerosol particles) radiative forcing. As best estimate, a direct radiative forcing of -0.5 $\pm$ 0.4 $\mathrm{W\,m^{-2}}$ is estimated for global anthropogenic aerosol based on model computations and observations (Chapter 2, IPCC, 2007). In case of the indirect radiative forcing (also referred as Twomey effect; Twomey (1977)), which describes the influence of aerosol particles as cloud and ice nuclei, the forcing is estimated to be -0.7 [-1.1, +0.4][2] $\mathrm{W\,m^{-2}}$ (Chapter 2; IPCC, 2007).

Often, the influence of absorbing aerosol type on the radiative forcing is studied. Absorbing aerosol contains BC and various mixtures which include this component. Estimations of BC radiative forcing often lead to different results, as mentioned by Sato et al. (2003). The authors used measurements of Aerosol Optical Depth (AOD) performed at AERONET (Aerosol Robotic Network; AERONET (2012)) stations to discriminate the radiative forcing of BC from other substances and inferred a climate forcing of $\sim 1\,\mathrm{W\,m^{-2}}$. Chandra et al. (2004) studied various possibilities of mixtures of BC with other substances and found distinct differences between the forcing dependent on the mixture composition. The importance in case of the direct radiative forcing is summarized by Cook and Highwood (2004) who found a higher radiative forcing caused by absorbing aerosol than by carbon dioxide regionally. Wendisch et al. (2006) used EARLINET lidar data to determine the radiative forcing and found good correlations in case of European aerosol of continental and highly industrialized sites but difficulties in case of marine aerosol.

Large uncertainties occur in case of the semi-direct radiative effect (IPCC, 2007). The absorption by BC can cause warming of the air, which can offset the cooling which is estimated for the indirect aerosol effect (Lohmann and Feichter, 2001). The existence of BC within the atmosphere and their absorption of solar radiation increases the atmospheric heating resulting in a decrease of the cloud cover (e.g., Ackerman et al., 2000). Whereas aerosol, located within a cloud layer, can lead to a decrease of the cloud fraction (positive semi-direct effect), absorbing aerosol above the cloud cause a stabilization of the underlying atmosphere and can therefore increase the cloud fraction (negative semi-direct effect). This behavior was studied by Johnson et al. (2004) who analyzed strato-cumulus clouds within a marine environment. By means of a global model, Allen and Sherwood (2010) estimated a semi-direct effect at the surface of 0.5 $\mathrm{W\,m^{-2}}$ globally, caused by the decrease of mid-level clouds due to the heating by anthropogenic aerosol. Results of various studies dealing with the vertical distribu-

---

[2] Within the brackets the 90% confidence ranges are given. It is given as A [-X, +Y] with the lower limit of (A - X) and the upper limit of (A + Y).

tion of absorbing aerosol and its influence on the radiative forcing are summarized by Koch and Del Genio (2010). The authors also mentioned the need to perform further experimental and model studies of radiative effects in various environments.

Model studies

Often, aerosol-cloud-radiation models are used to estimate the aerosol radiative forcing. Satellite data are useful for evaluating this effect combined with surface flux observations as it is done by Kim et al. (2008). For detailed calculations of the radiative forcing, the chemical composition of the atmospheric particles, their size as well as their vertical distribution are required. In-situ observation data can provide such information. Iorga et al. (2007) used data of aerosol mass distribution and analyzed the fraction of total carbon (TC), BC and inorganic ions. By Mie calculation obtained at different relative humidities (RHs) the direct radiative forcing at various European sites was estimated. The authors found a significant heating effect caused by BC. Based on several observations of aerosol optical properties in Spain and Austria, Horvath et al. (2002) determined a negative aerosol forcing at the surface and only slightly negative aerosol forcing at top of atmosphere (TOA). Observation data are also used by Meloni et al. (2003) as input parameters for model calculations. They use the solar zenith angle, vertical profiles of pressure, temperature, air density, and ozone as well as the aerosol single scattering albedo, asymmetry factor, and optical depth at each layer for cloud-free cases within the Mediterranean region. With this information, a decrease of the downward irradiance caused by aerosols is estimated.

To understand the processes behind different values of radiative forcing of specific substances and their mixtures, models may close the gaps between individual observations. A comprehensive study to determine the aerosol radiative forcing was done within AeroCom (Kinne et al., 2006). Computed optical properties of several global models are compared to each other and with measurements. Good agreement between simulation and observation of AOD is found, whereas the computation of the radiative forcing differs distinctly due to the different descriptions of the aerosol composition within the individual models. The usage of regional models with a smaller scale is helpful in describing a realistic atmospheric aerosol load, performing comparisons with optical properties and determining the interaction processes between the particles and the atmosphere. Simulations of few days on a regional scale can lead to a further understanding of the interaction of aerosols and therefore on the estimation of optical properties, as done by (e.g., Vogel et al., 2009). Matthias (2008) performed model simulation of the years 2000 and 2001 for the European domain. The author concentrated on the computation of the aerosol distribution and compared the results with PM observation data and AOD. Better agreements are found during winter time compared to summer. A seasonal behavior regarding the agreement between observed and simulated AOD within Europe was also analyzed by Péré et al. (2010). But the agreements do not only depend on season but also on the meteorological situation as described by Marmer and Langmann (2007).

1.1 Aims of this work

The regional transport model COSMO – MUSCAT (Consortium for Small-scale Modeling – MultiScale Atmospheric Transport Model) is used to perform model computations for a summer (19 – 26 July 2006) and winter period (16 – 26 February 2007). By means of this model, chemical compounds are described. Based on the various chemical substances, specific optical parameters are computed and compared with observation data. Thus, an important part of this work is to set model results into relation to space-based lidar observations performed on board the CALIPSO satellite. These lidar observations are performed continuously and provide information about the vertical distribution of the backscatter coefficients as well as the occurrence of specific aerosol types. Based on these information, it should be possible to analyze the capability of the model to calculate vertical backscatter profiles caused by different aerosol types for these specific time periods in Europe. Due to the large number of available data, a statistical analysis of the results is possible. First results of this study are presented by Meier et al. (2012b) and are currently prepared for a more comprehensive publication.

In this thesis, the description of the vertical distribution of chemical compounds at the lateral model boundaries is also analyzed. The correct description of the vertical distribution is essential to determine the transport of compounds from outside into the model domain as well as their behavior within the atmosphere. Different approaches are analyzed here and information about the general agreement between the observed and simulated PM, the vertical backscatter profile and the column information about the AOD is shown. Most of the results presented here have been published recently by Meier et al. (2012b).

Three different model setups are used to determine the radiative effects of the aerosol during both simulation periods. The direct radiative effect caused by the aerosols during summer and winter are analyzed. Due to the presence of the particles within the atmosphere, dynamical effects are influenced. The absorption and scattering of radiation leads to temperature change in the atmosphere. This semi-direct effect is also studied within this thesis. Selected results about the radiative effects simulated by means of COSMO – MUSCAT have also been published by Meier et al. (2012a).

In the last part of this thesis, a sensitivity study is presented. The analysis of the variation of computation results using different horizontal resolutions of the model grid and the performance of model simulations with different restart conditions is shown to identify necessary steps toward model improvement.

Chapter 2

Model description

2.1 The COSMO – MUSCAT model system

The results presented here, are obtained from the regional transport model COSMO – MUSCAT. This model system is an online-coupling between the weather forecast model COSMO, that is the operational weather forecast model of the *Deutscher Wetterdienst* (German Weather Service – DWD) and the 3-dimensional chemistry transport model MUSCAT that has been developed at the Leibniz – Institute for Tropospheric Research. Both models have their own time step size control. The coupling process provides time-averaged wind fields as well as time-interpolated fields of various meteorological parameters from COSMO to MUSCAT. COSMO – MUSCAT has been successfully used for simulations of emission, transport and deposition of Saharan dust (Laurent et al., 2010) and for studies regarding its direct and semi-direct radiative effects (Helmert et al., 2007). Furthermore, detailed sensitivity studies about the influence of specific grid resolutions and meteorological forcing in the simulation of the European aerosol have been performed recently (Wolke et al., 2012). Here it is shown how significant meteorological effects influence the concentrations of PM whereas Renner and Wolke (2010) presented results of the regional model simulating secondary inorganic aerosols. Comparisons with other regional models were performed to evaluate COSMO – MUSCAT and its ability to compute PM concentrations up to $10\,\mu$m (PM_{10}) (Stern et al., 2008; Wolke et al., 2012).

The regional model COSMO (former LM – *Lokal Modell*) is provided by the DWD and is utilized within the operational service (Steppeler et al., 2003). It is a 3-dimensional non-hydrostatic meteorological model which uses reanalyzed input data from the global model GME (Global Model Europe, also developed by the DWD; Majewski et al. (2002)). Computations are performed with rotated coordinates. These rotated coordinates can be transformed to the normal geographical coordinates after the model calculations. In the vertical direction a terrain dependent coordinate is used. The height of each layer and therefore the geopotential is not changed (Schulz and Schättler, 2009). The various variables are defined at grid points and the time integration is performed with a fixed time interval. The distance between the individual grid points is constant.

The determination of the impact of aerosol distributions on radiative fluxes is an important part of this work. The radiation scheme, which is used in the meteorological model, is based on Ritter and Geleyn (1992). A δ-two-stream radiative solver is used and considers the influence of aerosols, clouds and gaseous trace elements on the radiation by absorption, scattering and emission. Three solar ($1.53-4.64\,\mu$m, $0.7-1.53\,\mu$m, $0.25-0.7\,\mu$m) and five thermal ($20.0-104.5\,\mu$m, $12.5-20.0\,\mu$m, $8.33-9.01\,\mu$m and $10.31-12.5\,\mu$m, $9.01-10.31\,\mu$m, $4.642-8.33\,\mu$m) bands are taken into account. Regarding the aerosol, the radiative impact for five different aerosol types (continental, urban, maritime, volcanic and stratospheric), which are fixed in space and time, is described (Tanré et al., 1984). Within Figure 2.1 an example of the optical thickness at 550 nm representing the sum of urban, marine, land and desert aerosol (Figure 2.1 (a)) as well as the sum of urban, marine, and land aerosol (Figure 2.1 (b)) are shown. A distinct smooth and homogeneous distribution of the aerosol types is shown here, whereby the vertical distribution of the individual aerosol types is described by an exponential decay with increasing height (Hohenegger and Vidale, 2005). These distributions are also independent from the relative humidity. This Figure also represents clearly the influences of dust aerosol in European regions. The δ-two-stream radiative transfer scheme of Ritter and Geleyn (1992) uses these information of the optical depths as well as of the single scattering albedo (Section A.3) and the asymmetry parameter (Section A.3).

The parametrization of the wet convection within COSMO is based on the mass flux scheme described by Tiedtke (1989). A differentiation between shallow, penetrative and midlevel convection is implemented within COSMO. As described by Schulz and Schättler (2009), the determination of the vertical heat, humidity and convective precipitation is based on a stationary cloud model for up- and down-drafts. It depends on the temperature whether the precipitation, which reaches the ground is classified as rain or as snow. Precipitation, described within COSMO, is separated into three different categories (next to water vapor in the gaseous phase): Cloud water, rain water and snow. Cloud water is only determined for those grid cells with $\mathrm{RH} = 100\%$ and therefore the cloud cover fraction is also 100%. For those cases with $\mathrm{RH} < 100\%$ a calculation of the partial cloud cover is done. This calculation depends on the relative humidity, the height and the convection process.

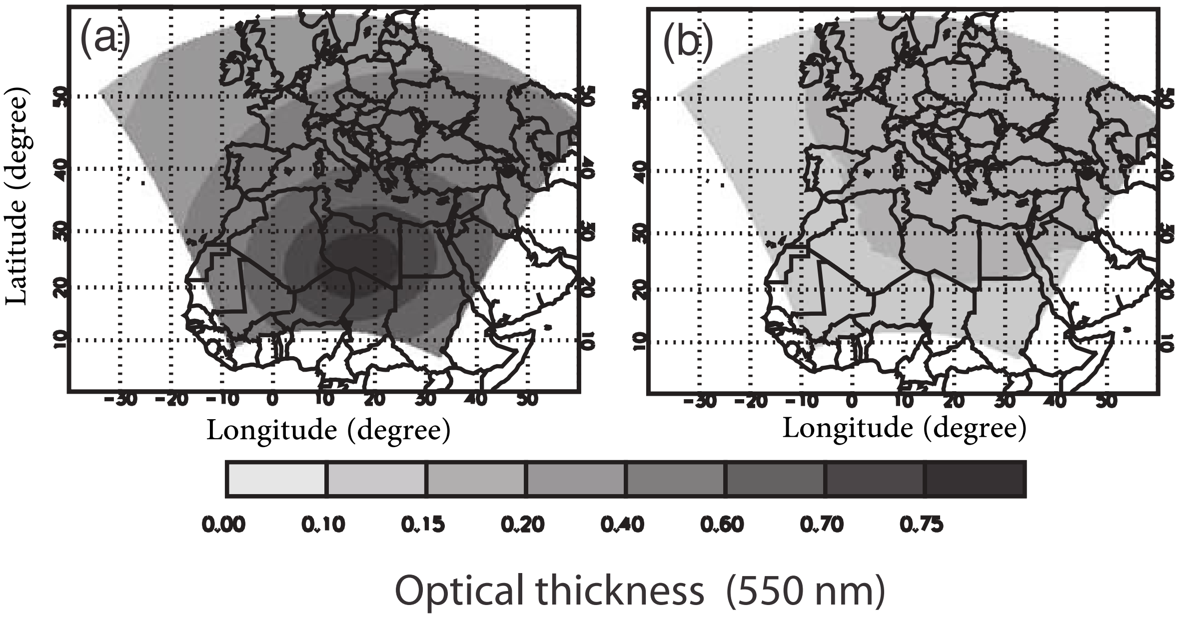

Figure 2.1: Optical thickness at 550 nm wavelength derived from the sum of urban, maritime, land, and desert aerosol, using the (a) aerosol climatology of Tanré et al. (1984), and (b) aerosol climatology based on the sum of urban, maritime, and land aerosol without desert component. Figure taken from Helmert et al. (2007).

The transport model MUSCAT (Wolke et al., 2004, 2012) includes emission, transformation processes and the transport of aerosol species up to 2.5 and 10 μm diameter. Advection processes for the horizontal direction are performed using an implicit – explicit time integration scheme, which is described in detail by Wolke and Knoth (2000). RACM (Regional Atmospheric Chemistry Mechanism; Stockwell et al. (1997)) is implemented in MUSCAT and is used for the description of the gas-phase chemistry. Local emissions of chemical compounds are used from EMEP/CORINAIR (European Monitoring and Evaluation Programme/Co-ordinated Information on the Environment in the European Community-AIR; EMEP/CORINAIR (2012)) as input data for MUSCAT. The time resolved anthropogenic emissions are included as point, line and area sources. The computation of the total mass of chemical compounds and aerosols is done within MUSCAT. MUSCAT does not calculate size distributions for individual compounds and substances in its current configuration.

Individual grid cells of MUSCAT can be subdivided. Different resolutions allow to take a closer look at e.g., dispersion processes in urban regions or in the near of point sources. For the studies presented in this work, this feature was not used, grid cells over the model domain have same grid sizes.

2.2 Description of lateral model boundaries

The description of the vertical distribution of chemical compounds and substances is cause for uncertainty within regional transport models. Especially at the lateral model boundaries such a description is necessary because of the transport of compounds from outside into the model domain and the location of specific compounds within the atmosphere. The location of absorbing substances within the vertical atmospheric column significantly influences the semi-direct forcing (SDF) (Johnson et al., 2004). Therefore, the vertical distribution of primary particulate matter up to 2.5 μm ($PPM_{2.5}$) and 10 μm (PPM_{10}) is prescribed at the model boundaries, which are important for the European aerosol. The formation of secondary aerosol (sulfate and nitrate species) from different sources is assumed to occur entirely within the model domain, no description at the lateral model boundaries is done for those species. Representative surface concentrations of $8.0\,\mu g\,m^{-3}$ for the summer and of $6.0\,\mu g\,m^{-3}$ for the winter period for $PPM_{2.5}$ are determined based on EMEP observation data (EMEP, 2012). Additionally, a maximum surface concentration difference PPM_{10} - $PPM_{2.5} = 2.0\,\mu g\,m^{-3}$ was set for both simulation periods.

For a realistic description of substances, studied here, vertical distribution profiles are required. For this, lidar observations (at 355 nm) performed at the EARLINET (Section 3.1.1) station in Aberystwyth, United Kingdom (52.4° N, 4.1° W) from 2000 to 2002 are used. This station represents the aerosol conditions near the western boundary of the European model domain. Wandinger et al. (2004) combined these long-term observation profiles depending on season and the origin of the air mass to typical climatological profiles. The lidar profiles are based on the observations representing clean atmospheric conditions from northerly and westerly flows. For model calculations, the lidar profiles are simplified and are described by three layers. In Figure 2.2, the vertical profiles based on these climatological lidar data are presented, which were used at all four lateral model boundaries in case of $PPM_{2.5}$ for 19 – 26 July 2006 and 16 – 26 February 2006. In case of the summer period the maximum concentration of $8.0\,\mu g\,m^{-3}$ ranges from the surface to 700 m. Between 700 m and 2000 m the concentration decreases to the minimum value of $0.8\,\mu g\,m^{-3}$ which is constant up to the model top (8000 m). During the winter period the maximum concentration of $6.0\,\mu g\,m^{-3}$ ranges from the surface to 300 m above the ground. The concentration decreases constantly to the minimum value of $0.6\,\mu g\,m^{-3}$ at 2000 m altitude. The $PPM_{2.5}$ concentration of $0.6\,\mu g\,m^{-3}$ remains constant up to 8000 m. A general decrease of the concentration by 10% with increasing altitude is assumed. Uncertainties in this description are due to the lack of observations of the vertical distribution of chemical compounds. A recent publication of Müller et al. (2011) presented vertical profiles of volume concentrations derived from lidar observations in Leipzig (Germany). Here a decrease of the volume concentration of around 20% was found. Therefore, an uncertainty in this description has to be expected. The shape of the concentration profiles remains constant during the entire simulation period. This description for the lateral model boundaries is used for most of the model calculations. Nevertheless, other boundary descriptions were also tested.

A so-called Standard Profile represents the default setup which was used in previous simulations. This profile does not depend on season or region. It is described by a constant (at maximum value) concentration from the surface to 700 m. The concentration decreases between 700 m and 900 m and remains constant (at minimum value) up to the model top (8000 m). This vertical description was tested for both simulation periods with their individual mass concentrations.

Individual lidar profiles measured one day before model calculation period starts were also used to describe the vertical distribution of $PPM_{2.5}$ and PPM_{10} - $PPM_{2.5}$ at the lat-

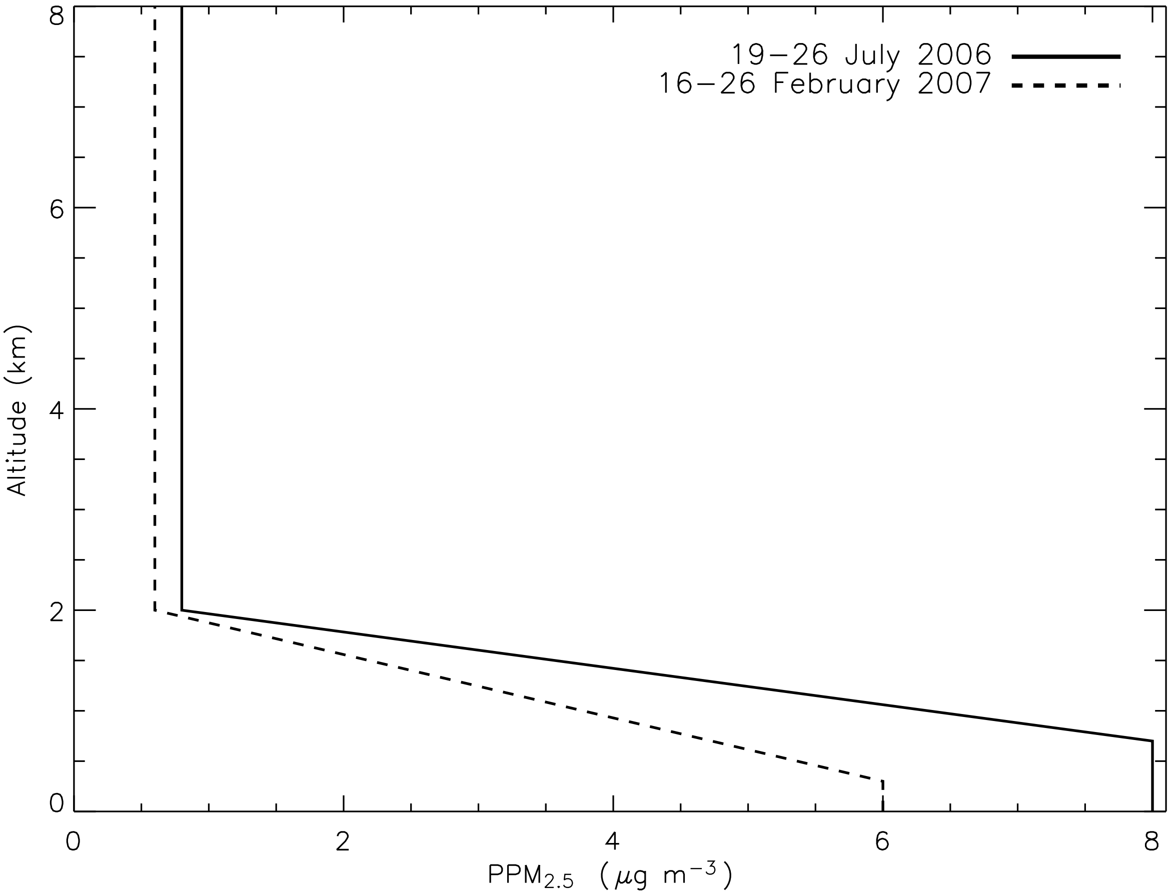

Figure 2.2: Climatological vertical profiles of $PPM_{2.5}$ used at the four lateral model boundaries for the summer (continuous line) and winter (dashed line) simulation period.

eral model boundaries. For the summer case, lidar observations performed on 17 July 2006 (because of the 24 h forerun of COSMO; Page 19) at four EARLINET stations are employed. The lidar stations located in Greece (Thessaloniki, 13:28 – 14:01 UTC; 355 and 532 nm), Poland (Belsk, 12:06 – 12:15 UTC and 18:27 – 18:33 UTC; 532 nm), Belarus (Minsk, 16:06 – 20:53 UTC, 351 nm) and Italy (L'Aqulia, 20:24 – 20:53 UTC; 351 nm) provided data. Based on these data, a representative profile for $PPM_{2.5}$ and PPM_{10} - $PPM_{2.5}$ at the lateral model boundaries is estimated. From the ground to 2000 m, the maximum concentration is held constant. From 2000 m to 4000 m it decreases to the minimum concentration. Above 4000 m the concentration (minimum) remains constant to the model top.

Because of the meteorological situation, only one EARLINET station (Potenza, Italy (00:50 – 12:00 UTC; 355, 532 and 1064 nm)) performed lidar observation on 14 February 2007. Therefore, additional observations performed on 15 February 2007 were used as well: Ispra, Italy (12:12 – 23:47 UTC; 532 nm), Saint Michel, France (18:30 – 20:00 UTC; 532 nm) and Palaiseau, France (10:00 – 16:00 UTC; 532 nm). These concentration profiles are described by a maximum concentration between the ground and 600 m. From 600 m to 2000 m the concentration decreases to its minimum and remains constant from 2000 m to 8000 m. As for the Standard Profile, this kind of model setup is also tested for 19 – 26 July 2006 and 16 – 26 February 2007, respectively.

Recently, the various descriptions of the lateral model boundaries are published by Meier et al. (2012b).

2.3 Aerosol type and optical properties

"Urban" and "continental" aerosol types are dominating within the European area. Whereas the original version of the COSMO – MUSCAT model considers both types at the same time, they are differentiated in this work. It is difficult to clearly discriminate between "urban" and "continental" aerosol. Here, the fraction of elemental carbon (EC) on $PM_{2.5}$ was used to distinguish between "urban" and "continental" aerosol type. The $PM_{2.5}$ concentration is calculated as sum of simulated $PPM_{2.5}$, ammonium nitrate (NH_4NO_3), sulfuric acid (H_2SO_4) and ammonium sulfate ($(NH_4)_2SO_4$) for each model grid cell. $PPM_{2.5}$ includes e.g., EC and primary organic particles. EC concentrations are also calculated separately by MUSCAT. For calculations of optical properties it is therefore necessary to separate EC from $PPM_{2.5}$ because of the highly absorbing nature of EC at solar wavelengths (Horvath, 1993). In the following, $PPM_{2.5}$ without EC is termed $PPM^*_{2.5}$. It must be mentioned that marine aerosol and mineral dust is not included in $PPM_{2.5}$ or elsewhere of the model version used here. Thus, computations of the transport of Saharan dust to Europe as well as the existence of marine aerosol over sea surface and in coastal regions is not computed by COSMO – MUSCAT.

Unknown material, which is often measured but not analyzed (Weijers et al., 2011; Spindler et al., 2010; Putaud et al., 2010) is also not represented by the model. Therefore, discrepancies between simulated and observed data may be expected. Regarding the fraction of EC on simulated $PM_{2.5}$ it is more likely, that a high amount of absorbing material is representative for "urban" aerosol type.

Several measurements of the chemical composition of $PM_{2.5}$ have been performed in the recent years, which can be used to make a proper discrimination between "urban" and "continental" aerosol. For example, Weijers et al. (2011) presented results from five stations in The Netherlands. The authors observed the increase of the average fraction of EC on $PM_{2.5}$ from rural (EC: 9 – 12%) to urban (15%) and kerbside (20%) locations during a one-year campaign. Lower fractions were found in the south-west of Spain with significant differences between rural (3%) and urban (5%) as well as between warm (rural: 2.4%, urban: 3.5%) and cold (rural: 3.8%, urban: 6.3%) seasons (de la Campa et al., 2009). Long-term observations are performed at the continental rural background station in Melpitz (Germany). Strong dependencies between the EC fraction on $PM_{2.5}$ and air mass were observed by Spindler et al. (2010). Values of 7 – 9% (summer) and 7% (winter) of EC fraction were found for westerly air masses and 9 – 10% (summer) and 12 – 13% (winter) for easterly air masses. The observations in the north of Europe (Kotka, Finland) showed the contributions of BC[1] to $PM_{2.5}$ between 8%±3% (24-h sampling) and 1% – 64% (1-h time resolution) (Aurela et al., 2010). A comprehensive summary of chemical composition of the European aerosol was done by Putaud et al. (2010). Data from 60 stations across Europe, representing conditions within rural, urban and kerbside locations were summarized. Rural locations in Central Europe contain 5% of EC on $PM_{2.5}$, whereas urban stations contain 7% (north-west Europe), 8% (Southern Europe) and 14% (Central Europe) EC fraction. Highest fractions of 21% EC were found in kerbside regions in Central Europe. Putaud et al. (2010) mentioned the difficulties of using different techniques for the determination of EC, so, the EC results may differ by a factor of 2.

In this work, an EC fraction higher than 20% is defined to classify the aerosol mass as "urban"; otherwise it is classified as "continental". In the experimental observations discussed here, an EC fraction below 20% is usually measured, which may lead to

---

[1] BC is measured by optical techniques, EC by thermal techniques. Both nomenclature describe the same element (Hitzenberger et al., 2006). Differences between individual analyzing methods are shown by Schmid et al. (2001).

misinterpretation of the result. Therefore a model calculation (for summer and winter period) is also performed with an EC limit of 5% (Sim_{EC5}; see also Table 2.1) to estimate the differences and the model sensitivity.

For determinations of optical properties in the model, like the extinction coefficient, several assumptions have to be made. Within MUSCAT the dry mass of the individual compounds $\mathrm{PPM}^*_{2.5}$, EC, $(NH_4)_2SO_4$, NH_4NO_3 and H_2SO_4 is calculated. Depending on their chemical composition, the size distribution and the ambient relative humidity, the atmospheric particles are able to absorb water and may grow, which can be described by the Köhler theory (Köhler, 1921). The growth factor (GF) is calculated from the dependence of the particle diameter on humidity. A detailed theoretical and practical analysis of the growth factor concept is given by Nowak (2005). The particle growth behavior exhibits a hysteresis behavior (Tang et al., 1981). It was also shown by Tang et al. (1981) that the growth of a single salt particle differs from the growth of a multicomponent particle. Regarding the description of the particle growth within the COSMO – MUSCAT model, empirical parameterizations (based on measurements of Tang (1996)) are used, similarly to other studies (Eichler et al., 2008; Meier et al., 2009). In case of NH_4NO_3 the hygroscopic growth factor $\mathrm{GF}_{NH_4NO_3}$ is calculated as follows:

$$\mathrm{GF}_{\mathrm{NH_4NO_3}} = 0.0004\, e^{\left(\frac{\mathrm{RH}}{12.1}\right)} + 1.2 \quad (\text{for RH} \leq 95\%)\,. \tag{2.1}$$

The determination of the growth behavior at larger humidities is difficult to determine (e.g., RH≥98% in Wex et al. (2005, 2006)). Textor et al. (2006) showed the differences between individual aerosol models regarding the treatment of this behavior. In this work, the particle growth is limited up to RH = 95%. In case of $\mathrm{PPM}^*_{2.5}$ and EC it is assumed that these substances do not absorb water (Weingartner et al., 1997; Massling et al., 2005).

Further calculation steps summarize the determination of the dry volume (V_i^{dry}) of the individual substance (i), based on their calculated mass (m_i) and density (ρ_i). By using the humidity dependent growth factor (GF_i), the total wet volume (V_i^{tot}) of the substance is calculated. Thus, the density of the mixture substance-water (ρ_i^{mix}) and the total mass (m_i^{tot}) can be estimated:

$$V_i^{dry} = \frac{m_i}{\rho_i} \tag{2.2}$$

$$V_i^{tot} = V_i^{dry} \cdot \mathrm{GF}_i^3 \tag{2.3}$$

$$\rho_i^{mix} = \rho_i \cdot \frac{V_i^{dry}}{V_i^{tot}} + \rho_{water} \cdot \frac{V_i^{tot} - V_i^{dry}}{V_i^{tot}} \tag{2.4}$$

$$m_i^{tot} = \rho_i^{mix} \cdot V_i^{tot}. \tag{2.5}$$

This kind of description of the growth behavior includes some simplifications, which definitely offer the possibility for further and detailed studies.

The total mass is used to determine the extinction coefficient for the individual substances (α_i):

$$\alpha_i = m_i^{tot} \cdot \mathrm{MEE}_i. \tag{2.6}$$

The mass extinction efficiency (MEE) represents the radiation extinction of the aerosol per unit mass. It is an important parameter to determine the contribution of individual compounds or aerosols to the radiative effect (Bagtasa et al., 2006). However, the choice of the correct MEE for the individual compounds provides some difficulties. The range of the available MEE which was used in different models can be very broad (Table 4, Kinne et al., 2006). MEE depends on the substance (Mallet et al., 2003), the wavelength (Takemura et al., 2002), the relative humidity (Penner et al., 2002) and the size of the particle (Penner et al., 2002). Within the atmosphere, the occurrence of individual compounds is very rare. Often mixtures of different substances lead to another MEE (Kim et al., 2008). Lagrosas et al. (2005) determined a mean MEE based on lidar and ground suspended particulate matter (SPM). In cases of well mixed boundary layer a good correlation between lidar and SPM is found and average MEE values of $4-12\,\mathrm{m}^2\,\mathrm{g}^{-1}$ are calculated, representing conditions within the ground layer. In the current work, MEE values given by Kinne et al. (2006) are used, which apply to the individual compounds under dry conditions, like sulfate $= 8.5\,\mathrm{m}^2\,\mathrm{g}^{-1}$, EC $= 8.9\,\mathrm{m}^2\,\mathrm{g}^{-1}$ and $\mathrm{PPM}_{2.5} = 5.7\,\mathrm{m}^2\,\mathrm{g}^{-1}$. In case of nitrate, only one value of $1.24\,\mathrm{m}^2\,\mathrm{g}^{-1}$ is given in the literature, which represents wet nitrate under urban conditions (Mallet et al., 2003). Finally, for the substances which are used in this study, the following values are used:

- $\mathrm{MEE}_{\mathrm{PPM}^*_{2.5}} = 5.7\,\mathrm{m}^2\,\mathrm{g}^{-1}$
- $\mathrm{MEE}_{\mathrm{EC}} = 8.9\,\mathrm{m}^2\,\mathrm{g}^{-1}$
- $\mathrm{MEE}_{(\mathrm{NH}_4)_2\mathrm{SO}_4}\ (\mathrm{dry}) = 8.5\,\mathrm{m}^2\,\mathrm{g}^{-1}$
- $\mathrm{MEE}_{\mathrm{NH}_4\mathrm{NO}_3}\ (\mathrm{wet}) = 1.24\,\mathrm{m}^2\,\mathrm{g}^{-1}$
- $\mathrm{MEE}_{\mathrm{H}_2\mathrm{SO}_4}\ (\mathrm{dry}) = 8.5\,\mathrm{m}^2\,\mathrm{g}^{-1}$.

Nevertheless, considerable uncertainties have to be expected when using different values of MEE. The MEE approach is empirical and definitely offers the possibility for future sensitivity studies.

The total extinction coefficient is computed based on the sum of the individual extinction coefficients: $\alpha_{PPM^*_{2.5}}$, α_{EC}, $\alpha_{(NH_4)_2SO_4}$, $\alpha_{NH_4NO_3}$ and $\alpha_{H_2SO_4}$.

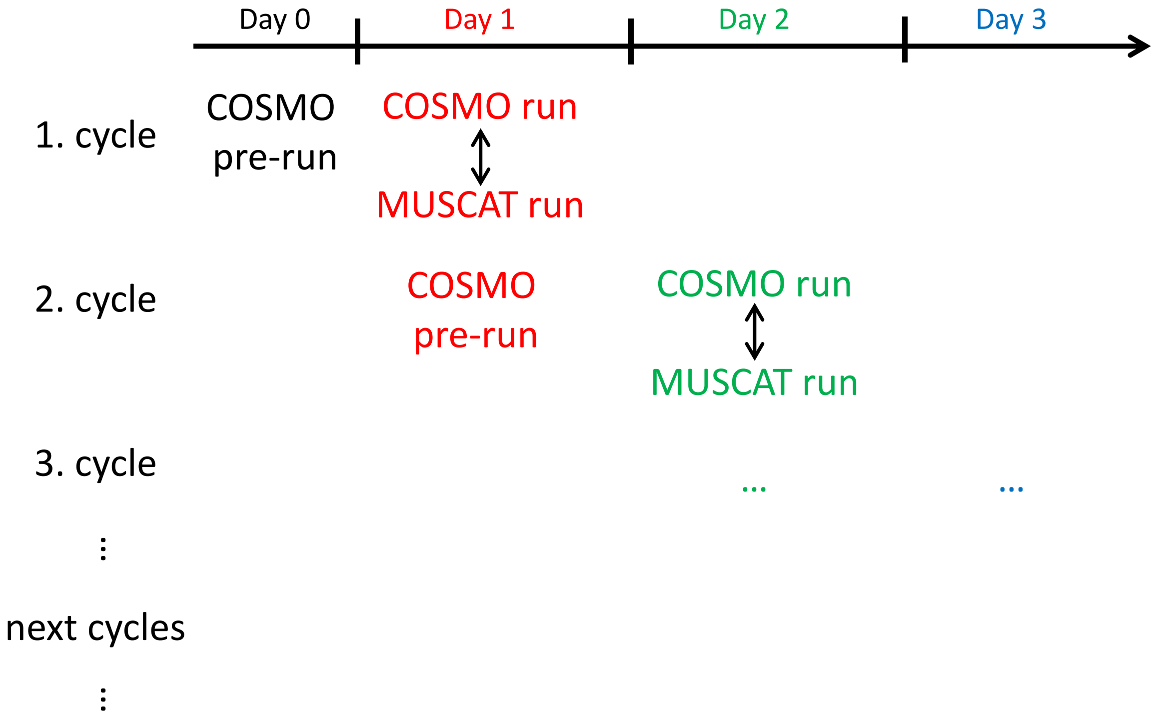

Figure 2.3: Scheme of cycle performance with COSMO – MUSCAT. Adapted from Fig. 1, published by Wolke et al. (2012)

Depending on the classification whether an aerosol is defined as “urban” or as “continental”, the optical depths of the aerosol types for each model grid cell can be calculated. This information is used by the radiation scheme of the meteorological model COSMO to determine the influence of the aerosol on radiation as well as on dynamical parameters. The individual aerosol distribution has an impact on the meteorological parameters, which on the other hand influences the spatial and temporal aerosol distribution (here termed “feedback”). It has to be mentioned that the formation of “urban” and “continental” aerosol mass, its determination of the optical depth and the transfer of these information to the radiation scheme of COSMO, changes the original description for these both aerosol types, which is described by Tanré et al. (1984). The information for the other aerosol types (maritime, volcanic and stratospheric aerosol), based on the Tanré scheme remains unmodified. Therefore, simulations performed with the new description of “urban” and “continental” aerosol and their influences on the radiation and on the dynamics, will differ from the original setup.

2.4 Model setup

The COSMO – MUSCAT model computations are performed with a horizontal resolution of 28 km x 28 km with 156 x 136 horizontal grid cells. The position of the lower left corner of the model domain is located at 10.1° W, 27.5° N and the vertical resolution comprises 40 vertical layers with a model top of MUSCAT at 8 km. In general, model calculations are performed with cycles (Figure 2.3): COSMO performs calculations for 24 hours alone. Afterwards, MUSCAT is started and both models run in parallel for 24 hours. At the start of the MUSCAT run, MUSCAT uses the aerosol distribution of the previous cycle. After that, COSMO is restarted again alone. This model calculation starts one day before the time period of interest. The cycle approach ensures that the deviations in meteorological fields between the model and reality remain small. In the following, the classification Sim_{Basic} represents the general simulation with the climatological profiles to describe the vertical distribution at the lateral model boundaries, the separation between "urban" and "continental" aerosol types with a threshold of 20% of EC, the hygroscopic growth up to RH = 95% (no growth for EC and $\text{PPM}^{*}_{2.5}$), the acceptance of the feedback process and the horizontal resolution of 28 km x 28 km with restart conditions of COSMO – MUSCAT. Besides the Sim_{Basic} simulations, other model setups, which are partly introduced in this Section, are also used to indentify the dependency of the model on various parameters. In Table 2.1 these individual model setups are summarized.

Table 2.1: Summary of individual model setups used for the summer as well as for the winter period.

Classification	Description
Sim_{Basic}	horizontal resolution: 28 km x 28 km (156 x 136 grid cells); restart condition; climatological lidar profile at the lateral model boundaries; EC threshold: 20%; hygroscopic growth up to RH = 95% (no growth for EC and $\mathrm{PPM}^{*}_{2.5}$); feedback
$\mathrm{Sim}_{Standard}$	like Sim_{Basic}, but with the Standard Profile to describe the lateral model boundaries
Sim_{Ind}	like Sim_{Basic}, but with the individual lidar profiles to describe the lateral model boundaries
Sim_{dry}	like Sim_{Basic}, but without hygroscopic growth for all substances (dry conditions for all chemical substances)
Sim_{noEmi}	like Sim_{Basic}, but without local emissions within the entire model domain
$\mathrm{Sim}_{noTrans}$	like Sim_{Basic}, but without transport of substances from outside into the model domain
Sim_{long}	like Sim_{Basic}, but without cycles (COSMO performs its calculation alone for 24 hours and then MUSCAT is started and both run in parallel till the end of the simulation period)
Sim_{14km}	like Sim_{Basic}, but with a horizontal resolution of 14 km x 14 km (312 x 272 grid cells)
Sim_{EC5}	like Sim_{Basic}, but a threshold of 5% for EC fraction to separate between “urban” and “continental” aerosol types
$\mathrm{Sim}_{NoAerosol}$	like Sim_{Basic}, but without impact of “urban” and “continental” aerosol on the solar radiation within COSMO – MUSCAT
$\mathrm{Sim}_{AerosolNoFB}$	like Sim_{Basic}, but urban and continental aerosol types influence the radiation only; without influence on further processes and therefore without feedback
Sim_{Tanre}	in general like Sim_{Basic} but with the original description (Tanré scheme) of “urban” and “continental” aerosol for the radiation scheme of COSMO

Chapter 3

Observation data

3.1 Vertical backscatter coefficients

For the profiling of the atmosphere, remote-sensing lidar measurements can be used (Weitkamp, 2005). This technique is used at the ground as well as on aircrafts and on satellites. Light pulses of a specific wavelength (λ) are generated by a laser. Atmospheric particles and molecules cause an absorption and a scattering of the laser beam. Backscattered laser light is received and converted into an electrical signal which can be described by the lidar equation (see also Section 1.4, Weitkamp (2005)):

$$P(R,\lambda) = K\,G(R)\,\beta(R,\lambda)\underbrace{\exp\left[-2\int_0^R \alpha(r,\lambda)dr\right]}_{T(R,\lambda)} \tag{3.1}$$

with $P(R,\lambda)$ as the power which is received from the distance R of a specific wavelength λ. K describes the performance of the lidar system, G a geometric factor, β represents the backscatter coefficient, α the extinction caused by aerosols and molecules and T the transmission which can take values between 0 and 1. Based on the magnitude of the received backscatter signal combined with the distance, information about various atmospheric parameters (e.g., temperature, wind and relative humidity) and the detection of aerosols and clouds is possible. The backscatter coefficient $\beta(R,\lambda)$, mentioned here, is a corrected value. An attenuation of the emitted radiation through the atmosphere occurs which can be very distinct for thick aerosol layers and clouds. The corrected value $\beta(R,\lambda)$ is determined based on the attenuated signal $\beta'(R,\lambda)$ and

Table 3.1: EARLINET stations providing data used for this study. The numbers within the last two columns represent the date of the observation. The number of available profiles is given in brackets. The lidar profiles are based on vertical backscatter coefficients obtained at 532 nm and 510 nm (only Sofia).

Station	Latitude (degree)	Longitude (degree)	Altitude (m)	July 2006	February 2007
Barcelona (Spain)	41.4	2.2	115	24 (1)	19 (1)
Bilthoven (The Netherlands)	52.1	5.2	5	24 (1)	
Granada (Spain)	37.2	-3.6	680	24 (1)	16 (4)
Ispra (Italy)	45.8	8.6	225		22 (12), 26 (1)
Leipzig (Germany)	51.4	12.4	90	24 (2)	17 (1), 21 (1), 22 (1)
Madrid (Spain)	40.5	-3.7	669	20 (1), 24 (1), 25 (1)	
Napoli (Italy)	40.8	14.3	118	24 (1)	21 (1)
Palaiseau (France)	48.7	2.2	162		18 (2), 26 (5)
Potenza (Italy)	40.6	15.8	760	24 (1)	
Saint Michel (France)	43.9	5.7	683		18 (4), 26 (1)
Sofia (Bulgaria)	42.7	24.4	550	24 (14), 25 (4)	
Thessaloniki (Greece)	40.7	23.0	60	19 (2), 20 (1), 21 (2), 23 (22), 24 (12), 25 (5)	

the transmission:

$$\beta(R,\lambda) = \frac{\beta'(R,\lambda)}{T(R,\lambda)}. \tag{3.2}$$

The calculation of the vertical extinction profile can be obtained by using the extinction-to-backscatter (lidar) ratio (S):

$$\alpha = \beta\, S. \tag{3.3}$$

The choice of the lidar ratio strongly depends on the aerosol type with low values ($\sim$23 sr at $\lambda = 532$ nm) for aerosol of marine origin and higher values ($\sim$53 sr at $\lambda = 532$ nm) for aerosol of urban origin in Europe (Table 1, Müller et al., 2007).

3.1.1 Ground-based lidar profiles

Since 2000, observations from ground-based lidar stations in Europe are assembled within EARLINET (EARLINET, 2012). The large number of data, based on such long-term observation, allows to analyze aerosol properties depending on the air mass (Wandinger et al., 2004) and derive particle characteristics (Mattis et al., 2008). EARLINET lidar profiles provide information about the occurrence, the transport and the optical properties of specific aerosol types as presented by Ansmann et al. (2003) in case of Saharan dust transport and by Ansmann et al. (2010) in case of the transport of volcanic aerosol within Europe. Currently, at about 27 stations measurements of vertical profiles of extinction and backscatter coefficients are performed. In Table 3.1 those stations are summarized, which are used for this study together with the number of profiles (within brackets) which are available for both time periods.

In general, observations are performed three times a week at the same time to obtain information about the vertical and horizontal distribution of aerosol and its transport within Europe (Bösenberg et al., 2003). For instance, Wandinger et al. (2004) used lidar observations at different EARLINET sites to analyze the modification of air masses regarding their planetary boundary layer (PBL) and particle optical depth. Additionally, intensive measurements are performed for special cases. The summary of data from several stations is the basis for statistical analysis, examination of optical aerosol properties on a continental scale and the tracking of certain events, like Saharan dust (e.g., Müller et al., 2003), volcanic eruptions (e.g., Ansmann et al., 2010) or high aerosol load in the free troposphere (e.g., Mattis et al., 2003). The observations are performed by using multi spectral backscatter lidar often in combination with Raman lidar (Bösenberg et al., 2003). Intercomparison campaigns of lidars, used for the EARLINET network, assure the comparability of the individual data (Pappalardo et al., 2004).

Vertical profiles of extinction and backscatter coefficients at EARLINET stations are average profiles which represent the atmospheric condition for a specific time range. The beginning as well as the end of the observation periods are known for each average profile. This information is needed when comparison with model simulations are done. Model outputs are saved hourly, which leads to discrepancies when comparing simulation data with observation data, like ground-based lidar observations. The model outputs are therefore interpolated to the time of the observation.

3.1.2 Space-based lidar profiles

The CALIPSO (Cloud-Aerosol Lidar and Infrared Pathfinder Satellite Observation) satellite was launched in April 2006 (Winker et al., 2009). It flies in constellation with currently three other satellites (CloudSat, Aura and Aqua) within the A-Train formation (Stephens et al., 2002). Continuously measurements are performed between 82° N and 82° S at a sun – synchronous polar orbit at 705 km altitude. On board the satellite three instruments are placed:

- Cloud-Aerosol Lidar with Orthogonal Polarization (CALIOP)
- Wide Field Camera (WFC)
- Imaging Infrared Radiometer (IIR).

CALIOP is the main instrument performing measurements of vertical backscatter coefficients, whereas WFC and IIR are useful instruments to view the atmosphere, which is observed by the lidar to get additional information about the measurement conditions (Winker et al., 2009). The general task of this mission is to broaden the knowledge of aerosol and cloud properties and their influence on the climate. CALIPSO observations are useful for improving observationally-based estimates of direct and indirect aerosol radiative forcing, the characterization of the surface longwave radiative fluxes and atmospheric heating rates as well as to improve model parameterizations of cloud-climate feedbacks (Winker et al., 2006).

Measurements of backscatter coefficients are performed at two different wavelengths (532 nm and 1064 nm) by using a near-nadir viewing polarization lidar. Because of the distance between satellite and earth surface the beam diameter at the surface is ~ 70 m with a footprint at every 335 m (horizontal resolution). Filters are used to reduce the background illumination. Design and function of CALIOP are summarized in detail by Winker et al. (2009).

The large amount of data from CALIPSO observations offers the possibility to perform a variety of studies. Because of the dense structure, dust storm events, their transport and optical properties are often in the focus of scientific studies, whereas difficulties to discriminate between clouds and dust layers are mentioned by Liu et al. (2004, 2009). Liu et al. (2008) used the satellite observation data to get information about the height-resolved global distribution of dust aerosols. These kind of information can help to estimate the influence of dust particles on the climate.
Another important part of CALIPSO data usage is the information about the global cloud distribution and their properties. Discrimination between water and ice clouds (Hu et al., 2010) as well as the determination of cloud phase and the orientation of ice crystals (Yoshida et al., 2010) is of big interest regarding their effect on earth climate. Continuous measurements by the CALIPSO satellite offer the possibility to statistically analyze the vertical cloud structure and compare these results to a cloud model (Rossow and Zhang, 2010). Location of tropical clouds and their precipitation are also evaluated by Zhang et al. (2010) by using a Community Atmosphere Model version 3 (CAM3).
Ground-based lidar observations are performed since several years and can therefore

help to evaluate the space-based observations. Comparisons between ground-based, airborne and CALIOP observations have been performed by Chazette et al. (2010). The observations in the lower troposphere point to the ability of CALIOP to determine the structure of aerosol layers with AOD ($\lambda = 532\,\mathrm{nm}$) lower than 0.3, with a lower limit of 0.1 during day and of 0.07 during night. Ground-based lidar measurements, performed at the EARLINET stations, are used for a comprehensive comparison with CALIPSO data by Pappalardo et al. (2010). The authors found a generally good performance of CALIPSO level 1 data (continuous single-shot profiles) whereas differences occur mainly below 2 km but without significant bias.

A detailed sensitivity study of the extinction coefficient (level 2, version 2) of the CALIOP measurements is done by Kacenelenbogen et al. (2011). Next to the CALIOP observations, the authors used observation data from MODIS (Moderate Resolution Imaging Spectroradiometer; King et al. (1992)), POLDER (Polarization and Directionality of the Earth's Reflectances; Deschamps et al. (1994)), AERONET and HSRL (High Spectral Resolution Lidar; Hair et al. (2008)) performed on 4 August 2007, for intensive studies. In case of the CALIOP AOD, the authors identified the low signal-to-noise ratio of CALIOP, what causes a misclassification of the aerosol layer. Additionally, errors of the lidar ratio and of the calibration coefficient for day-time observations of attenuated backscatter profiles can occur.

Among others, problems concerning the underestimation of the multiple scattering effect are mentioned. This was also noted by Wandinger et al. (2010) who compared ground- and space-based extinction coefficients and lidar ratios and found significant differences for desert dust.

Detailed studies about the agreement between CALIOP observations and model simulations are performed by Yu et al. (2010) and Koffi et al. (2012). The large amount of available data based on CALIOP observations are potentially very useful for detailed model studies. The authors performed model simulations for 12 (Yu et al., 2010) and 13 (Koffi et al., 2012) regions, which are nearly identical. For these different places, the occurrence of specific aerosol types, like dust, marine or industrial pollution is identified. Yu et al. (2010) performed the comparison for 12 regions by means of one model (GOCART; e.g., Chin et al. (2000); Ginoux et al. (2001); Textor et al. (2006)) from June 2006 to November 2007. The authors found good agreements between CALIOP measured and GOCART computed aerosol extinction scale heights and lidar ratios. Differences occur in case of the reproduction of e.g., aerosol extinction over the Indian sub-continent and for dust source regions. Koffi et al. (2012) used 12 global models from AeroCom to reproduce CALIOP observations from 2007 to 2009. The analysis of the extinction mean height, computed by the different models and derived from CALIOP data, helps to identify strengths and weaknesses of the model for specific regions and time segments.

CALIOP backscatter coefficients

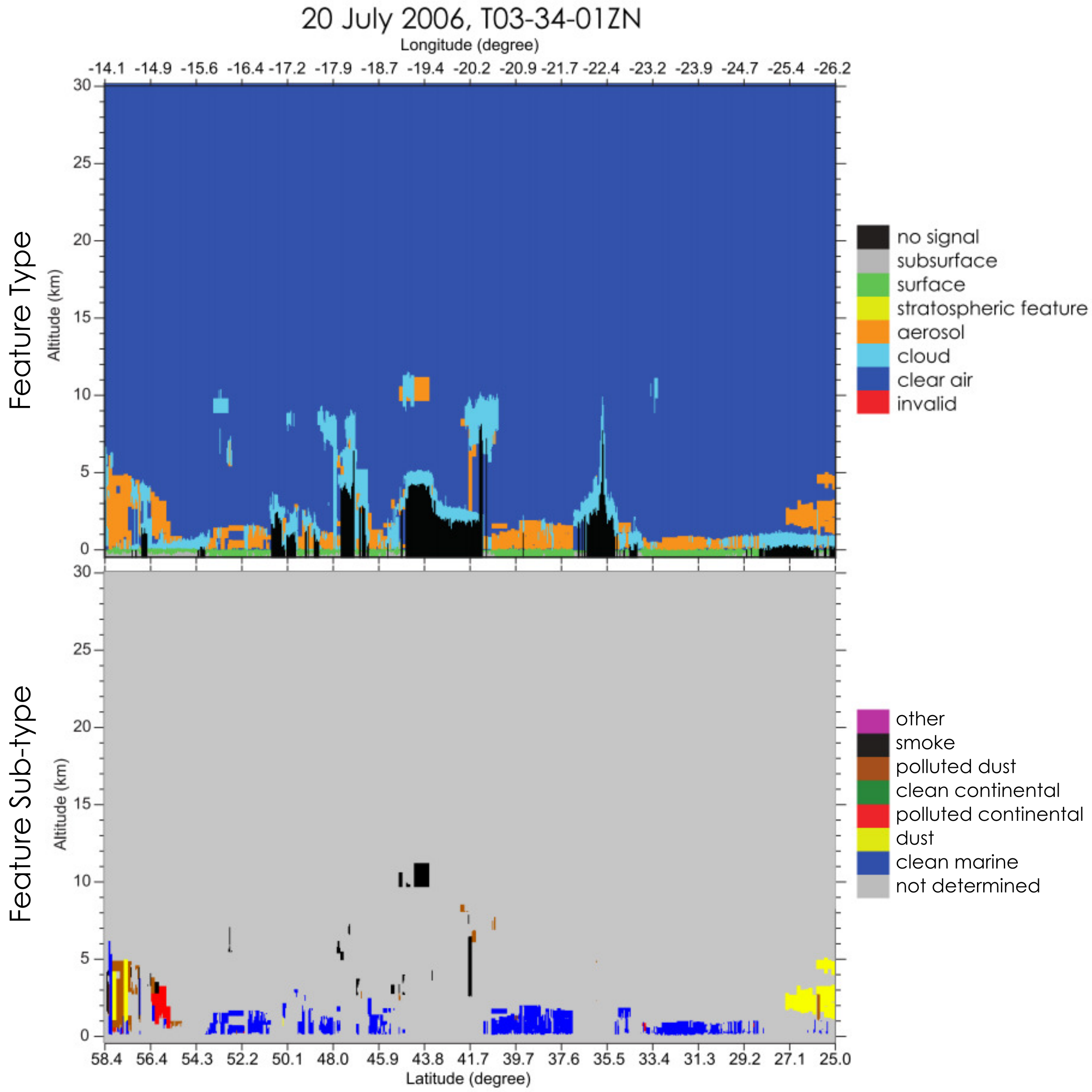

Figure 3.1: Vertical feature mask (upper panel) and aerosol subtypes (lower panel) based on the CALIPSO overpass on 20 July 2006 (CALIPSO time: T03-34-01ZN) for a specific geographical range.

Various data sets of the CALIOP observations are available. For this study it is decided to use these data which are recommended for studies: Data with a horizontal resolution of 5 km and labeled as level 2, version 3.01 (CAL_LID_L2_05kmAPro-Prov-V3-01; CALIPSO L2 V3.01 (2012)). Additionally, data with a horizontal resolution of 40 km (level 2, version 2.01; CAL_LID_L2_40kmAProCal-Beta-V2-01; CALIPSO L2 V2.01 (2012)) are used as well, though these data are not recommended for publications. Both data sets are available at the homepage of the ASDC (Atmospheric Science Data Center; ASDC (2012)) and contain information about the aerosol profiles only.

Vertical backscatter profiles with a horizontal resolution of 5 and 40 km are determined based on CALIOP rawdata (CALIPSO L1B, 2012). These rawdata contain single-shot profiles of attenuated backscatter coefficients. Young and Vaughan (2009) describe the conversion of attenuated backscatter coefficient into backscatter coefficient in case of CALIOP lidar profiles in detail. Backscatter values can be caused by clouds, aerosol or other atmospheric features. It is assumed that each vertical backscatter profile contains clouds and/or aerosol. Further, the molecular backscattering is known and can be modeled. Therefore, discrepancies of the molecular backscattering has to be caused by clouds and/or aerosols and random noise. In a first step, a threshold for each profile is determined, which makes sure that backscatter coefficients above these values are trustworthy and caused by clouds or aerosols. A detailed description of the threshold detection is given by Vaughan et al. (2009). If the threshold is exceeded within a specific altitude range, feature (e.g., aerosol and cloud) boundaries are determined. Horizontal and vertical averaging of CALIOP backscatter values produces higher contrasts between weak backscatter values, caused by disperse aerosols and clear air. By using a high resolution cloud-clearing algorithm, cloud-free profiles can be generated. In cases where the detection limit does not show the occurrence of clouds or aerosols, a default value of -9999 is set instead of a backscatter value (CALIPSO L2 V3.01, 2012). However, this procedure does not mean that the air is free of aerosol when a default value of -9999 is used.

Backscatter coefficients of aerosols are weaker than those of clouds. Therefore, the averaging over specific distances (vertical and/or horizontal) offers the possibility to detect also weak backscatter values. It has to be mentioned, that CALIOP data with a horizontal resolution of 40 km were available at first. But the request for aerosol backscatter profiles with a higher horizontal resolution leads to the preparation of the CALIOP data set with a horizontal resolution of 5 km. The analysis of the backscatter profiles with the 40 km horizontal resolution is different from the 5 km CALIOP data. In case of the coarse resolution the backscattering below an aerosol or cloud layer is not analyzed and thus often no backscatter values are available near the surface. For CALIOP data with the fine horizontal resolution continuous profiles between the surface and a distinct aerosol or cloud layer are generated.

In case of CALIOP data with 5 km horizontal resolution, side by side profiles are sometimes identical because of the weak aerosol backscattering, whereas with the coarser horizontal resolution such identical profiles are rare.

Profiles with horizontal resolution of 5 km contain information about the backscatter coefficients from -0.44 km to 29.84 km with 399 height levels in total, whereas a higher vertical resolution is available within the tropospheric region. In case of the horizontal resolution of 40 km the vertical profiles of backscatter values are available between -0.35 km and 29.75 km with 199 height levels in total.

CALIOP data of level 2 (version 2.01 and version 3.01) are screened and averaged for specific horizontal and vertical distances by ASDC, but further screenings are necessary by the user. The CALIOP data set with the horizontal resolution of 5 km contains information about the Atmospheric Volume Description (AVD) and the Cloud-Aerosol Discrimination (CAD) for each bin with the same horizontal resolution as for the backscatter coefficients.
The AVD contains information about special features (no signal, subsurface, surface, stratospheric feature, aerosol, cloud, clear air and invalid, Figure 3.1 (upper panel)). For the aerosol feature, classification into clean marine, dust, polluted continental, clean continental, polluted dust, smoke and other aerosol types is done (Figure 3.1, lower panel). It is mentioned in Section 2.3 that the version of the regional model used here does not contain marine and dust aerosol types. By using the AVD it is thus possible to remove these aerosol types from the CALIOP data for future model comparisons.
In case of cloud and aerosol features, additional information is available. The CAD algorithm describes the confidence of the detected features and helps to determine a correct lidar ratio (Liu et al., 2004, 2009). It also makes sure that aerosol layers are not contaminated by clouds or take a dense aerosol layer (like dust) as a cloud. Therefore probability distribution functions (PDFs) are used, where optical and physical differences of clouds and aerosols are used for the discrimination (Liu et al., 2004). Input information for the PDFs are

- the layer averaged attenuated backscatter coefficient at 532 nm,
- the attenuated total backscatter color ratio $(\chi)^1$,
- the volume depolarization ratio $(\delta_V)^1$,
- the integrated attenuated backscatter from the top to the base of the layer,
- the midlayer heights
- and the midlayer temperature.

---

[1] Section A.3

The results are given as percentiles ranging from -100 to 100 (negative values represent aerosol and positive values cloud features). The higher the absolute CAD value, the better the confidence in the data, whereas difficulties occur at the edges of clouds, layers where clouds and aerosols are mixed and layers below dense clouds (Liu et al., 2009).

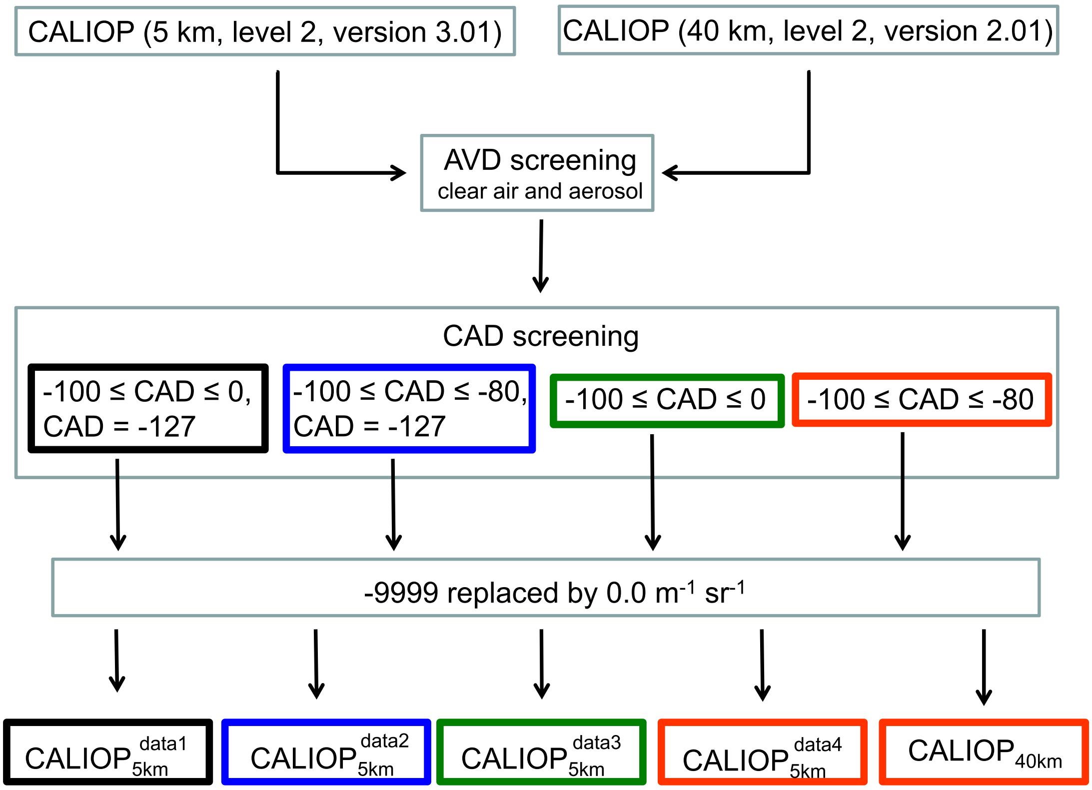

Figure 3.2: Flow chart of CALIOP data preparation.

CALIOP data have to be prepared before using the experimentally observed profiles of backscatter coefficients for comparisons with model results. It is decided to compile five different data sets, containing CALIOP data. Different limitations are used to create these CALIOP data sets to analyze the magnitude of the discrepancies among the data for a summer and a winter period. In Figure 3.2 a sketch summarizes the compilation of these data sets.

The AVD as well as the screening with the CAD score are applied to CALIOP data with the 5 and the 40 km horizontal resolution (Figure 3.2). For CALIOP data with a horizontal resolution of 5 km, the comparison between AVD and CAD is quite easy because of the same vertical and horizontal resolutions. The data with the horizontal resolution of 40 km is also screened by using the AVD and CAD with the 5 km horizontal resolution. Thus, the information of the AVD profiles within the 40 km distance is

used. The same procedure is done with the CAD score for the horizontal and vertical distance.
As the first step, the AVD screening is used to exclude vertical profiles of backscatter coefficients where other atmospheric features than aerosol and clear air are found. As mentioned before, CALIOP data used here is prepared by ASDC and contain backscatter coefficients caused by identified aerosols only. The sorting out these vertical profiles where e.g., clouds were identified, ensures that all final profiles are definitely without cloud influence.
For the second step, the CAD score is used. In one case (Figure 3.2, black box) it is decided to allow a large CAD score range from -100 to 0. Within this range, backscatter coefficients are caused by aerosols, but with different confidence. Additionally, a CAD score of -127 is allowed. This value is not described within the CALIOP data manuals but refers clearly to those range bins where the backscatter coefficients were set to the default value of -9999. Thus, vertical profiles containing only values of -9999 are also present.
For a second case (Figure 3.2, blue box), the CAD score range is limited from -100 to -80, whereas a CAD score of -127 is allowed as well. The range of $-100 \leq \mathrm{CAD} \leq -80$ is quite narrow compared to the range for high confidence ($-100 \leq \mathrm{CAD} \leq -70$) which is given by Liu et al. (2009), but it is assumed that the backscatter values of that individual bin are definitely caused by aerosols. That means, the vertical profiles where the aerosol CAD scores are not in accordance to the allowed CAD score range, are excluded. This second approach is in a clear contrast to the first approach.
The evaluation of the third CALIOP data set (Figure 3.2, green box) offers the elimination of those vertical profiles where only default values of -9999 are found, whereas the CAD score involves all confidences for aerosol determination ($-100 \leq \mathrm{CAD} \leq 0$). This data set is comparable with the first one, but does not include vertical profiles where only values of -9999 are found.
Another calculation is done for CALIOP data with 5 and 40 km horizontal resolution. Here, the CAD score is limited from -100 to -80 and profiles, which contain only values of -9999 are sorted out as well (Figure 3.2, red boxes). This approach represents the application of the strictest limitations used for the CALIOP data.

It is unlikely that profiles do not contain any aerosol, thus the default value of -9999 is not realistic. It is decided to remove all values of -9999 from all data sets (Figure 3.2) and replace them by a backscatter value of $0.0\,\mathrm{m}^{-1}\,\mathrm{sr}^{-1}$, representing the lowest limit of backscatter values. Thus, vertical profiles containing backscatter values of $0.0\,\mathrm{m}^{-1}\,\mathrm{sr}^{-1}$ are created and can be found in data sets with 5 km horizontal resolution ($\mathrm{CALIOP}_{5km}^{data1}$, $\mathrm{CALIOP}_{5km}^{data2}$, $\mathrm{CALIOP}_{5km}^{data3}$ and $\mathrm{CALIOP}_{5km}^{data4}$) and with the coarse

Table 3.2: Characteristics of the CALIOP data sets ($\text{CALIOP}^{data1}_{5km}$, $\text{CALIOP}^{data2}_{5km}$, $\text{CALIOP}^{data3}_{5km}$, $\text{CALIOP}^{data4}_{5km}$, CALIOP_{40km}) during 19 – 26 July 2006.

$\text{CALIOP}^{data1}_{5km}$

	All data	Without dust aerosol type	Without marine aerosol type	Without marine and dust aerosol type
Number of profiles	11925	9294	9496	7175
Number of values	1581152	1232208	1259110	951220
Number of $\beta = 0.0\,\text{m}^{-1}\,\text{sr}^{-1}$	1229900	1003325	977674	780306
Number of $\beta < 0.0\,\text{m}^{-1}\,\text{sr}^{-1}$	3775	2705	2876	1855
β_{min} ($\text{m}^{-1}\,\text{sr}^{-1}$)	$-5.6\,\text{x}\,10^{-5}$	$-5.6\,\text{x}\,10^{-5}$	$-5.6\,\text{x}\,10^{-5}$	$-5.6\,\text{x}\,10^{-5}$
β_{max} ($\text{m}^{-1}\,\text{sr}^{-1}$)	$1.4\,\text{x}\,10^{-4}$	$1.2\,\text{x}\,10^{-4}$	$1.4\,\text{x}\,10^{-4}$	$9.7\,\text{x}\,10^{-5}$
β_{mean} ($\text{m}^{-1}\,\text{sr}^{-1}$)	$3.1\,\text{x}\,10^{-7}$	$2.6\,\text{x}\,10^{-7}$	$3.0\,\text{x}\,10^{-7}$	$2.4\,\text{x}\,10^{-7}$

$\text{CALIOP}^{data2}_{5km}$

	All data	Without dust aerosol type	Without marine aerosol type	Without marine and dust aerosol type
Number of profiles	10529	8428	8289	6464
Number of values	1395975	1117391	1098986	856956
Number of $\beta = 0.0\,\text{m}^{-1}\,\text{sr}^{-1}$	1097687	914743	864584	707383
Number of $\beta < 0.0\,\text{m}^{-1}\,\text{sr}^{-1}$	3299	2320	2446	1513
β_{min} ($\text{m}^{-1}\,\text{sr}^{-1}$)	$-5.6\,\text{x}\,10^{-5}$	$-5.6\,\text{x}\,10^{-5}$	$-5.6\,\text{x}\,10^{-5}$	$-5.6\,\text{x}\,10^{-5}$
β_{max} ($\text{m}^{-1}\,\text{sr}^{-1}$)	$1.4\,\text{x}\,10^{-4}$	$9.65\,\text{x}\,10^{-5}$	$1.4\,\text{x}\,10^{-4}$	$9.65\,\text{x}\,10^{-5}$
β_{mean} ($\text{m}^{-1}\,\text{sr}^{-1}$)	$3.0\,\text{x}\,10^{-7}$	$2.47\,\text{x}\,10^{-7}$	$2.93\,\text{x}\,10^{-7}$	$2.35\,\text{x}\,10^{-7}$

$\text{CALIOP}^{data3}_{5km}$

	All data	Without dust aerosol type	Without marine aerosol type	Without marine and dust aerosol type
Number of profiles	10095	7464	7667	5346
Number of values	1337980	989036	1016061	708171
Number of $\beta = 0.0\,\text{m}^{-1}\,\text{sr}^{-1}$	986728	760153	734625	537257
Number of $\beta < 0.0\,\text{m}^{-1}\,\text{sr}^{-1}$	3775	2705	2876	1855
β_{min} ($\text{m}^{-1}\,\text{sr}^{-1}$)	$-5.6\,\text{x}\,10^{-5}$	$-5.6\,\text{x}\,10^{-5}$	$-5.6\,\text{x}\,10^{-5}$	$-5.6\,\text{x}\,10^{-5}$
β_{max} ($\text{m}^{-1}\,\text{sr}^{-1}$)	$1.4\,\text{x}\,10^{-4}$	$1.2\,\text{x}\,10^{-4}$	$1.4\,\text{x}\,10^{-4}$	$9.7\,\text{x}\,10^{-5}$
β_{mean} ($\text{m}^{-1}\,\text{sr}^{-1}$)	$3.6\,\text{x}\,10^{-7}$	$3.2\,\text{x}\,10^{-7}$	$3.7\,\text{x}\,10^{-7}$	$3.2\,\text{x}\,10^{-7}$

$\text{CALIOP}^{data4}_{5km}$

	All data	Without dust aerosol type	Without marine aerosol type	Without marine and dust aerosol type
Number of profiles	9762	7160	7375	5086
Number of values	1293669	948610	977184	673578
Number of $\beta = 0.0\,\text{m}^{-1}\,\text{sr}^{-1}$	973867	739631	721812	517960
Number of $\beta < 0.0\,\text{m}^{-1}\,\text{sr}^{-1}$	3071	2263	2284	1523
β_{min} ($\text{m}^{-1}\,\text{sr}^{-1}$)	$-5.6\,\text{x}\,10^{-5}$	$-5.6\,\text{x}\,10^{-5}$	$-5.6\,\text{x}\,10^{-5}$	$-5.6\,\text{x}\,10^{-5}$
β_{max} ($\text{m}^{-1}\,\text{sr}^{-1}$)	$1.4\,\text{x}\,10^{-4}$	$9.4\,\text{x}\,10^{-5}$	$1.4\,\text{x}\,10^{-4}$	$9.4\,\text{x}\,10^{-5}$
β_{mean} ($\text{m}^{-1}\,\text{sr}^{-1}$)	$3.4\,\text{x}\,10^{-7}$	$3.1\,\text{x}\,10^{-7}$	$3.5\,\text{x}\,10^{-7}$	$3.2\,\text{x}\,10^{-7}$

CALIOP_{40km}

	All data	Without dust aerosol type	Without marine aerosol type	Without marine and dust aerosol type
Number of profiles	778	530	511	324
Number of values	51049	34990	33170	21197
Number of $\beta = 0.0\,\text{m}^{-1}\,\text{sr}^{-1}$	41829	29313	27031	17887
Number of $\beta < 0.0\,\text{m}^{-1}\,\text{sr}^{-1}$	1	1	0	0
β_{min} ($\text{m}^{-1}\,\text{sr}^{-1}$)	$-2.6\,\text{x}\,10^{-8}$	$-2.6\,\text{x}\,10^{-8}$	0.0	0.0
β_{max} ($\text{m}^{-1}\,\text{sr}^{-1}$)	$2.8\,\text{x}\,10^{-5}$	$2.8\,\text{x}\,10^{-5}$	$1.1\,\text{x}\,10^{-5}$	$1.1\,\text{x}\,10^{-5}$
β_{mean} ($\text{m}^{-1}\,\text{sr}^{-1}$)	$2.5\,\text{x}\,10^{-7}$	$2.2\,\text{x}\,10^{-7}$	$2.4\,\text{x}\,10^{-7}$	$2.0\,\text{x}\,10^{-7}$

horizontal resolution (CALIOP$_{40km}$). The default value of -9999 often occurs at higher altitudes where the backscattering by aerosols can be very weak and thus below the backscatter detection limit.

As mentioned, within the model version used here, marine and dust aerosol type are not implemented and thus offer the focus on anthropogenic aerosol. It is decided to remove consecutively all these backscatter profiles where marine or dust aerosol types are detected by means of the AVD information. Thus, CALIOP data containing backscatter coefficients of all aerosol types, without backscatter values of marine aerosol, without backscatter values of dust aerosol and data sets without the backscatter values of both aerosol types are generated for both simulation periods and data sets. Some characteristics of the various data sets are summarized in Table 3.2 for the summer case and in Table 3.3 for the winter case.

Both tables show a large fraction of backscatter values which are equal to $0.0\,\mathrm{m}^{-1}\,\mathrm{sr}^{-1}$. During July 2006, fractions of 78% (CALIOP$_{5km}^{data1}$), 79% (CALIOP$_{5km}^{data2}$), 74% (CALIOP$_{5km}^{data3}$), 75% (CALIOP$_{5km}^{data4}$) and 82% (CALIOP$_{40km}$) are found, including all aerosol types. During the winter period, the fractions for the individual data sets are higher: 87% (CALIOP$_{5km}^{data1}$, CALIOP$_{5km}^{data2}$ and CALIOP$_{40km}$), 82% (CALIOP$_{5km}^{data3}$) and 84% (CALIOP$_{5km}^{data4}$). Excluding backscatter coefficients caused by marine or dust aerosol type, changes the fractions of values with $\beta = 0.0\,\mathrm{m}^{-1}\,\mathrm{sr}^{-1}$, but do not differ significantly from the data set which includes backscatter values of all aerosol types. Whereas a high fraction of values with $\beta = 0.0\,\mathrm{m}^{-1}\,\mathrm{sr}^{-1}$ is found, the fraction for $\beta < 0.0\,\mathrm{m}^{-1}\,\mathrm{sr}^{-1}$ is quite low with a maximum of 0.3% only (Tables 3.2 – 3.3). In case of CALIOP data with a horizontal resolution of 40 km, the fraction of negative backscatter values is very low or equal to zero. It was decided to substitute negative backscatter values not for values of $0.0\,\mathrm{m}^{-1}\,\mathrm{sr}^{-1}$, because values lower than zero are caused due to noise and compensate too high positive backscatter values.

CALIOP data with a horizontal resolution of 40 km are clearly different from those with a higher resolution in case of the minimum and maximum backscatter values (Tables 3.2 – 3.3). The range from minimum to maximum backscatter values is smaller for CALIOP$_{40km}$ than for CALIOP$_{5km}^{data1}$, CALIOP$_{5km}^{data2}$, CALIOP$_{5km}^{data3}$ and CALIOP$_{5km}^{data4}$, whereas the change of minimum and maximum values after sorting out backscatter values caused by marine or dust aerosol is often not significant. The average backscatter coefficients of the individual data sets (all data, without dust aerosol type, without marine aerosol type, without marine and dust aerosol type) of CALIOP$_{5km}^{data1}$ and CALIOP$_{5km}^{data2}$ as well as of CALIOP$_{5km}^{data3}$ and CALIOP$_{5km}^{data4}$ are often similar. This is found for both simulation periods and shows the distinct influence of the vertical profiles which contain values of $0.0\,\mathrm{m}^{-1}\,\mathrm{sr}^{-1}$ only, whereas the influence of the narrow CAD range from -100 to -80 in contrast to $-100 \leq \mathrm{CAD} \leq 0$ seems to influence the statistical data only weakly. The average backscatter coefficient of CALIOP$_{40km}$ differs often from those with the higher horizontal resolution and is always lower than the other ones (Tables 3.2 – 3.3).

Figure 3.3 shows the average vertical profiles of backscatter coefficients based on the five different CALIOP data sets for both summer and winter period. In general, all profiles are similar in shape and magnitude of the vertical backscatter values during 19 – 26 July 2006 and 16 – 26 February 2007. For both simulation periods, the formation of the PBL is well represented by CALIOP$^{data1}_{5km}$, CALIOP$^{data2}_{5km}$, CALIOP$^{data3}_{5km}$, CALIOP$^{data4}_{5km}$ and CALIOP$_{40km}$. The shape of the profiles as well as the magnitude of the average backscatter values shows no cloud contamination of the CALIOP data showing a successful data screening. As mentioned, default values of -9999 were replaced by backscatter coefficients of $0.0\,\mathrm{m^{-1}\,sr^{-1}}$ for all five CALIOP data sets for the summer and winter period. Thus, the average CALIOP profiles represent the lowest limit of observed CALIOP data, whereas the upper limit remains unknown in this study.

For all data sets, the backscatter values near the surface are close to zero, an effect which is not very likely, because aerosol is definitely available near the surface and thus causes backscatter coefficients larger than zero. But only in case of CALIOP$_{40km}$ (all data, without and marine and dust aerosol type) the first backscatter coefficient above the surface is equal to zero, which is not the case for data of CALIOP$^{data1}_{5km}$, CALIOP$^{data2}_{5km}$, CALIOP$^{data3}_{5km}$ and CALIOP$^{data4}_{5km}$. This is caused by the different analysis for CALIOP data with 5 and 40 km horizontal resolution, as mentioned before.

Results based on CALIOP$^{data1}_{5km}$ are similar to CALIOP$^{data2}_{5km}$ and CALIOP$^{data3}_{5km}$ are similar to CALIOP$^{data4}_{5km}$. This is also shown in Figure 3.3. Especially, during July 2006, the average profiles of CALIOP$^{data1}_{5km}$ and CALIOP$^{data2}_{5km}$ are close together with highest discrepancies of $8.5\,\mathrm{x}\,10^{-5}\,\mathrm{m^{-1}\,sr^{-1}}$ at 3.8 km altitude (all data) and $4.9\,\mathrm{x}\,10^{-5}\,\mathrm{m^{-1}\,sr^{-1}}$ at 2.1 km altitude (without marine and dust aerosol type) only. Both profiles often contain lower backscatter values compared to CALIOP$^{data3}_{5km}$ and CALIOP$^{data4}_{5km}$ due to the higher number of $\beta = 0.0\,\mathrm{m^{-1}\,sr^{-1}}$ which leads to the calculation of lower average backscatter values (Table 3.2). The largest discrepancies between CALIOP$^{data3}_{5km}$ and CALIOP$^{data4}_{5km}$ are $1.6\,\mathrm{x}\,10^{-4}\,\mathrm{m^{-1}\,sr^{-1}}$ (all data) and $1.1\,\mathrm{x}\,10^{-4}\,\mathrm{m^{-1}\,sr^{-1}}$ (without marine and dust aerosol type) near the surface during summer. After excluding backscatter coefficients which are related to the existence of marine and dust aerosol types, a distinct separation of the average profiles of CALIOP$^{data1}_{5km}$ and CALIOP$^{data2}_{5km}$ from CALIOP$^{data3}_{5km}$ and CALIOP$^{data4}_{5km}$ during summer is found (Figure 3.3, left panel).

A similar behavior is also found for the winter simulation period (Figure 3.3, right panel). Results based on CALIOP$^{data3}_{5km}$ lead to highest backscatter values in con-

Table 3.3: Characteristics of the CALIOP data sets (CALIOP$^{data1}_{5km}$, CALIOP$^{data2}_{5km}$, CALIOP$^{data3}_{5km}$, CALIOP$^{data4}_{5km}$, CALIOP$_{40km}$) during 16 – 26 February 2007.

CALIOP$^{data1}_{5km}$

	All data	Without dust aerosol type	Without marine aerosol type	Without marine and dust aerosol type
Number of profiles	9487	8258	6402	5313
Number of values	1246993	1086221	842176	699871
Number of $\beta = 0.0\,\mathrm{m}^{-1}\,\mathrm{sr}^{-1}$	1081487	959352	745982	637620
Number of $\beta < 0.0\,\mathrm{m}^{-1}\,\mathrm{sr}^{-1}$	2136	1603	1558	1078
β_{min} ($\mathrm{m}^{-1}\,\mathrm{sr}^{-1}$)	$-1.4\,\mathrm{x}\,10^{-4}$	$-1.4\,\mathrm{x}\,10^{-4}$	$-4.2\,\mathrm{x}\,10^{-5}$	$-4.2\,\mathrm{x}\,10^{-5}$
β_{max} ($\mathrm{m}^{-1}\,\mathrm{sr}^{-1}$)	$4.3\,\mathrm{x}\,10^{-4}$	$2.1\,\mathrm{x}\,10^{-4}$	$4.3\,\mathrm{x}\,10^{-4}$	$2.1\,\mathrm{x}\,10^{-4}$
β_{mean} ($\mathrm{m}^{-1}\,\mathrm{sr}^{-1}$)	$3.5\,\mathrm{x}\,10^{-7}$	$2.7\,\mathrm{x}\,10^{-7}$	$3.1\,\mathrm{x}\,10^{-7}$	$2.0\,\mathrm{x}\,10^{-7}$

CALIOP$^{data2}_{5km}$

	All data	Without dust aerosol type	Without marine aerosol type	Without marine and dust aerosol type
Number of profiles	8555	7602	5771	4920
Number of values	1124690	999900	759314	648007
Number of $\beta = 0.0\,\mathrm{m}^{-1}\,\mathrm{sr}^{-1}$	979732	886707	676515	593396
Number of $\beta < 0.0\,\mathrm{m}^{-1}\,\mathrm{sr}^{-1}$	1653	1293	1204	873
β_{min} ($\mathrm{m}^{-1}\,\mathrm{sr}^{-1}$)	$-4.2\,\mathrm{x}\,10^{-5}$	$-4.2\,\mathrm{x}\,10^{-5}$	$-4.2\,\mathrm{x}\,10^{-5}$	$-4.2\,\mathrm{x}\,10^{-5}$
β_{max} ($\mathrm{m}^{-1}\,\mathrm{sr}^{-1}$)	$4.3\,\mathrm{x}\,10^{-4}$	$2.3\,\mathrm{x}\,10^{-4}$	$4.3\,\mathrm{x}\,10^{-4}$	$2.3\,\mathrm{x}\,10^{-4}$
β_{mean} ($\mathrm{m}^{-1}\,\mathrm{sr}^{-1}$)	$3.3\,\mathrm{x}\,10^{-7}$	$2.6\,\mathrm{x}\,10^{-7}$	$2.9\,\mathrm{x}\,10^{-7}$	$1.8\,\mathrm{x}\,10^{-7}$

CALIOP$^{data3}_{5km}$

	All data	Without dust aerosol type	Without marine aerosol type	Without marine and dust aerosol type
Number of profiles	7143	5925	4157	3079
Number of values	944611	785059	549987	408902
Number of $\beta = 0.0\,\mathrm{m}^{-1}\,\mathrm{sr}^{-1}$	779105	658190	453793	346651
Number of $\beta < 0.0\,\mathrm{m}^{-1}\,\mathrm{sr}^{-1}$	2136	1603	1558	1078
β_{min} ($\mathrm{m}^{-1}\,\mathrm{sr}^{-1}$)	$-1.4\,\mathrm{x}\,10^{-4}$	$-1.4\,\mathrm{x}\,10^{-4}$	$-4.2\,\mathrm{x}\,10^{-5}$	$-4.2\,\mathrm{x}\,10^{-5}$
β_{max} ($\mathrm{m}^{-1}\,\mathrm{sr}^{-1}$)	$4.3\,\mathrm{x}\,10^{-4}$	$2.1\,\mathrm{x}\,10^{-4}$	$4.3\,\mathrm{x}\,10^{-4}$	$2.1\,\mathrm{x}\,10^{-4}$
β_{mean} ($\mathrm{m}^{-1}\,\mathrm{sr}^{-1}$)	$4.6\,\mathrm{x}\,10^{-7}$	$3.8\,\mathrm{x}\,10^{-7}$	$4.8\,\mathrm{x}\,10^{-7}$	$3.4\,\mathrm{x}\,10^{-7}$

CALIOP$^{data4}_{5km}$

	All data	Without dust aerosol type	Without marine aerosol type	Without marine and dust aerosol type
Number of profiles	6912	5769	3946	2933
Number of values	909649	760028	520638	388154
Number of $\beta = 0.0\,\mathrm{m}^{-1}\,\mathrm{sr}^{-1}$	762637	647475	435910	333815
Number of $\beta < 0.0\,\mathrm{m}^{-1}\,\mathrm{sr}^{-1}$	1457	1010	1009	641
β_{min} ($\mathrm{m}^{-1}\,\mathrm{sr}^{-1}$)	$-4.2\,\mathrm{x}\,10^{-5}$	$-4.2\,\mathrm{x}\,10^{-5}$	$-4.2\,\mathrm{x}\,10^{-5}$	$-4.2\,\mathrm{x}\,10^{-5}$
β_{max} ($\mathrm{m}^{-1}\,\mathrm{sr}^{-1}$)	$1.9\,\mathrm{x}\,10^{-4}$	$1.3\,\mathrm{x}\,10^{-4}$	$1.9\,\mathrm{x}\,10^{-4}$	$1.3\,\mathrm{x}\,10^{-4}$
β_{mean} ($\mathrm{m}^{-1}\,\mathrm{sr}^{-1}$)	$4.1\,\mathrm{x}\,10^{-7}$	$3.4\,\mathrm{x}\,10^{-7}$	$4.2\,\mathrm{x}\,10^{-7}$	$2.9\,\mathrm{x}\,10^{-7}$

CALIOP$_{40km}$

	All data	Without dust aerosol type	Without marine aerosol type	Without marine and dust aerosol type
Number of profiles	425	333	206	133
Number of values	28019	22024	13351	8629
Number of $\beta = 0.0\,\mathrm{m}^{-1}\,\mathrm{sr}^{-1}$	24464	19525	11461	7616
Number of $\beta < 0.0\,\mathrm{m}^{-1}\,\mathrm{sr}^{-1}$	3	2	3	2
β_{min} ($\mathrm{m}^{-1}\,\mathrm{sr}^{-1}$)	$-2.6\,\mathrm{x}\,10^{-8}$	$-2.6\,\mathrm{x}\,10^{-8}$	$-2.6\,\mathrm{x}\,10^{-8}$	$-2.6\,\mathrm{x}\,10^{-8}$
β_{max} ($\mathrm{m}^{-1}\,\mathrm{sr}^{-1}$)	$4.8\,\mathrm{x}\,10^{-5}$	$4.0\,\mathrm{x}\,10^{-5}$	$4.8\,\mathrm{x}\,10^{-5}$	$1.0\,\mathrm{x}\,10^{-5}$
β_{mean} ($\mathrm{m}^{-1}\,\mathrm{sr}^{-1}$)	$2.6\,\mathrm{x}\,10^{-7}$	$2.1\,\mathrm{x}\,10^{-7}$	$2.5\,\mathrm{x}\,10^{-7}$	$1.3\,\mathrm{x}\,10^{-7}$

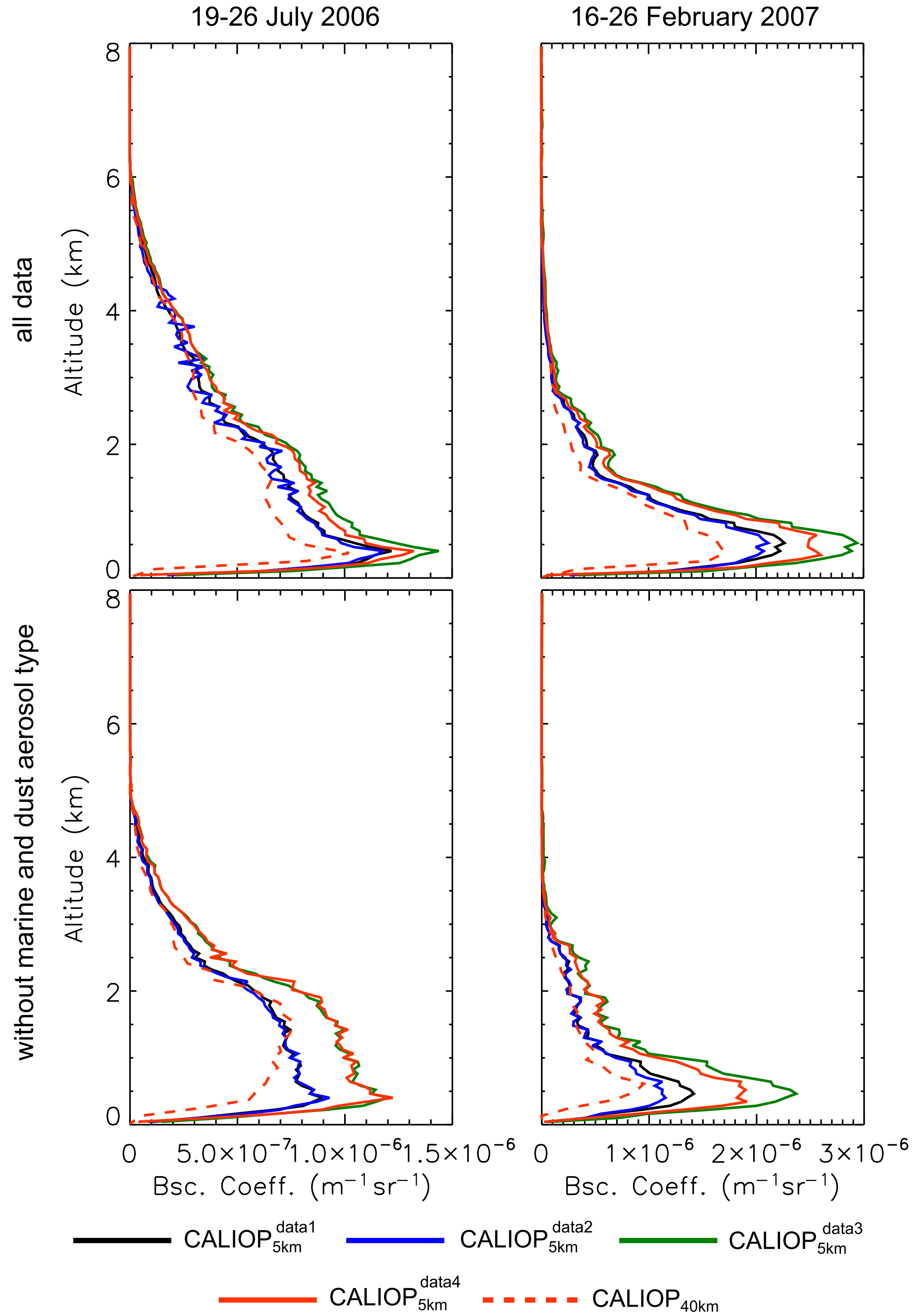

Figure 3.3: Average vertical profiles of backscatter coefficients, determined based on CALIOP$_{5km}^{data1}$ (black line), CALIOP$_{5km}^{data2}$ (blue line), CALIOP$_{5km}^{data3}$ (green line), CALIOP$_{5km}^{data4}$ (red line), CALIOP$_{40km}$ (dashed red line), for the data sets including all aerosol types (upper panel) and without marine and dust influence (lower panel) for the summer (left panel) and winter (right panel) period.

trast to the other CALIOP data sets before and after excluding backscatter values caused by marine and dust aerosol type. The vertical profiles of CALIOP$^{data1}_{5km}$ and CALIOP$^{data2}_{5km}$ are close together as well as those of CALIOP$^{data3}_{5km}$ and CALIOP$^{data4}_{5km}$. Largest discrepancies of $1.9\,\mathrm{x}\,10^{-4}\,\mathrm{m}^{-1}\,\mathrm{sr}^{-1}$ (at 0.46 km) are determined before sorting out backscatter values of marine and dust aerosol and of $3.0\,\mathrm{x}\,10^{-4}\,\mathrm{m}^{-1}\,\mathrm{sr}^{-1}$ (at 0.46 km) after sorting out between CALIOP$^{data1}_{5km}$ and CALIOP$^{data2}_{5km}$ during winter. The maximum differences between CALIOP$^{data3}_{5km}$ and CALIOP$^{data4}_{5km}$ are higher for this time period (all data: $4.5\,\mathrm{x}\,10^{-4}\,\mathrm{m}^{-1}\,\mathrm{sr}^{-1}$ at 0.52 km; without marine and dust aerosol type: $5.1\,\mathrm{x}\,10^{-4}\,\mathrm{m}^{-1}\,\mathrm{sr}^{-1}$ at 0.46 km).
For both simulation periods and for average CALIOP profiles before and after sorting out marine and dust caused backscatter coefficients, results with a horizontal resolution of 40 km (CALIOP$_{40km}$) are always lower than with a horizontal resolution of 5 km (CALIOP$^{data1}_{5km}$, CALIOP$^{data2}_{5km}$, CALIOP$^{data3}_{5km}$, CALIOP$^{data4}_{5km}$).

Figure 3.4 shows the location of vertical backscatter profiles after AVD and CAD screening based on CALIOP$^{data4}_{5km}$ (upper panel) and CALIOP$_{40km}$ (lower panel) horizontal resolution. The differently colored dots represent the data where marine (blue) or dust (yellow) aerosol was found. If both aerosol types are detected in one vertical profile, the location is represented by a green dot in Figure 3.4. The black dots are the location of the backscatter profiles without marine and dust aerosol types. Note that the high resolution of 5 km causes a very narrow location of the dots for the individual backscatter profiles, which can therefore overlap each other. Tables 3.2 – 3.3 helps to identify the actual number of the various profiles and individual backscatter coefficients.
For the summer case, a high number of vertical backscatter profiles is identified to contain dust, especially in the southern region of Europe. The fraction of backscatter profiles containing dust (27%) is nearly the same as the fraction of backscatter profiles containing marine aerosol (24%) for data of CALIOP$^{data4}_{5km}$ (Table 3.2). In case of the various data sets with 5 km horizontal resolution, these fractions are the highest ones. 20% of the profiles contain dust caused backscatter coefficients in case of CALIOP$^{data2}_{5km}$, which is the lowest fraction in contrast to CALIOP$^{data1}_{5km}$ (22%) and CALIOP$^{data3}_{5km}$ (26%). The fraction of these profiles containing marine caused backscatter coefficients during summer time is also slightly lower for CALIOP$^{data1}_{5km}$ (20%), CALIOP$^{data2}_{5km}$ (21%) and CALIOP$^{data3}_{5km}$ (24%) compared to the fraction of dust containing profiles. In case of the 40 km horizontal resolution, the fractions of profiles containing dust (32%) or marine (34%) aerosol are higher.
During winter, the fraction of dust containing profiles decreases significantly for all CALIOP data sets (CALIOP$^{data1}_{5km}$: 13%, CALIOP$^{data2}_{5km}$: 11%, CALIOP$^{data3}_{5km}$: 17%,

CALIOP$^{data4}_{5km}$: 17%, CALIOP$_{40km}$: 22%). On the other hand, the fraction of vertical profiles which contain backscatter coefficients related to marine aerosol type increases during the winter time (CALIOP$^{data1}_{5km}$: 33%, CALIOP$^{data2}_{5km}$: 33%, CALIOP$^{data3}_{5km}$: 42%, CALIOP$^{data4}_{5km}$: 43%, CALIOP$_{40km}$: 52%).

Backscatter coefficients, caused by dust aerosols, are also detected in the north of Europe e.g., Norway, Sweden and Great Britain, during July 2006. It cannot be ruled out, Saharan dust was transported to that region. However, the very scattered locations of dust detection can also be a hint of the misinterpretation of a cloud as a dust layer, which was also mentioned by Liu et al. (2004, 2009). For the winter case, backscatter

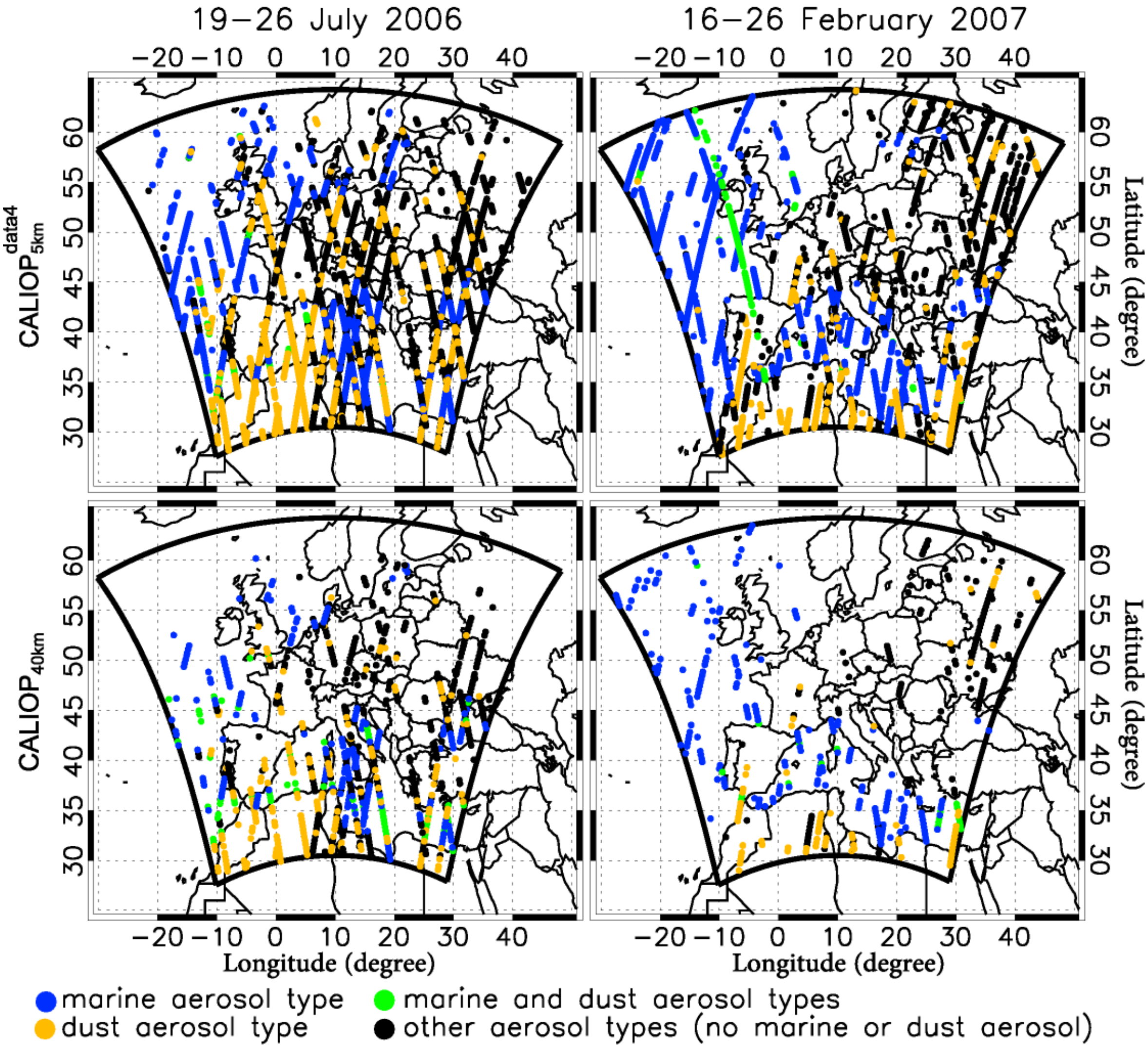

Figure 3.4: Location of vertical backscatter profiles where marine aerosol type (blue dots), dust aerosol type (yellow dots), marine and dust aerosol types (green dots) and other aerosol types (black dots) are found for the summer (left panel) and the winter (right panel) period based on CALIOP data with 5 (CALIOP$^{data4}_{5km}$) and 40 km (CALIOP$_{40km}$) horizontal resolution.

profiles containing dust are also found in e.g., Norway, Sweden, Finland and Russia. There a misinterpretation is likely.
In case of marine aerosol, the location of the backscatter profiles is particularly noticeable for both simulation periods (Figure 3.4). The CALIOP identification algorithm of the various aerosol types does not identify the marine aerosol type over land surface. In fact, sea salt is also found in continental regions, like Melpitz (Germany), a location far away from oceanic sources (Figure 5, Putaud et al., 2010). When eliminating those profiles which contain marine aerosol type to compare with the simulated data it has to be expected that backscatter values caused by marine aerosol are still present in the data over land after the screening process and can cause discrepancies between model and observation data.

Without question, CALIOP data are useful to get information about the vertical structure of the atmosphere. Additionally, information about the occurrence of specific aerosol types can help to identify important transport processes. But it is also shown in this section, that some information concerning the CALIOP data, needs to be more clarified. For instance, setting the backscatter values, depending on the circumstances, to default values of -9999 is not a realistic approach. Further, using the CAD score can be very helpful to make sure that aerosol is existing at a specific location. But a lot of information is getting lost, when the CAD score is used to sort out specific backscatter profiles. It is obvious, that the identification of specific aerosol types by CALIOP, leads to an important development of models regarding their ability to compute the occurrence and properties of these types. But especially in case of the identification of the marine aerosol, significant difficulties occur.

CALIOP data preparation for model comparison

Vertical profiles of CALIOP backscatter coefficients are used for comparisons with simulated profiles. The horizontal resolution of the model grid cells is 28 km x 28 km and 14 km x 14 km, respectively, which differs from the horizontal resolution of the CALIOP data (5 km, 40 km). Representative backscatter profiles have to be determined which can be used for further comparisons. The geographic coordinates as well as the observation time (UTC) of the lidar profiles are known. The output of the model simulations is saved every hour (UTC) which is not in accordance to the observation time. Thus, simulated backscatter profiles for every ten minute are calculated by linear interpolation of the hourly results. The simulation results which is closest to the observation time is compared to the CALIOP profile.

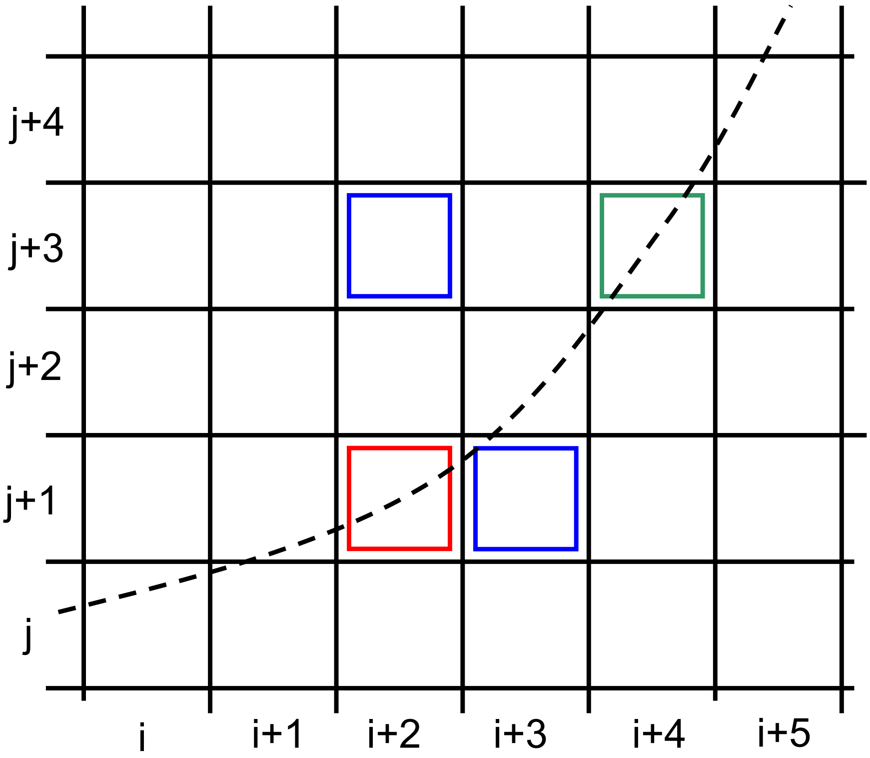

Figure 3.5: Sector of the model grid (black lines) with the location of a start position (red box) and stop positions (blue and green boxes). The dashed line represents a potential CALIPSO track over the model domain.

A second task is to determine the correct model grid cell where the CALIOP profile is located. CALIOP backscatter profiles with a horizontal resolution of 5 km and 40 km are average profiles based on 15 (5 km) and 60 (40 km) single-shot profiles (Young and Vaughan, 2009). The geographic position of the first and the last single-shot profile, which is used for the calculation of the average backscatter profile, is known. By means of these positions, the corresponding model grid cell is determined by using the Jordan curve theorem as described in Section A.1. Due to the different horizontal resolution of the CALIOP profiles and the model grid, as well as due to the CALIPSO flight track two results are possible:

1. First and last single-shot CALIOP backscatter profile, which limits the average backscatter profile geographically, are located within the same model grid cell.
2. First and last single-shot CALIOP backscatter profile are located in different model grid cells.

If the first case is true, the comparison between the average CALIOP backscatter profile (5 km or 40 km) with the simulation result is quite easy. If the second case is true, further analysis is needed:

1. The location of the model grid cells, determined for the first (Figure 3.5, red box) and the last (Figure 3.5, blue boxes) single-shot CALIOP backscatter profile, which limits the average CALIOP backscatter profile geographically, differs for only one direction.
2. The location of the model grid cells, determined for the first (Figure 3.5, red box) and the last (Figure 3.5, green box) single-shot CALIOP backscatter profile differs for both horizontal directions.

If the first case is true, simulated backscatter profiles of the model grid cells, determined for the first and the last single-shot profile and of those grid cells located in between, are used to calculate an average simulated backscatter profile. This average simulated backscatter profile can be used for comparisons with the observed backscatter profile (5 km, 40 km). If the second case is true, the CALIPSO flight track over the European domain is used to get additional information. The flight track (Figure 3.5, dashed line) between the geographic positions of the first and last single-shot profile is described by a polynomial fit of 4^{th} order. This section is divided into ten subsections, whose geographic positions are determined in the model grid. Finally, those simulated backscatter profiles where the first and the last single-shot profiles are found and of the model grid cells which are crossed by CALIPSO are used to calculate an average simulated backscatter profile. This profile is used for comparisons with the observed CALIOP backscatter profile with a horizontal resolution of 5 km or 40 km, respectively.

3.2 Aerosol optical depth

Long-term observations of AOD (also referred as τ_λ) are performed at several ground-based stations by AERONET. Worldwide, observations at around 682 stations are obtained (AERONET, 2012). The measurements are performed by using automatic sun and sky scanning spectral radiometers. Direct sun measurements are performed at eight wavelengths (standard: 440 nm, 670 nm, 870 nm, 940 nm and 1020 nm) whereas sky measurements are performed at 440 nm, 670 nm, 870 nm and 1020 nm (Holben et al., 1998). The AOD is defined as the degree of light transmission by absorption or scattering caused by aerosols:

$$\tau_\lambda = \int_{z_g}^{z_{TOA}} \alpha\left(\lambda, z\right) dz \tag{3.4}$$

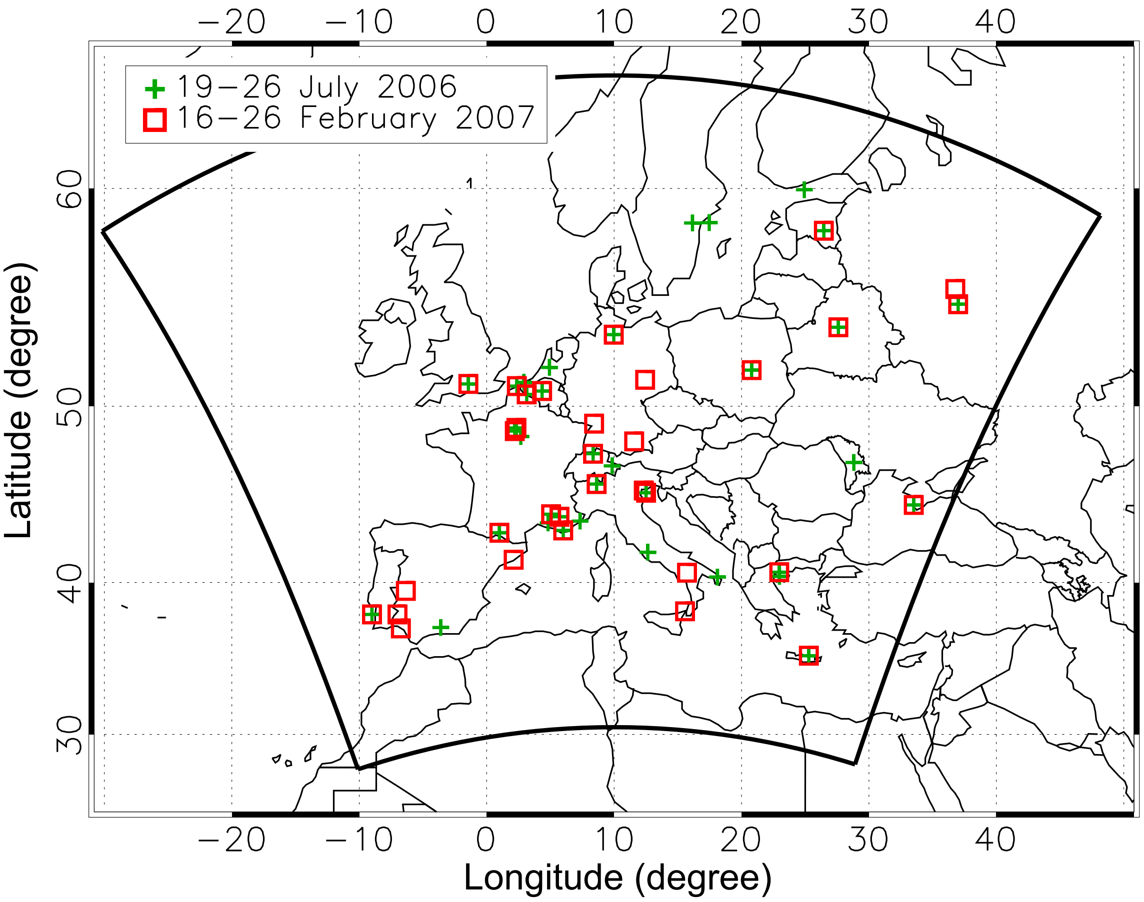

Figure 3.6: Location of AERONET stations used for this study. Green (red) crosses (boxes) represent those stations used for the summer (winter) period. The black lines indicate the lateral boundaries of the model domain.

with z_g as the altitude at ground level and z_{TOA} the altitude at TOA (Tombette et al., 2008). AERONET AOD values are provided for three different quality levels. Level 1.0 summarizes the unscreened data, level 1.5 data are cloud-screened and level 2.0 are cloud-screened and quality-assured (Smirnov et al., 2000). Based on calibration processes, reliable values of AOD are larger than 0.002 − 0.005 and an uncertainty of $\sim$0.01 − 0.02 (dependent on the wavelength) is given (Eck et al., 1999).

Holben et al. (2001) compiled a first aerosol climatology based on AERONET measurements. There, regions dominated by different aerosol types, were compared. Low mean annual values (0.08) of AOD ($\lambda = 500\,\text{nm}$) were found at island sites with clean oceanic conditions, whereas dust influenced sites are represented by higher annual mean AOD (0.44 − 0.55). While AOD can be used as an indicator of the attenuation of sunlight by atmospheric particles, the Ångström exponent (å) can be used to characterize

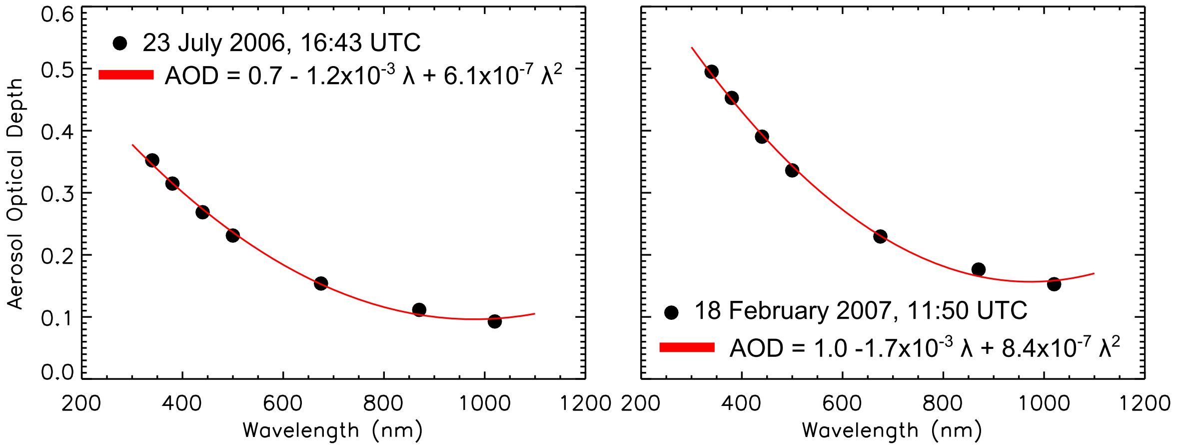

Figure 3.7: AOD data performed on 23 July 2006 (left graph) and on 18 February 2007 (right graph) in Hamburg, Germany. The black circles represents the measured AOD at different wavelengths (λ) and the red line represents the second order polynomial fit.

the size of such particles. It is derived from the dependency of AOD on the wavelength:

$$\mathring{a}_{\lambda_1,\lambda_2} = -\frac{dln\tau}{dln\lambda}. \tag{3.5}$$

The Ångström exponent decreases with increasing particle size. Holben et al. (2001) found Ångström exponents ($\lambda = 440 - 870\,\mathrm{nm}$) from 1.7 to 2.1 in South America and Southern Africa, indicating the presence of small particles caused by combustion processes. Optical properties of different aerosol types at different locations are also compared by Dubovik et al. (2002). Dependent on the location, the average AOD ($\lambda = 440\,\mathrm{nm}$) and the Ångström exponent ($\lambda = 440 - 870\,\mathrm{nm}$) can vary for urban-industrial and mixed aerosol (AOD: 0.24 – 0.43, å: 1.2 – 2.5), biomass burning aerosol (AOD: 0.38 – 0.80, å: 1.2 – 2.1) and desert dust and oceanic aerosol (AOD: 0.04 – 0.39, å: 0.0 – 1.6). Omar et al. (2005) used the large amount of AERONET data to categorize the aerosol properties by a cluster analysis, resulting in six categories (desert dust, biomass burning, background/rural, polluted continental, polluted marine and dirty pollution). Lowest values (0.036) of AOD ($\lambda = 673\,\mathrm{nm}$) are found for aerosol with rural background and high values (0.327) for desert dust aerosol. Desert dust particles are generally large, therefore an Ångström exponent ($\lambda = 441 - 673\,\mathrm{nm}$) of 0.608 is found for dust aerosol which is lower than for industrial polluted aerosol (å = 1.597).

In this study, level 2.0 data from 47 European AERONET stations are used. 36 AERONET stations obtained observations during 19 – 26 July 2006 and 33 stations during 16 – 26 February 2007. Not all stations performed measurements each day of the individual simulation period. Figure 3.6 represents the location of these stations for the summer and winter simulation period.

As mentioned before, AOD observations are performed at specific wavelengths. The wavelength dependence of the AOD is analyzed in detail by Eck et al. (1999) and also presented by Kaskaoutis and Kambezidis (2006) for the area of Athens (Greece). The wavelength dependencies of biomass burning aerosol, urban/industrial aerosol and desert dust aerosol are described by using a linear fit and a second-order polynomial fit. It is shown, that the usage of a second-order polynomial fit works best with only small differences between observed and computed AOD (uncertainty: $\sim 0.01 - 0.02$). An example of such a second-order polynomial fit is shown in Figure 3.7. AOD observation performed on 23 July 2006 and on 18 February 2007 in Hamburg (Germany) are used here. The AOD at 532 nm is determined for all observation data enabling comparisons between simulated ($\lambda = 550\,\mathrm{nm}$) and observed AOD.

3.3 Surface particle concentration

Within the EMEP programme (EMEP, 2012), observation data of e.g., PM, heavy metals, persistent organic pollutants and ground level ozone are collected and compiled (Simpson et al., 2003). Observations are performed at different sites in Europe over long time periods and during specific measurement campaigns. Therefore, these observation data are often used in several publications to compare with simulated data (e.g., Matthias, 2008; Péré et al., 2010; Solmon et al., 2006). Quaas et al. (2009) used EMEP observation of the near-surface sulfur dioxide and sulfate observation to analyze the aerosol indirect effect. Intensive measurement campaigns, like the EMEP EC/OC (organic carbon) campaign, are used to analyze new EC emission inventories of the regional EMEP model (Tsyro et al., 2007).

EMEP surface observation data of $\mathrm{PM}_{2.5}$ and EC as well as of SO_4^{2-} are used here. Such measurements are of major interest for comparisons with model simulations. Table 3.4 summarizes station names, location and available data during 19 – 26 July 2006 and 16 – 26 February 2007. In most cases, the temporal resolution of the observation is 24 hours. To get comparable results, those station data with a temporal resolution of 1 hour are converted into daily averages. The hourly saved model results of COSMO – MUSCAT are also converted into daily averages. Information about SO_4^{2-} concentrations are not individually saved from model simulations and are determined based on the fraction of the ion molar mass on the molar mass of the compounds $\mathrm{H}_2\mathrm{SO}_4$ and $(\mathrm{NH}_4)_2\mathrm{SO}_4$.

Table 3.4: EMEP stations and the availability of $PM_{2.5}$, EC and SO_4^{2-} during 19 – 26 July 2006 and 16 – 26 February 2007.

	Latitude	Longitude	Altitude	19 – 26 July 2006			16 – 26 February 2007		
Station	(degree)	(degree)	[m]	$PM_{2.5}$	EC	SO_4^{2-}	$PM_{2.5}$	EC	SO_4^{2-}
Aspvreten (Sweden)	58.8	17.4	20	x	-	-	x	-	-
Auchencorth Moss (United Kingdom)	55.8	-3.2	260	-	-	-	x	-	-
Barcarrota (Spain)	38.5	-6.9	393	x	-	x	x	-	x
Birkenes (Norway)	58.4	8.3	190	x	x	-	-	-	-
Cabo de Creus (Spain)	42.3	3.3	23	x	-	x	x	-	x
Campisabalos (Spain)	41.3	-3.1	1360	x	-	x	x	-	x
Chaumont (Switzerland)	47.1	7.0	1137	x	-	-	-	-	-
Els Torms (Spain)	41.4	0.7	470	x	-	x	x	-	x
Harwell (United Kingdom)	51.6	-1.3	137	x	-	-	x	-	-
Illmitz (Austria)	47.8	16.8	117	x	-	-	x	-	-
Iskrba (Slovenia)	45.6	14.9	520	x	-	-	x	-	-
Ispra (Italy)	45.8	8.6	209	x	x	x	x	x	x
Kosetice (Czech Republic)	49.6	15.1	534	x	-	-	x	-	-
Langenbrügge (Germany)	52.8	10.8	74	x	-	-	x	-	-
Mace Head (Ireland)	53.2	-9.5	15	x	-	-	x	-	-
Melpitz (Germany)	52.5	12.9	86	x	x	x	x	x	x
Montelibretti (Italy)	42.1	12.6	48	x	-	x	x	-	x
Montseny (Spain)	41.8	2.4	700	-	-	x	-	-	-
Niembro (Spain)	43.4	-4.9	134	x	-	x	x	-	x
O Saviñao (Spain)	43.2	-7.7	506	x	-	x	x	-	x
Payerne (Switzerland)	46.8	6.9	489	x	-	-	x	-	-
Penausende (Spain)	41.3	-5.9	985	x	-	x	x	-	x
Rigi (Switzerland)	47.1	8.5	1031	-	-	-	x	-	-
Risco Llamo (Spain)	39.5	-4.4	1241	x	-	x	x	-	x
Schauinsland (Germany)	47.9	7.9	1205	x	-	-	x	-	-
Vavihill (Sweden)	56.0	13.2	175	x	-	-	x	-	-
Viznar (Spain)	37.2	-3.5	1265	x	-	x	x	-	x
Zarra (Spain)	39.1	-1.1	885	x	-	x	x	-	x

Chapter 4

Simulation periods

4.1 Summer period: 19 – 26 July 2006

To present a general overview about the meteorological situation during 19 – 26 July 2006, horizontal maps of the daily average atmospheric pressure and the air flow at about 5.5 km height as well as the daily sums of precipitation are presented in Figures 4.1 – 4.2. Additionally, vertical profiles based on radiosonde observations of temperature and wind speed are shown in Figure 4.3 (left panels). Stations, located in the north, east, south, west and in the middle of the model domain are used where observations throughout the entire simulation period were performed. These profiles shall give an impression on the scatter of the individual parameters and the rough differences between the measurements performed at the individual radiosonde stations.

The summer simulation period started with a high-pressure system located over Middle Europe, whereas over the Atlantic and the east of Europe a trough was situated (Figure 4.1, left panel). Short rainfall events and thunderstorms occurred in the south of Europe, with highest precipitation (14 l m^{-2} and 18 l m^{-2}) in the north of Lisbon (Portugal) and Spain (Verein Berliner Wetterkarte e.V., 2006-2007). These precipitation events are well represented by the COSMO computation as shown in Figure 4.1 (right panel). Relatively high air temperatures near the surface were measured by radiosondes (Figure 4.3) at 00 UTC (18.8° C (Brindisi; Italy) – 22.4° C (Valentia; Ireland)) and 12 UTC (25° C (Valentia) – 30° C (Meiningen; Germany)) across Europe. Radiosondes in the north (Sundsvall Harnosand; Sweden) measured temperatures of 10° C (00 UTC) and 17° C (12 UTC) near the surface.
Throughout the summer simulation period, relatively constant meteorological condi-

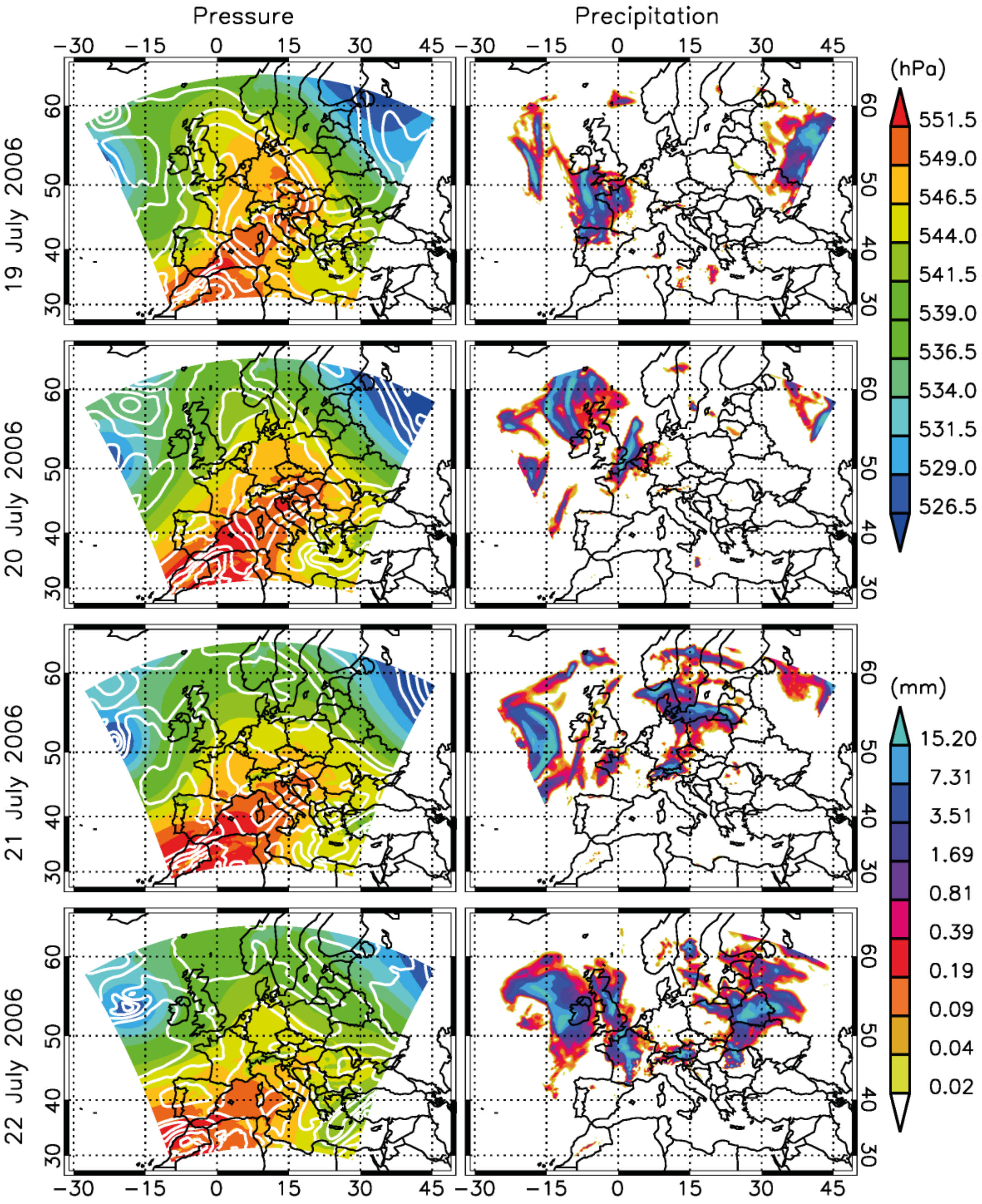

Figure 4.1: Left panel: Daily average (19 – 22 July 2006) of the atmospheric pressure (hPa) at nearly 5.5 km altitude. The white lines represent the air flow. Right panel: Daily sum of the precipitation (mm); the scale marking is logarithmic. Results are computed by the meteorological model COSMO.

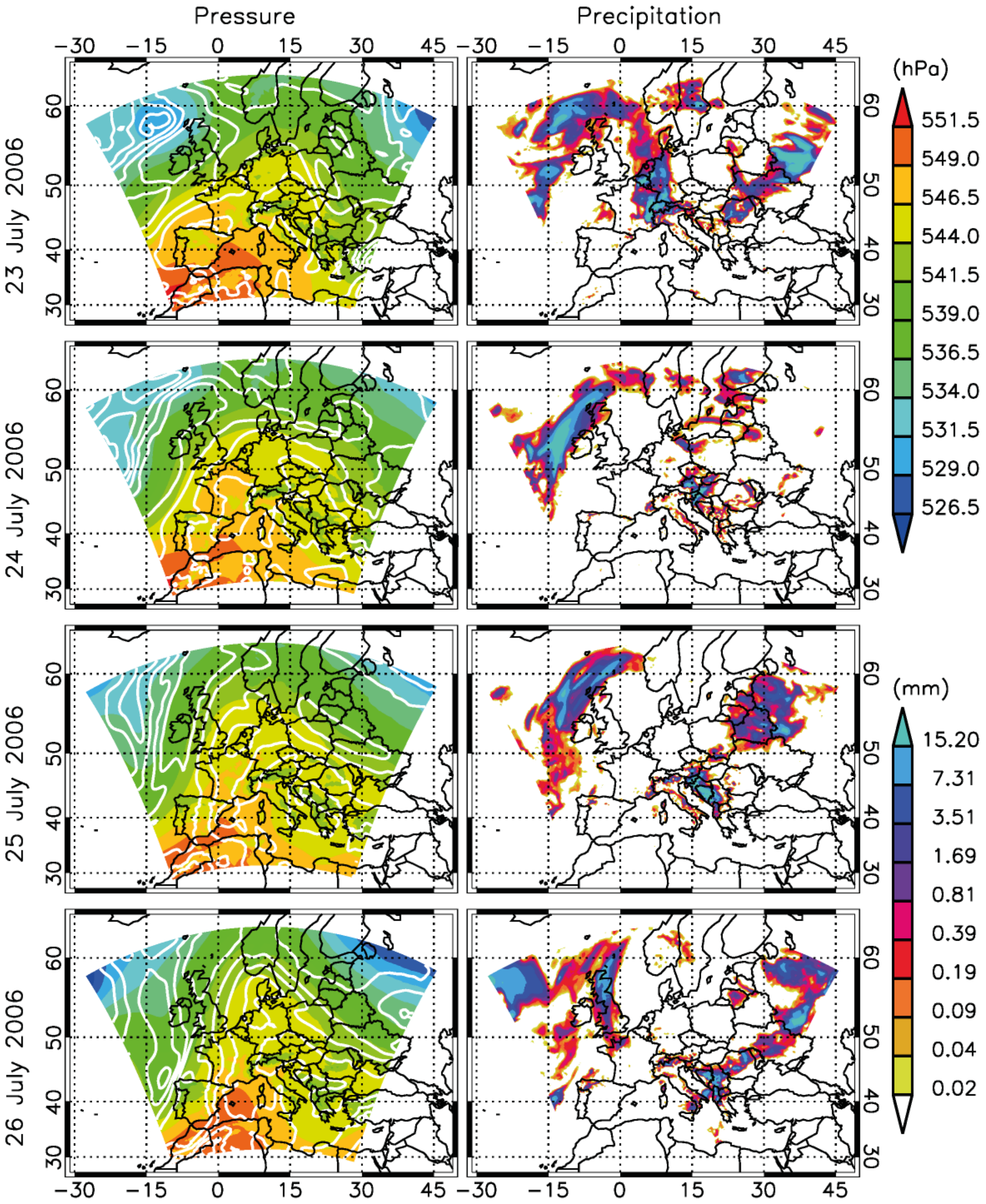

Figure 4.2: Left panel: Daily average (23 – 26 July 2006) of the atmospheric pressure (hPa) at nearly 5.5 km altitude. The white lines represent the air flow. Right panel: Daily sum of the precipitation (mm); the scale marking is logarithmic. Results are computed by the meteorological model COSMO.

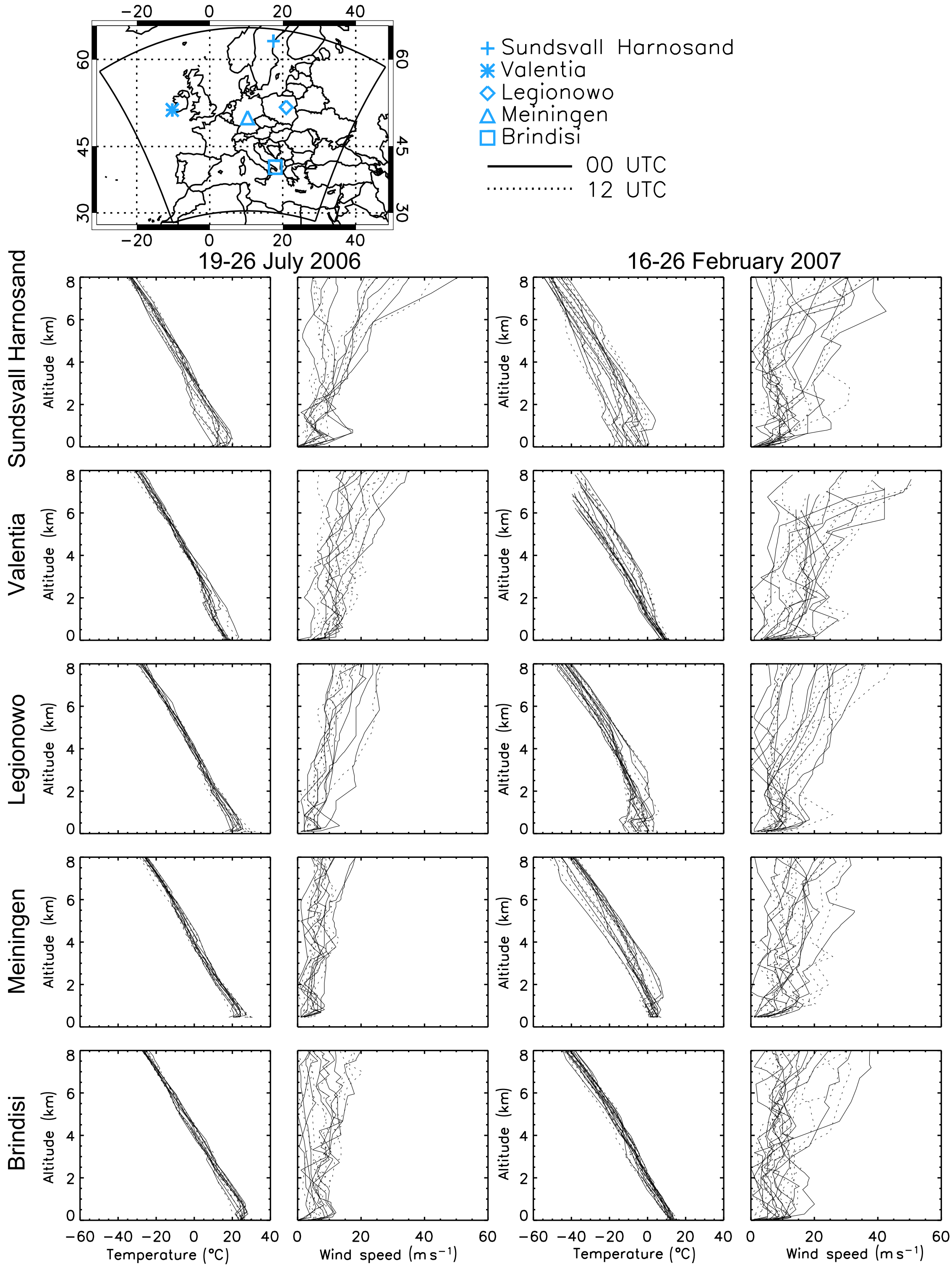

Figure 4.3: Vertical profiles of temperature (° C) and wind speed (m s^{-1}) observed by radiosondes in Sundsvall Harnosand (station number: 02365; 17.5° E, 62.5° N), Brindisi (station number: 13275; 20.4° E, 44.8° N), Legionowo (station number: 12374; 21.0° E, 52.4° N), Meiningen (station number: 10548; 10.4° E, 50.6° N) and Valentia (station number: 03953; 10.3° W, 51.9° N). The continuous lines always represent measurements performed at 00 UTC and dotted lines measurements performed at 12 UTC (University of Wyoming, 2012).

tions appeared with only weak disturbances and scattered precipitation events. As presented in Figure 4.3 (left panel) similar temperature profiles were measured by the radiosondes at the various stations in Europe. Measurements at 00 UTC represent a minimum temperature difference of 5.2 K (Meiningen) and a maximum difference of 10.6 K (Sundsvall Harnosand) near the surface for the entire summer simulation period. At the model top, at about 8 km, the lowest temperature difference was found in Brindisi ($\Delta \mathrm{T} = 4.8\,\mathrm{K}$) and the highest in Legionowo ($\Delta \mathrm{T} = 9.3\,\mathrm{K}$) at 00 UTC. The daytime observations show small differences between the individual observations.

On 20 July 2006, less precipitation occurred than the day before and thus slightly higher or nearly equal temperatures were observed by the radiosondes. During the night and in the morning hours of 21 July a weak convergence zone passed Germany and caused thunderstorms and rainfalls between 16 and $22\,\mathrm{l\,m^{-2}}$ (Verein Berliner Wetterkarte e.V., 2006-2007). The simulated 24-hour precipitation sum represents this convergence zone with its rainfalls. Here, rainfalls ($\geq 7.31\,\mathrm{mm}$) occurred over the Alps, the Baltic Sea and Denmark. Behind the convergence zone a weak cooling was observed and thus highest air temperatures near the surface were measured in Brindisi (31.8° C) and Legionowo (32.2° C) at 12 UTC (Figure 4.3). Since 19 July 2006, the high pressure system shifted slightly into southern direction with a slight weakening effect (Verein Berliner Wetterkarte e.V., 2006-2007), which is well reproduced by the model (Figure 4.1). The model is in accordance to the observations and computes precipitation in France which was caused by subtropical air masses and air coming from the Bay of Biscay. On 23 July, thunderstorms in the west of Germany caused precipitation events ($18\,\mathrm{l\,m^{-2}}$ in the near of Koblenz) and gust of wind up to $28\,\mathrm{m\,s^{-1}}$ (Verein Berliner Wetterkarte e.V., 2006-2007). The media reported the occurrence of a tornado in Germany. The model computes the weakening effect of the high pressure system over Middle Europe. Precipitation events are simulated over the Atlantic Ocean, the Benelux countries and parts of Germany and Switzerland (Figure 4.2). The cooling effect, caused by these rainfall events, was measured by the radiosondes in Meiningen (00 UTC: 18.2° C, 12 UTC: 21° C), whereas at the northern radiosonde station (Sundsvall Harnosand) temperatures of 23.6° C (12 UTC) near the surface were measured. In Brindisi and Legionowo, temperatures of ∼30° C near the surface were observed (Figure 4.3). During the following days, the high-pressure system over Middle Europe experienced a new shift into northern direction (Figure 4.2, left panel) and transported warm air into the north of Europe. The center of the heat was located in the south of France (Verein Berliner Wetterkarte e.V., 2006-2007). On 26 July 2006, the summer simulation period ended, characterized by the location of a high-pressure system over Middle Europe. This pressure system caused temperatures up to 30° C. In the south-east of France and in northern Italy local thunderstorms with precipitation

Figure 4.4: MODIS fire map for the time period 20 July 2006 to 29 July 2006 (NASA/GSFC, 2012). The red dots represent the location of individual fires.

up to $13\,\mathrm{l\,m^{-2}}$ (France) and $49\,\mathrm{l\,m^{-2}}$ (Italy) were reported (Verein Berliner Wetterkarte e.V., 2006-2007). The simulation of the high pressure pattern and the rainfall events in northern Italy are well reproduced by the model, whereas the model computes the precipitation events only in the north of France.

As consequence of relatively high air temperatures during the summer period, several fire events occurred. Figure 4.4 shows the location of fires detected by MODIS on board the Terra and Aqua satellites[1] (NASA/GSFC, 2012). In Figure 4.4 fires, observed between 20 July and 29 July 2006 are shown. Main regions of fire occurrence are found next to the Black Sea. In that region, no or very weak rainfalls occurred, which is also computed by the COSMO model (Figures 4.1 – 4.2). In Spain, in Italy, in Germany and in the United Kingdom fire events were also detected. But because of precipitation events, the amount of fires remained small. Aerosol from biomass burning is not implemented within this model version. Therefore, the comparison of aerosol data (e.g., $\mathrm{PM}_{2.5}$, EC, AOD or backscatter coefficient) could also show discrepancies between simulation and observation results because of this missing aerosol type.

Dust, transported from the Saharan desert to Europe, is not simulated by that model version. However, during 19 – 26 July 2006 transport of Saharan dust was observed. The DREAM (Dust REgional Atmospheric Model) model from the Barcelona Supercomputing center (DREAM, 2012; Nickovic et al., 2001) simulated this event

---

[1] The algorithm of fire detection is described in detail by Giglio et al. (2003).

(Figure 4.5). During the entire simulation period, Spain was mainly affected by this Saharan dust and highest dust loads ($40 - 160\,\mu\mathrm{g\,m^{-3}}$) occurred between 19 July and 22 July 2006. France, Switzerland, parts of Italy and the western part of the Mediterranean Sea were also under the influence of the Saharan dust. Here dust loads up to $80\,\mu\mathrm{g\,m^{-3}}$ were computed by the DREAM model.

In Figures 4.1 – 4.2 the air flow (white lines) at about 5.5 km altitude is shown. Caused by the location of high pressure system over Europe during July 2006, relatively low wind speeds occurred. Observations, performed by radiosondes during this time period at stations located at the northern, eastern, southern and western model boundaries and in the middle of the model domain (Figure 4.3) also indicate this appearance. Near the surface, wind speeds of 0.0 or $1.0\,\mathrm{m\,s^{-1}}$ were observed at all radiosonde stations. However, maximum wind speeds of $5.1\,\mathrm{m\,s^{-1}}$ (Sundsvall Harnosand), $7.2\,\mathrm{m\,s^{-1}}$ (Valentia) and $4.1\,\mathrm{m\,s^{-1}}$ (Legionowo, Meiningen and Brindisi) were also measured. At about 5.5 km average wind speeds of $14.4\,\mathrm{m\,s^{-1}}$ (Sundsvall Harnosand), $15.8\,\mathrm{m\,s^{-1}}$ (Valentia), $13.3\,\mathrm{m\,s^{-1}}$ (Legionowo), $6.5\,\mathrm{m\,s^{-1}}$ (Meiningen) and $7.1\,\mathrm{m\,s^{-1}}$ (Brindisi) were detected during the summer simulation period. Higher wind speeds were often observed in relation with thunderstorms and therefore did not last over long time periods. Due to low wind speeds particles accumulated in the atmosphere. Precipitation events often are only short and do not much deplete aerosol loads.

4.2 Winter period: 16 – 26 February 2007

As presented for the summer simulation period, horizontal maps of the atmospheric pressure and the air flow at about 5.5 km altitude, as well as the daily sum of precipitation are presented in Figures 4.6 – 4.8. In Figure 4.3 (right panels) the profiles of temperature and wind speed measurements, obtained at the known radiosonde stations across Europe, are shown for the winter simulation period as well.

In contrast to the summer time period, the winter period was strongly characterized by precipitation events. The simulation results (Figures 4.6 – 4.8, right panel) do also show the occurrence of large-scale precipitation events for each day of that period. It appears that the model tends to overestimate the precipitation events. Thus, model overestimations of wet deposition of atmospheric particles can occur. The unrealistic simulation of precipitation events and therefore of deposition rates and PM concentrations were also mentioned by Wolke et al. (2012).

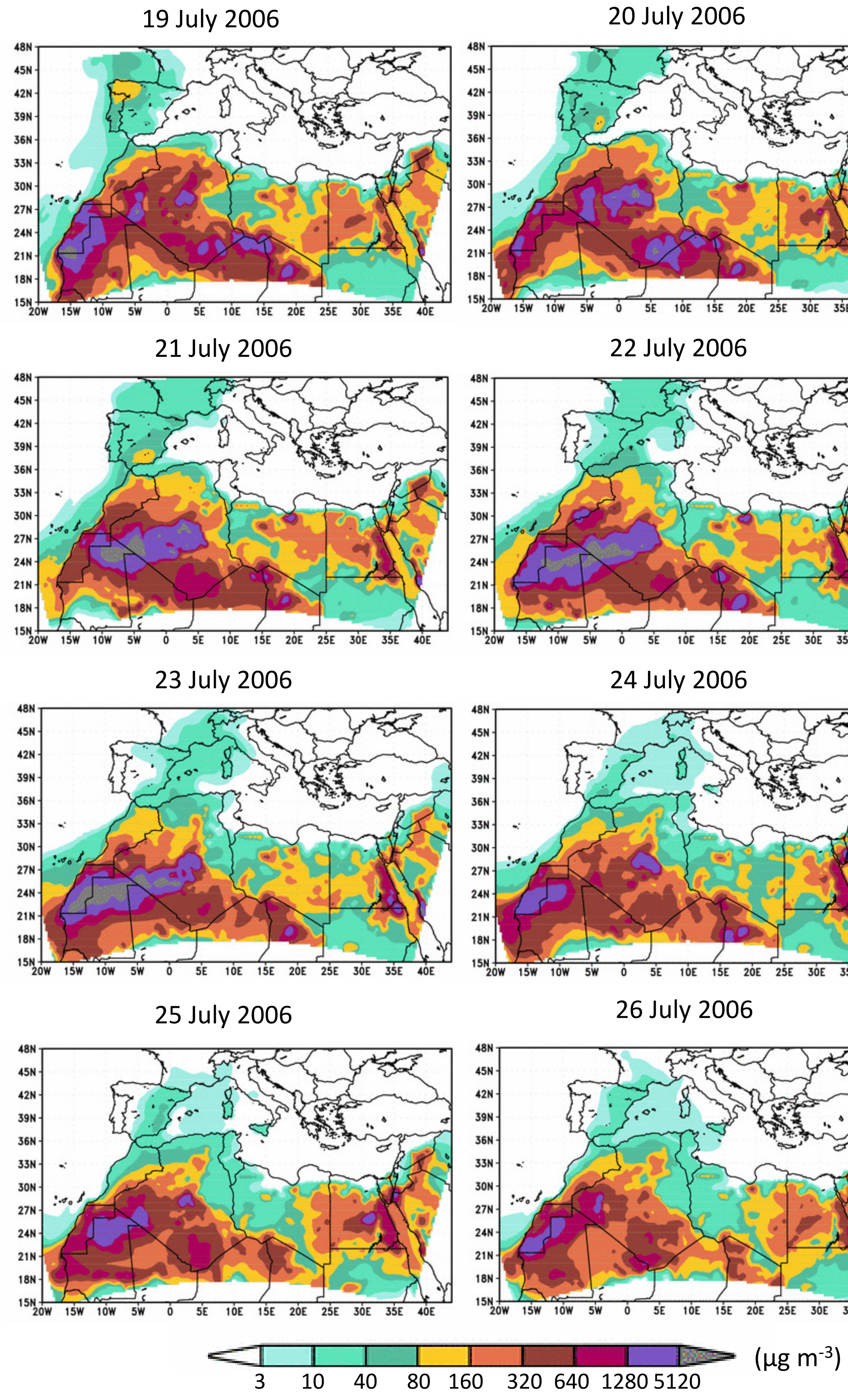

Figure 4.5: Dust concentration forecast ($\mu g\, m^{-3}$) of the lowest level of the DREAM model at 12 UTC (DREAM, 2012).

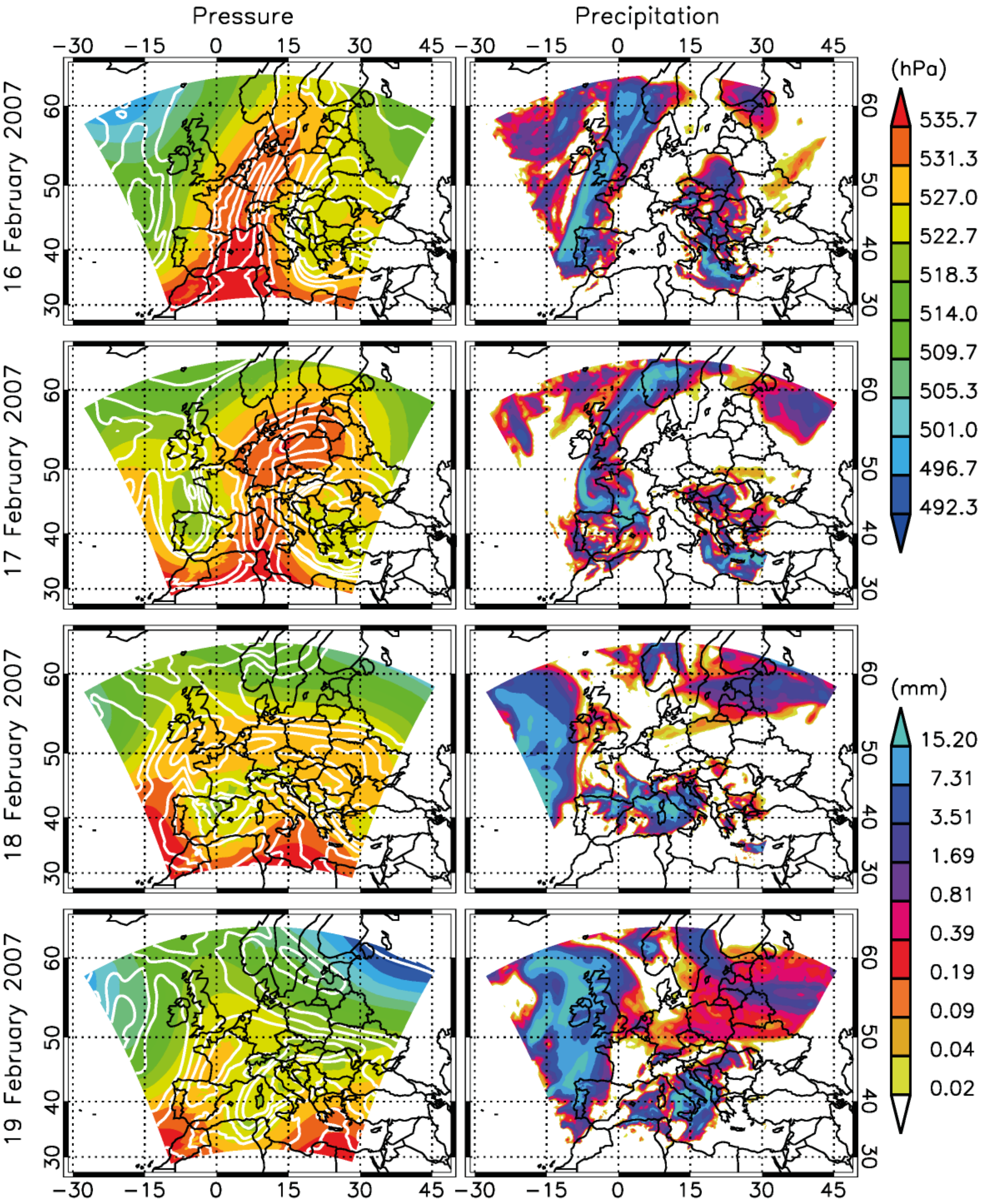

Figure 4.6: Left panel: Daily average (16 – 19 February 2007) of the atmospheric pressure (hPa) at nearly 5.5 km altitude. The white lines represent the air flow. Right panel: Daily sum of the precipitation (mm); the scale marking is logarithmic. Results are computed by the meteorological model COSMO.

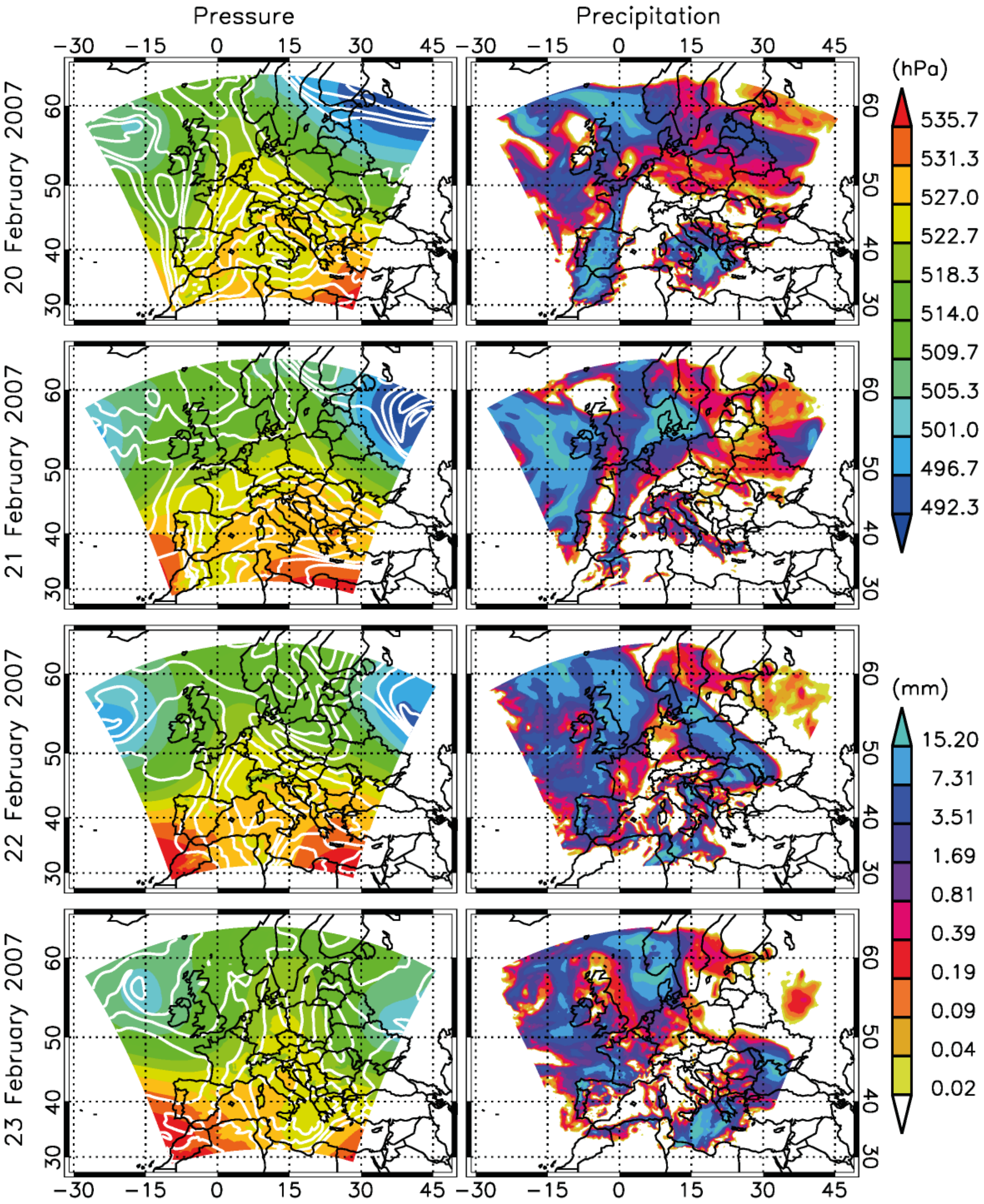

Figure 4.7: Left panel: Daily average (20 – 23 February 2007) of the atmospheric pressure (hPa) at nearly 5.5 km altitude. The white lines represent the air flow. Right panel: Daily sum of the precipitation (mm); the scale marking is logarithmic. Results are computed by the meteorological model COSMO.

The winter simulation period started with a high-pressure ridge over Middle Europe and Scandinavia. At the western side of this ridge COSMO computes large-scale precipitation events. Precipitation also occurred in the east and over the Balkan area caused by an upper low pressure zone (Verein Berliner Wetterkarte e.V., 2006-2007). Low air temperatures (00 UTC: -6.1° C, 12 UTC: -0.9° C) in the north, observed by the radiosonde in Sundsvall Harnosand, document the location of this high-pressure system. In the west (radiosonde: Valentia) and in the south (Brindisi) of the model domain, temperature values near the surface of 6.2 – 9.8° C at 00 UTC and of 7.4 – 9.4° C at 12 UTC were measured. In the middle (Meiningen) of the model domain and in the east (Legionowo), the temperatures near the surface were close to 0.0° C. The following day was characterized by two low-pressure systems at the western side of the high-pressure system. Here, precipitation in Spain and France occurred with 37 l m^{-2} (La Coruna) what was only roughly simulated by the model (Figure 4.6). The position of the air flow lines in Figure 4.6 (left panel) indicates the increase of the wind speed due to the eddy over the Bay of Biscay and the high-pressure system over Middle Europe. A shift of the high-pressure system into eastern direction appeared on 18 February 2007. Thus, low temperatures of approximately -20° C were observed during the night in the Ukraine (Verein Berliner Wetterkarte e.V., 2006-2007). Several precipitation events are simulated for the entire model domain by the meteorological model COSMO on 19 February. At the coast of Algier, rainfall up to 20 l m^{-2} was observed (Verein Berliner Wetterkarte e.V., 2006-2007). The model also computes rainfall events in that region, but with less amount ($\leq$ 15.2 mm). The high-level eddy moved from the Iberian Peninsula to the south. Over the sea, with its relatively high water temperatures, rainfall events over the Mediterranean Sea and the bordered areas were caused by the atmospheric instability (Verein Berliner Wetterkarte e.V., 2006-2007). In Valentia, precipitation up to 36 l m^{-2} was measured within 24-hours (Verein Berliner Wetterkarte e.V., 2006-2007). Because of the cloud cover there, the radiosondes measured only small differences between night- and day-time temperatures near the surface (00 UTC: 9.2° C, 12 UTC: 11.2° C) and at about 5.5 km altitude (00 UTC: -17.5° C, 12 UTC: -19.5° C). The wind speed was relatively constant during that day with $\sim$7 m s^{-1} near the ground from the south-east direction (Figure 4.3). On 20 February 2007, large-scale precipitation events are simulated for nearly the entire model domain (Figure 4.6). However, only rainfalls of 20 l m^{-2} (Naples, Italy) and 34 l m^{-2} (Capri, Italy) were observed (Verein Berliner Wetterkarte e.V., 2006-2007), which are comparable with the simulation. On 20 February, the pattern of the pressure at 5.5 km altitude shows small pressure differences over Middle Europe. Therefore, low wind speeds occurred in that region, though the northeast was under the influence of subpolar maritime air and the southwest under the influence of subtropical maritime air.

Due to these two air masses, distinct temperature gradients between north and south occurred. Based on the radiosonde observations in Sundvall Harnosand, in the north, and Brindisi, in the south, a north-south temperature gradient up to 17 K (00 UTC) and 22 K (12 UTC) was detected near the surface. On 21 February 2007, the temperature gradients increased up to 28 K during the night and 26 K during the day. As consequence of cold air, heavy snowfall events occurred in Denmark. In Aalborg, precipitation up to 12.5 $\mathrm{l\,m^{-2}}$ occurred (Verein Berliner Wetterkarte e.V., 2006-2007), what is in agreement with the simulation results (Figure 4.6, right panel). On 22 February

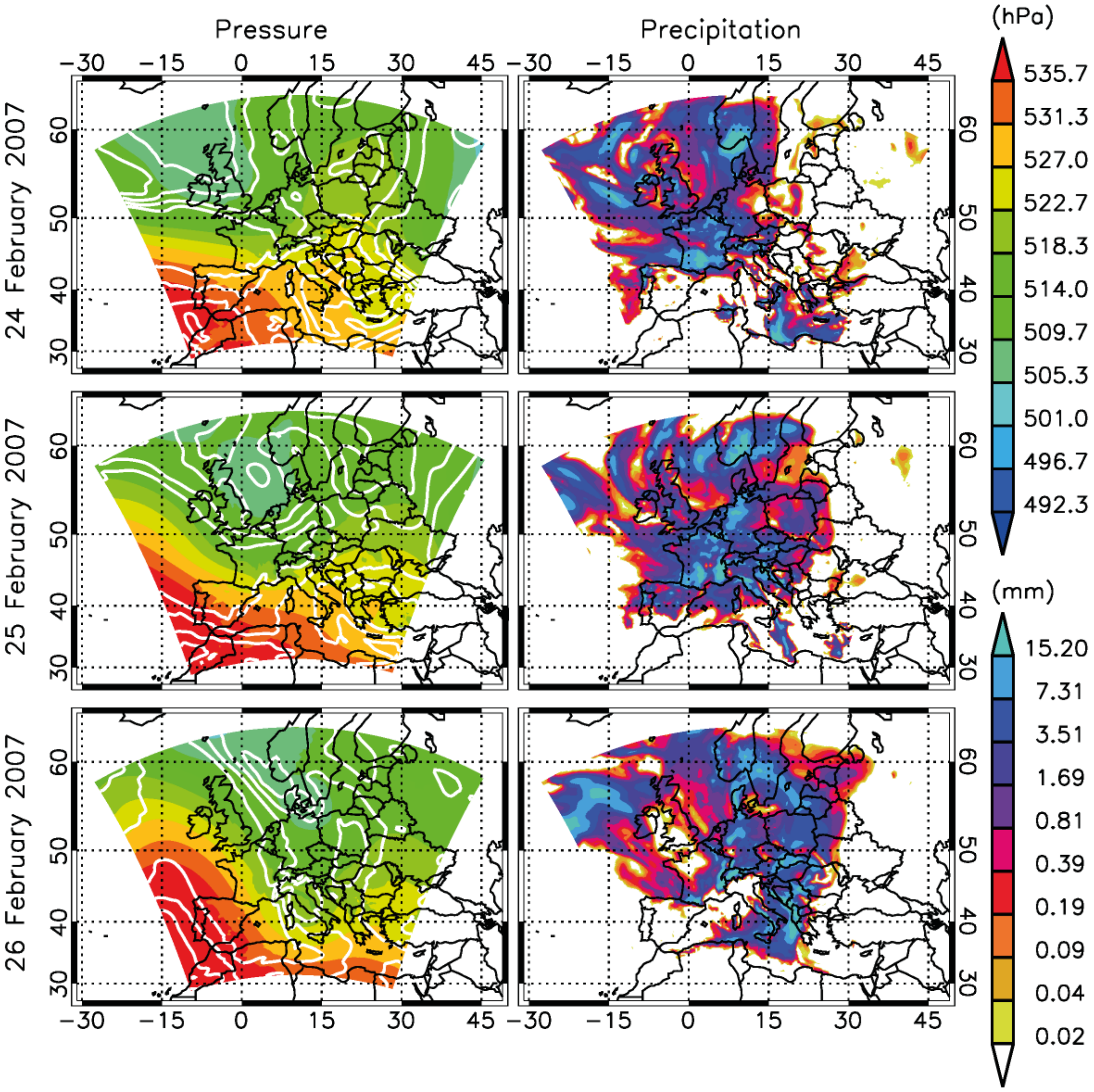

Figure 4.8: Left panel: Daily average (24 – 26 February 2007) of the atmospheric pressure (hPa) at nearly 5.5 km altitude. The white lines represent the air flow. Right panel: Daily sum of the precipitation (mm); the scale marking is logarithmic. Results are computed by the meteorological model COSMO.

2007, the temperature gradient over Middle Europe was still significant and shifted only slightly into southern direction, whereas relatively high temperatures were observed in Germany with 4.8° C at 00 UTC and 7.2° C at 12 UTC near the surface (Figure 4.3, Meiningen). Apart from parts of the eastern model domain, precipitation events are simulated by COSMO everywhere. In the north of Germany, precipitation between 10 and 20 $\mathrm{l\,m^{-2}}$ were measured (Verein Berliner Wetterkarte e.V., 2006-2007). Denmark was under the influence of snowfalls (Aalborg: 28 $\mathrm{l\,m^{-2}}$ within 24 hours). Precipitation is also simulated in Denmark by COSMO but with a lower magnitude ($\leq$ 7.31 mm). On 23 February, low pressure gradients in Europe caused only weak wind speeds near the surface (00 UTC: 1 – 5 $\mathrm{m\,s^{-1}}$, 12 UTC: 1 – 7 $\mathrm{m\,s^{-1}}$) at all five radiosonde stations. In Legionowo, the temperature decreased further. Here, night-time values of ∼ -10° C (00 UTC) and day-time values of ∼ -7° C were measured (Figure 4.3), which is caused by cold air from the continent with arctic character (Verein Berliner Wetterkarte e.V., 2006-2007). A high-pressure system was situated over Russia on 25 February (Verein Berliner Wetterkarte e.V., 2006-2007). Therefore, the transport of arctic air into the region of the Black Sea occurred. Snowfall occurred in Turkey, what is also computed by COSMO (Figure 4.8, right panel). This precipitation event was small compared to the precipitation events that occurred in other parts of the European model domain. A low-pressure system over Great Britain and the North Sea caused rainfall events in Germany. The radiosonde station in Sundsvall Harnosand measured -3.3° C (00 UTC) and -1.7° C (12 UTC) and the station in Meiningen measured 5.6° C (00 UTC) and 5° C (12 UTC) (Figure 4.3). Thus, in Denmark thawing started and decreased the snow cover (Verein Berliner Wetterkarte e.V., 2006-2007). The simulation period ended on 26 February 2007 with relatively mild air in the east. At the radiosonde station in Legionowo, night-time temperatures of -3.1° C and day-time temperatures of -0.1° C were observed near the surface, which is an increase of 3 K and 3.4 K, respectively, to the day before. In Germany, the influence of the mild and maritime air was also observed. The low-pressure system moved from the North Sea to the north of Germany (Figure 4.8, left panel) (Verein Berliner Wetterkarte e.V., 2006-2007). The instability of this maritime air caused several rainfall events (Figure 4.8, right panel).

Due to large-scale and long-lasting precipitation events, as well as due to the higher wind speeds compared to the summer period, particles within the atmosphere did not accumulate. High wind speeds could be able to transport atmospheric particles from outside into the model domain and within the model area. However, rain- and snowfall events removed these particles and thus limited the transport and loads of atmospheric substances throughout the entire European model domain.

Chapter 5

Results

5.1 Model evaluation with space-based lidar observations

It is explained in Section 3.1.2, that for each CALIOP observation profile of the various data sets (CALIOP$_{5km}^{data1}$, CALIOP$_{5km}^{data2}$, CALIOP$_{5km}^{data3}$, CALIOP$_{5km}^{data4}$, CALIOP$_{40km}$), a vertical backscatter profile, based on model simulations is determined. Due to the large amount of available CALIOP profiles for both time periods, direct model-data comparisons of individual profiles are not feasible, whereas a statistical analysis can be performed. The vertical resolution of simulated and measured backscatter profiles differs. Between surface and 8 km altitude 30 height levels are available from the model computations. CALIOP profiles provide 133 (5 km horizontal resolution) and 67 (40 km horizontal resolution) height levels for the same height range. Therefore, average backscatter coefficients are determined for each 500 m height level between surface and 8 km. This is done for each individual profile (experimentally observed and computed). Direct comparison of the individual observed and computed backscatter values is possible and can be used for statistical analysis. Computed results are based on the model setup Sim$_{Basic}$ (Table 2.1).

Figure 5.1 shows the number-normalized frequency distribution of the difference of backscatter values determined between Sim$_{Basic}$ and CALIOP$_{5km}^{data1}$ (first panel), Sim$_{Basic}$ and CALIOP$_{5km}^{data2}$ (second panel), Sim$_{Basic}$ and CALIOP$_{5km}^{data3}$ (third panel), Sim$_{Basic}$ and CALIOP$_{5km}^{data4}$ (forth panel) and Sim$_{Basic}$ and CALIOP$_{40km}$ (lower panel). As mentioned, the backscatter coefficients used here, refer to 500 m height levels between surface and 8 km altitude. The individual distributions, shown for the summer

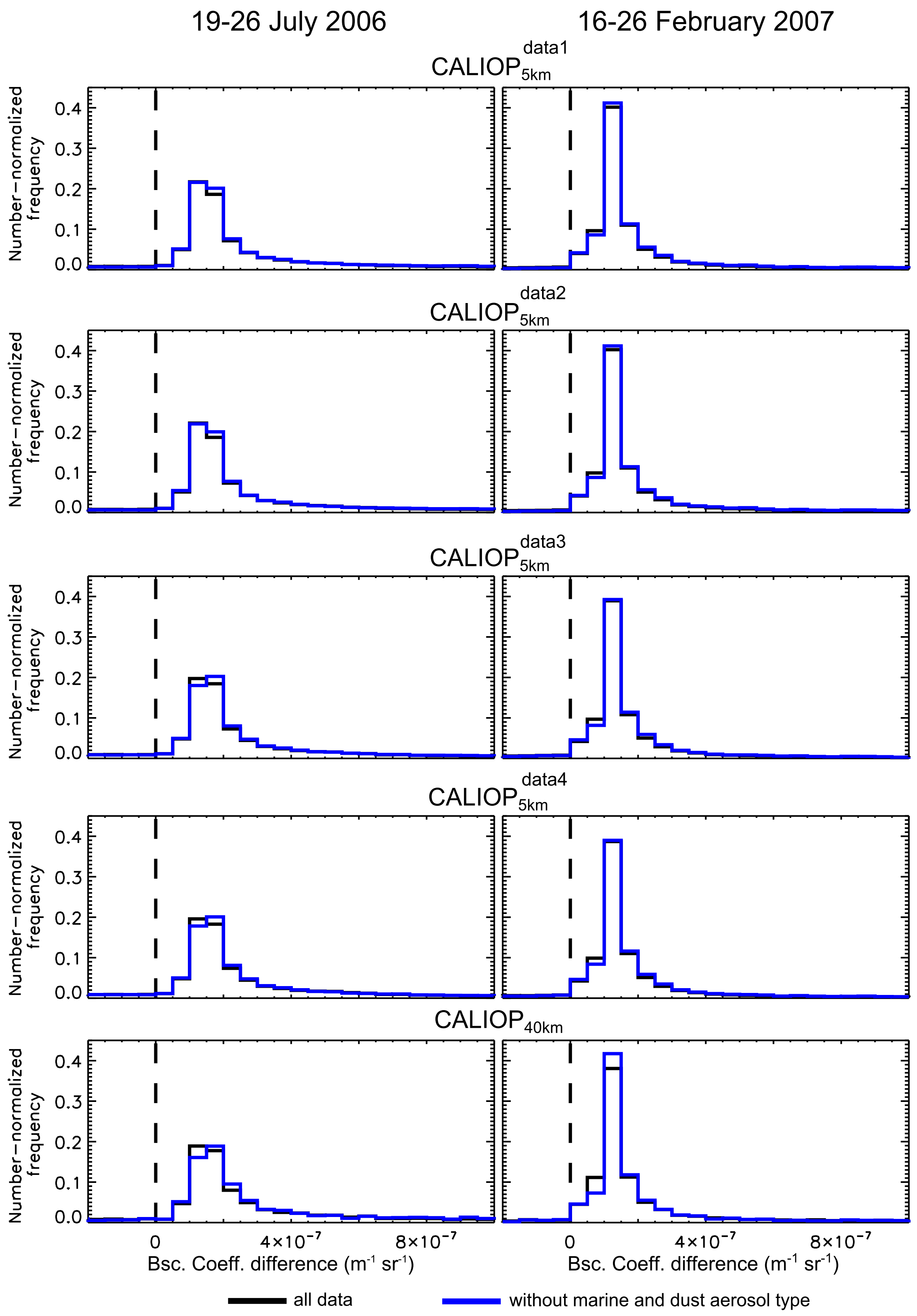

Figure 5.1: Number-normalized frequency distribution of the difference between the individual backscatter coefficients of the computed (Sim_{Basic}) and the various CALIOP data ($\text{CALIOP}^{data1}_{5km}$, $\text{CALIOP}^{data2}_{5km}$, $\text{CALIOP}^{data3}_{5km}$, $\text{CALIOP}^{data4}_{5km}$, CALIOP_{40km}) located between surface and 8 km altitude for both time periods.

(left panel) and winter (right panel) period, do not include any information about the height dependent agreement between computed and experimentally observed backscatter values. The figure contains the distributions when using backscatter values based on all aerosol types (black line) and without marine and dust caused backscatter coefficients (blue line). It is significant, that the difference between the individual distribution of the individual data sets is small, implementing that excluding marine and dust caused backscatter coefficients leads to no distinct improvement regarding the agreement between model and observation data. Sorting out the backscatter coefficients which are related to the existence of marine and dust particles is done because the model version used here does not include the description of marine and dust aerosol and thus focus on the simulation of anthropogenic aerosol within Europe.

It is also remarkable, that for all data sets and both summer and winter period, computed backscatter values based on Sim_{Basic} simulations result in higher values compared to the CALIOP observed data. Table 5.1 summarizes some statistical parameters about the calculated differences between computed and observed backscatter coefficients (minimum backscatter coefficient difference: $\Delta\,\beta_{min}$, maximum backscatter coefficient difference: $\Delta\,\beta_{max}$, average backscatter coefficient difference: $\Delta\,\beta_{mean}$, median backscatter coefficient difference; $\Delta\,\beta_{median}$, standard deviation of backscatter coefficient difference: $\Delta\,\beta_{stddev}$, N: number of available values). These parameters clearly show the differences between both simulation periods. In most cases, the range from minimum to maximum backscatter difference is higher during winter compared to summer. This is also reflected by the standard deviation which reaches a maximum value of $1.1\,\mathrm{x}\,10^{-6}\,\mathrm{m}^{-1}\,\mathrm{sr}^{-1}$ ($\mathrm{CALIOP}_{5km}^{data2}$, all data) for the summer case and of $1.9\,\mathrm{x}\,10^{-6}\,\mathrm{m}^{-1}\,\mathrm{sr}^{-1}$ ($\mathrm{CALIOP}_{5km}^{data3}$, without marine and dust aerosol type) for the winter case (Table 5.1). In case of the summer simulation period, a shift into higher positive average backscatter coefficient differences is determined when excluding backscatter values caused by marine and dust aerosol. On the other hand, the median of the backscatter difference remains nearly unmodified. Equal values of median backscatter difference are also found for all data sets during February 2007. However, for some cases a negative average backscatter difference can be determined which is not clearly shown in Figure 5.1 (right panel). Negative average differences are calculated when using $\mathrm{CALIOP}_{5km}^{data1}$ (all data), $\mathrm{CALIOP}_{5km}^{data2}$ (all data), $\mathrm{CALIOP}_{5km}^{data3}$ (all data, without marine and dust aerosol type) and $\mathrm{CALIOP}_{5km}^{data4}$ (all data) (Table 5.1).

For both summer and winter period, comparisons between computed and CALIOP data with a coarse horizontal resolution (CALIOP_{40km}) lead to different results in contrast to the comparisons between Sim_{Basic} data and $\mathrm{CALIOP}_{5km}^{data1}$, $\mathrm{CALIOP}_{5km}^{data2}$, $\mathrm{CALIOP}_{5km}^{data3}$ and $\mathrm{CALIOP}_{5km}^{data4}$ (Table 5.1). When using CALIOP_{40km}, a smaller range between minimum and maximum backscatter difference is found. Additionally, the av-

Table 5.1: Statistical parameters determined based in the differences between computed (Sim_{Basic}) and experimentally observed ($\mathrm{CALIOP}^{data1}_{5km}$, $\mathrm{CALIOP}^{data2}_{5km}$, $\mathrm{CALIOP}^{data3}_{5km}$, $\mathrm{CALIOP}^{data4}_{5km}$, CALIOP_{40km}) backscatter coefficients between surface and 8 km altitude. Unit of $\Delta\,\beta_{min}$, $\Delta\,\beta_{max}$, $\Delta\,\beta_{mean}$, $\Delta\,\beta_{median}$, $\Delta\,\beta_{stddev}$: $\mathrm{m}^{-1}\,\mathrm{sr}^{-1}$. N: Total number of available data.

19 – 26 July 2006							
		$\Delta\,\beta_{min}$	$\Delta\,\beta_{max}$	$\Delta\,\beta_{mean}$	$\Delta\,\beta_{median}$	$\Delta\,\beta_{stddev}$	N
$\mathrm{CALIOP}^{data1}_{5km}$	all data	-5.4 x 10^{-5}	1.1 x 10^{-5}	1.6 x 10^{-7}	1.6 x 10^{-7}	1.0 x 10^{-6}	66439
	without marine and dust aerosol type	-3.8 x 10^{-5}	1.1 x 10^{-5}	2.4 x 10^{-7}	1.6 x 10^{-7}	0.8 x 10^{-6}	42670
$\mathrm{CALIOP}^{data2}_{5km}$	all data	-5.4 x 10^{-5}	1.0 x 10^{-5}	1.7 x 10^{-7}	1.6 x 10^{-7}	1.1 x 10^{-6}	59796
	without marine and dust aerosol type	-3.8 x 10^{-5}	1.0 x 10^{-5}	2.4 x 10^{-7}	1.6 x 10^{-7}	0.8 x 10^{-6}	39062
$\mathrm{CALIOP}^{data3}_{5km}$	all data	-5.4 x 10^{-5}	1.1 x 10^{-5}	1.3 x 10^{-7}	1.6 x 10^{-7}	1.0 x 10^{-6}	56866
	without marine and dust aerosol type	-3.8 x 10^{-5}	1.1 x 10^{-5}	2.1 x 10^{-7}	1.6 x 10^{-7}	0.9 x 10^{-6}	32779
$\mathrm{CALIOP}^{data4}_{5km}$	all data	-5.4 x 10^{-5}	1.0 x 10^{-5}	1.5 x 10^{-7}	1.6 x 10^{-7}	1.0 x 10^{-6}	55255
	without marine and dust aerosol type	-2.7 x 10^{-5}	1.0 x 10^{-5}	2.0 x 10^{-7}	1.7 x 10^{-7}	1.0 x 10^{-6}	31455
CALIOP_{40km}	all data	-1.0 x 10^{-5}	0.9 x 10^{-5}	2.7 x 10^{-7}	1.7 x 10^{-7}	0.8 x 10^{-6}	10246
	without marine and dust aerosol type	-0.7 x 10^{-5}	0.9 x 10^{-5}	3.5 x 10^{-7}	1.9 x 10^{-7}	0.8 x 10^{-6}	4360
16 – 26 February 2007							
		$\Delta\,\beta_{min}$	$\Delta\,\beta_{max}$	$\Delta\,\beta_{mean}$	$\Delta\,\beta_{median}$	$\Delta\,\beta_{stddev}$	N
$\mathrm{CALIOP}^{data1}_{5km}$	all data	-7.2 x 10^{-5}	2.0 x 10^{-5}	-0.4 x 10^{-7}	1.3 x 10^{-7}	1.5 x 10^{-6}	50702
	without marine and dust aerosol type	-7.2 x 10^{-5}	2.0 x 10^{-5}	0.9 x 10^{-7}	1.3 x 10^{-7}	1.5 x 10^{-6}	29561
$\mathrm{CALIOP}^{data2}_{5km}$	all data	-9.9 x 10^{-5}	2.0 x 10^{-5}	-0.3 x 10^{-7}	1.3 x 10^{-7}	1.6 x 10^{-6}	46351
	without marine and dust aerosol type	-9.9 x 10^{-5}	2.0 x 10^{-5}	1.0 x 10^{-7}	1.3 x 10^{-7}	1.6 x 10^{-6}	27574
$\mathrm{CALIOP}^{data3}_{5km}$	all data	-7.2 x 10^{-5}	1.9 x 10^{-5}	-1.3 x 10^{-7}	1.3 x 10^{-7}	1.7 x 10^{-6}	40258
	without marine and dust aerosol type	-7.2 x 10^{-5}	1.9 x 10^{-5}	-0.3 x 10^{-7}	1.3 x 10^{-7}	1.9 x 10^{-6}	19100
$\mathrm{CALIOP}^{data4}_{5km}$	all data	-4.2 x 10^{-5}	1.9 x 10^{-5}	-0.8 x 10^{-7}	1.3 x 10^{-7}	1.4 x 10^{-6}	38938
	without marine and dust aerosol type	-4.2 x 10^{-5}	1.9 x 10^{-5}	0.3 x 10^{-7}	1.3 x 10^{-7}	1.5 x 10^{-6}	18262
CALIOP_{40km}	all data	-2.5 x 10^{-5}	0.7 x 10^{-5}	0.7 x 10^{-7}	1.3 x 10^{-7}	1.0 x 10^{-6}	5402
	without marine and dust aerosol type	-0.4 x 10^{-5}	0.7 x 10^{-5}	2.0 x 10^{-7}	1.3 x 10^{-7}	0.5 x 10^{-6}	1812

erage backscatter difference is clearly different compared to the other CALIOP data sets and leads to higher average backscatter values during July 2006 and February 2007. Comparisons between Sim_{Basic} and CALIOP data with 5 km horizontal resolution lead to quite similar results for both simulation periods, whereas the results are in contrast to comparisons between Sim_{Basic} and CALIOP_{40km} data. In case of the summer period, the effect of sorting out backscatter values caused by marine and dust aerosol leads to a distinct change in case of the minimum backscatter values. Thus, high backscatter values, observed by CALIOP, are sorted out during July 2006. Such an effect is not determined during February 2007. Both periods clearly show a change of the average backscatter differences when sorting out marine and dust caused backscatter values (Table 5.1).

5.1.1 Vertical profile

Figure 5.2 illustrates the effect of sorting out backscatter coefficients caused by dust and marine aerosol types. The absolute difference between computed (Sim_{Basic}) and experimentally observed ($\mathrm{CALIOP}_{5km}^{data1}$) backscatter values, resolved for each vertical profile and 500 m height level from the surface up to 8 km, is calculated. In the upper panel of Figure 5.2, the difference of backscatter values, including all kind of aerosol types, is shown, whereas the lower panel represents results after sorting out dust and marine caused backscatter values. The data refer to a CALIPSO overflight on 22 July 2006 during night-time (track time: T01-42-42ZN). CALIPSO crossed the Baltic Sea, Germany, the Mediterranean Sea and the African continent. Saharan dust was transported during that time period from the African continent to the European continent (see Section 4.1), which is shown in Figure 5.2 (upper panel) quite well. The blue colors represent the underestimation of observed CALIOP backscatter values by the model. Due to the missing dust within this model setup, strong negative backscatter differences are found over the African continent and the Mediterranean Sea. Near the surface and up to about 2 km altitude, the overestimation of the backscatter coefficients by the model setup Sim_{Basic} is shown by the red color for nearly the entire flight track. At height layers above 4 km mainly yellow colors are represented, showing overestimations by the model computations as well. At these height levels, CALIOP backscatter values are clearly lower than the computed values. It is often the case that at higher height levels values of -9999 were set by ASDC which were replaced by backscatter values of $0.0\,\mathrm{m}^{-1}\,\mathrm{sr}^{-1}$ (Figure 3.2).

Over the African continent, dust affects nearly the entire vertical column from the surface and is transported into higher altitudes over the Mediterranean Sea (Figure 5.2,

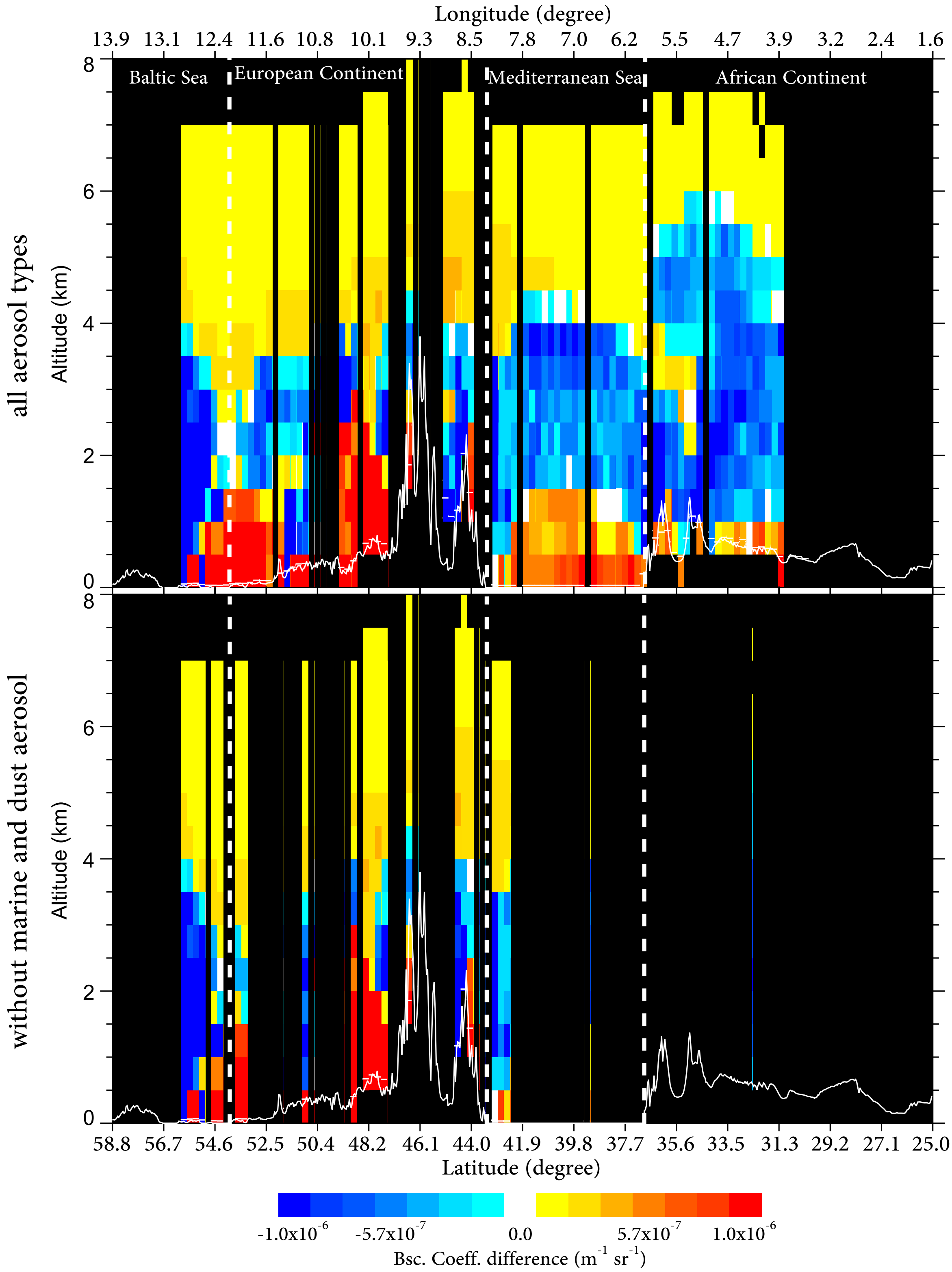

Figure 5.2: Difference of backscatter coefficients ($m^{-1}\,sr^{-1}$) determined between Sim_{Basic} and $\mathrm{CALIOP}^{data1}_{5km}$ for the CALIPSO track on 22 July 2006 (track time: T01-42-42ZN) before (upper panel) and after (lower panel) sorting out backscatter values based on dust and marine aerosol type. The continuous white line represents the surface height measured by CALIOP and the dashed white line different geographic areas.

upper panel). The model is not able to compute the backscatter values for this entire domain. Over the European continent as well as above the Alps the occurrence of Saharan dust decreases and now regions where the model overestimates the observed backscattering are found as well. After sorting out values caused by marine and dust aerosol, several CALIOP profiles, observed over Africa and the Mediterranean Sea, are removed from the data set. Additionally, profiles over Europe are removed that may be due to the occurrence of transported dust in these regions (Figure 5.2, lower panel). Before excluding backscatter values of dust and marine aerosol character, the calculated average difference of $-7.2 \times 10^{-8}\,\mathrm{m}^{-1}\,\mathrm{sr}^{-1}$ (number of values: 2872) is determined for this CALIPSO track. An improvement regarding the agreement is found after sorting out marine and dust caused backscatter values, the average backscatter difference is now: $-5.0 \times 10^{-8}\,\mathrm{m}^{-1}\,\mathrm{sr}^{-1}$ (number of values: 909).

For a proper handling of all available data, average vertical backscatter profiles, representing each individual simulation period, are determined. The profiles, used to calculate the average profiles, refer to the model grid cells as described in Section 3.1.2 on Page 38. Thus, an equal number of CALIOP and model profiles is used which refer to each other to calculate the individual observed and computed profiles of backscatter coefficients. The average profiles, based on observation and simulation are computed for 5 km and 40 km horizontal resolutions (Figure 5.3). Black colored lines represent the results for backscatter coefficients based on all aerosol types, whereas blue lines represent results without backscatter values of marine and dust origin. In the upper panel of Figure 5.3, comparisons between experimentally observed (continuous lines) and simulated (dashed lines) backscatter profiles are shown for the summer period and in the lower panel for the winter period.

During summer, the overestimation by the model Sim_{Basic} is found for all five CALIOP data sets ($\mathrm{CALIOP}^{data1}_{5km}$, $\mathrm{CALIOP}^{data2}_{5km}$, $\mathrm{CALIOP}^{data3}_{5km}$, $\mathrm{CALIOP}^{data4}_{5km}$, CALIOP_{40km}) before and after sorting out marine and dust caused backscatter coefficients. During winter, cases of underestimations are found as well. For both simulation periods and CALIOP data sets the model is able to reproduce the shape of the vertical backscatter profile successfully. In case of the summer period, the PBL between surface and ~ 2 km and in case of the winter period the formation of the maximum backscatter values at ~ 1 km altitude are computed.

As mentioned in Section 3.1.2, the fraction of backscatter values, identified to be caused by marine aerosol, is higher during 16 – 26 February 2007 than during 19 – 26 July 2006. Perhaps, this is the reason for the difference of the experimentally observed vertical backscatter profiles before and after sorting out marine and dust caused backscatter values for the winter case for all data sets (Figure 5.3, lower panel). Distinct dif-

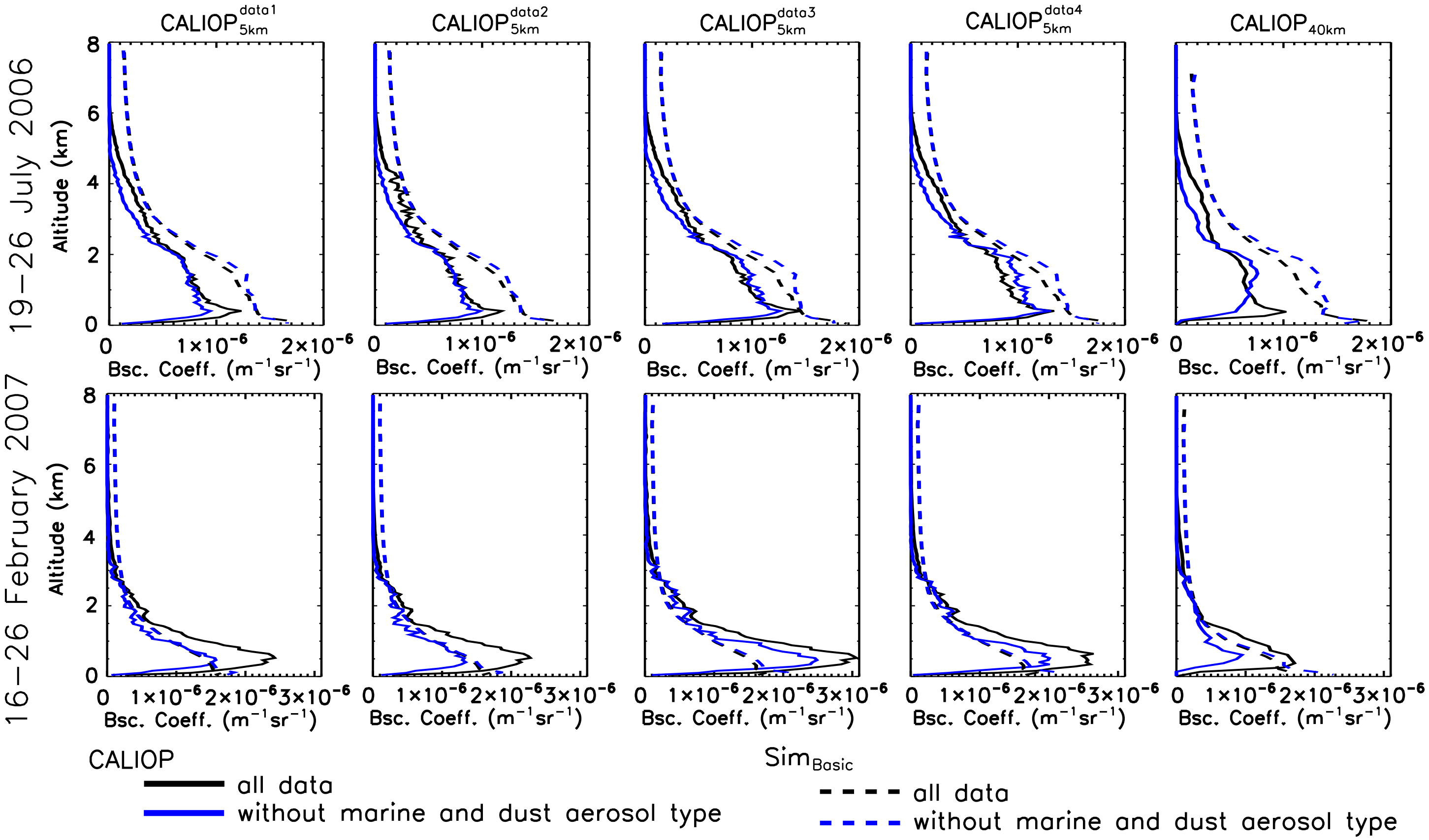

Figure 5.3: Average vertical backscatter profiles for data based on 5 km horizontal resolution (CALIOP$^{data1}_{5km}$, CALIOP$^{data2}_{5km}$, CALIOP$^{data3}_{5km}$, CALIOP$^{data4}_{5km}$) and 40 km horizontal resolution (CALIOP$_{40km}$). Continuous line: CALIOP backscatter profiles. Dashed line: Backscatter profile based on Sim$_{Basic}$ computations. Black/blue color: Including/Excluding backscatter coefficients of marine and dust aerosol type.

ferences occur within the PBL. For the summer case, such discrepancy between the CALIOP profiles including backscatter values of all aerosol types and without marine and dust aerosol is not found (Figure 5.3). During summer, the fraction of dust caused backscatter values was higher than of marine backscatter values. Dust particles are mainly transported at altitudes above the PBL. Thus, at height levels above 2.0 km differences between the vertical profiles including all aerosol types (black continuous line) and without backscatter values of marine and dust origin (blue continuous line) are found.

For detailed studies about the analysis of the agreement between the computed and the experimentally observed backscatter profiles the absolute (A_{bias}) and relative bias (R_{bias}) for each 500 m height level are determined based on the profiles shown in Figure 5.3. The biases are calculated by means of:

$$A_{bias} = \beta_S - \beta_O \tag{5.1}$$

$$R_{bias} = \left(\frac{\beta_S - \beta_O}{\beta_O}\right) \cdot 100\% \tag{5.2}$$

with β_O as observed and β_S as simulated backscatter value for each 500 m height level between surface and 8 km altitude based on the average profiles. These values are summarized for both simulation periods for the 5 and 40 km horizontal resolution in Table 5.2. The table includes information about the absolute and relative biases using data from the data set which includes all kind of aerosol types (A_{bias}^{all}, R_{bias}^{all}) and without both marine and dust aerosol-caused backscatter coefficients (A_{bias}^{md}, R_{bias}^{md}). Values up to a height level of 4.5 km are shown here. Above that layer it occurs that the CALIOP observed backscatter values are often equal to zero and thus the determination of the relative bias is not possible. The increase of the absolute and relative bias with increasing height can be very significant. On the other hand, the magnitude of the absolute bias is often in the range of the observed backscatter coefficients. During summer, an improvement is found for comparisons with $\text{CALIOP}_{5km}^{data4}$, after sorting out marine and dust caused backscatter coefficients. But this effect is only determined for the altitude range from 0.5 km to 2.0 km (Table 5.2). $\text{CALIOP}_{5km}^{data4}$ represents the data set determined based on the strictest rules next to CALIOP_{40km} (Section 3.1.2, Figure 3.2). But best agreements between surface and 4.5 km are found for comparisons between Sim_{Basic} and $\text{CALIOP}_{5km}^{data3}$ (all data) for the entire profile (Figure 5.3). Here, the absolute bias ranges from $0.6 \times 10^{-7}\,\text{m}^{-1}\,\text{sr}^{-1}$ (3.5 – 4.0 km) to $5.6 \times 10^{-7}\,\text{m}^{-1}\,\text{sr}^{-1}$ (0.0 – 0.5 km) and the relative bias from 22% to 52% for the same height levels (Table 5.2). Largest discrepancies are found for comparisons between model and CALIOP_{40km} (Table 5.2).

Table 5.2: Individual A_{bias} (x $10^{-7}\,m^{-1}\,sr^{-1}$) and R_{bias} (%) for each 500 m height level determined between surface and 4.5 km altitude for the different data sets $CALIOP_{5km}^{data1}$, $CALIOP_{5km}^{data2}$, $CALIOP_{5km}^{data3}$, $CALIOP_{5km}^{data4}$ and $CALIOP_{40km}$ for summer and winter period. The superscript “all” represents the results when taking all aerosol types into account and “md” when sorting out backscatter coefficients caused by marine and dust aerosol.

19 – 26 July 2006

	$CALIOP_{5km}^{data1}$				$CALIOP_{5km}^{data2}$				$CALIOP_{5km}^{data3}$				$CALIOP_{5km}^{data4}$				$CALIOP_{40km}$			
Altitude (km)	A_{bias}^{all}	R_{bias}^{all}	A_{bias}^{md}	R_{bias}^{md}	A_{bias}^{all}	R_{bias}^{all}	A_{bias}^{md}	R_{bias}^{md}	A_{bias}^{all}	R_{bias}^{all}	A_{bias}^{md}	R_{bias}^{md}	A_{bias}^{all}	R_{bias}^{all}	A_{bias}^{md}	R_{bias}^{md}	A_{bias}^{all}	R_{bias}^{all}	A_{bias}^{md}	R_{bias}^{md}
0.0 – 0.5	6.4	71	8.3	124	6.6	76	8.0	117	5.6	52	7.0	78	6.9	74	7.4	87	10.2	182	12.0	394
0.5 – 1.0	3.9	42	5.1	62	4.0	45	4.9	58	2.9	27	3.5	32	3.7	37	3.5	33	5.6	79	7.4	112
1.0 – 1.5	4.1	51	5.3	71	3.9	50	4.8	63	3.3	35	4.0	41	3.6	40	3.6	36	4.9	76	6.0	83
1.5 – 2.0	3.2	45	4.3	63	3.0	44	3.9	59	2.6	31	3.4	37	2.5	32	2.8	30	4.0	67	5.1	74
2.0 – 2.5	2.0	37	3.0	62	1.9	38	2.9	62	1.6	26	2.4	39	1.8	30	2.2	35	3.2	79	4.0	102
2.5 – 3.0	1.3	35	2.3	76	1.5	44	2.3	84	1.1	25	2.0	50	1.3	30	2.0	53	2.2	70	3.3	151
3.0 – 3.5	1.0	34	2.1	116	1.0	33	2.1	125	0.8	23	2.0	82	1.0	30	2.0	87	1.6	57	2.8	192
3.5 – 4.0	0.8	35	1.9	171	0.7	28	1.9	185	0.6	22	1.8	124	0.6	24	1.9	135	1.1	51	2.6	380
4.0 – 4.5	0.9	62	1.8	292	0.8	46	1.8	340	0.8	45	1.7	218	0.9	49	1.8	242	1.3	97	2.3	783

16 – 26 February 2007

	$CALIOP_{5km}^{data1}$				$CALIOP_{5km}^{data2}$				$CALIOP_{5km}^{data3}$				$CALIOP_{5km}^{data4}$				$CALIOP_{40km}$			
Altitude (km)	A_{bias}^{all}	R_{bias}^{all}	A_{bias}^{md}	R_{bias}^{md}	A_{bias}^{all}	R_{bias}^{all}	A_{bias}^{md}	R_{bias}^{md}	A_{bias}^{all}	R_{bias}^{all}	A_{bias}^{md}	R_{bias}^{md}	A_{bias}^{all}	R_{bias}^{all}	A_{bias}^{md}	R_{bias}^{md}	A_{bias}^{all}	R_{bias}^{all}	A_{bias}^{md}	R_{bias}^{md}
0.0 – 0.5	-1.6	-9	6.2	61	-0.8	-5	7.4	81	-5.3	-24	1.9	12	-2.3	-12	5.6	42	4.6	43	14.6	400
0.5 – 1.0	-8.8	-43	-0.7	-6	-8.0	-41	0.3	2	-13.2	-51	-6.7	-34	-10.6	-46	-3.8	-22	-3.1	-23	4.9	74
1.0 – 1.5	-3.0	-29	1.4	24	-3.0	-29	1.3	23	-5.1	-39	-1.4	-15	-4.3	-35	0.05	1	-2.2	-28	1.6	40
1.5 – 2.0	-1.0	-19	0.7	18	-0.8	-16	0.7	19	-2.3	-34	-1.4	-24	-1.8	-28	-1.0	-19	0.0	0	0.3	9
2.0 – 2.5	-0.9	-24	0.1	4	-0.9	-24	-0.09	-3	-1.9	-39	-1.5	-36	-1.5	-34	-1.1	-29	0.2	9	0.05	3
2.5 – 3.0	0.4	21	0.8	61	0.4	24	0.8	55	-0.1	-6	-0.05	-2	0.2	7	0.2	8	0.7	53	0.7	65
3.0 – 3.5	0.8	83	1.3	259	1.0	109	1.5	405	0.6	45	1.0	126	0.8	79	1.4	284	0.8	92	1.4	480
3.5 – 4.0	1.0	186	1.4	912	1.1	254	1.5	2613	0.9	126	1.3	533	1.0	167	1.5	1645	0.9	168	1.5	4988
4.0 – 4.5	1.0	262	1.2	1009	1.1	460	1.3	7077	0.9	186	1.2	601	1.0	291	1.3	4699	1.0	325	1.3	13897

A different result is found for the winter time period. Often, an improvement in case of the comparison of computed and experimentally observed backscatter values is found after excluding marine and dust caused backscatter values. This kind of improvement it mainly related to height levels from 0.5 km to 2.5 km, whereas between surface and 0.5 km as well as at higher height levels distinct discrepancies are found. Nevertheless, the magnitude of absolute and relative biases for the winter case are often better than for the summer case. During February 2007, the continuous overestimation by the model is also not found as during summer (Figure 5.3). In case of CALIOP$_{5km}^{data1}$, CALIOP$_{5km}^{data2}$, CALIOP$_{5km}^{data4}$ and CALIOP$_{40km}$ the absolute and relative biases shift from negative to positive values for some height levels. Quite good agreements are found between Sim$_{Basic}$ and CALIOP$_{5km}^{data3}$ without the influence of marine and dust aerosol. Here, lowest biases of $0.05 \times 10^{-7}\,\mathrm{m}^{-1}\,\mathrm{sr}^{-1}$ and of 1% are determined between 1.0 – 1.5 km. In case of CALIOP$_{40km}$ a perfect agreement of $0.0\,\mathrm{m}^{-1}\,\mathrm{sr}^{-1}$ and 0% (1.5 – 2.0 km) is also found when taking all kind of aerosols into account.

Based on the comparisons between observed and simulated average vertical backscatter profiles it seems that the strict rules, used for CALIOP$_{5km}^{data4}$ and CALIOP$_{40km}$, lead to best results. But this kind of comparison does not contain any information which CALIOP data set is most recommendable for model comparisons of that kind.

5.1.2 Comparison between day- and night-time CALIOP observations

CALIOP backscatter profiles with a horizontal resolution of 5 km contain information about the observation time including whether the observation time is at day or night. Such information is important, because the background illumination, like sunlight influences the lidar measurements mainly during day-time. In case of night-time, measurements have a higher signal-to-noise ratio than during day-time. It is mentioned by Vaughan et al. (2009) that this behavior influences the number of features which are found by the feature finder. The different conditions during day and night offers a detailed analysis of the calibration algorithms used for CALIOP data (Powell et al., 2008, 2009). In case of the night-time calibration coefficients, a discrimination between the 532 nm parallel and perpendicular channel is done (Powell et al., 2009). Signals from 30 to 34 km altitude are used (because this region is quite free of aerosols but also leads to a acceptable large backscatter signal of the mean molecular number density) for comparisons with a scattering model to determine the calibration coefficients. Powell et al. (2008) explains, that day-time calibration values are calculated by means of an interpolation of the adjacent night-time data. Night-time calibration coefficients are quite constant over the darkest segment of the orbit. But the authors also mention the rapid change within short time when the satellite is affected by sunlight. Day-time calibration coefficients are based on the night-time coefficients, but it was shown that these day-time calibration values are not constant.

Mamouri et al. (2009) used 40 coincidental lidar profiles obtained by CALIOP and at the ground-based station in Athens (Greece) to analyze the agreements during day- and night-time. The authors determined a larger mean bias for day-time observations (22%) than for night-time observations (8%) between 3 and 10 km altitude. In a recent study, performed by Koffi et al. (2012), only night-time mean annual vertical profiles are used for comparisons between CALIOP data and AeroCom simulations, because of a better signal-to-noise ratio during night-time than during day-time. CALIOP provides information about the structure of aerosol layers with a lower limit of 0.07 during night and of 0.1 during day at 532 nm (Chazette et al., 2010). A detailed study of the day and night differences is performed by Wu et al. (2011). The authors found larger day-time noises over land and bright surfaces, like snow, ice and desert. Night-time

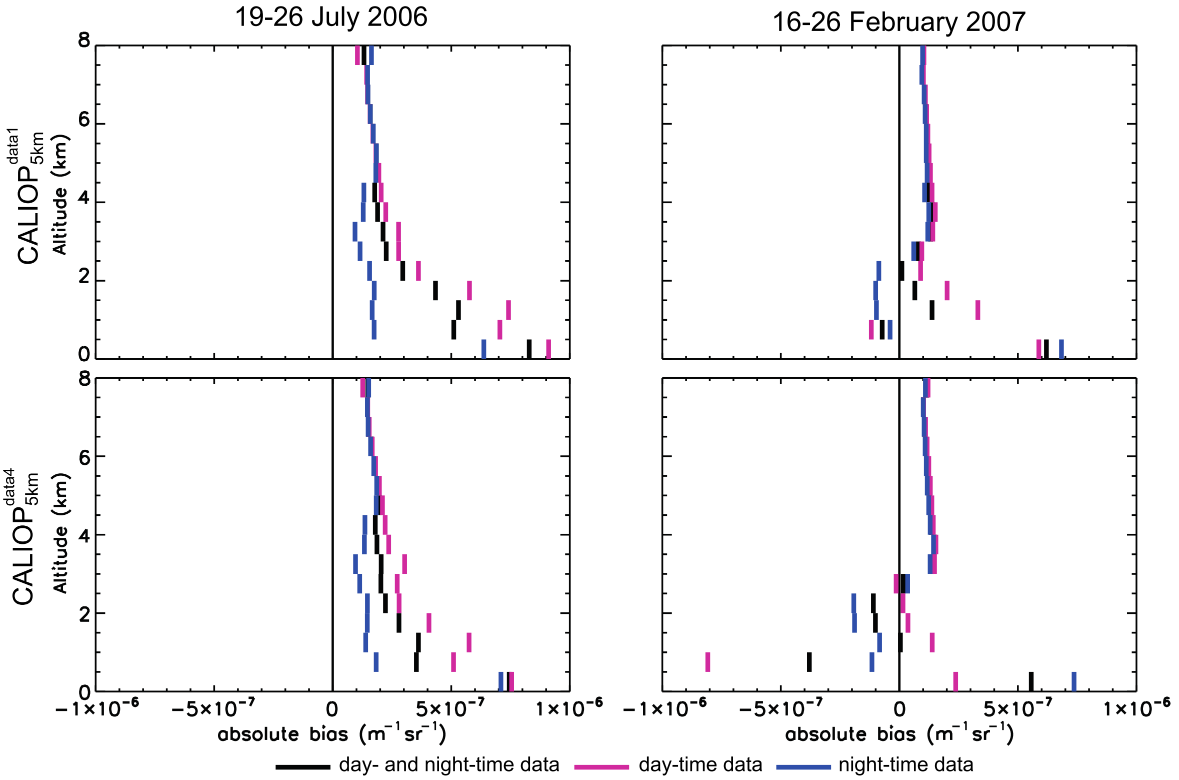

Figure 5.4: Absolute bias (A_{bias}) for each 500 m level between surface and 8 km altitude for all time (black lines), day-time (pink line) and night-time (blue lines) observations for data without marine and dust aerosol during 19 – 26 July 2006 (left panel) and 16 – 26 February 2007 (right panel). Within the upper panel results when using $\mathrm{CALIOP}^{data1}_{5km}$ data and in the lower panel when using $\mathrm{CALIOP}^{data4}_{5km}$ data are shown.

noises, which are generally lower, increase in so-called radiation-hard regions, like auroral ovals and in the South Atlantic Anomaly. Obviously, discrepancies between day- and night-time CALIOP observations can be found and have to be handled with care, but the calibration algorithms, presented by Powell et al. (2008, 2009) are assessed and validated continuously.

In Figure 5.4 day- and night-time absolute biases are shown for both simulation periods based on the data set without marine and dust aerosol type. Here, results, when using CALIOP$_{5km}^{data1}$ and CALIOP$_{5km}^{data4}$, are shown. For a better orientation, the values of A$_{bias}^{md}$ for CALIOP$_{5km}^{data1}$ and CALIOP$_{5km}^{data4}$, which include both day- and night-time data, are plotted as well as black lines in Figure 5.4. It is decided to present the absolute bias here, due to the distinct increase of the relative bias mainly at higher altitudes (Table 5.2). Additionally, Table 5.3 contains the absolute bias based on the determination of backscatter coefficient between Sim$_{Basic}$ and CALIOP$_{5km}^{data1}$, CALIOP$_{5km}^{data2}$, CALIOP$_{5km}^{data3}$ and CALIOP$_{5km}^{data4}$ between surface and 4.5 km altitude.

As in the previous works, distinct differences between day and night are found. During summer, the results based on CALIOP$_{5km}^{data1}$ and CALIOP$_{5km}^{data4}$ (Figure 5.4) clearly show a better agreement between experimentally observed and computed backscatter coefficients during night-time (blue lines) for nearly all height levels. Between surface and 0.5 km altitude, differences between day-time, night-time and data including both day- and night-time values, remain small. Discrepancies between the individual data sets increase with increasing altitude up to 4.5 km altitude in case of CALIOP$_{5km}^{data1}$ and CALIOP$_{5km}^{data4}$ (Figure 5.4, left panel). For instance, night-time absolute biases range from $1.0 \times 10^{-7}\,\mathrm{m^{-1}\,sr^{-1}}$ to $1.8 \times 10^{-7}\,\mathrm{m^{-1}\,sr^{-1}}$ between 0.5 and 4.5 km in case of CALIOP$_{5km}^{data4}$, whereas day-time values range from $2.2 \times 10^{-7}\,\mathrm{m^{-1}\,sr^{-1}}$ to $5.8 \times 10^{-7}\,\mathrm{m^{-1}\,sr^{-1}}$ for the same altitude range (Table 5.3). The higher variability of the lidar signal at day-time disturbs the backscatter signal at higher altitudes more strongly, probably due to the lower backscatter signal caused by lower aerosol concentration.

In case of the winter period, a different result is found when comparing day- and night-time data (Figure 5.4, right panel; Table 5.3). Differences between day-, night- and day-and-night-time data are small at altitudes above 2.5 km. Between surface and 2.5 km altitude it is often the case that day-time values lead to better agreements between computed and observed backscatter coefficients.

It can be assumed, that a seasonal dependency is found here. But for a final decision, a larger amount of data, representing the seasons, has to be analyzed.

It is in accordance for both time periods, that data including the backscatter val-

Table 5.3: Individual A_{bias} ($x\,10^{-7}\,m^{-1}\,sr^{-1}$) for each 500 m height level determined between surface and 4.5 km altitude for the different data sets $CALIOP_{5km}^{data1}$, $CALIOP_{5km}^{data2}$, $CALIOP_{5km}^{data3}$ and $CALIOP_{5km}^{data4}$ for the summer and winter period during day- and night-time conditions. The superscript "all" represents the results when taking all aerosol types into account and "md" when sorting backscatter coefficients caused by marine and dust aerosol out.

19 – 26 July 2006																
	$CALIOP_{5km}^{data1}$				$CALIOP_{5km}^{data2}$				$CALIOP_{5km}^{data3}$				$CALIOP_{5km}^{data4}$			
	day		night		day		night		day		night		day		night	
Altitude (km)	A_{bias}^{all}	A_{bias}^{md}	A_{bias}^{all}	A_{bias}^{md}	A_{bias}^{all}	A_{bias}^{md}	A_{bias}^{all}	A_{bias}^{md}	A_{bias}^{all}	A_{bias}^{md}	A_{bias}^{all}	A_{bias}^{md}	A_{bias}^{all}	A_{bias}^{md}	A_{bias}^{all}	A_{bias}^{md}
0.0 – 0.5	7.1	9.1	5.0	6.4	7.2	8.7	5.4	6.4	6.0	7.7	4.8	6.0	7.1	7.6	6.6	7.1
0.5 – 1.0	5.8	7.1	1.0	1.7	5.8	6.6	1.2	1.8	4.7	5.4	0.7	1.3	5.3	5.1	1.9	1.8
1.0 – 1.5	6.2	7.4	0.8	1.7	5.8	6.8	0.9	1.4	5.5	6.5	0.6	1.3	5.5	5.8	1.4	1.4
1.5 – 2.0	4.6	5.8	0.9	1.7	4.3	5.3	0.9	1.5	4.1	5.0	0.7	1.5	3.9	4.1	1.0	1.5
2.0 – 2.5	2.7	3.6	0.7	1.6	2.6	3.4	0.8	1.6	2.4	3.2	0.6	1.4	2.6	2.8	0.8	1.5
2.5 – 3.0	2.0	2.8	0.3	1.2	2.1	2.9	0.5	1.2	1.8	2.6	0.3	1.0	1.9	2.7	0.4	1.1
3.0 – 3.5	1.5	2.8	0.2	0.9	1.3	2.8	0.5	1.0	1.3	2.9	0.2	0.9	1.5	3.0	-0.06	1.0
3.5 – 4.0	1.1	2.2	0.3	1.3	0.7	2.2	0.5	1.3	0.9	2.3	0.3	1.2	0.9	2.4	0.07	1.3
4.0 – 4.5	1.2	2.0	0.5	1.3	0.8	2.1	0.7	1.4	1.0	2.1	0.5	1.3	1.1	2.2	0.6	1.4
16 – 26 February 2007																
	$CALIOP_{5km}^{data1}$				$CALIOP_{5km}^{data2}$				$CALIOP_{5km}^{data3}$				$CALIOP_{5km}^{data4}$			
	day		night		day		night		day		night		day		night	
Altitude (km)	A_{bias}^{all}	A_{bias}^{md}	A_{bias}^{all}	A_{bias}^{md}	A_{bias}^{all}	A_{bias}^{md}	A_{bias}^{all}	A_{bias}^{md}	A_{bias}^{all}	A_{bias}^{md}	A_{bias}^{all}	A_{bias}^{md}	A_{bias}^{all}	A_{bias}^{md}	A_{bias}^{all}	A_{bias}^{md}
0.0 – 0.5	-1.1	5.9	-2.0	6.8	0.2	7.5	-1.6	7.5	-7.9	-2.3	-3.7	4.5	-4.7	2.4	-1.0	7.4
0.5 – 1.0	-5.5	-1.2	-11.9	-0.4	-3.3	1.1	-12.3	-0.8	-12.5	-12.9	-13.8	-2.5	-8.9	-8.1	-11.7	-1.2
1.0 – 1.5	1.4	3.3	-7.1	-1.0	1.1	2.8	-6.7	-0.5	-0.8	0.0	-8.2	-2.4	0.3	1.4	-7.2	-0.8
1.5 – 2.0	0.9	2.0	-2.9	-1.0	0.6	1.8	-2.3	-0.7	-0.7	-0.4	-3.5	-2.1	-0.3	0.4	-2.8	-1.9
2.0 – 2.5	-0.4	0.9	-1.4	-0.9	-0.5	0.8	-1.4	-1.2	-2.1	-1.5	-1.7	-1.6	-1.5	0.2	-1.5	-1.9
2.5 – 3.0	0.6	1.0	0.1	0.6	0.5	0.9	0.3	0.6	-0.3	-0.7	-0.01	0.4	0.0	-0.1	0.2	0.3
3.0 – 3.5	1.1	1.4	0.6	1.2	1.2	1.6	0.7	1.4	0.7	0.9	0.5	1.1	1.1	1.5	0.7	1.3
3.5 – 4.0	1.3	1.5	0.7	1.2	1.4	1.5	0.8	1.4	1.3	1.5	0.6	1.2	1.3	1.5	0.8	1.4
4.0 – 4.5	1.2	1.4	0.7	1.1	1.3	1.4	1.0	1.3	1.2	1.4	0.7	1.0	1.2	1.4	0.9	1.3

ues of all aerosol types are often better than those without marine and dust caused backscatter values as summarized in Table 5.3. This effect is found for nearly all CALIOP data sets (CALIOP$_{5km}^{data1}$, CALIOP$_{5km}^{data2}$, CALIOP$_{5km}^{data3}$, CALIOP$_{5km}^{data4}$). Differences between the results of the individual data sets also occur but remain quite small. In case of the summer period it is found that day- and night-time backscatter differences when using CALIOP$_{5km}^{data1}$ values are often similar to those backscatter differences when using CALIOP$_{5km}^{data2}$, CALIOP$_{5km}^{data3}$ or CALIOP$_{5km}^{data4}$. During February 2007, discrepancies between the results of the individual data sets are sometimes larger. For instance, an absolute bias of $\mathrm{A}_{bias}^{md} = 1.1 \,\mathrm{x}\, 10^{-7}\,\mathrm{m}^{-1}\,\mathrm{sr}^{-1}$ is determined for CALIOP$_{5km}^{data2}$ and of $\mathrm{A}_{bias}^{md} = \text{-}12.9 \,\mathrm{x}\, 10^{-7}\,\mathrm{m}^{-1}\,\mathrm{sr}^{-1}$ for CALIOP$_{5km}^{data3}$ between 0.5 km and 1.0 km altitude (Table 5.3).

5.1.3 Conclusion

In this chapter, the simulated and experimentally observed vertical backscatter profiles are compared. Observation data are based on continuous measurements by the space-based lidar CALIOP. These data are available with a horizontal resolution of 5 and 40 km and are compiled based on different limitations as described in Section 3.1.2. Five different CALIOP data sets are available: CALIOP$_{5km}^{data1}$, CALIOP$_{5km}^{data2}$, CALIOP$_{5km}^{data3}$, CALIOP$_{5km}^{data4}$ and CALIOP$_{40km}$. CALIOP backscatter values are classified according to the aerosol type (marine, dust or other aerosol type). The time periods are chosen for evaluation of the model quality: a summer (8 days) and a winter (11 days) period. For the model version used here, marine aerosol as well as dust particles are not described. Thus, comparisons in regions with marine and dust aerosol lead to distinct differences between model and experimental observation. The backscatter coefficients influenced by marine and dust particles are sorted out. Thus, the five CALIOP data sets including observation data with backscatter values of all aerosol types as well as without the influence of marine and dust aerosol are created.

Comparisons of individual backscatter values based on Sim$_{Basic}$ data and the various CALIOP results, which are determined for each 500 m height level between surface and 8 km altitude, show a general overestimation of the observed backscatter values by the model. This overestimation is found in case of backscatter values of all aerosol types and without marine and dust particles. Further, sorting out backscatter values which are related to the existence of marine and dust particles does not necessarily leads to an improvement of the average backscatter difference determined between Sim$_{Basic}$ and CALIOP data. Comparisons of model results with CALIOP data of the coarse horizontal resolution of 40 km are clearly different compared to comparisons between

model and CALIOP data with 5 km horizontal resolution.
Based on the individual profiles, average backscatter profiles based on simulation and observation are determined, representing the conditions for the individual simulation periods. The model is able to reproduce the average observed vertical backscatter profiles including backscatter values of all aerosol types and without marine and dust aerosol successfully for both summer and winter period. Sorting out marine and dust caused backscatter values leads to a distinct decrease of the backscatter values mainly within the PBL during February 2007, probably due to the existence of marine aerosol in that region. In case of the summer period an effect at height levels above the PBL is found. Dust particles are transported at higher altitudes and due to the sorting out, a decrease of the average backscatter coefficients at height levels above 2.5 km is determined. During July 2006, a significant improvement when comparing data without marine and dust backscatter values is not found in contrast to February 2007. Discrepancies between CALIOP data and model results can also be caused by an inadequate identification of marine aerosol by CALIOP, because CALIOP identifies marine aerosol only over sea surface and does not take into account the existence in coastal regions or the transport of marine aerosol over land surface.
The discrimination for day- and night-time observations and their agreement with simulated data is also shown here. Especially for the summer period a better agreement is found for night-time data than for day-time observations.

5.2 Model evaluation with ground-based observations

5.2.1 Simulation results of spatio-temporal distribution of European aerosol

Based on the individual simulation results of EC, $PPM_{2.5}$, H_2SO_4, NH_4NO_3 and $(NH_4)_2SO_4$, performed with the Sim_{Basic} model setup, the total mass $PM_{2.5}$ is determined. Average $PM_{2.5}$ values for the entire model domain within the near surface layer based on the hourly model output are shown in Figure 5.5 for summer and winter. In case of the summer simulation period, an average $PM_{2.5}$ concentration of $7.1\,\mathrm{x}\,10^{-6}\,\mathrm{g\,m^{-3}}$ is found (minimum: $2.0\,\mathrm{x}\,10^{-6}\,\mathrm{g\,m^{-3}}$, maximum: $2.6\,\mathrm{x}\,10^{-5}\,\mathrm{g\,m^{-3}}$) near the surface, whereas during the winter period an average value of $6.2\,\mathrm{x}\,10^{-6}\,\mathrm{g\,m^{-3}}$ is determined (minimum: $1.3\,\mathrm{x}\,10^{-6}\,\mathrm{g\,m^{-3}}$, maximum: $4.9\,\mathrm{x}\,10^{-5}\,\mathrm{g\,m^{-3}}$). These values

Table 5.4: Fractions of H_2SO_4, NH_4NO_3, $(NH_4)_2SO_4$, EC and $PPM_{2.5}$ in $PM_{2.5}$. The individual values are presented as daily averages as well as averages for the entire simulation periods for the near surface layer. Within the brackets the minimum and maximum fractions are presented.

		H_2SO_4	NH_4NO_3	$(NH_4)_2SO_4$	EC	$PPM_{2.5}$
July 2006	19	0.00 (0.00 – 0.10)	0.00 (0.00 – 0.19)	0.20 (0.08 – 0.51)	0.20 (0.10 – 0.23)	0.60 (0.35 – 0.70)
	20	0.00 (0.00 – 0.28)	0.01 (0.00 – 0.39)	0.33 (0.07 – 0.76)	0.16 (0.05 – 0.23)	0.50 (0.15 – 0.72)
	21	0.01 (0.00 – 0.38)	0.01 (0.00 – 0.47)	0.39 (0.06 – 0.78)	0.14 (0.04 – 0.23)	0.45 (0.12 – 0.73)
	22	0.01 (0.00 – 0.45)	0.01 (0.00 – 0.48)	0.42 (0.07 – 0.81)	0.13 (0.03 – 0.23)	0.42 (0.11 – 0.72)
	23	0.02 (0.00 – 0.41)	0.01 (0.00 – 0.48)	0.43 (0.07 – 0.82)	0.13 (0.03 – 0.24)	0.41 (0.11 – 0.70)
	24	0.02 (0.00 – 0.43)	0.02 (0.00 – 0.49)	0.45 (0.07 – 0.83)	0.12 (0.02 – 0.23)	0.39 (0.11 – 0.70)
	25	0.02 (0.00 – 0.47)	0.01 (0.00 – 0.46)	0.48 (0.06 – 0.85)	0.12 (0.02 – 0.23)	0.37 (0.11 – 0.70)
	26	0.02 (0.00 – 0.49)	0.02 (0.00 – 0.52)	0.46 (0.07 – 0.85)	0.12 (0.03 – 0.23)	0.38 (0.10 – 0.70)
	19 – 26	0.01 (0.00 – 0.30)	0.01 (0.00 – 0.30)	0.40 (0.08 – 0.75)	0.14 (0.04 – 0.23)	0.43 (0.18 – 0.69)
February 2007	16	0.00 (0.00 – 0.38)	0.05 (0.00 – 0.22)	0.23 (0.11 – 0.63)	0.27 (0.08 – 0.35)	0.45 (0.16 – 0.67)
	17	0.00 (0.00 – 0.23)	0.06 (0.00 – 0.35)	0.33 (0.10 – 0.78)	0.21 (0.06 – 0.36)	0.39 (0.14 – 0.67)
	18	0.00 (0.00 – 0.25)	0.05 (0.00 – 0.33)	0.35 (0.10 – 0.78)	0.20 (0.05 – 0.36)	0.39 (0.14 – 0.65)
	19	0.00 (0.00 – 0.47)	0.06 (0.00 – 0.36)	0.38 (0.09 – 0.80)	0.19 (0.02 – 0.36)	0.37 (0.10 – 0.65)
	20	0.00 (0.00 – 0.29)	0.06 (0.00 – 0.39)	0.38 (0.10 – 0.86)	0.19 (0.02 – 0.36)	0.37 (0.10 – 0.66)
	21	0.01 (0.00 – 0.53)	0.05 (0.00 – 0.36)	0.38 (0.10 – 0.86)	0.19 (0.02 – 0.36)	0.37 (0.06 – 0.67)
	22	0.01 (0.00 – 0.40)	0.05 (0.00 – 0.41)	0.36 (0.10 – 0.89)	0.20 (0.02 – 0.36)	0.38 (0.07 – 0.68)
	23	0.01 (0.00 – 0.46)	0.05 (0.00 – 0.37)	0.34 (0.11 – 0.85)	0.21 (0.02 – 0.36)	0.39 (0.10 – 0.68)
	24	0.01 (0.00 – 0.84)	0.05 (0.00 – 0.32)	0.35 (0.00 – 0.84)	0.21 (0.02 – 0.37)	0.39 (0.09 – 0.70)
	25	0.01 (0.00 – 0.49)	0.04 (0.00 – 0.32)	0.36 (0.05 – 0.81)	0.21 (0.03 – 0.36)	0.39 (0.10 – 0.69)
	26	0.00 (0.00 – 0.24)	0.04 (0.00 – 0.39)	0.34 (0.09 – 0.83)	0.21 (0.04 – 0.36)	0.40 (0.12 – 0.69)
	16 – 26	0.01 (0.00 – 0.18)	0.05 (0.00 – 0.28)	0.35 (0.11 – 0.74)	0.21 (0.05 – 0.35)	0.38 (0.14 – 0.67)

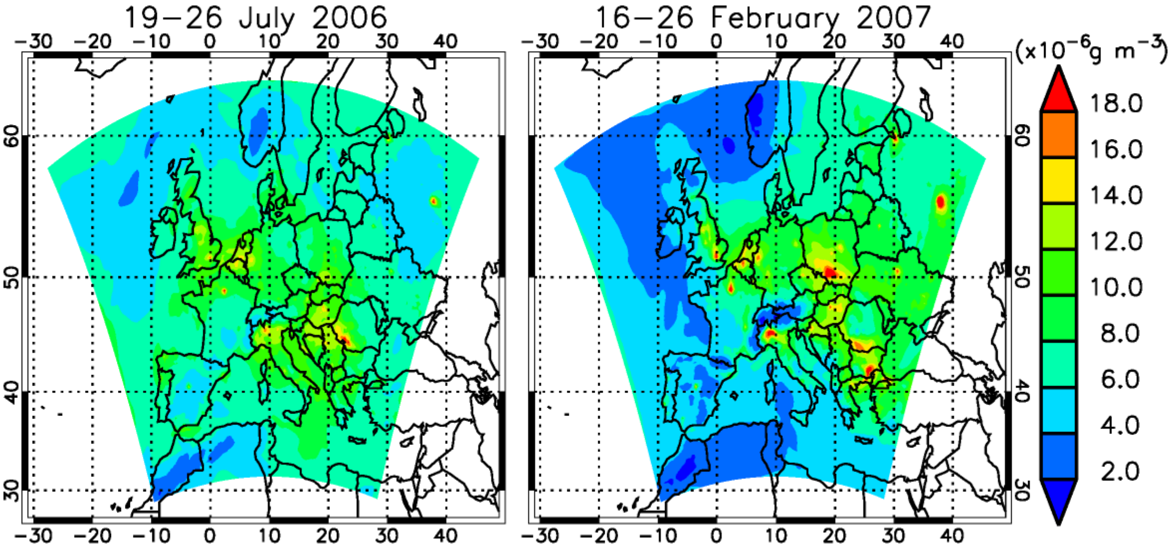

Figure 5.5: Maps of average $PM_{2.5}$ for 19 − 26 July 2006 and 16 − 26 February 2007. The values show the simulation result within the lowest model layer.

represent the different conditions during both time periods. As mentioned in Chapter 4, a high accumulation of atmospheric particles was possible during the summer. In case of the winter period, particles are often removed out of the atmosphere because of several precipitation events. Due to this meteorological character a lower average $PM_{2.5}$ concentration is simulated during February 2007. It is shown in Figure 5.5 that during July 2006 nearly the entire model domain contains $PM_{2.5}$ concentrations larger than $6.0 \times 10^{-6}\,g\,m^{-3}$. During the winter period the $PM_{2.5}$ concentration tends to be larger than $6.0 \times 10^{-6}\,g\,m^{-3}$ in Middle Europe and in the east and north-east of the model domain. Those high concentrations are partly due to the fact that the winter simulation period is also a heating period. Additionally, during winter time, the boundary layer is lower than during the summer time and thus results in a less atmospheric mixing. Both facts could contribute to the regionally higher maximum $PM_{2.5}$ concentration during the winter period compared to the summer period.
In general, low $PM_{2.5}$ values are computed over the ocean. Here, on average a $PM_{2.5}$ concentration of $6.8 \times 10^{-6}\,g\,m^{-3}$ (summer) and of $4.9 \times 10^{-6}\,g\,m^{-3}$ (winter) is found. In contrast, over land surface, average concentrations of $7.1 \times 10^{-6}\,g\,m^{-3}$ and $6.9 \times 10^{-6}\,g\,m^{-3}$ for the summer and the winter period, respectively, are computed caused by the local emissions. Hot spot regions, like large cities and their surroundings (e.g., Paris, London, Milan, Moscow, Benelux and the Balkan area) are clearly visible for both time periods. Here, the $PM_{2.5}$ concentration reaches values larger than $1.6 \times 10^{-5}\,g\,m^{-3}$.

On average, the main fractions of the $PM_{2.5}$ concentrations are caused by $PPM_{2.5}$ and $(NH_4)_2SO_4$ for both time periods as summarized in Table 5.4. For the entire sum-

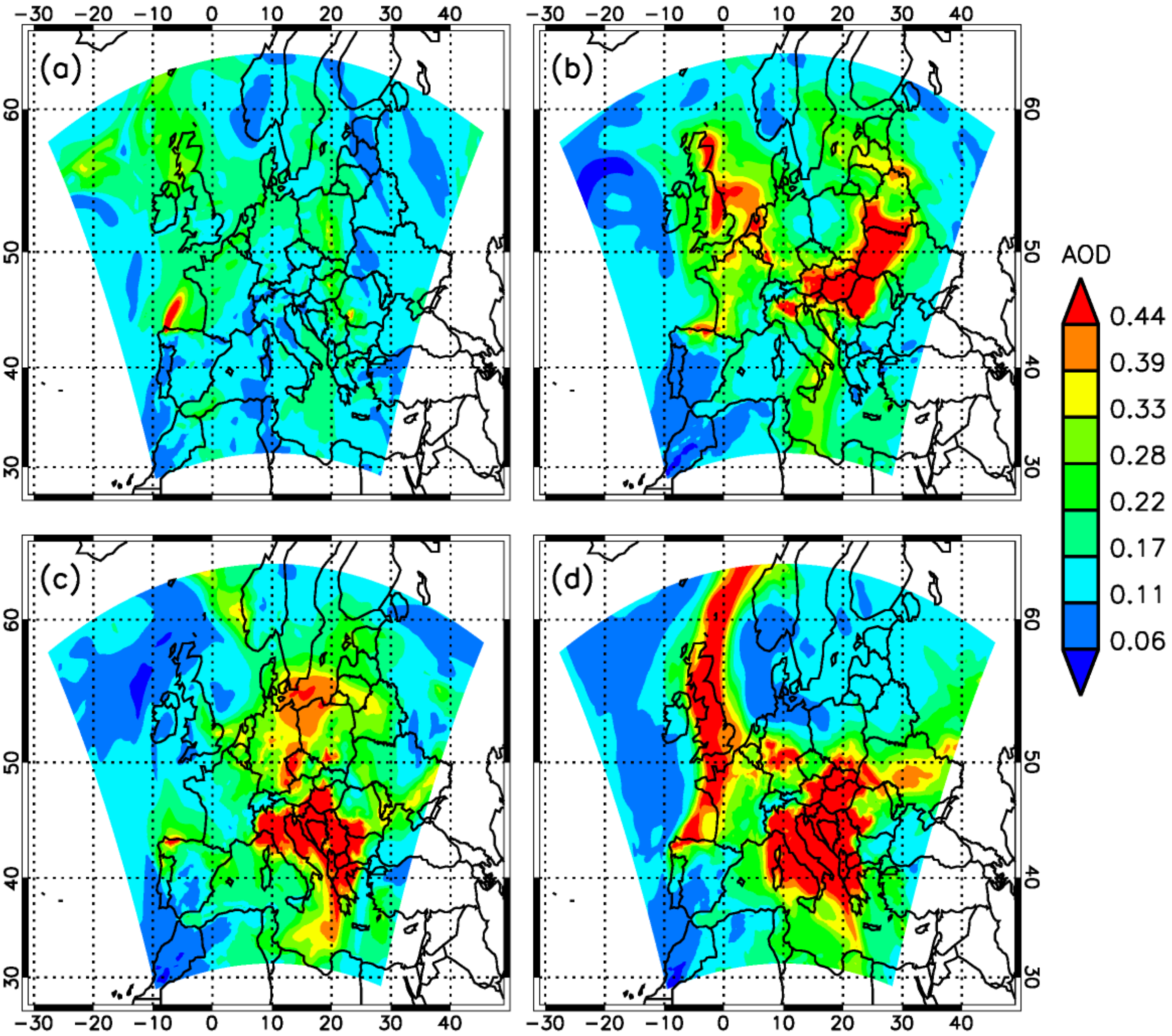

Figure 5.6: Maps of daily average AOD on (a) 20 July 2006, (b) 22 July 2006, (c) 24 July 2006, and (d) 26 July 2006.

mer simulation period, fractions of 0.43 and 0.4 are found for $PPM_{2.5}$ and $(NH_4)_2SO_4$. These fractions are slightly lower during the winter period ($PPM_{2.5}$: 0.38, $(NH_4)_2SO_4$: 0.35). Lowest fractions are determined for H_2SO_4 and NH_4NO_3 for July 2006 and February 2007. Especially the contribution of H_2SO_4 to $PM_{2.5}$ is negligible throughout both time periods (Table 5.4). Highest EC fractions (summer: 0.20, winter: 0.27) occur during the first day of model simulation for both time periods. Throughout the entire summer simulation period the average EC fraction is below 20%. Thus, due to the definition of "urban" and "continental" aerosol (see Section 2.3), mainly "continental" aerosol will be simulated. Only at few locations, larger EC fractions (23% – 24%) are determined (Table 5.4). During the winter period, due to the domestic heating, higher fractions of EC are simulated. Despite on 19 – 21 February 2007, daily average EC fractions are larger than 20%. Thus, more "urban" than "continental" aerosol will be computed.

Based on the concentrations of H_2SO_4, NH_4NO_3, $(NH_4)_2SO_4$, EC and $PPM_{2.5}$ the individual extinction coefficients (α_i) are determined (Section 2.3, Equation 2.6) for each model grid cell. The sum of these extinction coefficients at the individual altitudes offers the possibility to calculate the AOD by means of:

$$\tau = \sum_{l} \sum_{i=1}^{5} \alpha_i \tag{5.3}$$

with l as atmospheric layer and i as number of the individual species (Meier et al., 2012b). The daily average AOD for every second day is shown in Figure 5.6 (summer period) and in Figure 5.7 (winter period) to illustrate the daily variability of the AOD during summer and winter time. The average AOD values, representing the AOD during 19 – 26 July 2006 and during 16 – 26 February 2007, are shown in Figure 5.8 (upper panel). Additionally, Table 5.5 contains minimum (τ_{min}), maximum (τ_{max}) and average (τ_{mean}) AOD values for every single day and for the entire simulation periods. Both simulation periods start with relatively low AOD as secondary aerosols are only formed after some time. On average, an AOD of 0.11 ($\tau_{min} = 0.04$, $\tau_{max} = 0.36$) is determined on 19 July 2009 and of 0.10 ($\tau_{min} = 0.03$, $\tau_{max} = 0.76$) on 16 February 2007 (Table 5.5). From day to day, the highest optical depths during July 2006 are computed over the European continent in the middle of the model domain. Here, distinct values of $\tau \geq 0.44$ are found over the Bay of Biscay (Figure 5.6, (a) – (d)), Belarus, Ukraine, Hungary and Romania (Figure 5.6 (b) and (d)), Germany, the Benelux, United Kingdom and the North Sea (Figure 5.6 (b)) as well as over the Balkan area (Figure 5.6 (c – d)). The average AOD for the entire model domain increases stepwise from 0.11 on 19 July to 0.25 on 26 July, whereas mostly over land surface (0.10 – 0.27) the daily average AOD is higher than over sea surface (0.12 – 0.21; Table 5.5). High maximum values are computed for the summer simulation period. An exception are the values up to 1.74, determined on 26 July 2006, which is found over sea surface (Table 5.5).

In general, lower daily AOD results are also determined over sea surface (0.09 – 0.16) than over land surface (0.10 – 0.18) during February 2007 (Table 5.5). In contrast to the summer simulation period, the difference between minimum and maximum daily AOD for the entire model domain is not as distinct during the winter time. As mentioned before, lowest daily AOD results of 0.10 are determined on 16 February and highest daily average values of 0.15 on 20 February and 22 – 24 February 2007 (Table 5.5). Figure 5.7 shows larger values ($\tau > 0.22$) in the middle and in the east of the model domain for nearly the entire period. Computed values of AOD, in the Balkan area or in the south-east of the model domain, can reach large areas with values larger than 0.44. On 17, 23 and 25 February a transport of atmospheric particles from the

northern boundary into the model domain occurs (Figure 5.7 (a) and (d – f)), whereas the graphs, representing the conditions on 19, 21 and 23 February (Figure 5.7 (b – d)) show the transport from the eastern direction into the model domain. Despite the low average daily AOD, determined for the winter period (compared to the summer time), high maximum optical depth is also found during February 2007. On 22 February 2007, a maximum AOD of 2.23 is computed (Table 5.5), whereas highest AOD values are computed over land surface due to the local emissions.
Average AOD results are shown in Figure 5.8 (upper panel) for the entire simulation periods. Highest values ($\tau = 0.19$) are computed for the summer case, whereas during the winter period an average AOD of 0.14 for the entire model domain is calculated (Table 5.5). Compared to the average surface distribution of $PM_{2.5}$ (Figure 5.5) lowest AOD values are also found over sea surface for July 2006 (0.18) and February 2007 (0.12). At the lateral model boundaries low values are computed, compared to the land surface. During summer time, significantly high AOD data are found over the Balkan domain. Here, values larger than 0.4 are detected. In other regions within Europe, the AOD ranges from 0.17 to 0.33 during 19 – 26 July 2006. Because of the weak potential of particle accumulation during the winter time, optical depths are often lower than during summer time. Regarding the land surface, an average value of 0.14 is found during winter (Table 5.5). In contrast, an average AOD of 0.21 is determined for July 2006 over land surface (Table 5.5). As during the summer period, the Balkan domain shows high AOD during February 2007, as well. In contrast to the summer, AOD values between 0.17 and 0.33 are mainly located over the east and south-east part of the model domain.

The role of local emissions, compared to aerosol transport, is evaluated by comparing Sim_{Basic} and Sim_{noEmi} (Table 2.1). The relatively high AOD over the south-east part of the model domain (for both simulation periods) is caused by local particle emissions. The relative differences of AOD ($\tau_{relDiff}$) for each model grid cell are determined by using

$$\tau_{relDiff} = \frac{Result\ 1 - Result\ 2}{Result\ 2} \tag{5.4}$$

where $Result1$ represents the AOD determined by Sim_{Basic} and $Result2$ the AOD determined by Sim_{noEmi} (Meier et al., 2012b). Additionally, the relative AOD difference between Sim_{Basic} and $\mathrm{Sim}_{noTrans}$ (Table 2.1) is calculated. Based on this calculation, information about the transport-influenced AOD can be determined for both simulation periods. Differences between the Sim_{Basic} computation and the emission-only AOD, and the transport-only AOD are shown in Figure 5.8 in the middle and lower panels for summer and winter. For both time periods the transport of atmospheric particles from outside into the model domain affects all regions next to the lateral model boundaries,

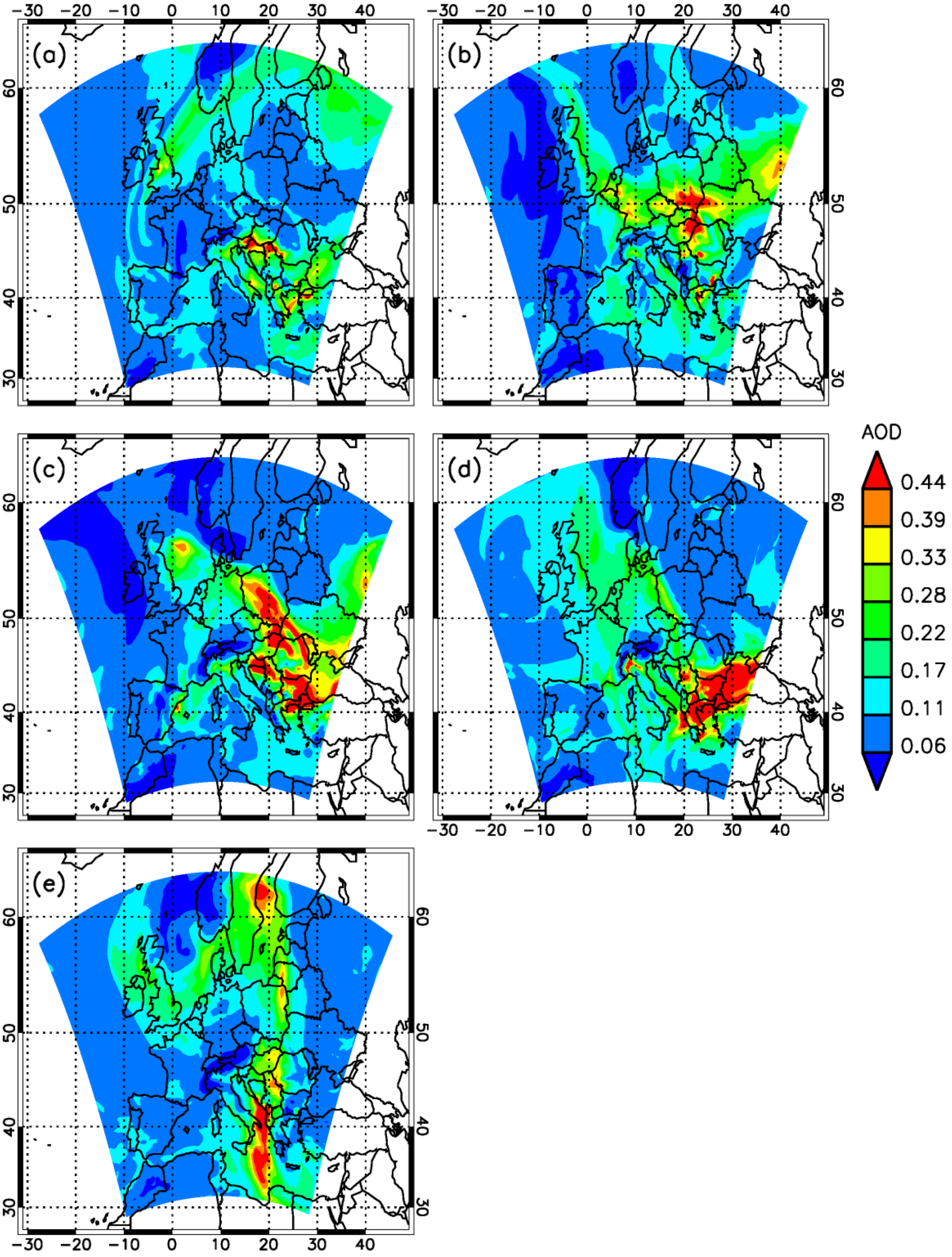

Figure 5.7: Maps of daily average AOD on (a) 17 February 2007, (b) 19 February 2007, (c) 21 February 2007, (d) 23 February 2007, and (e) 25 February 2007.

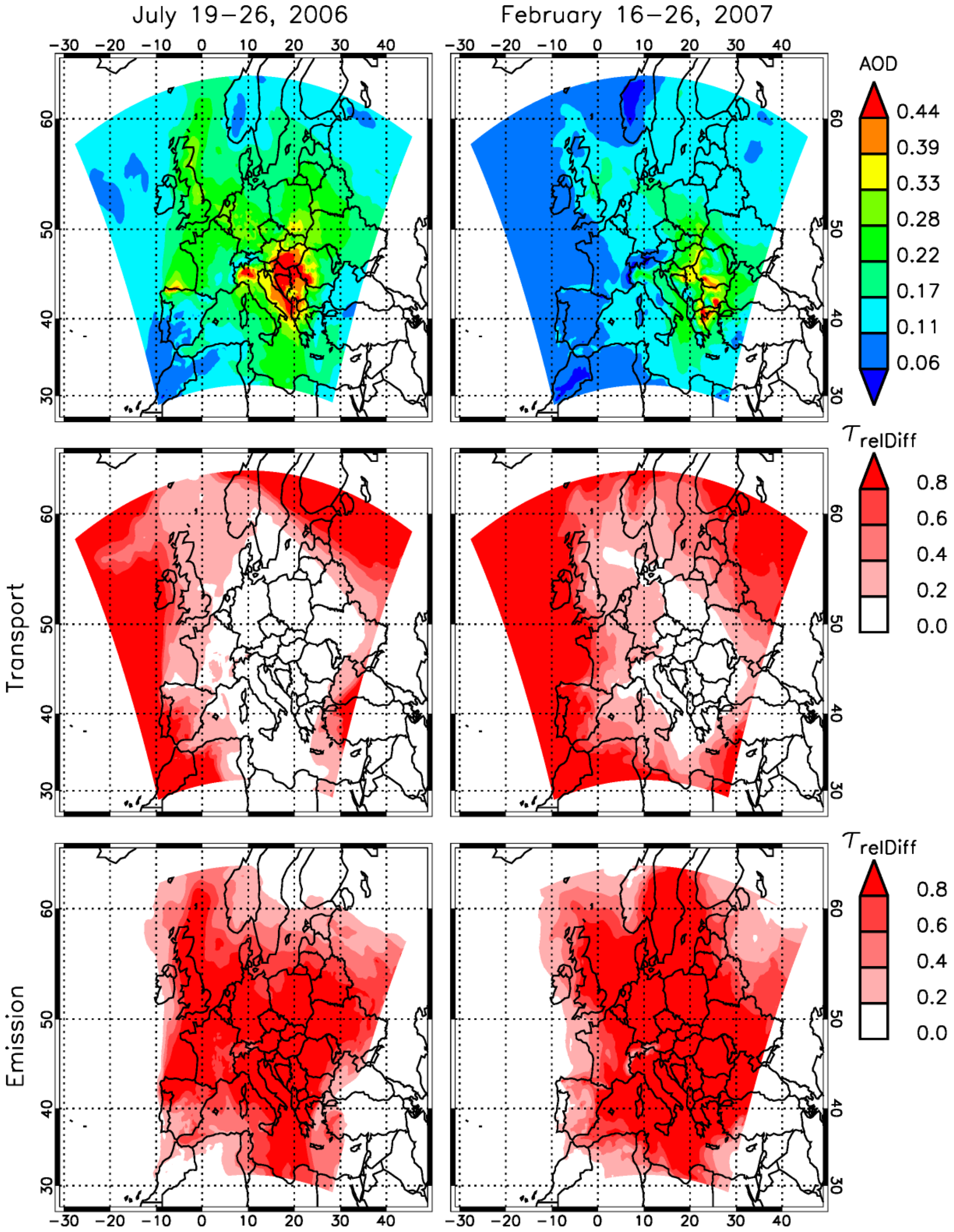

Figure 5.8: Maps of average AOD (upper panel), relative differences based on average AOD computed with Sim_{Basic} and $\text{Sim}_{noTrans}$ (middle panel) and relative differences based on average AOD computed with Sim_{Basic} and Sim_{noEmi} (lower panel) for summer and winter.

Table 5.5: Minimum (τ_{min}), maximum (τ_{max}) and average (τ_{mean}) values of the daily average AOD and average AOD values of the entire simulation periods during 19 – 26 July 2006 and 16 – 26 February 2007. Data refer to the entire model domain (including land and sea surface), to sea surface (100% sea surface within the model grid cell; 7594 grid cells) and to land surface (100% land surface within the model grid cell; 6083 grid cells).

		entire domain			land surface			sea surface		
		τ_{min}	τ_{max}	τ_{mean}	τ_{min}	τ_{max}	τ_{mean}	τ_{min}	τ_{max}	τ_{mean}
July 2006	19	0.04	0.36	0.11	0.04	0.27	0.10	0.07	0.24	0.12
	20	0.06	0.92	0.15	0.06	0.46	0.14	0.08	0.66	0.16
	21	0.07	0.93	0.18	0.07	0.75	0.18	0.07	0.69	0.18
	22	0.02	0.89	0.20	0.03	0.89	0.23	0.02	0.55	0.17
	23	0.05	1.18	0.21	0.05	1.18	0.23	0.05	0.62	0.18
	24	0.04	1.48	0.21	0.05	1.48	0.23	0.04	0.63	0.18
	25	0.03	1.60	0.23	0.05	1.60	0.27	0.03	1.06	0.20
	26	0.04	1.74	0.25	0.04	1.50	0.27	0.06	1.74	0.21
	19 – 26	0.05	0.63	0.19	0.05	0.63	0.21	0.08	0.53	0.18
February 2007	16	0.03	0.76	0.10	0.03	0.55	0.10	0.03	0.22	0.09
	17	0.01	0.61	0.13	0.01	0.61	0.12	0.05	0.48	0.12
	18	0.02	0.61	0.13	0.02	0.58	0.13	0.04	0.43	0.11
	19	0.02	1.28	0.14	0.03	0.68	0.16	0.04	0.44	0.11
	20	0.01	1.31	0.15	0.01	1.31	0.18	0.02	0.59	0.12
	21	0.01	1.41	0.14	0.01	1.37	0.16	0.01	0.92	0.11
	22	0.02	2.23	0.15	0.02	2.11	0.18	0.02	1.10	0.12
	23	0.01	1.38	0.15	0.02	1.29	0.14	0.03	1.31	0.15
	24	0.02	1.05	0.15	0.02	0.66	0.12	0.02	1.05	0.16
	25	0.02	0.60	0.14	0.02	0.51	0.12	0.02	0.60	0.14
	26	0.02	0.54	0.13	0.04	0.54	0.13	0.03	0.40	0.11
	16 – 26	0.04	0.81	0.14	0.04	0.53	0.14	0.06	0.46	0.12

whereas the influence is stronger during the winter simulation period than during July 2006. For both time periods the influence is strong at the western model boundary (due to westerly winds) as well as at the north-east part of the model domain. Here, the relative AOD difference is larger than 0.8. Those domains, which are located next to the western boundary are stronger influenced than other regions within the model domain, caused by the weather systems moving from west to east. In the middle of the model domain, the transport-influenced relative AOD difference decreases. During both time periods, transport from outside into the model domain as well as within the model domain, was limited. During July 2006 relatively low wind speeds and nearly constant meteorological conditions (Section 4.1) resulted in a low transport, whereas during February 2007 the high number of precipitation events (section 4.2) removed particles out of the atmosphere and thus hindered a strong transport of particles and their accumulation. Large areas in Middle Europe and in the south and south-east part of the model domain are nearly unaffected ($\tau_{relDiff} < 0.2$) by the transport during July 2006. In contrast to the summer time, the area, which is not influenced by transported particles, is smaller during February 2007, but also concentrated on the south-east model domain. In these regions, the AOD is mainly controlled by the local emission of particles (Figure 5.8, lower panel). Local emissions are very dominant within the entire model domain. Only at the western model boundary, where the transport was very strong during July 2006 and February 2007, the emission-influenced relative AOD difference is low ($\tau_{relDiff} < 0.2$). For nearly all other regions within the model domain, the influence by the emission is strong ($\tau_{relDiff} > 0.6$).

5.2.2 Sensitivity to aerosol profiles at the lateral model boundaries

The description of the vertical distribution at the lateral model boundary for simulation of the transport from outside into the model domain is explained in detail in Section 2.2. Two additional model setups ($\mathrm{Sim}_{Standard}$ and Sim_{Ind}; Table 2.1), with different vertical distributions at the lateral model boundaries, are tested for the summer and the winter simulation period.

Surface observations of PM chemistry at different places in Europe show gradients when moving from the north-west to the south to Central Europe (Putaud et al., 2010). Thus, the assumption of a maximum concentration of $8.0\,\mu\mathrm{g\,m^{-3}}$ (summer) and $6.0\,\mu\mathrm{g\,m^{-3}}$ (winter) in case of $\mathrm{PPM}_{2.5}$ and of $2.0\,\mu\mathrm{g\,m^{-3}}$ (summer and winter) in case of PPM_{10} - $\mathrm{PPM}_{2.5}$ at each lateral boundary might result in an incorrect transport simulation. Due to this, weighting factors at each lateral model boundary and for all three model setups (Sim_{Basic}, $\mathrm{Sim}_{Standard}$, Sim_{Ind}) are determined. For this, the ratio between measured and simulated AOD is calculated. Sun photometer measurements at AERONET stations located next to the model boundaries are used. Table 5.6 summarizes the AERONET stations which were used for this calculation. In some cases, AERONET stations, used here, are equal for both time periods, but the main focus was on available data based on four to five stations located near to the lateral model boundaries. Therefore, different stations can be used as well for both simulation periods.

Model simulations with weighting factors of 1.0 at each lateral model boundary and with the known concentrations are performed for the summer and winter periods by means of Sim_{Basic}, $\mathrm{Sim}_{Standard}$ and Sim_{Ind}. The mean ratio between simulated and observed AOD for each model boundary is calculated for both entire time periods

Table 5.6: AERONET stations, used for the determination of the mean weighting factors for each simulation period and lateral model boundary (Meier et al., 2012b).

Boundary	19 – 26 July 2006	16 – 26 February 2007
East	Minsk (Belarus; 27.6° E, 53.9° N)	Minsk
	Chisinau (Moldova; 28.8° E, 47° N)	Zvenigorod (Russia; 36.8° E, 55.7° N)
	Moscow (Russia; 37° E, 55° N)	Moscow
	Sevastopol (Ukraine; 33.5° E, 44.6° N)	Sevastopol
West	Cabo da Roca (Portugal; 9° W, 38° N)	Cabo da Roca
	Chilbolton (United Kingdom; 1.4° W, 51.1° N)	Chilbolton
	Evora (Portugal; 7° W, 38° N)	Evora
	Le Fauga (France; 1° E, 43° N)	Caceres (Spain; 6.3° W, 39.5° N)
		El Arenosillo (Spain; 6.7° W, 37.1° N)
North	Gustav Dalen Tower (Sweden; 17.5° E, 58.6° N)	Belsk (Belarus; 20.8° E, 51.7° N)
	Helsinki (Finland; 24.9° E, 59.9° N)	Cabauw (The Netherlands; 4.9° E, 52° N)
	SMHI (Sweden; 16.2° E, 58.6° N)	Hamburg (Germany; 10° E, 53.6° N)
	Toravere (Estonia; 26.5° E, 58.3° N)	Toravere
South	Epanomi (Greece; 23° E, 40.4° N)	Barcelona (Spain; 2.1° E, 41.4° E)
	Crete (Greece; 25.3° E, 35.3° N)	Crete
	Granada (Spain; 3.6° W, 37.2° N)	Messina (Italy; 15.6° E, 38.2° N)
	Lecce (Italy; 18.1° E, 40.3° N)	Potenza (Italy; 15.7° E, 40.6° N)
	Thessaloniki (Greece; 23° E, 40.6° N)	Thessaloniki

by using the data at stations mentioned in Table 5.6. The model output occurs at each hour, whereas AOD observations are obtained when measurements are possible. By interpolation, computed AOD values are determined for every 10 minutes based on the hourly model output. This model interpolation result which is close to the observation time is used to determine the ratio between simulated and experimentally observed AOD. The time-averaged ratios for each lateral model boundary (north, east, south, west) are presented in Table 5.7 for both simulation periods and the three model setups. To discriminate between model setups with weighting factors of 1.0 and those with individual weighting factors at each lateral model boundary, the model setups with individual weighting factors are named $\mathrm{Sim}_{Basic}^{weight}$, $\mathrm{Sim}_{Standard}^{weight}$ and $\mathrm{Sim}_{Ind}^{weight}$. The calculated weighting factors represent now a stronger limitation of the transport from outside into the model compared to the fixed weighting factor of 1.0 at each lateral model boundary. It is noticeable, that the individual weighting factors are very similar or equal, respectively, for all model setups during the winter simulation period (Table 5.7). In case of the summer simulation period, the weighting factors for $\mathrm{Sim}_{Basic}^{weight}$ and $\mathrm{Sim}_{Standard}^{weight}$ are equal, whereas the weighting factors for $\mathrm{Sim}_{Ind}^{weight}$ are different.

Table 5.7: Weighting factors calculated for each lateral model boundary of the individual model setups for each entire simulation period.

Model Setup	19 – 26 July 2006 North/East/South/West	16 – 26 February 2007 North/East/South/West
$\mathrm{Sim}_{Basic}^{weight}$	0.5/0.6/0.9/1.0	0.6/0.6/0.6/0.7
$\mathrm{Sim}_{Standard}^{weight}$	0.6/0.7/0.9/1.1	0.7/0.7/0.7/0.8
$\mathrm{Sim}_{Ind}^{weight}$	0.4/0.5/0.7/0.6	0.6/0.6/0.7/0.7

5.2.3 Evaluation with ground-based lidar data

As summarized in Table 3.1, during 19 – 26 July 2006, nine EARLINET stations performed observations of the vertical backscatter profiles. Caused by several precipitation events during 16 – 26 February 2007, observations at only seven EARLINET stations were performed. With several different model setups (Table 2.1) it is possible to analyze the model regarding various parameters and therefore its ability to evaluate the observed lidar profiles. Here, a first study deals with the agreement of the basic model setup Sim_{Basic}. Additionally, model results based on Sim_{dry} simulations are shown. That means, the hygroscopic growth, which is described in the model setup, is tested by comparing the results of Sim_{Basic} and Sim_{dry} in accordance to the measured vertical backscatter profile. As done in Section 5.2.5, the differences and improvements when using different kind of descriptions of the vertical distribution of chemical compounds at the lateral model boundaries ($\mathrm{Sim}_{Basic}^{weight}$, $\mathrm{Sim}_{Standard}^{weight}$, $\mathrm{Sim}_{Ind}^{weight}$) is analyzed.

Exemplary, in Figures 5.9 – 5.10 observed vertical backscatter coefficient profiles, obtained at different EARLINET stations, are plotted in comparison with simulated backscatter coefficient profiles based on three different model setups. In case of Figure 5.9, nine lidar profiles (continuous black lines) are shown which were measured on 24 July 2006. Nine lidar profiles, measured on different days and at different EARLINET stations during the winter time period, are presented in Figure 5.10. Vertical backscatter profiles, computed by Sim_{Basic}, are shown as dashed black lines in both figures. Compared to CALIOP observations, EARLINET lidar profiles often show not a clear decrease of the backscatter values in atmospheric layers near the surface. This could be due to the differences in observation. Whereas CALIOP observes the atmosphere from top to bottom, EARLINET measurements are done the other way around and thus the determination of aerosol layers can be influenced.

A good agreement of the vertical shape between observed and computed backscatter values is found for both simulation periods at the EARLINET stations, but exact agreements are not found. As mentioned in Section 4.1, the summer time period was also characterized by the transport of Saharan dust which is not described by this model

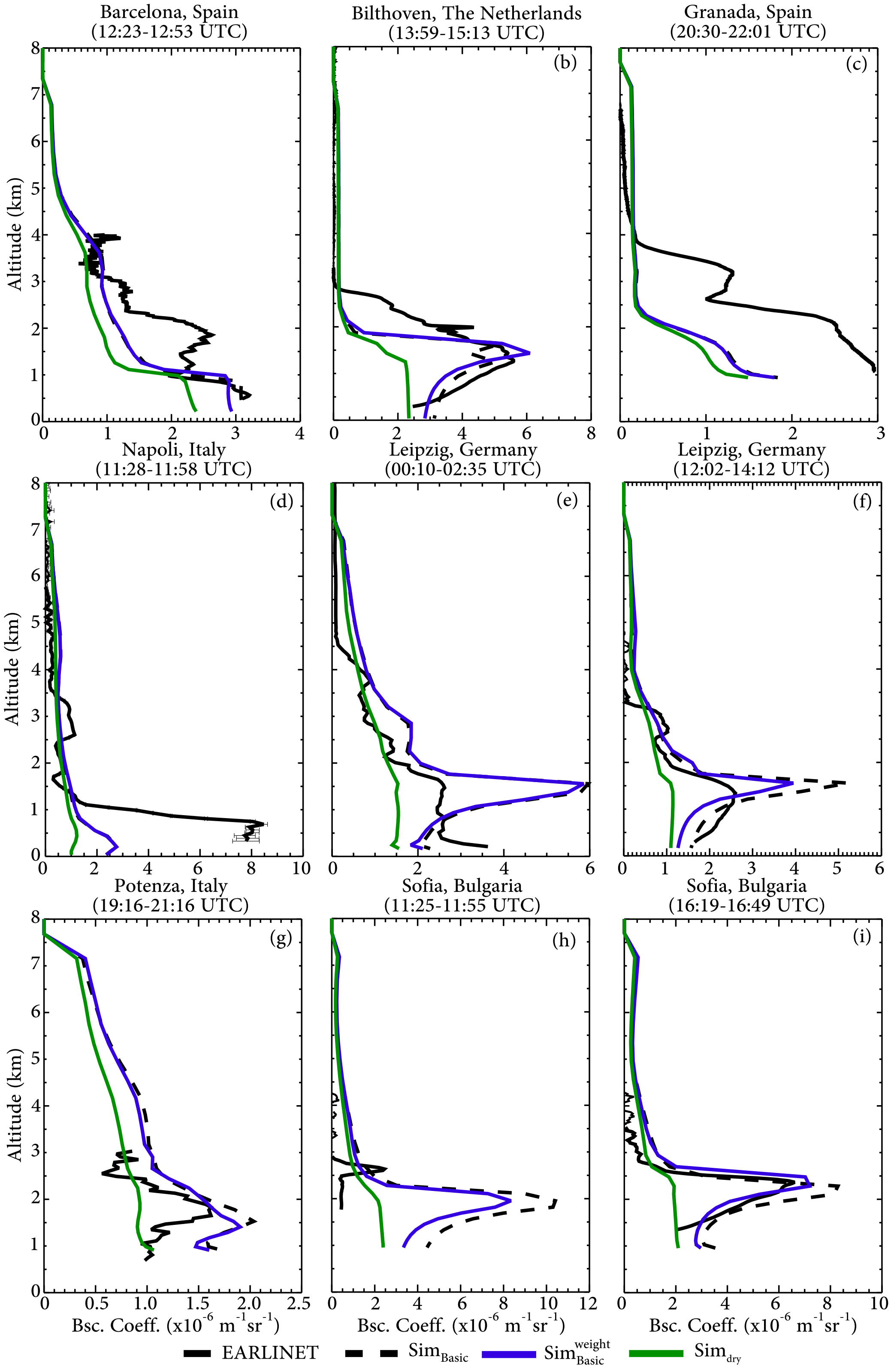

Figure 5.9: Vertical profiles of backscatter coefficients based on observation data at selected EARLINET stations ((a) Barcelona, (b) Bilthoven, (c) Granada, (d) Napoli, (e,f) Leipzig, (g) Potenza, (h,i) Sofia) in comparison with simulated profiles based on Sim$_{Basic}$, Sim$^{weight}_{Basic}$ and Sim$_{dry}$ model setups on 24 July 2006. Within the brackets the time of observation is written.

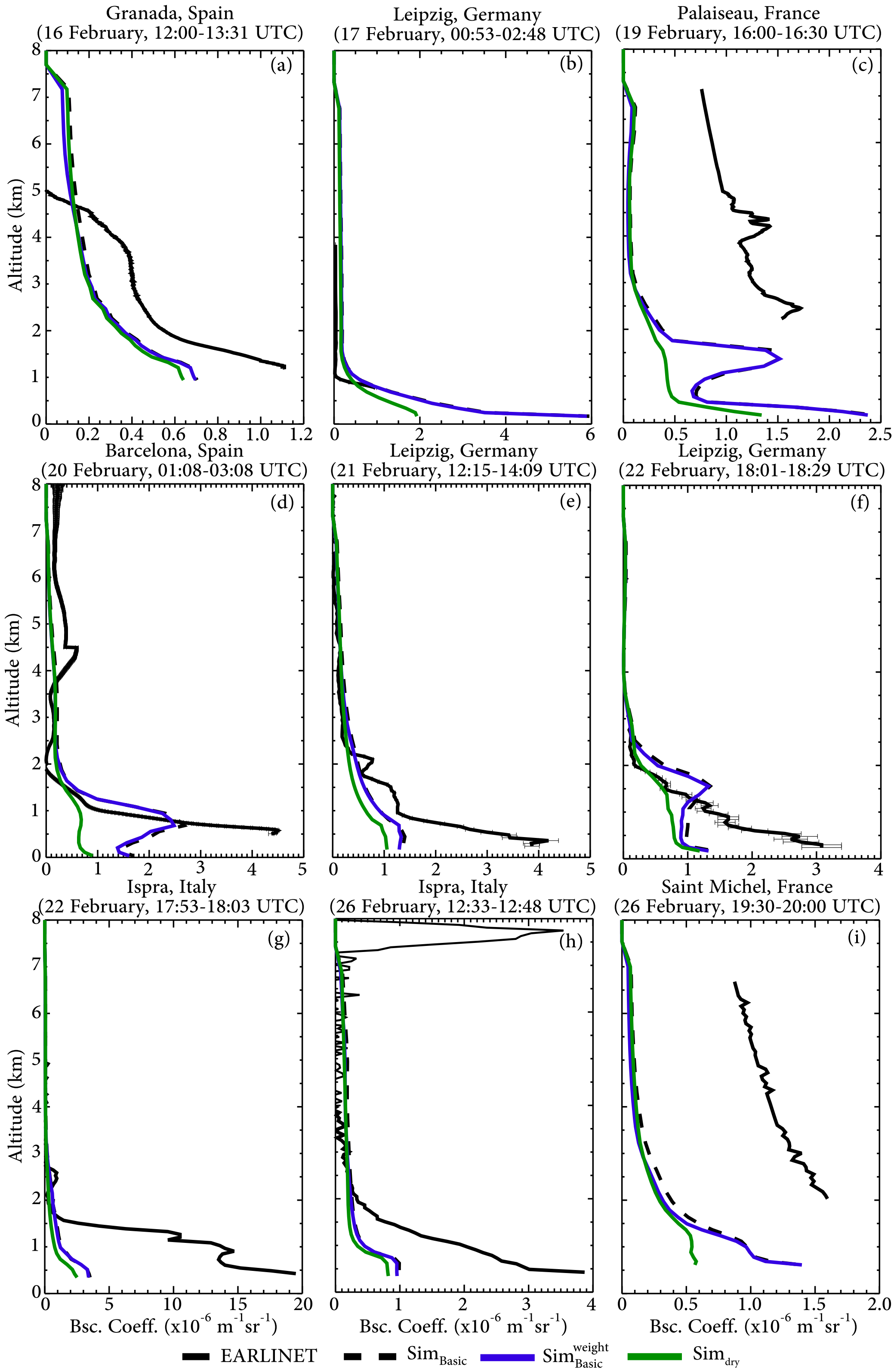

Figure 5.10: Vertical profiles of backscatter coefficients based on observation data at selected EARLINET stations for certain days ((a) Granada, (b, e, f) Leipzig, (c) Palaiseau, (d) Barcelona, (g, h) Ispra, (i) Saint Michel) in comparison with simulated profiles based on Sim$_{Basic}$, Sim$_{Basic}^{weight}$ and Sim$_{dry}$ model setups. Within the brackets the date as well as the time of observation is written.

version. In case of the observation profile at the EARLINET station in Barcelona (Figure 5.9 (a)) it can be assumed that dust particles have a distinct influence on the backscatter profile between 1.0 km and 3.5 km. Here, the model (dashed black line) clearly underestimates the measured backscatter coefficients, whereas below 1.0 km and above 3.5 km quite good results are achieved. A significant influence by atmospheric particles is also found in case of the station in Granada (Figure 5.9 (c)). But here, the model (Sim_{Basic}, dashed black line) underestimates the observed profile significantly for all height levels. The distribution as well as the magnitude of the backscatter profile, simulated by means of Sim_{dry} (continuous green line), is very similar to the Sim_{Basic} results at the dust-influenced stations Barcelona and Granada in Spain. This shows, that aerosol mass is missing in the model and differences between observation and simulation (Sim_{Basic}) are not caused by an misinterpretation of the hygroscopic growth within the model. An opposite example is presented on the basis of the measurement at the Dutch station in Bilthoven (Figure 5.9 (b)). A characteristic vertical backscatter profile with a distinct peak of $5.6\,\mathrm{x}\,10^{-6}\,\mathrm{m}^{-1}\,\mathrm{sr}^{-1}$ at 1.2 km is found. Results, based on Sim_{Basic} show a very good agreement of this shape as well as of the magnitude of the peak. Two peaks are simulated by the model at 1.3 km ($5.0\,\mathrm{x}\,10^{-6}\,\mathrm{m}^{-1}\,\mathrm{sr}^{-1}$) and at 1.6 km ($5.2\,\mathrm{x}\,10^{-6}\,\mathrm{m}^{-1}\,\mathrm{sr}^{-1}$). When comparing the simulation results without hygroscopic growth (Sim_{dry}, continuous green line), the shape as well as the magnitude of the simulated backscatter coefficients are different from the Sim_{Basic} results and the agreement to the lidar profile is worse.

At two Italian stations (Napoli, Potenza) different results of the comparison with simulated backscatter coefficients are found. Whereas distinct differences between observation and simulation (Sim_{Basic}) profiles are found for the EARLINET station in Napoli (Figure 5.9 (d)), better agreements are found for the station in Potenza (g). Napoli is located at the sea and thus under influence of marine aerosol, which is not described by that model setup. Thus, discrepancy, found within the boundary layer, can be caused by the existence of the marine aerosol which is not simulated here. In contrast, Potenza is located in land and therefore the influence of the marine aerosol can be expected to be weak. Thus, the simulation of the general shape as well the magnitude of the observed backscatter coefficients is quite successful.

For the EARLINET station in Leipzig, two lidar profiles are available, one representing night-time conditions (Figure 5.9 (e)) and the other one day-time conditions (Figure 5.9 (f)) on 24 July 2006. For both cases, the observed vertical backscatter profile (continuous black line) is overestimated by the model Sim_{Basic} (dashed black line). During night-time, the measured backscatter coefficients below 2.0 km represent homogeneous conditions. Highest values ($\beta = 3.6\,\mathrm{x}\,10^{-6}\,\mathrm{m}^{-1}\,\mathrm{sr}^{-1}$) are detected near the surface and between 390 m and 1.6 km with very similar backscatter coefficients of

$\sim 2.5 \times 10^{-6}\,\mathrm{m}^{-1}\,\mathrm{sr}^{-1}$. The model also tends to compute slightly higher values near the surface compared to the next model layer above but the nearly constant coefficients up to 1.6 km are not simulated. Here, the Sim_{Basic} setup calculates a distinct backscatter value of $6.0 \times 10^{-6}\,\mathrm{m}^{-1}\,\mathrm{sr}^{-1}$ at 1.6 km. During day-time, the observed vertical profile changes within the PBL and a maximum backscatter coefficient of $2.6 \times 10^{-6}\,\mathrm{m}^{-1}\,\mathrm{sr}^{-1}$ is now measured at 1.3 km altitude. The simulated day-time profile is very similar to the computed profile for the night-time with a slightly lower maximum value ($\beta = 5.2 \times 10^{-6}\,\mathrm{m}^{-1}\,\mathrm{sr}^{-1}$) at 1.6 km. Because of the very distinct vertical profile, simulated by the Sim_{Basic} model setup, for both cases, a misinterpretation of the hygroscopic growth can be assumed. Model results, based on the Sim_{dry} setup (continuous green line), lead to distinct lower backscatter coefficients without significant peak. For the night-time simulation a maximum relative humidity of 89% is computed at 1.6 km. During the day, the maximum humidity increases up to 99% at the same altitude which could cause a high hygroscopic growth and therefore the computation of high backscatter coefficients by means of Sim_{Basic}.
In Sofia, 14 vertical backscatter profiles are measured on 24 July 2006 (Table 3.1). In Figure 5.9 two ((h) 11:25 – 11:55 UTC, (i) 16:19 – 16:49 UTC) of these 14 profiles are shown. In case of the observation performed around noon, the model significantly overestimates the observed EARLINET lidar profile. For the afternoon observation a quite good agreement regarding the presentation of the peak and the general shape is found between the lidar profile (continuous black line) and the simulated vertical backscatter profile (dashed black line). As shown for the EARLINET station in Leipzig (Figure 5.9 (e – f)) significantly lower backscatter coefficients are found when using the model setup without hygroscopic growth (Sim_{dry}; continuous green line), indicating a high dependency of the particles on the relative humidity. For both profiles, presented here, a relative humidity up to 94% (at 2.0 km for 11:25 – 11:55 UTC) and up to 100% (at 2.3 km at 16:19 – 16:49 UTC) is computed. For the second example, the simulation of the aerosol mass as well as of the humidity and therefore of the hygroscopic growth fits well with the observed backscatter profile.

EARLINET lidar profiles, measured during 16 – 26 February 2007 are in a distinct contrast to those observed during 19 – 26 July 2006. Whereas the summer case profiles often show an increase of the backscatter coefficients with increasing height or very distinct aerosol layers caused by e.g., dust particles (Figure 5.9), the winter case profiles often show a smooth decrease of the backscatter coefficients with increasing height (Figure 5.10). As also presented for the summer time period, over- and underestimations by the model setup Sim_{Basic} as well as good agreements between observation and simulation are found during winter.

At the beginning of the simulation period, a quite good representation of the general shape of the vertical backscatter coefficient is computed (dashed black line) at the southern EARLINET station in Granada (Figure 5.10 (a)). But the model underestimates the magnitude of the measured backscatter coefficients (continuous black line). Due to several and long-lasting precipitation events during the winter period (Section 4.2) it could occur, that too much particle mass is removed out of the atmosphere by the model and thus causes an underestimation of observed data. On 16 February 2007, the model also computes slight precipitation events in the south of the Iberian Peninsula (Figure 4.6), which could be the reason of the lower backscatter coefficients simulated by Sim_{Basic}. On 17 February 2007, no rain- or snowfall events are computed for Germany (Figure 4.6), thus a good agreement between the measured and the simulated vertical backscatter profile is found for the EARLINET station in Leipzig (Figure 5.10 (b)). Additionally, the model (Sim_{Basic}, dashed black line) computes higher backscatter coefficients than it was observed.

At the French stations Palaiseau (Figure 5.10 (c)) on 19 February 2007 and Saint Michel (Figure 5.10 (i)) on 26 February 2007 distinct lidar profiles are measured throughout the entire simulation period. The profiles do often begin at relatively high altitudes despite the fact that Palaiseau is located 162 m above sea level (asl) and Saint Michel at 683 m asl (EARLINET, 2012). Thus, no information about backscatter coefficients within the boundary layer is available. For both locations the computed vertical backscatter profile (Sim_{Basic}) does not fit with the observed one. It has to be assumed that the observed lidar profiles at these stations during that time period are incorrect.

A quite good agreement is found for the lidar profile at the station in Barcelona (Figure 5.10 (d)). For those height levels, where comparisons are possible (above 506 m), significant differences primary occur at the lowest levels. At height levels above 700 m a successful representation of the vertical backscatter profile is simulated by the Sim_{Basic} model setup. Difficulties to compute the backscatter coefficients within the lowest atmospheric layers are also found at the EARLINET station in Leipzig on 21 and 22 February 2007 (Figure 5.10 (e–f)). The observed lidar profiles represent their maximum values near the surface. On 21 February 2007, a maximum backscatter coefficient of $\beta = 4.2 \times 10^{-6}\,\text{m}^{-1}\,\text{sr}^{-1}$ (at 360 m) is found. The following day, the maximum backscatter coefficient is $\beta = 3.1 \times 10^{-6}\,\text{m}^{-1}\,\text{sr}^{-1}$ at 240 m. The computed (dashed black line) profile on 21 February 2007 is quite good but shows a clear underrepresentation at the lowest levels. The following day, the model computes very similar backscatter coefficients with an average of $\beta = 1.1 \times 10^{-6}\,\text{m}^{-1}\,\text{sr}^{-1}$ between 244 m and 1.8 km. Such a behavior is not found in the observation profile where the backscatter value decreases constantly with increasing height. The discrepancies, which are found mainly in the PBL, are possibly caused by the simulated precipitation (Figure 4.7) and therefore due

to overestimation of the removal of atmospheric particles.
A lidar profile, measured on 22 February 2007, is also presented in Figure 5.10 (g). The Italian station in Ispra is located near the lake Lago Maggiore and is often influenced by air which is transported from Milano in the south-east. Quite large backscatter coefficients are observed during that day by the lidar. Here, a value of $20.0\,\mathrm{x}\,10^{-6}\,\mathrm{m}^{-1}\,\mathrm{sr}^{-1}$ is measured near the surface. Such a large value is not simulated by the Sim_{Basic} setup with a maximum backscatter coefficient of $3.5\,\mathrm{x}\,10^{-6}\,\mathrm{m}^{-1}\,\mathrm{sr}^{-1}$ only. As summarized in Table 3.1, twelve lidar profiles are available for the station in Ispra during that day. All these profiles are characterized by such high backscatter coefficients near the surface as presented in Figure 5.10 (g). For all these profiles the simulated vertical backscatter profiles are too low, what could be caused by the precipitation during that day (Figure 4.7). The removal of particles leads to general lower backscatter coefficients and thus to a distinct misinterpretation of the observed lidar profiles.
Between 22 and 26 February 2007 no lidar observations at the EARLINET stations were performed. Lidar observations were done at the station in Ispra on 26 February 2007 but show discrepancies between observation (continuous black line) and simulation (dashed black line) within the PBL. The observed maximum value ($\beta_{max} = 3.9\,\mathrm{x}\,10^{-6}$ $\mathrm{m}^{-1}\,\mathrm{sr}^{-1}$), near the surface, is lower than on 22 February 2007 but the model is only able to compute a maximum backscatter coefficient of $1.0\,\mathrm{x}\,10^{-6}\,\mathrm{m}^{-1}\,\mathrm{sr}^{-1}$. In addition to the discrepancy within the PBL, a significant difference is found at 7.3 – 8.0 km. A backscatter value of $3.5\,\mathrm{x}\,10^{-6}\,\mathrm{m}^{-1}\,\mathrm{sr}^{-1}$ is measured here. At such high altitudes the particle load as well as the relative humidity are low. Therefore, only low backscatter values are determined and thus the model is not able to reproduce the observation at this altitude.

The agreement between the observation profiles and the simulation profiles based on the Sim_{Basic} model setup is quite good. By calculating the mean absolute bias (A_{bias}^{mean}, Section A.1) an estimation about the discrepancies at different height levels is possible. For each 500 m height level an average backscatter coefficient is determined, individually for each experimentally observed and computed vertical backscatter profile. The differences between simulated and observed backscatter coefficients, implementing all available results for each 500 m height level, are summarized in Table 5.8. In the last column of Table 5.8 the total number of available values, found for each 500 m height level, is written. The relatively low number of available data limits an explicit statement regarding the general agreement between the various model setups of COSMO – MUSCAT and EARLINET lidar profiles as it was possible in case of CALIOP observations (Section 5.1). Thus, only a general tendency can be assumed based on the mean absolute biases.

Table 5.8: Mean absolute bias (x 10^{-7} m^{-1} sr^{-1}) determined for all model setups and for each 500 m height level between surface and 8 km. The values refer to the entire model simulations periods of 19 – 26 July 2006 and 16 – 26 February 2007.

	Altitude range (km)	Sim_{Basic}	Sim_{Basic}^{weight}	$Sim_{Standard}$	$Sim_{Standard}^{weight}$	Sim_{Ind}	Sim_{Ind}^{weight}	Sim_{dry}	N
19 – 26 July 2006	0.0 – 0.5	-11.9	-13.9	-14.4	-14.4	-11.8	-12.5	-20.5	5
	0.5 – 1.0	-9.4	-10.5	-11.0	-11.3	-7.4	-9.1	-17.0	37
	1.0 – 1.5	-5.1	-5.4	-5.8	-5.9	-2.9	-4.0	-11.8	57
	1.5 – 2.0	0.6	-1.1	-1.2	-1.6	1.5	0.2	-11.1	71
	2.0 – 2.5	4.2	4.0	4.1	3.6	6.2	5.1	-4.7	70
	2.5 – 3.0	4.0	3.6	3.4	3.4	5.0	4.6	0.0	70
	3.0 – 3.5	3.3	3.0	2.6	2.7	4.1	3.7	0.7	45
	3.5 – 4.0	2.9	2.8	2.7	2.7	3.9	3.3	1.2	42
	4.0 – 4.5	3.7	3.9	3.6	3.8	4.6	4.2	2.5	39
	4.5 – 5.0	2.4	2.4	2.4	2.5	2.8	2.4	1.8	26
	5.0 – 5.5	2.7	2.8	2.7	2.8	3.1	2.8	2.1	22
	5.5 – 6.0	3.1	3.3	3.2	3.3	3.7	3.4	2.5	14
	6.0 – 6.5	3.5	3.7	3.5	3.6	4.1	3.9	2.8	14
	6.5 – 7.0	3.4	3.6	3.6	3.5	4.1	3.8	2.8	15
	7.0 – 7.5	4.5	4.8	4.8	4.7	5.6	5.2	3.7	10
16 – 26 February 2007	0.0 – 0.5	-69.8	-70.8	-71.0	-71.1	-70.8	-70.8	-76.6	16
	0.5 – 1.0	-53.4	-53.5	-53.7	-53.8	-53.4	-53.5	-61.6	18
	1.0 – 1.5	-23.3	-23.7	-23.9	-24.0	-23.6	-23.7	-27.9	22
	1.5 – 2.0	-3.1	-3.4	-3.5	-3.6	-3.3	-3.4	-6.6	22
	2.0 – 2.5	-7.5	-7.8	-7.7	-7.9	-7.6	-7.8	-8.8	34
	2.5 – 3.0	-7.6	-7.9	-7.4	-7.9	-7.3	-7.8	-8.2	34
	3.0 – 3.5	-4.4	-4.6	-4.3	-4.6	-4.2	-4.6	-4.7	34
	3.5 – 4.0	-4.2	-4.4	-4.0	-4.5	-3.9	-4.4	-4.4	33
	4.0 – 4.5	-4.4	-4.6	-4.0	-4.6	-4.0	-4.6	-4.5	32
	4.5 – 5.0	-4.2	-4.4	-3.5	-4.4	-3.5	-4.4	-4.3	32
	5.0 – 5.5	-6.0	-6.2	-5.7	-6.2	-5.7	-6.2	-6.1	18
	5.5 – 6.0	-6.9	-7.1	-6.3	-7.1	-6.3	-7.1	-7.0	16
	6.0 – 6.5	-6.2	-6.5	-5.8	-6.4	-5.8	-6.5	-6.3	16
	6.5 – 7.0	-6.4	-6.6	-5.7	-6.6	-5.7	-6.6	-6.5	16

During the summer simulation period, the model setup Sim_{Basic} tends to underestimate the observed backscatter coefficients in the atmospheric layers near the surface. Above 1.5 km the model mainly overestimates the observation data. In case of the winter period, the computed backscatter values (Sim_{Basic}) are generally lower than the lidar data (Table 5.8). Best agreements are found for the height level 1.5 – 2.0 km during summer case. Here, the lowest discrepancy of $0.6 \,\mathrm{x}\, 10^{-7}\,\mathrm{m}^{-1}\,\mathrm{sr}^{-1}$ is determined and represents the transition region between the negative mean absolute bias near the surface and the positive mean absolute bias at altitudes higher than 2.0 km. From 2.0 to 7.5 km the average difference between Sim_{Basic} results and EARLINET data is quite constant with values ranging from $2.4 \,\mathrm{x}\, 10^{-7}\,\mathrm{m}^{-1}\,\mathrm{sr}^{-1}$ to $4.5 \,\mathrm{x}\, 10^{-7}\,\mathrm{m}^{-1}\,\mathrm{sr}^{-1}$ (Table 5.8). During the winter period, the mean absolute bias above 2.0 km covers a large range from $-7.6 \,\mathrm{x}\, 10^{-7}\,\mathrm{m}^{-1}\,\mathrm{sr}^{-1}$ to $-3.1 \,\mathrm{x}\, 10^{-7}\,\mathrm{m}^{-1}\,\mathrm{sr}^{-1}$. It was mentioned before, that overestimated removal of atmospheric particles due to precipitation events could cause the simulation of too low backscatter coefficients in Sim_{Basic}. Much less precipitation events are observed and simulated during July 2006 (Section 4.1). Nevertheless, the relatively high mean absolute bias below 1.5 km with the tendency of the regional model to underestimate the observed data during both periods shows the difficulty of the model to simulate the amount of atmospheric particles within the PBL correctly. Actually, this behavior is found for both simulation periods. Between surface and 1.5 km the mean absolute bias ranges from $-20.5 \,\mathrm{x}\, 10^{-7}\,\mathrm{m}^{-1}\,\mathrm{sr}^{-1}$ to $-11.8 \,\mathrm{x}\, 10^{-7}\,\mathrm{m}^{-1}\,\mathrm{sr}^{-1}$ during summer and from $-76.6 \,\mathrm{x}\, 10^{-7}\,\mathrm{m}^{-1}\,\mathrm{sr}^{-1}$ to $-29.3 \,\mathrm{x}\, 10^{-7}\,\mathrm{m}^{-1}\,\mathrm{sr}^{-1}$ during winter for comparisons with Sim_{dry} results (Table 5.8). At higher altitudes, simulations with dry aerosol sometimes lead to better agreements with observed data during summer. But often, simulations based on Sim_{Basic} and Sim_{dry} are similar at higher altitudes due to the decrease of the relative humidity with increasing altitude.
The discrepancies between EARLINET observation and model computation are nearly similar to those determined between CALIOP and model backscatter values (Section 5.1.1). During winter, the computed backscatter values are often also lower than the observed CALIOP values, whereas during summer cases of overestimations by the model setup occur.

As described in Section 5.2.2, different descriptions of the vertical distributions at the lateral model boundaries as well as individual weighting factors are used to identify the dependency of the model results based on these descriptions and to improve the model results by this method. Regarding the vertical distribution of the backscatter coefficients, which are determined based on the chemical compounds, Figures 5.9 – 5.10 show the results of $\mathrm{Sim}_{Basic}^{weight}$ simulations as continuous blue lines. No distinct difference compared to the model setup with the constant weighting factor of 1.0 at each model boundary (Sim_{Basic}) is found for both simulation periods and the examples shown here. In case of the dust influenced places like Barcelona (a) and Granada (c) (in Figure 5.9) similar results are achieved by Sim_{Basic} and $\mathrm{Sim}_{Basic}^{weight}$. This is also the case for the EARLINET station in Napoli where it has to be assumed that marine aerosol, which is not described by the model, causes the higher observed backscatter coefficients within the boundary layer compared to the simulation results. At the other stations, representing the conditions for the summer simulation period, differences between Sim_{Basic} and $\mathrm{Sim}_{Basic}^{weight}$ are computed (e.g., Bilthoven (b), Leipzig (f), Potenza (g) and Sofia (h – i)). Often, slightly lower backscatter values are determined by the $\mathrm{Sim}_{Basic}^{weight}$ setup compared to Sim_{Basic}. The calculated mean average bias, determined based on $\mathrm{Sim}_{Basic}^{weight}$ and EARLINET data, does not show a significant improvement when using Sim_{Basic} data for comparisons (Table 5.8). Between surface and 2.0 km, $\mathrm{Sim}_{Basic}^{weight}$ data also tend to worse agreements with observed backscatter coefficients, identified by the range of mean absolute bias ($\mathrm{A}_{bias}^{mean} = \text{-}13.9 \times 10^{-7} - \text{-}1.1 \times 10^{-7}\,\mathrm{m}^{-1}\,\mathrm{sr}^{-1}$. At higher height levels, similarities between $\mathrm{Sim}_{Basic}^{weight}$ and Sim_{Basic} are strong. This similarity is also found for the winter simulation period. As shown in Figure 5.9, nearly no differences are found for all height levels and throughout the entire time period for the model setup with the same weighting factor or the setup with individual weighting factors at the lateral model boundaries. The mean average bias, summarized in Table 5.8, underlines this result. Within the PBL, no differences between $\mathrm{Sim}_{Basic}^{weight}$ and Sim_{Basic} are determined based on the mean average bias as it is possible for the summer period.

The implementation of the other model setups, $\mathrm{Sim}_{Standard}^{weight}$ and $\mathrm{Sim}_{Ind}^{weight}$, leads to similar results as found with $\mathrm{Sim}_{Basic}^{weight}$ computation. In Figure 5.11 the various results of the mean average bias are shown as vertical distribution for the summer (left panel) as well as for the winter (right panel) simulation period (Table 5.8). Whereas these values differ between $\mathrm{Sim}_{Basic}^{weight}$, $\mathrm{Sim}_{Standard}^{weight}$ and $\mathrm{Sim}_{Ind}^{weight}$ for the summer period it is not the case for the winter period. During July 2006, simulation results, based on $\mathrm{Sim}_{Standard}^{weight}$, lead to no improvement compared to the EARLINET observations in regions below 2.0 km ($\mathrm{A}_{bias}^{mean} = \text{-}14.4 \times 10^{-7} - \text{-}1.6 \times 10^{-7}\,\mathrm{m}^{-1}\,\mathrm{sr}^{-1}$), whereas $\mathrm{Sim}_{Ind}^{weight}$ agrees best ($\mathrm{A}_{bias}^{mean} = \text{-}12.5 \times 10^{-7} - 0.2 \times 10^{-7}\,\mathrm{m}^{-1}\,\mathrm{sr}^{-1}$). Above 2.0 km, it is the other way around (Table 5.8, Figure 5.11 (left panel)). The differences between the individual model setups remain small when taking the mean absolute bias into account during February 2007 (Figure 5.11). For all setups, the agreements with the observed backscatter coefficients are better above 1.5 km, above the PBL. Different setups of aerosol profiles at the lateral model boundaries do not lead to large differences in the model domain for this model study.

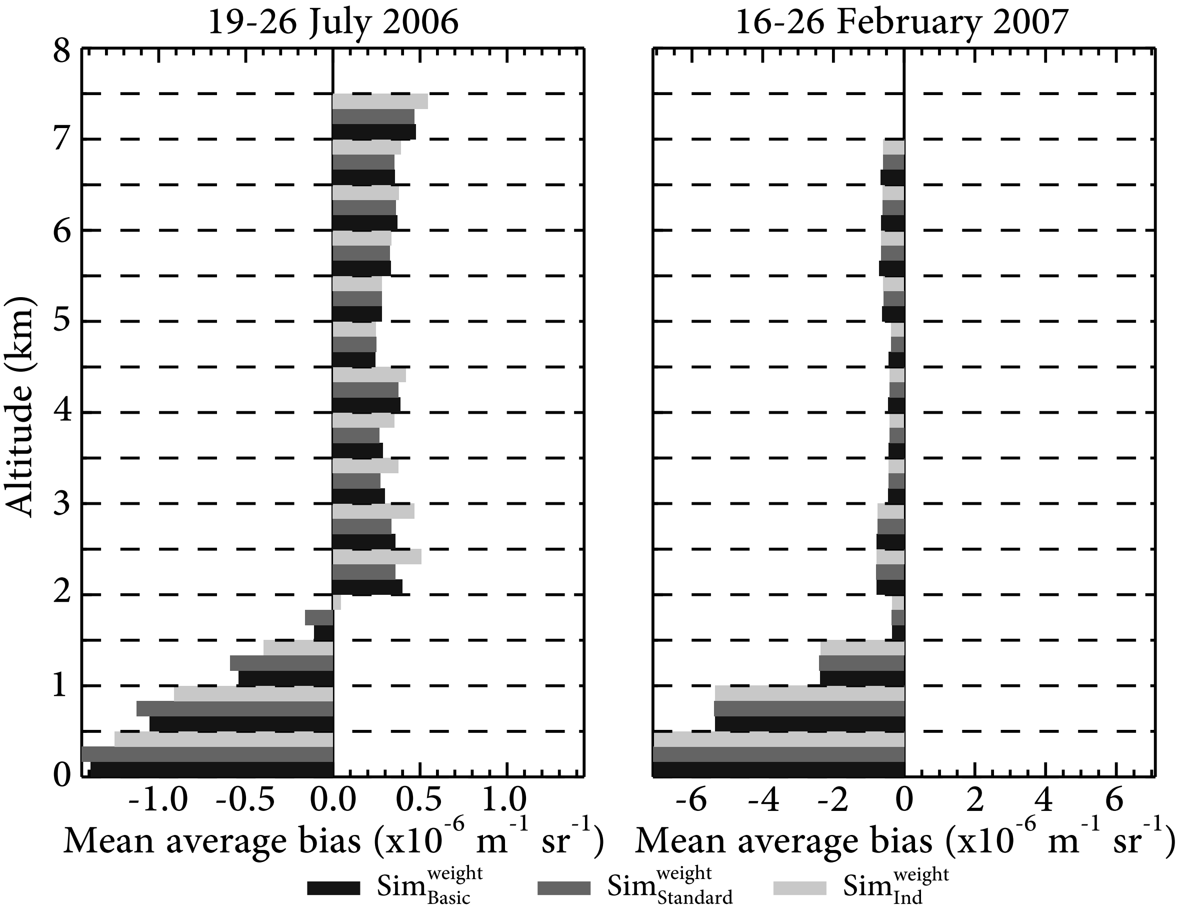

Figure 5.11: Vertical distribution of the mean average bias (x10^{-6} m^{-1} sr^{-1}), determined based on Sim$^{weight}_{Basic}$ (black bars), Sim$^{weight}_{Standard}$ (gray bars) and Sim$^{weight}_{Ind}$ (light gray bars) determined for the entire summer (left panel) and the entire winter (right panel) period. The dashed lines help to separate each 500 m height level from each other.

5.2.4 Evaluation with AERONET data

The introduction of individual weighting factors for a better description of the transport from outside into the European model domain does not lead to a significant improvement of the model simulations in case of comparisons with lidar profiles. Thus, it can not be expected that in case of AOD data significant differences between the various model setups are found. AOD values are calculated based on Equation 5.3. First, a general comparison between observed and simulated (Sim$_{Basic}$, Sim$^{weight}_{Basic}$ and Sim$_{dry}$) AOD as time series for selected AERONET stations is presented (Figures 5.13 – 5.15). Additionally, information about the time series of computed (by means of Sim$_{Basic}$) relative humidity is shown in Figures 5.13 – 5.15 for each AERONET station. Yellow bars in Figures 5.13 – 5.15 show the occurrence of relative humidities larger or equal than 95% within the vertical atmospheric column based on Sim$_{Basic}$ simulations. An

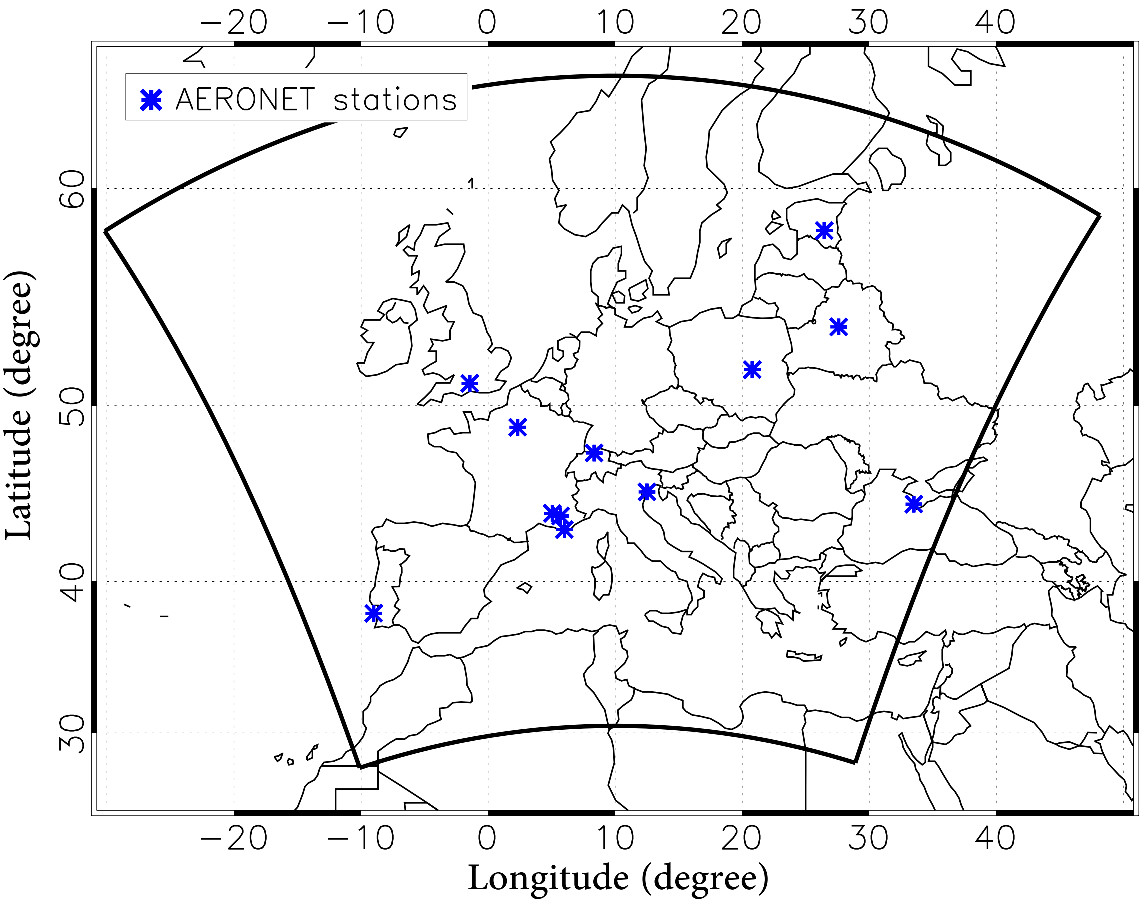

Figure 5.12: Blue asterisks represent the location of individual AERONET stations whose observation data are shown in Figures 5.13 – 5.15.

overview about the distribution of the AERONET stations in Europe, used for the presentation of the time series, is given in Figure 5.12.

In general, a good agreement between the observed (black crosses) and simulated ($\mathrm{Sim}_{Basic}^{weight}$: continuous blue line, Sim_{Basic}: dashed black line) AOD is found for both simulation periods and at the AERONET stations, presented here. Further, discrepancies between the simulated AOD by means of Sim_{Basic} and $\mathrm{Sim}_{Basic}^{weight}$ remain small. But, as shown in case of the comparison with EARLINET data, over- and underestimations of the observed AOD by the model ($\mathrm{Sim}_{Basic}^{weight}$, Sim_{Basic}) occur. For instance, significant overestimations are found at nearly all AERONET stations presented in Figures 5.13 – 5.15. During the summer simulation period, the AOD in Belsk (Ukraine), Cabo da Roca (Portugal), Minsk (Belarus) and Toravere (Estonia) is overestimated by the model setups Sim_{Basic} and $\mathrm{Sim}_{Basic}^{weight}$ for some days of the simulation period. Underestimations are also found, for instance for the stations in France, OHP Observatoire, Paris and Toulon, as well as in Sevastopol (Ukraine) and Laegeren (Switzerland). But in general, the agreement between observed and simulated AOD is very satisfying. During summer, it is often remarkable that the day-to-day variability of the observed

Table 5.9: Mean absolute bias (A_{bias}^{mean}), minimum ($\Delta\tau_{min}$) and maximum ($\Delta\tau_{max}$) differences between the individual model setups and observed AOD for the summer and for the winter time period.

	19 – 26 July 2006			16 – 26 February 2007		
Model Setup	A_{bias}^{mean}	$\Delta\tau_{min}$	$\Delta\tau_{max}$	A_{bias}^{mean}	$\Delta\tau_{min}$	$\Delta\tau_{max}$
Sim_{Basic}	0.01	-0.61	0.61	0.00	-1.82	1.83
$\text{Sim}_{Basic}^{weight}$	0.00	-0.64	0.68	-0.02	-1.82	1.66
$\text{Sim}_{Standard}$	-0.01	-0.64	0.64	-0.01	-1.82	1.66
$\text{Sim}_{Standard}^{weight}$	-0.01	-0.65	0.60	-0.02	-1.82	1.65
Sim_{Ind}	0.05	-0.58	0.67	0.00	-1.82	1.68
$\text{Sim}_{Ind}^{weight}$	0.03	-0.62	0.69	-0.01	-1.82	1.65

AOD is well reproduced by the model simulation based on Sim_{Basic} and $\text{Sim}_{Basic}^{weight}$ (Figures 5.13 – 5.15). At the AERONET stations in Chilbolton (United Kingdom) and Venice (Italy) a quite good agreement is found.
During 16 – 26 February 2007, the execution of AOD measurements was limited due to the precipitation events during that time. Thus, a lower number of data is available for comparisons with model results. The weak accumulation of particles during the winter simulation period also causes a lower AOD than it was observed during the summer time at the AERONET stations. At some stations, presented in Figures 5.13 – 5.15, a good representation of these low AODs is done (e.g., Belsk, Chilbolton, Sevastopol and Toravere) by the $\text{Sim}_{Basic}^{weight}$ and Sim_{Basic} simulations. In Toulon, Laegeren and Venice significant underestimations of the observed AOD are found, whereas the model ($\text{Sim}_{Basic}^{weight}$, Sim_{Basic}) also overestimates the actual AODs, as shown for Cabo da Roca.

For detailed comparisons about the agreement between observation and simulation, the mean absolute bias is determined, as it is done in case of the comparison with EARLINET lidar profiles (Section 5.2.3). It has to be noted, that simulated AODs are available for each hour in contrast to observed AOD. Thus, based on the hourly model output an interpolation algorithm is used to determine the simulated AOD for every 10 minutes. Interpolation results, which are temporal close to the AERONET measurement time, are used for the calculation of the mean absolute bias. In case of the summer time period, 9047 values and for the winter time period, 2977 values are available for comparisons. The values are summarized in Table 5.9. Additionally, in Figure 5.16 the absolute difference, determined based on computed and observed AOD, is shown as number-normalized frequency distributions. In Table 5.9 and Figure 5.16 information about the agreement between AERONET AOD and Sim_{Basic}, $\text{Sim}_{Basic}^{weight}$, $\text{Sim}_{Standard}$, $\text{Sim}_{Standard}^{weight}$, Sim_{Ind} and $\text{Sim}_{Ind}^{weight}$ results are summarized.

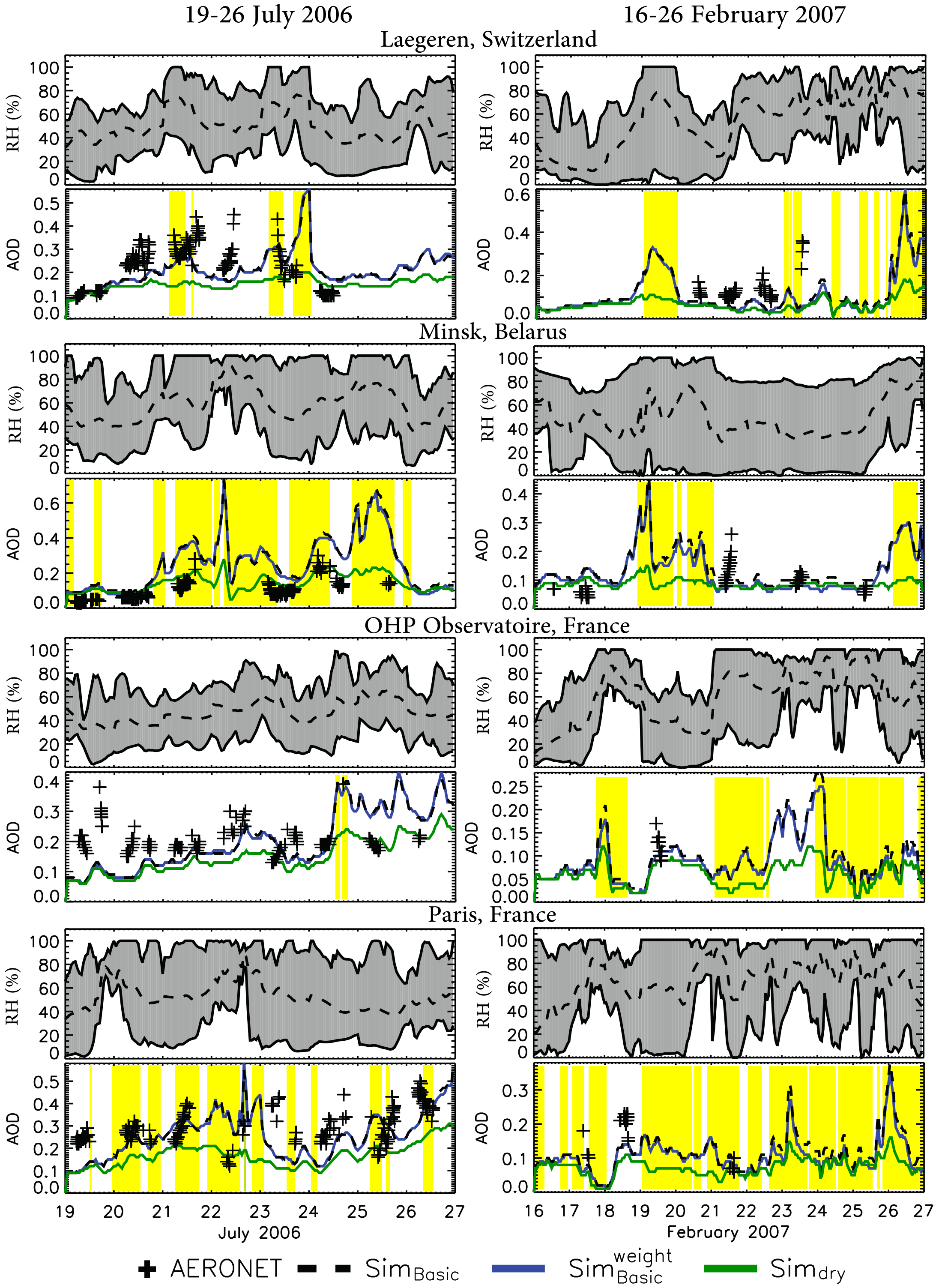

Figure 5.13: At four AERONET stations the simulated RH (based on Sim_{Basic}) is shown in the upper panels (dashed black line: average RH between 0.0 and 8.0 km, continuous black lines: minimum and maximum RH between 0.0 and 8.0 km). Within the lower panels the time series of observed (black crosses) and computed AOD (dashed black line: Sim_{Basic}, continuous blue line: $\mathrm{Sim}^{weight}_{Basic}$, continuous green line: Sim_{dry}) is shown (further comparisons are shown in Figures 5.14 – 5.15) during summer and winter. Yellow bars represent $\mathrm{RH}_{max} > 95\%$ based on Sim_{Basic} computation.

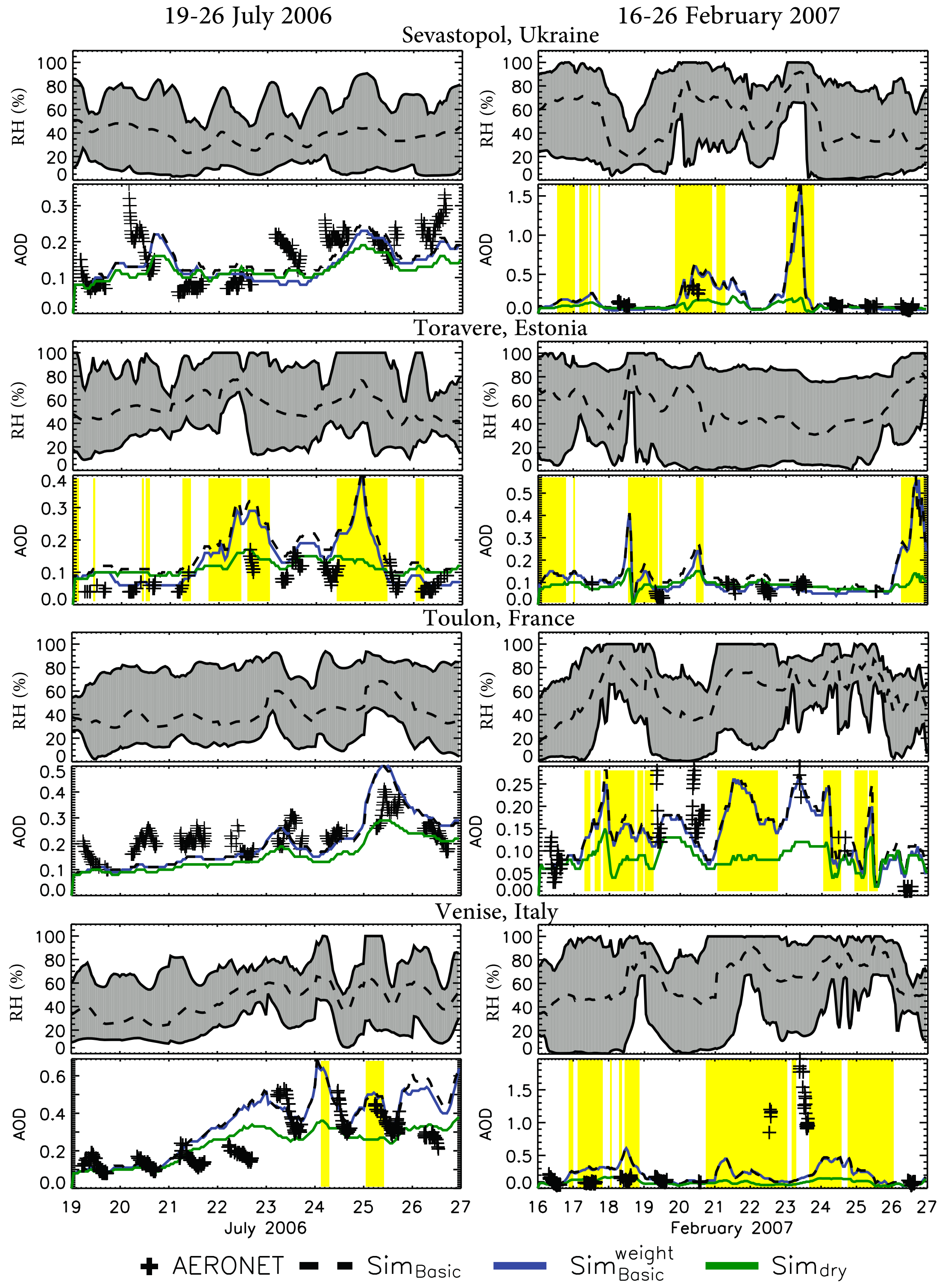

Figure 5.14: At four AERONET stations the simulated RH (based on Sim_{Basic}) is shown in the upper panels (dashed black line: average RH between 0.0 and 8.0 km, continuous black lines: minimum and maximum RH between 0.0 and 8.0 km). Within the lower panels the time series of observed (black crosses) and simulated AOD (dashed black line: Sim_{Basic}, continuous blue line: $\mathrm{Sim}_{Basic}^{weight}$, continuous green line: Sim_{dry}) is shown (further comparisons are shown in Figures 5.13 – 5.15) during summer and winter. Yellow bars represent RH_{max} >95% based on Sim_{Basic} computation.

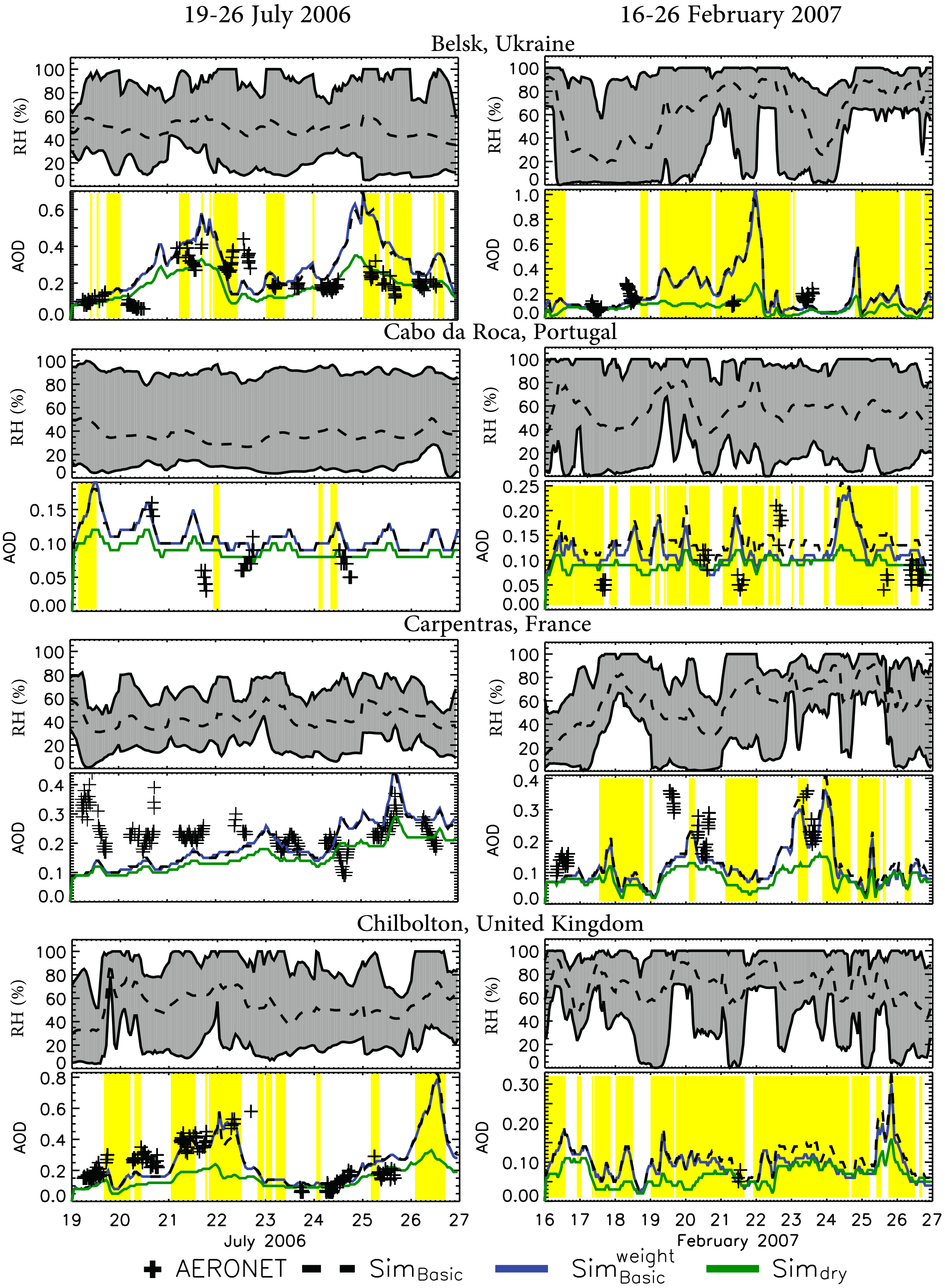

Figure 5.15: At four AERONET stations the simulated RH (based on Sim_{Basic}) is shown in the upper panels (dashed black line: average RH between 0.0 and 8.0 km, continuous black lines: minimum and maximum RH between 0.0 and 8.0 km). Within the lower panels the time series of observed (black crosses) and simulated AOD (dashed black line: Sim_{Basic}, continuous blue line: $\mathrm{Sim}^{weight}_{Basic}$, continuous green line: Sim_{dry}) is shown (further comparisons are shown in Figures 5.13 – 5.14) during summer and winter. Yellow bars represent RH_{max} >95% based on Sim_{Basic} computation.

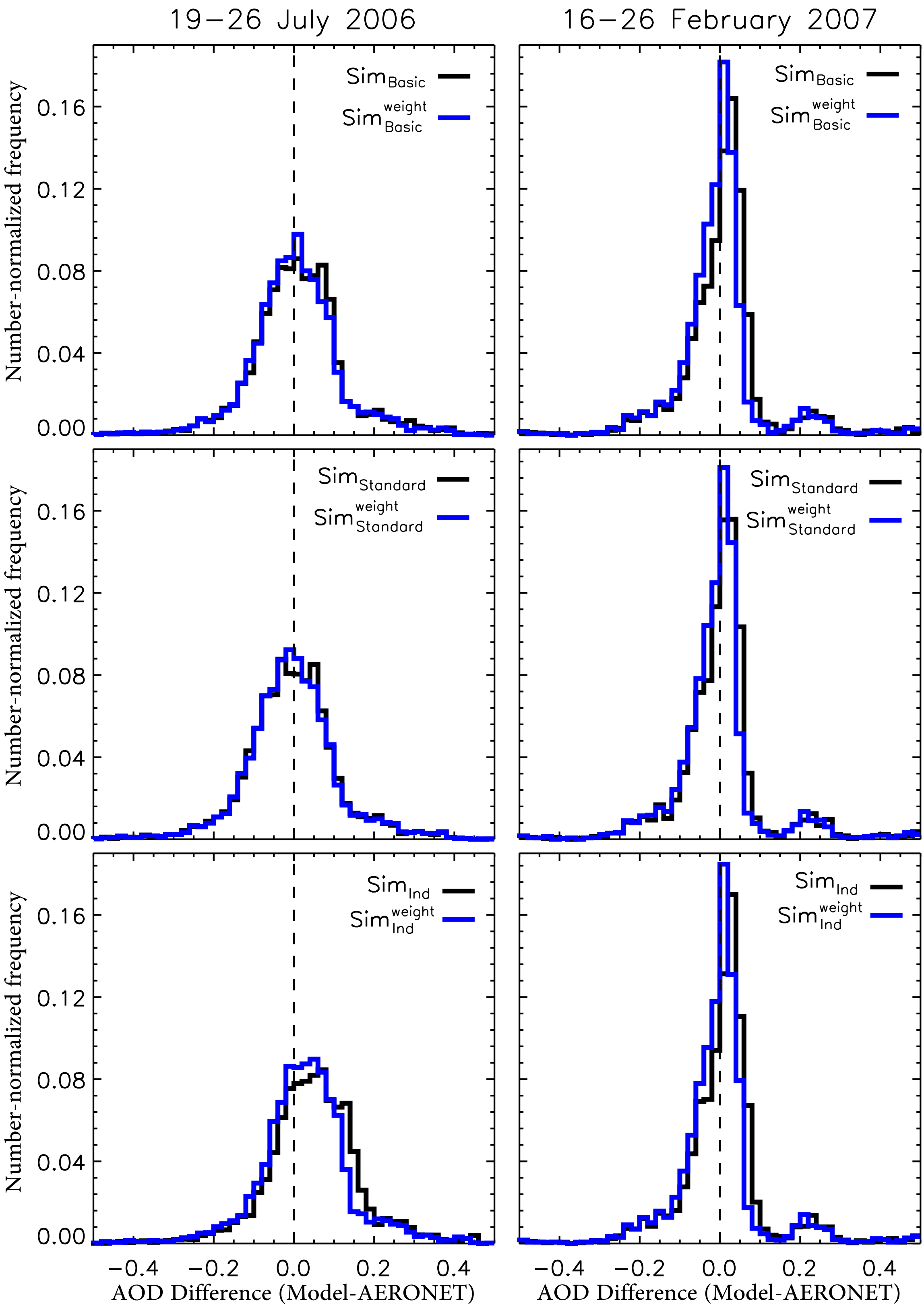

Figure 5.16: Number-normalized frequency distribution of absolute differences between simulated and observed AOD for 19 − 26 July 2006 (left panel) and 16 − 26 February 2007 (right panel). The continuous black (blue) line represents the results when using fixed (individual) weighting factors at each lateral model boundary.

Regarding the agreement between AERONET and $\mathrm{Sim}_{Basic}^{weight}$ AOD, whose results are presented in Figures 5.13 – 5.15, a quite successful agreement is found. A mean absolute bias of 0.00 is determined for the summer simulation period. The minimum and maximum absolute differences, which are also presented in Table 5.9, are relatively high, but do also point to an equal distribution of the results. As mentioned in Section 3.2, an uncertainty of the observed AOD of ∼ 0.01 – 0.02 is found by Eck et al. (1999), which depends on λ. Within the range of -0.02 – 0.02 16% of the data (AERONET compared with $\mathrm{Sim}_{Basic}^{weight}$) are found, whereas 43% are below the limit of -0.02 and 41% above the limit of 0.02. This shows a tendency of the model to underestimate the observed AOD. In case of the winter simulation period, a mean absolute bias of -0.02 is calculated when comparing $\mathrm{Sim}_{Basic}^{weight}$ data with AERONET results. Thus, the model tends to simulate too low AODs than it was measured at the European AERONET stations. This behavior is also found when taking the minimum and maximum differences (larger than during 19 – 26 July 2006) into account, with a distinct negative shift of the difference distribution. This is also shown in Figure 5.16 (upper right panel, blue line). 26% of the differences are found between -0.02 and 0.02, whereas 44% are below -0.02 and 31% above the limit of 0.02, underlining the tendency of the model to compute lower AOD values than it is observed.
The mean absolute bias, determined between experimentally observed and computed AOD partially underline the results when comparing CALIOP and model backscatter profiles.

The agreement between the observed AOD and the results based on the other model setups (Sim_{Basic} (also shown in Figures 5.13 – 5.15), $\mathrm{Sim}_{Standard}$, $\mathrm{Sim}_{Standard}^{weight}$, Sim_{Ind}, $\mathrm{Sim}_{Ind}^{weight}$) is also studied for the summer and winter simulation period. In Table 5.9 the mean absolute bias as well as the minimum and maximum difference between AERONET AOD and the individual model setups are summarized. Additionally, Figure 5.16 shows the distribution of the absolute differences between observation and simulation data. In general, the agreement of the individual model setups with the observation data is quite well. Small differences are found between the individual model setups for both simulation periods. Computation results, performed by means of the Sim_{Ind} and $\mathrm{Sim}_{Ind}^{weight}$ model setups and their agreement with measurement data, are in a distinct contrast to the other model simulations during the summer time (Figure 5.16, lower left panel). Here, the model tends to overestimate AERONET AOD. Such a behavior is not found during February 2007.
As shown in Figure 5.16 and in Table 5.9 a slight improvement is found when using individual weighting factors at the lateral model boundaries ($\mathrm{Sim}_{Basic}^{weight}$, $\mathrm{Sim}_{Standard}^{weight}$, $\mathrm{Sim}_{Ind}^{weight}$) in contrast to Sim_{Basic}, $\mathrm{Sim}_{Standard}$ and Sim_{Ind} during summer time pe-

riod. Despite the fact, that the mean absolute bias is equal in case of $\mathrm{Sim}_{Standard}$ and $\mathrm{Sim}_{Standard}^{weight}$ 14% of the absolute differences are found between -0.02 and 0.02 when using data of $\mathrm{Sim}_{Standard}$ computation and 15% when using $\mathrm{Sim}_{Standard}^{weight}$. Although, the range increases between minimum and maximum difference in case of $\mathrm{Sim}_{Ind}^{weight}$ (Table 5.9) compared to Sim_{Ind}, the fraction of values within the acceptable range of -0.02 and 0.02 increases (Sim_{Ind}: 13%, $\mathrm{Sim}_{Ind}^{weight}$: 15%) during summer.

It is significant, that the number-normalized distribution between summer and winter period are different for all model setups (Figure 5.16). In general, a higher fraction of values is found within the range from -0.02 to 0.02 during February 2007 (Sim_{Basic}: 20%, $\mathrm{Sim}_{Basic}^{weight}$: 26%, $\mathrm{Sim}_{Standard}$: 23%, $\mathrm{Sim}_{Standard}^{weight}$: 26%, Sim_{Ind}: 19%, $\mathrm{Sim}_{Ind}^{weight}$: 26%) compared to July 2006 (Sim_{Basic}: 14%, $\mathrm{Sim}_{Basic}^{weight}$: 16%, $\mathrm{Sim}_{Standard}$: 14%, $\mathrm{Sim}_{Standard}^{weight}$: 15%, Sim_{Ind}: 13%, $\mathrm{Sim}_{Ind}^{weight}$: 15%). But during February 2007, results, determined by means of Sim_{Ind} and $\mathrm{Sim}_{Ind}^{weight}$, are similar to the results based on the other four model setups, whereas during July 2006 differences occur in that case.

In Figures 5.13 – 5.15 the results of model simulations without hygroscopic growth and thus with dry aerosol mass (Sim_{dry}) are shown as continuous green lines. This model setup is performed with fixed weighting factors of 1.0 at each lateral model boundary for both simulation periods. Therefore, the results can be compared with the results of the Sim_{Basic} simulation (also shown in Figures 5.13 – 5.15 as dashed black line) and with observed AOD (black crosses).
As expected, calculated AODs based on the Sim_{dry} setup lead to lower AOD compared to model setups which take the hygroscopic growth into account. A misinterpretation of the hygroscopic growth can result in an under- as well as an overestimation of the observed AOD. For instance, a false simulation of the relative humidity leads to a wrong wet aerosol mass, which can be distinct at higher humidities. In Figure 5.15 the time series at the AERONET station in Belsk (Ukraine) during summer time represents a good representation of the observed AOD on 24 – 25 July 2006 when using Sim_{dry} results. Here, simulations under wet conditions are to effective and do not represent the real atmosphere. The computed time series of the relative humidity for this AERONET station shows maximum values up to 100% during that time. Similar results are also found for the stations in Minsk (Belarus), Toravere (Estonia) and Venice (Italy). Often, distinct AOD peaks are computed with the $\mathrm{Sim}_{Basic}^{weight}$ and Sim_{Basic} model setups for both simulation periods (e.g., July 2006: Chilbolton (United Kingdom), Laegeren (Switzerland), Minsk (Belarus), Toravere (Estonia), OHP Observatoire (France); February 2007: Laegeren (Switzerland), Toravere (Estonia), Toulon, Paris and OHP Observatoire (France), Sevastopol (Ukraine)) which can be

linked to maximum humidities larger or equal than 95% (yellow bars). In cases, when $\mathrm{Sim}_{Basic}^{weight}$ determines clearly higher AODs often no observation data are available to decide whether the simulation results are correct or not. Large differences between $\mathrm{Sim}_{Basic}^{weight}$ and Sim_{dry} indicate a very strong influence of the relative humidity during these peak events. AOD observations are not possible during very cloudy conditions or during precipitation events. The model is not limited for these cases. Thus, high AODs can be simulated caused by high relative humidity and thus do not have to be wrong. On average, Sim_{Basic} simulations compute the AOD up to 1.3 times larger than Sim_{dry} during the entire summer simulation period. During the winter period, the AOD of Sim_{Basic} is on average 1.5 times larger then with the Sim_{dry} setup.
The misinterpretation of the hygroscopic growth, the computation of false chemical compounds and their fractions, respectively, can also cause differences between observation and simulation. For instance, at the AERONET station in Sevastopol (Figure 5.14) Sim_{Basic}, $\mathrm{Sim}_{Basic}^{weight}$ and Sim_{dry} underestimate the observed AOD on 23 July 2006. Here, the simulated fraction of EC and $\mathrm{PPM}_{2.5}$ on $\mathrm{PM}_{2.5}$ reaches a maximum value of 0.94 and can have an average fraction of 0.79. Thus, the water uptake is limited in this case and therefore the computation of the individual extinction coefficients as well as of the AOD leads to lower AOD than it was observed. This effect is also found for other stations, like Paris and Laegeren (Figure 5.13) where discrepancies between AERONET and model AODs are found.
Additionally, the influence of Saharan dust is not computed by this model version. During July 2006, some AERONET stations were under the influence of the transported dust. At the AERONET station in Granada (Figure 5.17) this influence was significant. Simulation results, based on Sim_{Basic} and $\mathrm{Sim}_{Basic}^{weight}$, overlap each other for the entire period and are often lower than the observed AOD. Based on low Ångström exponents (440/870 nm) it can be assumed, that aerosol of natural origin, like marine or dust aerosol, was observed during that time. Following the classification after Omar et al. (2005), the Ångström exponent is often higher for continental, rural and urban pollution than for natural aerosol types. The Ångström exponent in Granada is often below 1.0 and thus points towards the observation of natural aerosol in particular on 19, 21 and 26 July (Figure 5.17).

To distinguish whether the misinterpretation of the water uptake by chemical compounds, the computation of these substances and their fractions or a missing aerosol type is the reason for differences between observation and simulation further studies are necessary. For instance, implementing Saharan dust in this model setup can help to identify the influence of this aerosol type on the determination of the AOD.

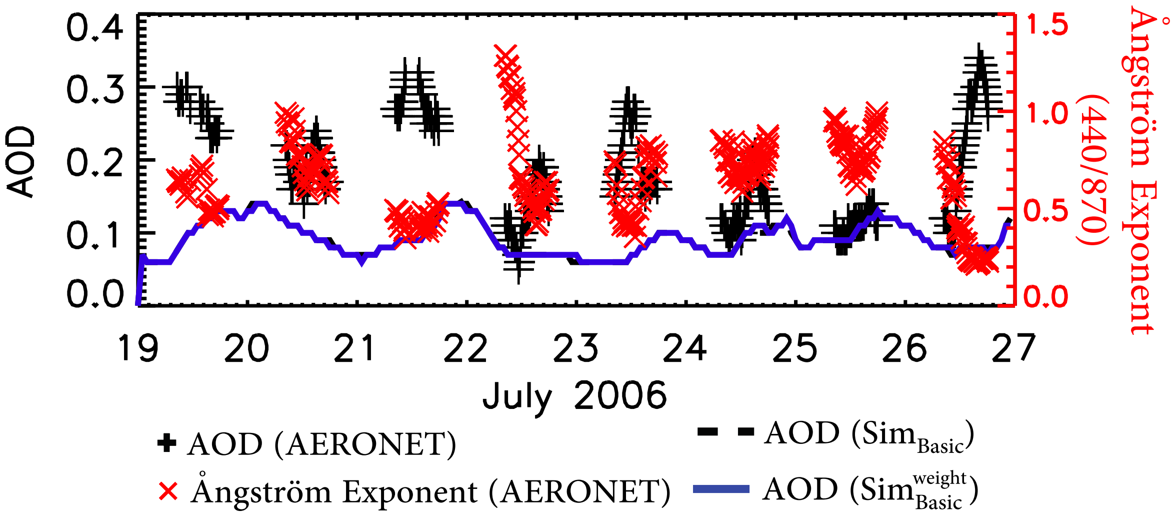

Figure 5.17: Time series of observed AOD (black crosses) and Ångström exponent (red crosses) at the AERONET station in Granada (Spain; 3.6° W, 37.2° N) during 19 – 26 July 2006. Simulated AOD is shown as dashed black line (Sim$_{Basic}$) and continuous blue line (Sim$^{weight}_{Basic}$).

5.2.5 Comparison with surface concentrations

In Figures 5.18 – 5.20 observed and simulated $PM_{2.5}$, SO_4^{2-} and EC concentration are compared. The model results are based on Sim$^{weight}_{Basic}$ computations.
Information about $PM_{2.5}$, SO_4^{2-} and EC concentrations are not available at each EMEP station for the summer and winter simulation period (Table 3.4). In case of EC only three EMEP stations performed observations during 19 – 26 July 2006 and only two during 16 – 26 February 2007. In case of the $PM_{2.5}$ concentration, eight EMEP stations are shown where observations were obtained for both simulation periods (Figures 5.18 – 5.19). If additional measurements of SO_4^{2-} concentrations are also done at these stations, these data are plotted as well and compared with simulated data.

A comparison between simulated data and surface observations of PM and specific chemical compounds is difficult because of the different resolutions. The observation data represent the situation at a specific point for a specific time period, whereas simulation results are representative for a specific model box with a definite horizontal and vertical resolution. Thus, disagreements between both datasets are expected. The model Sim$^{weight}_{Basic}$ is able to represent the day-to-day variability for $PM_{2.5}$ and SO_4^{2-} parameters (Figures 5.18 – 5.20), whereas often large differences between observed and simulated daily averages occur. In particular, $PM_{2.5}$ is often underestimated by the model, pointing to missing aerosol. Observation data show large fractions of unknown material which is included in $PM_{2.5}$ and PM_{10} (Spindler et al., 2010) and can thus not

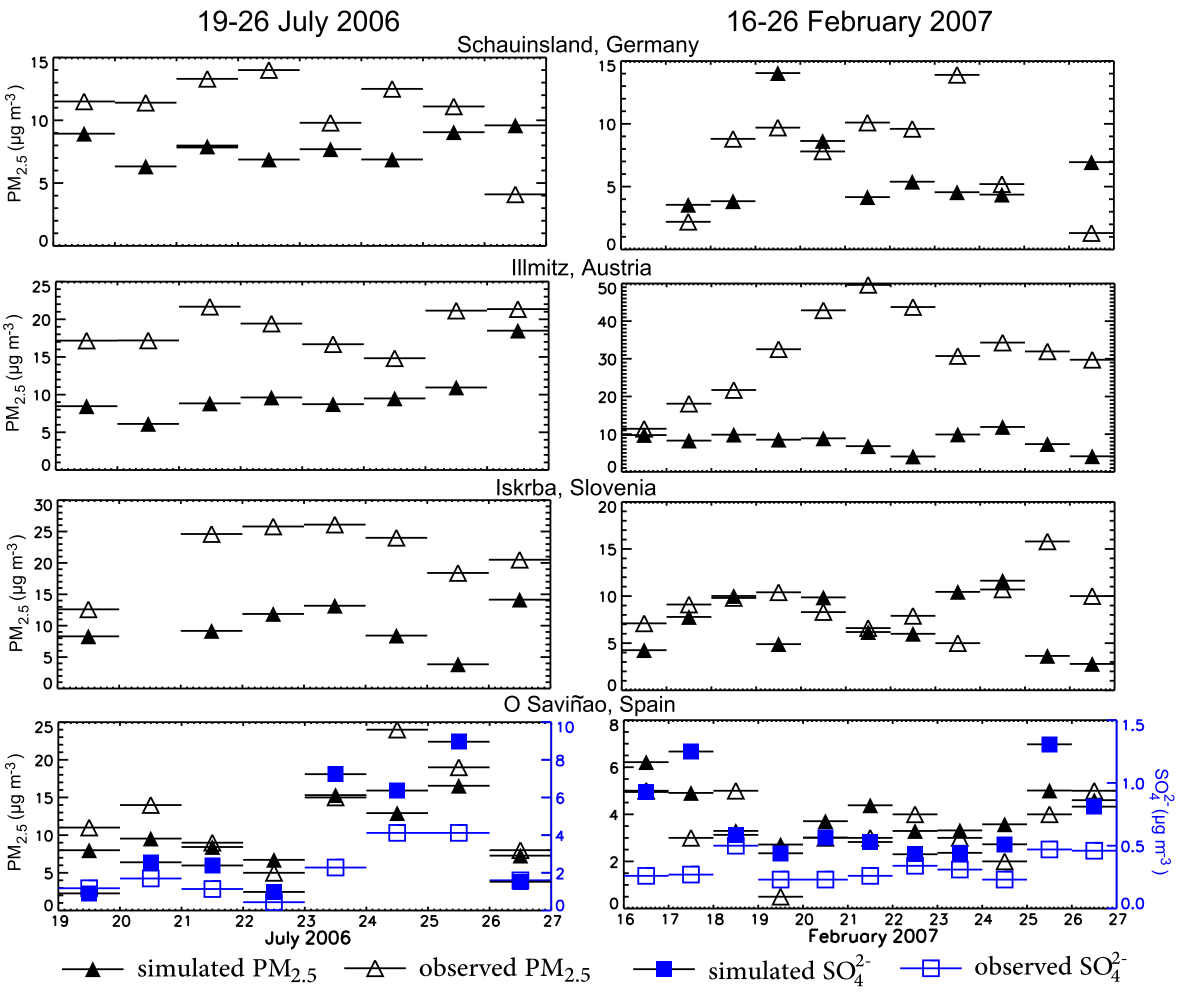

Figure 5.18: Daily average values of observed PM$_{2.5}$ (black open triangles) and SO$_4^{2-}$ (blue open squares) and simulated PM$_{2.5}$ (black filled triangles) and SO$_4^{2-}$ (blue filled squares) concentration at four EMEP stations (Schauinsland, Illmitz, Iskrba and O Saviñao). The results are based on simulations performed with the Sim$^{weight}_{Basic}$ model setup (Meier et al., 2012b).

computed by a model. The information about the mean absolute bias and the mean relative bias (R$^{mean}_{bias}$[1]), summarized in Table 5.10, shows lower values of the mean relative bias between simulated and observed PM$_{2.5}$ concentrations for the winter than for the summer case. In case of the mean absolute bias, PM$_{2.5}$ differences during summer are sometimes better then during winter time.

During the summer period, the southern regions of the European model domain were under the influence of Saharan dust (Figure 4.2). Thus, EMEP stations located in the South, like Barcarrota, Montelibretti, O Saviñao, Penausende and Viznar, represent large differences between observed and simulated PM$_{2.5}$ caused by the missing dust in the COSMO – MUSCAT version (Figures 5.18 – 5.19). The atmospheric dust parti-

---

[1] Section A.2, Equation A.2

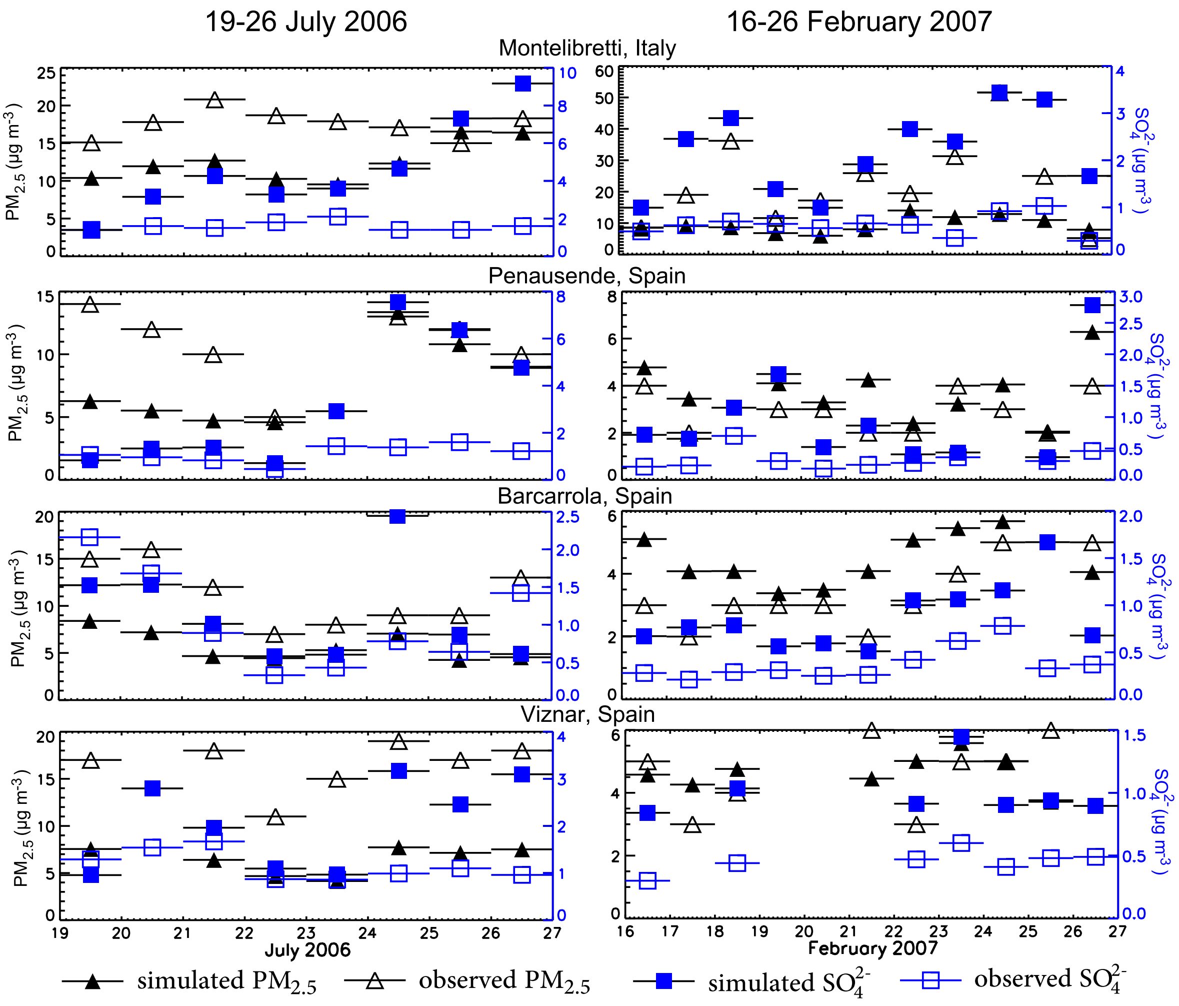

Figure 5.19: Daily average values of observed $PM_{2.5}$ (black open triangles) and SO_4^{2-} (blue open squares) and simulated $PM_{2.5}$ (black filled triangles) and SO_4^{2-} (blue filled squares) concentration at additional four EMEP stations (Montelibretti, Penausende, Barcarolla and Viznar). The results are based on simulations performed with the $\mathrm{Sim}_{Basic}^{weight}$ model setup (Meier et al., 2012b).

cles can cause significantly higher PM concentrations. As presented in Figure 4.5, the DREAM model computes a dust concentration of $< 3-80\,\mu g\,m^{-3}$ (for the region of Barcarrota), $< 3-40\,\mu g\,m^{-3}$ (for the region of Montelibretti), $< 3-160\,\mu g\,m^{-3}$ (for the region of O Saviñao), $< 3-160\,\mu g\,m^{-3}$ (for the region of Penausende) and $10-160\,\mu g\,m^{-3}$ (for the region of Viznar) which is missed by COSMO – MUSCAT. Nevertheless, the comparison for stations in Schauinsland, Iskrba, O Saviñao or Barcarrota show a good representation of the day-to-day variability. $PM_{2.5}$ data are mainly underestimated by the model, independent of the model setup, throughout the summer simulation period (Table 5.10).

In case of the winter simulation period such a distinct transport of aerosols, like Saharan dust did not occur. Thus, all individual model setups lead to satisfactory agree-

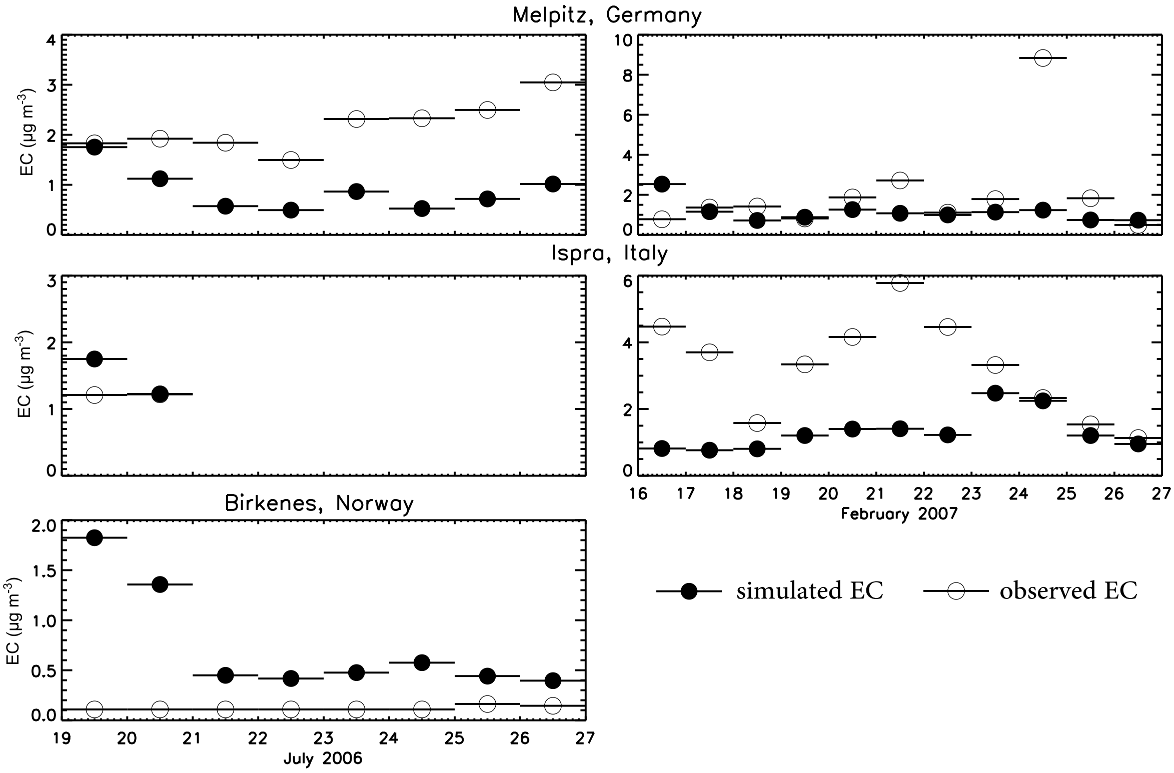

Figure 5.20: Daily average values of observed (black open circles) and simulated (black filled circles) EC at three EMEP stations (Melpitz, Ispra and Birkenes) during 19 – 26 July 2006 and two EMEP stations during 16 – 26 February 2007, respectively. The results are based on simulations performed with $\mathrm{Sim}_{Basic}^{weight}$.

ments in case of the mean relative bias ranging from -19.7% to -5.1% during the entire simulation period (Table 5.10). Whereas during the summer simulation period the underestimation of the observed $PM_{2.5}$ is very distinct, mean relative biases of $PM_{2.5}$ comparisons are smaller during February 2007. The agreements between observed and simulated daily averages of $PM_{2.5}$ are often satisfying e.g., at the EMEP station in Iskrba, O Saviñao or Penausende during February 2007. Significantly large differences are found for the station in Illmitz during the winter period (as for the summer). Because of local characteristics (Illmitz is located 117 m above sea level und thus the lowest place in Austria) the model is not able to resolve this specific topography. Therefore, the development of the PBL is not well represented in COSMO.

In general, the day-to-day variability of SO_4^{2-} daily averages is well reproduced at the three Spanish EMEP stations O Saviñao, Barcarrota and Viznar during both simulation periods. But large differences in total concentration (like for $PM_{2.5}$) do also occur. In contrast to $PM_{2.5}$ comparisons, the mean relative biases are better (104.4% – 107.7%) for all six model setups during summer than during winter (189.5% – 198.3%). Nevertheless, the discrepancies are quite high (Table 5.10). The model significantly overestimates the observed daily averages of SO_4^{2-} for summer and winter.

Only a limited comparison of daily averages of observed and simulated EC can be done here (Figure 5.20, Table 5.10). Whereas during July 2006 large values of the mean relative bias are determined for all six model setups the differences range from -29.7% to -20.2% during February 2007 (Table 5.10). The results, presented in Figure 5.20, show significant discrepancies at the EMEP stations depending on the simulation period. At the EMEP station in Melpitz (Figure 5.20) the daily EC concentrations are underestimated during summer (R_{bias}^{mean}: -70.4% (25 July) – -2.8% (19 July)) but agree well during winter exept for 16 February (R_{bias}^{mean}: -84.9% (24 February) – 230.1% (16 February)).

Intercomparisons of the various model setups, with focus on $PM_{2.5}$, EC and SO_4^{2-} concentrations, do no lead to a conclusion, whether one model setup is better than the other (Table 5.10). Results based on Sim_{Ind} computations lead to better agreements in case of $PM_{2.5}$ computation compared to Sim_{Basic} and $Sim_{Standard}$ during both summer and winter period. Sim_{Ind} results are clearly different from the other simulation results. In case of EC concentrations, worse results are found when using Sim_{Ind} during summer period in contrast to Sim_{Basic} and $Sim_{Standard}$, whereas only weak differences between the three model setups are found for the winter simulation period. Best results are achieved when using $Sim_{Standard}$ for the summer period and Sim_{Basic} for the winter case in case of the simulation of EC. For the performance of the SO_4^{2-} concentration, all model setups (Sim_{Basic}, $Sim_{Standard}$, Sim_{Ind}) are very similar, since SO_4^{2-} is not prescribed at the model boundaries. Simulations for the summer case are significantly better than for the winter time period. Since this difference between summer and winter is not obvious for AOD comparisons, this may hint towards too strong mixing at the boundary layer in COSMO, which would lead to a too strong dilution of $PM_{2.5}$ in the model.

5.2.6 Conclusion

Regional transport simulations for a summer (19 – 26 July 2006) and winter (16 – 26 February 2007) period are performed by COSMO – MUSCAT. The vertical distribution of $PPM_{2.5}$ and PPM_{10} at the lateral model boundaries is described by climatological profiles (as represented by the Sim_{Basic} setup) based on long-term lidar observations. The transport processes during both summer and winter periods are limited due to the individual meteorological situations. Lowest AODs are computed over sea surface mainly for both periods. Larger values are found e.g., in the Balkan region and Milano which points towards the importance of local aerosol sources.

Table 5.10: Information about mean absolute and relative bias of available data, calculated based on observed and simulated $PM_{2.5}$, SO_4^{2-} and EC concentrations for the entire simulation periods. The data are presented for the six different model setups: Sim_{Basic}, Sim^{weight}_{Basic}, $Sim_{Standard}$, $Sim^{weight}_{Standard}$, Sim_{Ind} and Sim^{weight}_{Ind}.

		19 – 26 July 2006			16 – 26 February 2007		
Substance	Model Setup	A^{mean}_{bias} ($g\,m^{-3}$)	R^{mean}_{bias} (%)	N	A^{mean}_{bias} ($g\,m^{-3}$)	R^{mean}_{bias} (%)	N
$PM_{2.5}$	Sim_{Basic}	-7.1×10^{-6}	-40.6	175	-7.4×10^{-6}	-7.8	225
	Sim^{weight}_{Basic}	-7.3×10^{-6}	-41.6	175	-7.8×10^{-6}	-17.3	225
	$Sim_{Standard}$	-8.0×10^{-6}	-48.1	175	-7.7×10^{-6}	-14.1	225
	$Sim^{weight}_{Standard}$	-7.9×10^{-6}	-47.5	175	-7.9×10^{-6}	-19.7	225
	Sim_{Ind}	-5.4×10^{-6}	-25.8	175	-7.3×10^{-6}	-5.1	225
	Sim^{weight}_{Ind}	-6.0×10^{-6}	-32.1	175	-7.8×10^{-6}	-15.3	225
EC	Sim_{Basic}	-0.2×10^{-6}	248.3	18	-1.3×10^{-6}	-20.2	22
	Sim^{weight}_{Basic}	-0.2×10^{-6}	226.7	18	-1.4×10^{-6}	-27.3	22
	$Sim_{Standard}$	-0.4×10^{-6}	157.1	18	-1.4×10^{-6}	-27.6	22
	$Sim^{weight}_{Standard}$	-0.4×10^{-6}	159.8	18	-1.4×10^{-6}	-29.7	22
	Sim_{Ind}	0.2×10^{-6}	408.2	18	-1.3×10^{-6}	-21.5	22
	Sim^{weight}_{Ind}	0.2×10^{-6}	376.6	18	-1.4×10^{-6}	-25.6	22
SO_4^{2-}	Sim_{Basic}	1.2×10^{-6}	107.7	98	1.0×10^{-6}	198.3	124
	Sim^{weight}_{Basic}	1.2×10^{-6}	106.0	98	1.0×10^{-6}	189.5	124
	$Sim_{Standard}$	1.2×10^{-6}	106.6	98	1.0×10^{-6}	196.3	124
	$Sim^{weight}_{Standard}$	1.2×10^{-6}	107.3	98	1.0×10^{-6}	191.5	124
	Sim_{Ind}	1.2×10^{-6}	106.7	98	1.0×10^{-6}	197.4	124
	Sim^{weight}_{Ind}	1.2×10^{-6}	104.4	98	1.0×10^{-6}	190.2	124

Next to the climatological profile, individual lidar profiles (Sim_{Ind}) as well as a Standard Profile ($\mathrm{Sim}_{Standard}$) are used to describe the vertical distribution of chemical compounds at the lateral model boundaries. Further, weighting factors are used to adjust these profiles individually for each model boundary. Therefore, the ratio between observed and simulated (Sim_{Basic}, Sim_{Ind}, $\mathrm{Sim}_{Standard}$) AOD data is computed leading to new model setups ($\mathrm{Sim}_{Basic}^{weight}$, $\mathrm{Sim}_{Ind}^{weight}$, $\mathrm{Sim}_{Standard}^{weight}$). Observed AOD data are used from AERONET stations located close to the model boundaries.

Comparisons between experimentally observed and simulated AODs (AERONET), vertical backscatter profiles (EARLINET) and particle concentrations at the surface level (EMEP) are shown for the individual model setups. In general, discrepancies between the results of the individual model setups are found to be very small for both summer and winter period. The measurement results agree well with the simulation. For instance, AERONET AODs are reproduced well also in case of the representation of the day-to-day variability. Particle concentrations at the surface level agree to some extent. However, it is challenging to compute correct concentrations of $\mathrm{PM}_{2.5}$, EC and SO_4^{2-}. Basically, the various model setups underestimate the observed concentrations, possibly caused by the different resolution. Whereas experimental observation data is representative for specific geographic location, model results cover a specific horizontal and vertical resolution. The vertical backscatter profiles are compared with ground-based lidar observations performed at EARLINET stations. It is found, that the vertical distribution is well reproduced by the regional model, also in case of the simulation of characteristic aerosol layers. The influence of the hygroscopic growth is studied as well. The implementation of the water uptake ability for specific chemical compounds leads to better results than using dry aerosol.

The similarity of the various model setups with different descriptions of the vertical distribution of chemical compounds at the lateral model boundaries indicates that for this model domain the meteorological situation which influences the aerosol transport is less important. The transport of the Saharan dust to southern Europe leads to increased optical thicknesses and particle concentrations in this region. This aerosol type is not described in this model setups and therefore causes discrepancies when comparing experimental observation and simulation data. In some cases, the usage of sun photometer AOD observations to adjust the concentration profiles at the lateral model boundaries improved the results compared to simulations without this adjustment. But distinct results can be found when performing model simulations with strong aerosol transport or for smaller model domains. Another approach can be the extraction of aerosol distributions from large scale (global) aerosol transport models or computed with General Circulation Models or chemistry transport models (CTMs). Thus, actual atmospheric conditions my be taken into account.

5.3 Radiative effects

Several studies have been performed to analyze the influence of absorbing aerosol at different altitudes within regional and global models. For instance, Fan et al. (2008) found a decrease of cloud cover fraction when absorbing aerosols are located above cumulus clouds, whereas Johnson et al. (2004) found an increase of cloud cover fraction when the aerosol is located above marine stratocumulus clouds. The various results, achieved by studies about the influence of absorbing aerosols on the cloud cover fractions, are summarized by Koch and Del Genio (2010), who also emphasizes the need for systematically research of the effects of absorbing aerosols at different heights, regions and environmental conditions.

5.3.1 Direct and semi-direct radiative effects

As described in Section 2, the mass of “urban” and “continental” aerosol is determined in the MUSCAT model. By using an EC limit of 20%, the mass of “continental” aerosol is larger compared to the mass of the “urban” aerosol during 19 – 26 July 2006 (average “urban” mass: $0.97\,\mathrm{g\,m^{-1}}$; average “continental” mass: $3.74\,\mathrm{g\,m^{-1}}$). Compared to the summer case, the mass of the computed “urban” and “continental” aerosol type during the winter simulation period is lower. But during winter, the average “continental” mass ($0.79\,\mathrm{g\,m^{-1}}$) is lower than the average “urban” mass ($1.81\,\mathrm{g\,m^{-1}}$). It is summarized in Table 5.4, that the average fraction of EC within the near surface layer is larger during February 2007 in contrast to July 2006. The winter simulation period also represents the heating period and thus a higher fraction of EC is assumed to be accumulated within the atmosphere.

The information about the “continental” and “urban” aerosol classification is transfered to the radiation scheme of COSMO. There, the influence of both aerosol types on solar and thermal radiation as well as on dynamical processes is calculated. This influence is computed by the Sim_{Basic} simulations for both simulation periods. Depending on the aerosol type (“continental” or “urban”), absorption as well as scattering by the aerosols differs. Depending on the aerosol distribution, the less absorbing character of the dominant “continental” aerosol during the summer period influences the determination of the solar and thermal radiation and thus of further processes and parameters. During the winter period “urban” aerosol mass dominates the atmosphere and therefore results in a more absorbing nature in contrast to the “continental” aerosol type. The magnitude of absorption and scattering processes within the atmosphere influences the atmospheric heating rates in different ways. The atmospheric heating rate is described by:

$$\frac{\partial T(z,t)}{\partial t} = -\frac{1}{\rho c_p} \cdot \frac{\partial F(z)}{\partial z} \tag{5.5}$$

which describes changes of the temperature (T) in the time (t), depending on the air density (ρ), the specific heat capacity for dry air ($c_p = 1005\,\mathrm{J\,K^{-1}\,kg^{-1}}$) and the change in the solar flux (F) by the altitude (z) (Wendisch et al., 2008). Depending on the heating rate, the stabilization of the atmosphere and thus on convective processes and the development of the PBL may change (Wendisch et al., 2008). To study changes in heating rate by the "urban" and "continental" aerosol, an additional model simulation is performed: $\mathrm{Sim}_{NoAerosol}$ (Table 2.1), where the impact of aerosol on solar and thermal radiation is not computed.

Average profiles of solar heating rates, thermal cooling rates and of extinction coefficients for the entire simulation periods are shown in Figure 5.21 for the Sim_{Basic} (continuous lines) and the $\mathrm{Sim}_{NoAerosol}$ (dashed lines) model setups. All profiles are averaged for the land surfaces. The black lines represent the average profiles based on cloud-free model grid cells. For the summer simulation period, 67 individual profiles are available for this calculation. The average total cloud cover (TCC) during winter (Figure 5.22, upper right panel) was always higher than 0% within the model grid cells and thus no average profiles are determined for cloud-free conditions. Additionally, the average profiles for all cloud fractions is shown as red lines in Figure 5.21. During the summer simulation period, a nearly constant solar heating rate is computed between surface and 2 km altitude for cloud-free conditions and when taking the forcing by "urban" and "continental" aerosol into account (Sim_{Basic}). Within that altitude range, the extinction coefficient (Figure 5.21, upper right panel, black line) varies from $3.5\,\mathrm{x}\,10^{-5}\,\mathrm{m^{-1}}$ to $5.1\,\mathrm{x}\,10^{-5}\,\mathrm{m^{-1}}$. An average AOD of 0.15 for this cloud-free case is determined, whereas 50% of the AOD is found between surface and 2 km altitude. For this layer the solar heating rate ranges from $1.2\,\mathrm{K\,d^{-1}}$ to $1.3\,\mathrm{K\,d^{-1}}$. This values fit quite well with the modeling study of Péré et al. (2011). The authors used the chemistry-transport model CHIMERE and the meteorological model WRF (Weather Research and Forecasting) and found heating rates between 0.65 and $1.2\,\mathrm{K\,d^{-1}}$ of the lower troposphere during a heat wave of summer 2003 over western Europe. Additionally, simulation results, performed of the past 150 years by Bauer and Menon (2012) by means of the climate model from the Goddard Institute for Space Studies, show relatively low heating rates caused by the absorbing aerosol. For the entire Northern Hemisphere a peak of the solar heating rate of $0.1\,\mathrm{K\,d^{-1}}$ is computed.

In this study, the computation of the solar heating rate without the "urban" and

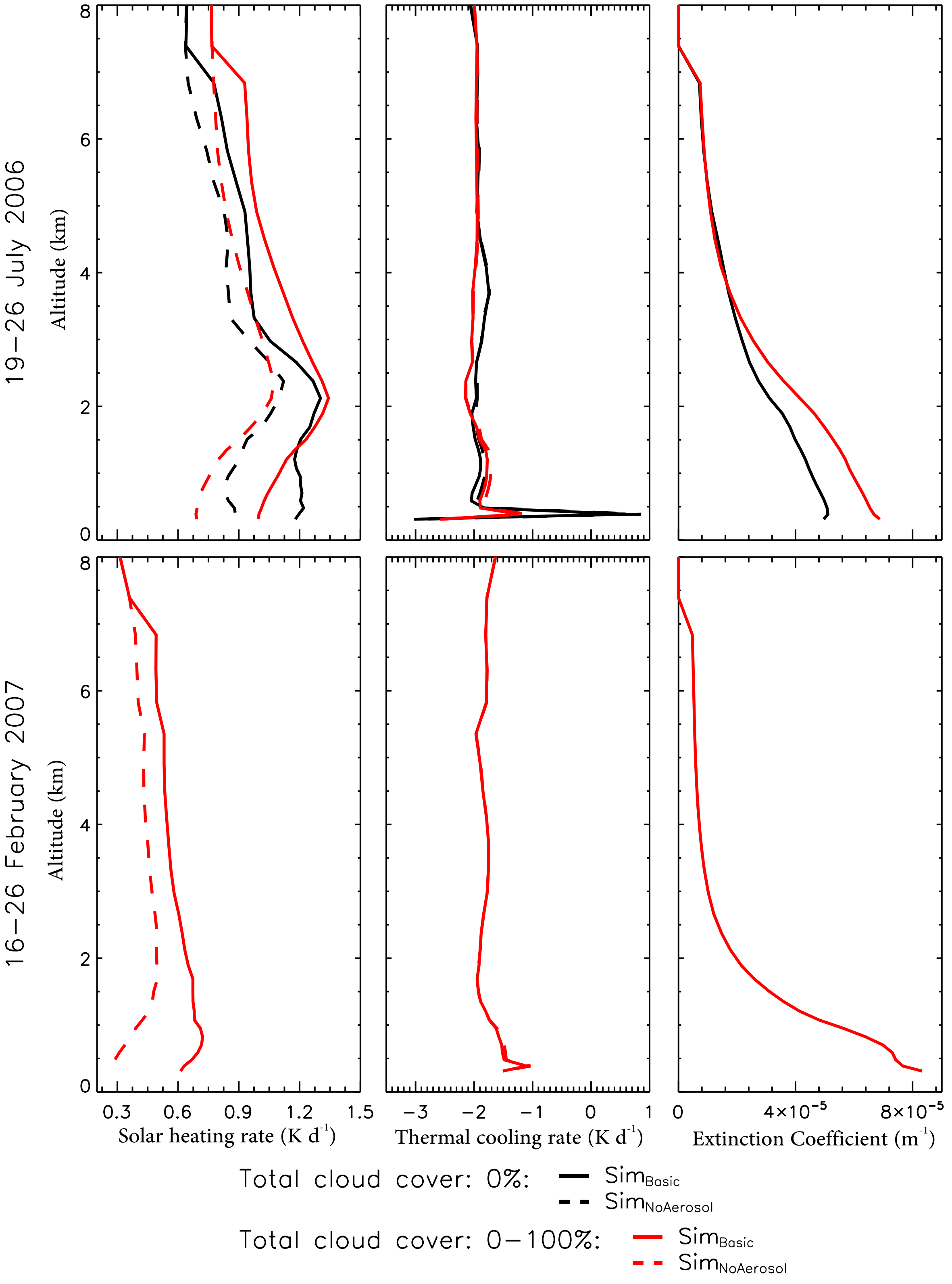

Figure 5.21: Average profiles of solar heating rates ($\mathrm{K\,d^{-1}}$) (left panel), of thermal cooling rates ($\mathrm{K\,d^{-1}}$) (middle panel) and of extinction coefficients ($\mathrm{m^{-1}}$) (right panel) during 19 − 26 July 2006 and 16 − 26 February 2007, computed over land surface for cloud-free grid boxes (black lines) as well as for all kind of cloud fractions (red lines). Continuous line: Sim_{Basic}. Dashed line: $\mathrm{Sim}_{NoAerosol}$.

“continental” aerosol (Sim$_{NoAerosol}$) leads to smaller values and varies from 0.8 K d^{-1} to 1.1 K d^{-1} between surface and 2 km altitude during summer time (Figure 5.21, upper left panel). Therefore, differences between 0.2 K d^{-1} and 0.4 K d^{-1} occur between Sim$_{Basic}$ and Sim$_{NoAerosol}$ in case of the solar heating rates (total cloud cover: 0%, land surface) between surface and 2 km altitude. The average solar heating rates for all kind of cloud fractions (red lines) are lower between surface and ∼ 1.3 km altitude for the Sim$_{Basic}$ setup and between surface and 2.5 km altitude for the Sim$_{NoAerosol}$ setup. Above this layer, the solar heating for cloudy conditions is stronger than for the cloud-free case. Between surface and 2 km altitude the average difference of the solar heating rates between Sim$_{Basic}$ and Sim$_{NoAerosol}$ (all cloud fractions) is 0.3 K d^{-1}. For the cloud-free case only 67 individual profiles were used. For all kind of cloud cover fractions 6083 individual profiles are available. Thus, direct comparisons between both data sets are limited. Nevertheless, the same behavior of lower solar heating rates near the surface and higher values in the height for cloudy conditions are also observed by Sievers (2004, Fig. 70), who used satellite data to determine the solar heating rates.

Concerning the thermal cooling rate (Figure 5.21, upper middle panel) during July 2006, very similar results are found for both model setups, Sim$_{Basic}$ and Sim$_{NoAerosol}$. The values of the cloud-free case range from -3.0 K d^{-1} (∼200 m) to 0.6 K d^{-1} (∼277 m) and back to -1.8 K d^{-1} (∼371 m). Above this layer, the thermal cooling reaches an average value of -1.9 K d^{-1}. For the cloudy case, the range between minimum and maximum thermal cooling rates is not as large as for the cloud-free case but with distinct values of -2.6 K d^{-1} and -1.2 K d^{-1} near the surface. Thermal cooling rates of -2.9 K d^{-1} where also found by Péré et al. (2011) within the lower part of the atmospheric boundary layer for a summer case study.

During the winter simulation period, higher solar heating rates are also determined when taking “urban” and “continental” aerosol into account (Figure 5.21, lower left panel, continuous red line). Near the surface, a value of 0.6 K d^{-1} is found. This is about 50% lower than during the summer period. At 825 m the maximum is reached at 0.7 K d^{-1}. The extinction coefficients for this altitude range vary from 6.4 x 10^{-5} to 8.3 x 10^{-5} m^{-1} (Figure 5.21, lower right panel, continuous red line). Without the “urban” and “continental” aerosol (Sim$_{NoAerosol}$) the solar heating rate is up to 0.4 times lower than with the “urban” and the “continental” aerosol (Sim$_{Basic}$) during February 2007. In case of the thermal cooling, the values range from -1.5 K d^{-1} near the surface up to -1.1 K d^{-1} at 387 m and back to -1.5 K d^{-1} at ∼480 m (Figure 5.21, lower middle panel, dashed red line). Above, the average thermal cooling rate is -1.8 K d^{-1}.

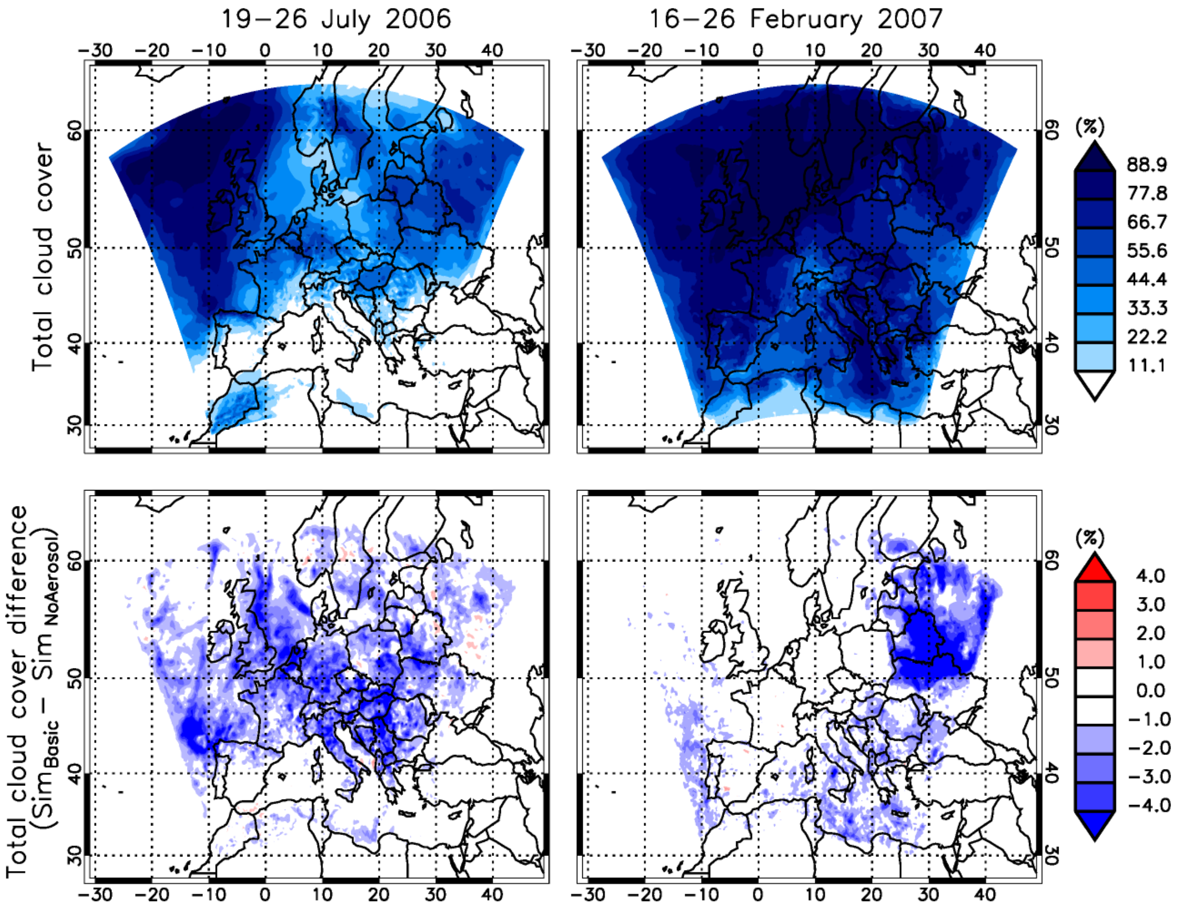

Figure 5.22: Total cloud cover, simulated with Sim_{Basic} (upper panel) and difference of the total cloud cover between the Sim_{Basic} and the $\mathrm{Sim}_{NoAerosol}$ setup (lower panel) during 19 – 26 July 2006 and 16 – 26 February 2007.

To separate the combined changes in the radiative fluxes by aerosol and the dynamic response of the atmosphere from the radiative effects alone, an additional run, $\mathrm{Sim}_{AerosolNoFB}$ (Table 2.1), was carried out. When performing model simulations based on the $\mathrm{Sim}_{AerosolNoFB}$ setup, "urban" and "continental" aerosol types are only allowed to influence the radiation but without any further influences on dynamical processes and thus without any feedback. For this, the COSMO radiation routine is called twice (Meier et al., 2012a). In a first computation the aerosol forcing by "urban" and "continental" aerosol is determined and within a second step the computation is done without any forcing. The dynamical processes are therefore equal to the $\mathrm{Sim}_{NoAerosol}$ setup. Based on the three model setups Sim_{Basic}, $\mathrm{Sim}_{NoAerosol}$ and $\mathrm{Sim}_{AerosolNoFB}$ calculations of the differences of radiation flux densities provide information about the

- Radiative effect (RE), which includes the direct radiative effect of the aerosol and the effect of changes due to the impact of the direct forcing e.g., on cloud cover, computed as differences of radiation flux densities of Sim_{Basic} and $\mathrm{Sim}_{NoAerosol}$.

There is no influence on the sea surface temperature (SST) by the RE; SST is held constant.
$\mathrm{RE} = \mathrm{F}_{TOA,surface}(\mathrm{Sim}_{Basic})$ - $\mathrm{F}_{TOA,surface}(\mathrm{Sim}_{NoAerosol})$;

- The direct radiative forcing (DRF), which describes the effect of the aerosols on the radiation fluxes without including effects of changed atmospheric dynamics, computed as difference between $\mathrm{Sim}_{AerosolNoFB}$ and $\mathrm{Sim}_{NoAerosol}$.
  $\mathrm{DRF} = \mathrm{F}_{TOA,surface}(\mathrm{Sim}_{AerosolNoFB})$ - $\mathrm{F}_{TOA,surface}(\mathrm{Sim}_{NoAerosol})$;
- The semi-radiative effect (SRE), which is caused by the changes on atmospheric dynamics e.g., due to cloud changes, without considering the aerosol DRF, computed as difference between Sim_{Basic} and $\mathrm{Sim}_{AerosolNoFB}$.
  $\mathrm{SRE} = \mathrm{F}_{TOA,surface}(\mathrm{Sim}_{Basic})$ - $\mathrm{F}_{TOA,surface}(\mathrm{Sim}_{AerosolNoFB})$;

as also described by Meier et al. (2012a).

Figure 5.23 shows the solar RE, DRF and SRE, and Figure 5.24 shows the thermal RE, DRF and SRE for the summer and winter simulation period near the surface as well as at TOA. The results of the RE are based on the aerosol DRF plus the SRE. The SRE reflects the change of the total cloud cover.
Concerning the solar DRF, mainly negative values are found at the surface for both simulation periods. The attenuation of the solar flux by “urban” and “continental” aerosol leads to an average value of -16.3 $\mathrm{W\,m^{-2}}$ for July 2006 and of -6.3 $\mathrm{W\,m^{-2}}$ for February 2007 at the surface (Table 5.8). The presence of the computed aerosol influences the thermal DRF at the surface as well but with a much smaller magnitude (Figure 5.24). On average, an increase of the thermal flux is found for the summer and the winter simulation period (summer: 0.9 $\mathrm{W\,m^{-2}}$, winter: 0.4 $\mathrm{W\,m^{-2}}$; Table 5.9), which is an artifact of the Tanré parameterization. Therefore the thermal DRF should not be overstated. In regions of higher AOD (Figure 5.8, upper panel), the solar and thermal DRF is stronger than in other regions (see also Figure 5.25, upper and middle panel). AOD and surface solar DRF show negative correlation (Pearson correlation (PC)) of -0.7 for the summer case and a weaker correlation for the winter case (PC = -0.4) regarding the solar DRF. On the other hand, a positive correlation between AOD and surface thermal DRF is found for both simulation periods, whereas the correlation during winter (PC = 0.7) is slightly better than during the summer period (PC = 0.6).
In case of the solar DRF at TOA, an average value of -1.0 $\mathrm{W\,m^{-2}}$ (summer) and of 2.7 $\mathrm{W\,m^{-2}}$ (winter) is determined. A positive correlation between solar DRF at TOA and total cloud cover can be found (Figure 5.25; lower panel). At total cloud covers larger than 40% (PC = 0.8) a positive forcing is determined. On average, a total cloud

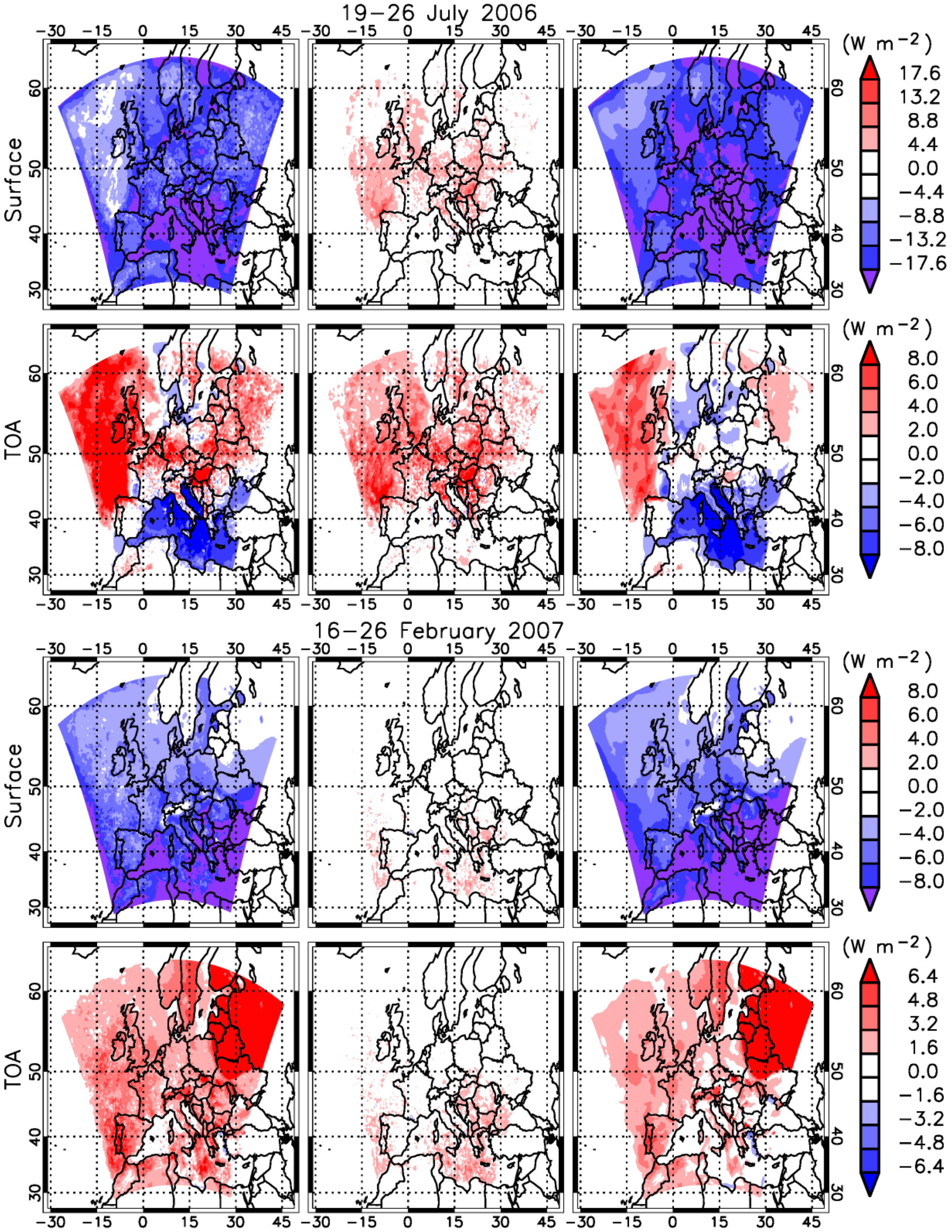

Figure 5.23: Solar RE, solar SRE and solar DRF near the surface and at the TOA for the whole summer (19 – 26 July 2006; Meier et al. (2012a)) and winter (16 – 26 February 2007) period.

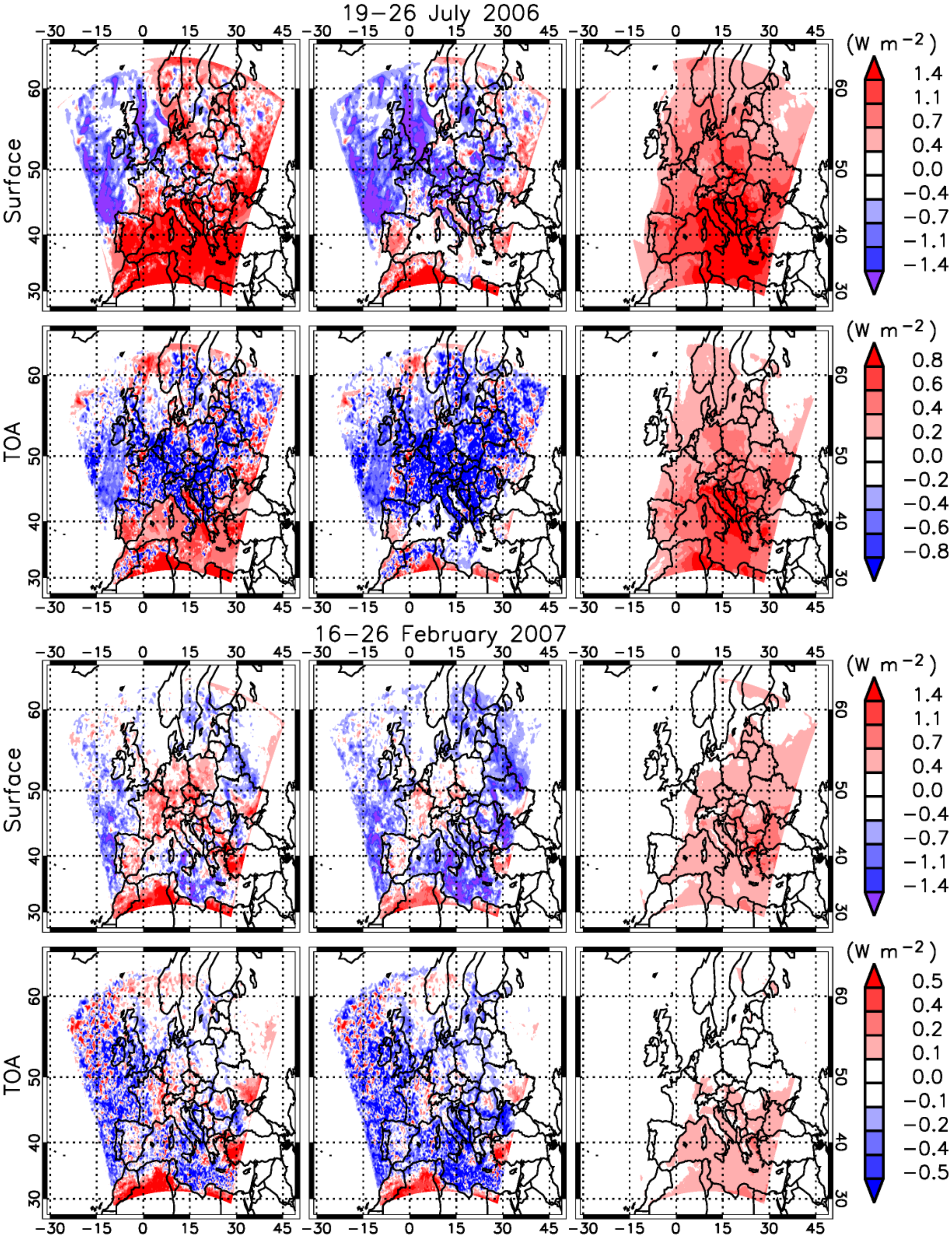

Figure 5.24: Thermal RE, thermal SRE and thermal DRF near the surface and at the TOA for the whole summer (19 – 26 July 2006) and winter (16 – 26 February 2007) period.

Table 5.11: Average differences of total cloud cover and 2 m temperatures between Sim_{Basic} and $\mathrm{Sim}_{NoAerosol}$ results and average values of solar (Meier et al., 2012a) and thermal RE, DRF and SRE at the surface and the TOA for summer and winter.

	19 – 26 July 2006	16 – 26 February 2007
Total cloud cover difference (%)		
entire period	-1.0	-0.7
00 UTC	-0.9	-0.4
12 UTC	-1.4	-1.6
2 m temperature difference (K), land surface		
entire period	-0.14	-0.10
00 UTC	-0.03	-0.02
12 UTC	-0.24	-0.25
Solar radiative forcing (W m^{-2}), surface, entire domain, entire period		
RE	-13.7	-5.6
DRF	-16.3	-6.3
SRE	2.6	0.7
Solar radiative forcing (W m^{-2}), TOA, entire domain, entire period		
RE	1.5	3.6
DRF	-1.0	2.7
SRE	2.4	0.9
Solar radiative forcing (W m^{-2}), TOA, sea domain, entire period		
RE	1.0	2.6
DRF	-1.3	1.5
SRE	2.3	1.1
Solar radiative forcing (W m^{-2}), TOA, land domain, entire period		
RE	2.4	4.4
DRF	-0.3	3.6
SRE	2.7	0.8
Thermal radiative forcing (W m^{-2}), surface, entire domain, entire period		
RE	0.9	0.2
DRF	0.9	0.4
SRE	-0.1	-0.2
Thermal radiative forcing (W m^{-2}), TOA, entire domain, entire period		
RE	0.1	0.0
DRF	0.4	0.1
SRE	-0.3	-0.1
Thermal radiative forcing (W m^{-2}), TOA, sea domain, entire period		
RE	0.1	-0.1
DRF	0.3	0.1
SRE	-0.2	-0.2
Thermal radiative forcing (W m^{-2}), TOA, land domain, entire period		
RE	0.1	0.2
DRF	0.5	0.1
SRE	-0.4	0.1

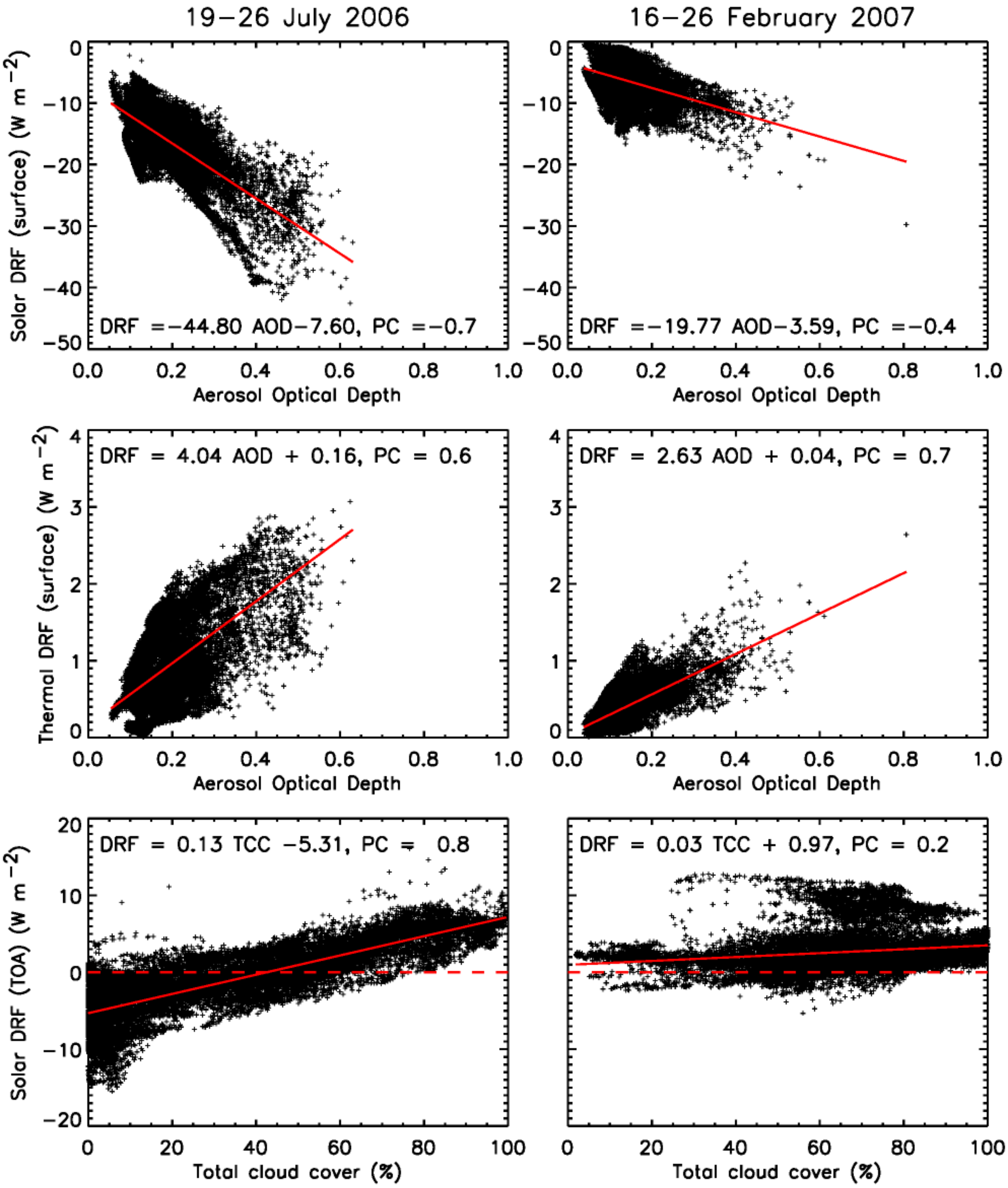

Figure 5.25: Correlation study between AOD and surface solar DRF (upper panel), between AOD and surface thermal DRF (middle panel) as well as between solar DRF at TOA and the total cloud cover (lower panel) for the both model simulation periods. The continuous red line represents the linear function and the dashed red line, in the lower panel, represents the location of zero solar DRF at TOA for all cloud cover fractions.

cover fraction larger than 40% is mainly simulated over the Atlantic Ocean and the north-east of the model domain, whereas over the southern part of the European model domain cloud fractions lower than 10% are determined (Figure 5.22). The limit of 40% fits quite well with the cloud fraction found by Chand et al. (2009). The authors used satellite data performed during July – October of 2006 and 2007 over the southeastern Atlantic Ocean to analyze the DRF. At a cloud cover fraction larger than 0.4, the forcing at TOA shifts from negative to positive values. As shown in Figure 5.25, this positive correlation between solar DRF at TOA and the total cloud cover fraction is weaker for the winter simulation period. Here, the correlation is only 0.2 and no clear cloud fraction limit for the change between positive and negative solar DRF at the TOA can be determined. The positive correlation is due to absorbing aerosol located above clouds. Due to the higher cloud cover in the winter period, the DRF is positive at most grid points.
Regarding the surface albedo, a relatively dark surface like a cloud-free ocean (e.g., Mediterranean Sea; Figure 5.22) leads to a negative solar DRF at TOA (Figure 5.23). For the summer as well as for the winter period, the solar DRF above the sea surface indicates a stronger negative forcing than over the land surface. A solar DRF at TOA of -1.3 $\mathrm{W\,m^{-2}}$ over sea surface and of -0.3 $\mathrm{W\,m^{-2}}$ over land surface is determined for the summer case (Table 5.8). During February 2007, over sea surface a solar DRF of 1.5 $\mathrm{W\,m^{-2}}$ and over land surface of 3.6 $\mathrm{W\,m^{-2}}$ at the TOA is found (Table 5.8).

“Urban” and “continental” aerosol types cause a small average positive thermal DRF at TOA (Figure 5.24) and thus an increase of the thermal direct effect at the TOA. For the entire model domain a thermal DRF at TOA during July 2006 of 0.4 $\mathrm{W\,m^{-2}}$ is computed which is higher than during February 2007 (0.1 $\mathrm{W\,m^{-2}}$; Table 5.8). Differences between land and sea surface are only found for July 2006. Here, an average thermal DRF at TOA of 0.5 $\mathrm{W\,m^{-2}}$ is determined for land surface and of 0.3 $\mathrm{W\,m^{-2}}$ for sea surface, respectively. In case of the winter simulation period, the average values of the thermal DRF at TOA over land and sea surface are equal for the entire model domain. Correlations between thermal DRF at TOA and total cloud cover are negative with the forcing only evident in cloud-free conditions (summer: PC = -0.7; winter: PC = -0.6).

It is shown in Figure 5.22 and in Table 5.11 that the average total cloud cover fraction decreases if “urban” and “continental” aerosols are present and the atmosphere can respond to the aerosol forcing. During July 2006, nearly the entire model domain, except the south, are affected whereas during February 2007, a distinct cloud reduction is found in the north-east. For the entire simulation period an average decrease of -1.0% (summer) and of -0.7% (winter) is computed, which is smaller during night-time and higher during day-time (Table 5.11). This reduction of cloud cover leads to positive solar SRE at TOA and surface. Mainly in regions with high total cloud cover fraction (Figure 5.22) the simulated solar SRE at the surface is positive (Figure 5.23). Incoming solar radiation is absorbed by the atmospheric particles, increases the heating rates and thus decreases the average cloud fraction (Figure 5.22, lower panel; Table 5.8). On average, positive solar SRE at the surface are determined for the summer (2.6 $\mathrm{W\,m^{-2}}$) and the winter (0.7 $\mathrm{W\,m^{-2}}$) simulation period. Regarding the thermal surface SRE, positive values are mainly found in regions with low cloud cover fraction, whereas no significant correlation is found for both time periods (summer: PC = -0.5; winter: PC = -0.3). On average, negative thermal SRE are determined for July 2006 (-0.1 $\mathrm{W\,m^{-2}}$) and February 2007 (-0.2 $\mathrm{W\,m^{-2}}$). More thermal cooling due to less clouds since the reduction in cloud cover leads to lower albedos.

The solar SRE at the TOA is mainly positive over the entire model domain. During July 2006, the effect is stronger (2.4 $\mathrm{W\,m^{-2}}$) than during February 2007 (0.9 $\mathrm{W\,m^{-2}}$). In contrast to the solar DRF at TOA the solar SRE is nearly equal over land and sea surfaces (Table 5.8). Mainly negative thermal SRE at TOA is computed for summer and winter, respectively. But during the winter simulation period a positive effect is found over land surface (Table 5.8).

The sum of the solar/thermal DRF and SRE simulations leads to a general negative solar RE and a positive thermal RE near the surface (Table: 5.8). Average values of -13.7 $\mathrm{W\,m^{-2}}$ (summer) and of -5.6 $\mathrm{W\,m^{-2}}$ (winter) are computed for the solar RE near the surface in case of the entire model domain. In case of the thermal RE, average values of 0.9 $\mathrm{W\,m^{-2}}$ (summer) and 0.2 $\mathrm{W\,m^{-2}}$ (winter) are found near the surface. Due to the occurrence of positive and negative values, the solar average RE at TOA is lower (summer: 1.5 $\mathrm{W\,m^{-2}}$, winter: 3.6 $\mathrm{W\,m^{-2}}$) than near the surface and very weak in case of the thermal RE at TOA (summer: 0.1 $\mathrm{W\,m^{-2}}$; winter: 0.0 $\mathrm{W\,m^{-2}}$).

As mentioned by Sakaeda et al. (2011), a strong cooling is closely connected with a strong negative radiative effect near the surface. Thus, absorbing aerosol leads to changes of the 2 m temperature as it is shown in Table 5.8 for both summer and winter period. Because of the fixed SST, 2 m temperatures refer to the land surface only. During the summer simulation period, lower temperatures are determined, caused by the general negative RE during that time. On average, a decrease of -0.14 K is found. For the winter time the effect on the 2 m temperature is not as strong as during July 2006, but it is nevertheless distinct (-0.1 K). Additionally, it is obvious that the influence on the 2 m temperature is significant during day-time (average over all 12 UTC model

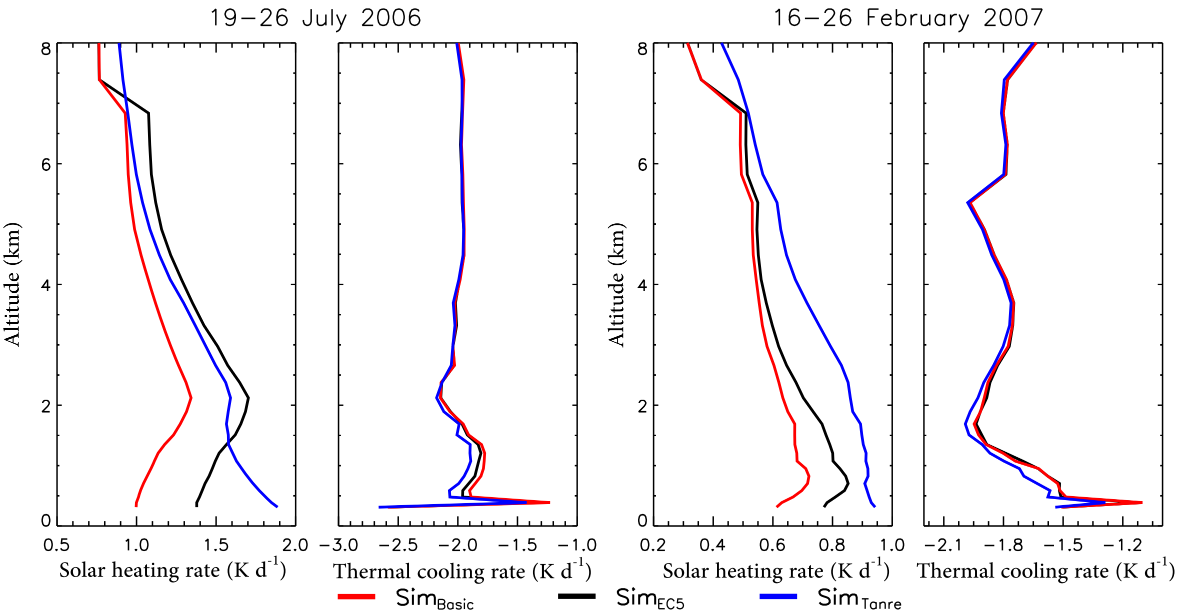

Figure 5.26: Solar heating and thermal cooling rates as averages for the entire simulation periods (19 – 26 July 2006, 16 – 26 February 2007) over land surface and for all kind of cloud fractions within the individual model grid cells. Red line: Sim_{Basic} (also shown in Figure 5.21). Black line: Sim_{EC5}. Blue line: Sim_{Tanre}.

simulations). Here, a cooling by -0.24 K (summer) and -0.25 K (winter) is calculated (Table 5.8). An average cooling of -0.03 K (summer) and of -0.02 K (winter) is found for night-time (average over all 00 UTC model simulations) data, indicating the dominant role of the solar forcing by the aerosols on surface temperatures.

5.3.2 Sensitivity to aerosol properties

In Table 2.1 the model setups, Sim_{EC5} and Sim_{Tanre} are introduced, which are used for sensitivity studies of the radiative effects of the model. In case of Sim_{EC5} the limit to distinguish between "urban" and "continental" aerosol type is set to an EC fraction of 5% on $\mathrm{PM}_{2.5}$ compared to 20% for the Sim_{Basic} setup. Thus, the ratio between "urban" and "continental" aerosol type changes significantly compared to Sim_{Basic} simulations. Now, an average (for the entire simulation periods) mass of $0.33\,\mathrm{g\,m^{-1}}$ is determined for the "continental" aerosol ($\mathrm{Sim}_{Basic} = 3.74\,\mathrm{g\,m^{-1}}$) and of $4.41\,\mathrm{g\,m^{-1}}$ for the "urban" aerosol type ($\mathrm{Sim}_{Basic} = 0.97\,\mathrm{g\,m^{-1}}$) in case of 19 – 26 July 2006. During 16 – 26 February 2007, $0.12\,\mathrm{g\,m^{-1}}$ ($\mathrm{Sim}_{Basic} = 0.79\,\mathrm{g\,m^{-1}}$) and $2.48\,\mathrm{g\,m^{-1}}$ ($\mathrm{Sim}_{Basic} = 1.81\,\mathrm{g\,m^{-1}}$) are calculated for "continental" and "urban" aerosol mass by means of Sim_{EC5}.

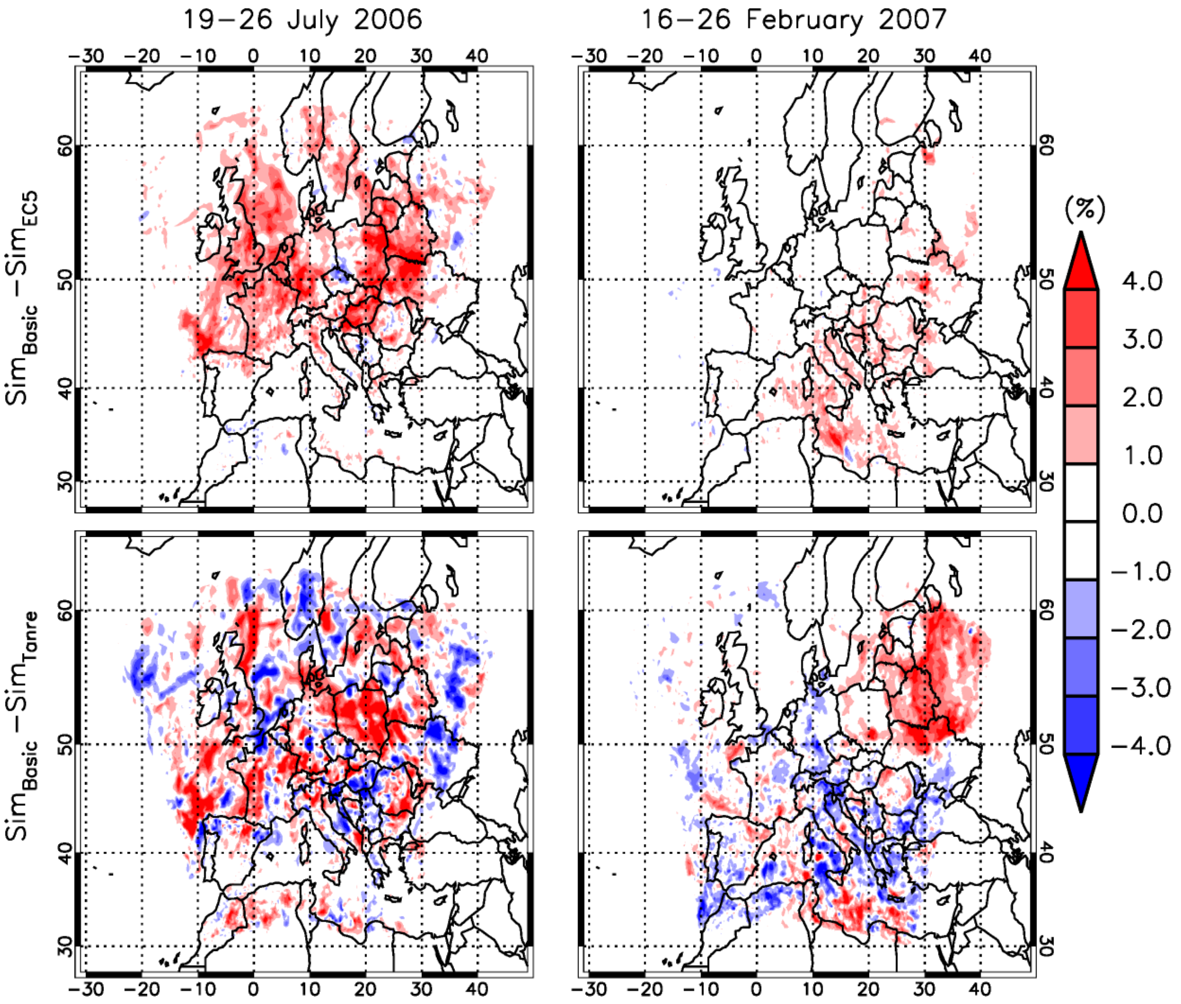

Figure 5.27: Difference of total cloud cover fractions (%) for the entire simulation periods (left panel: 19 – 26 July 2006, right panel: 16 – 26 February 2007). Differences are determined between Sim$_{Basic}$ and Sim$_{EC5}$ (upper panel) as well as between Sim$_{Basic}$ and Sim$_{Tanre}$ (lower panel).

Within the original setup the Tanré scheme (Tanré et al., 1984) is used, with five typical aerosol types (Section 2.3). The description of the optical properties of marine, stratospheric and volcanic aerosol types in the Sim$_{Basic}$ setup is equal to the Tanré scheme. In Sim$_{Basic}$ either "urban" or "continental" aerosol type can exist in the individual model grid cells, whereas by means of the Tanré scheme both types can coexist. Additionally, the mass of "urban" and "continental" aerosol type is calculated within MUSCAT and transferred to the radiation scheme of COSMO. In case of the Tanré scheme a climatological map, which includes the optical properties for the individual aerosol types, is used, that is constant in time. A comparison between Sim$_{Basic}$ and Sim$_{Tanre}$ shall identify the difference between both model setups.

Due to the different amount of "urban" and "continental" aerosol type computed by Sim$_{Basic}$ and Sim$_{EC5}$ as well as the usage of climatological information regarding the distribution of "urban" and "continental" aerosol (Sim$_{Tanre}$) feedback processes and therefore radiation fluxes and dynamical processes between the individual model setups are expected to differ. The influence, caused by the computed aerosol on solar and thermal heating rates, is presented in Figure 5.26. Because of the different number of cloud-free grid cells between the individual model setups, all vertical profiles, located over land surface, are used, independent of the cloud cover fraction. 6083 profiles are found over land surface for both simulation periods to determine average solar and thermal heating rates. Results of Sim$_{Basic}$ simulations are also presented before in Figure 5.21 as continuous red lines. Additionally, differences between Sim$_{Basic}$ and Sim$_{EC5}$ as well as between Sim$_{Basic}$ and Sim$_{Tanre}$ regarding their simulated total cloud cover fraction and 2 m temperature are shown in Figure 5.27 and Figure 5.28. In Table 5.12, the differences of the total cloud cover fraction, the 2 m temperature, the solar and thermal flux near the surface and at TOA are summarized for both simulation periods.

Comparison between Sim$_{Basic}$ and Sim$_{EC5}$

Distinct larger solar heating rates are computed by Sim$_{EC5}$ (black line) compared to Sim$_{Basic}$ (red line) for both time periods (Figure 5.26). During the summer period, and between surface and 1.3 km, the Sim$_{EC5}$ and Sim$_{Basic}$ simulations produce lower solar heating rates than Sim$_{Tanre}$. Above 1.3 km, solar heating rates computed by Sim$_{EC5}$ are highest. Such a behavior is not found during the winter simulation period (Figure 5.26). Due to the different distribution of "urban" and "continental" aerosol, which is computed by Sim$_{EC5}$ and Sim$_{Basic}$, the general larger solar heating rates can be explained. On average (entire simulation period and considering the entire vertical column), the mass of "urban" aerosol is computed to be 4.41 μg m^{-1} during July 2006 and 2.48 μg m^{-1} during February 2007 by Sim$_{EC5}$. This is significantly larger than the results based on Sim$_{Basic}$ simulations ("urban" mass: summer: 0.97 μg m^{-1}, winter: 1.81 μg m^{-1}). Due to the higher amount of average "urban" aerosol type the absorption of solar radiation increases and leads to a higher average solar heating rate compared to Sim$_{Basic}$. The solar heating rate, computed by Sim$_{EC5}$ between surface and 2.0 km, is up to 0.38 K d^{-1} larger then computed by Sim$_{Basic}$ during the summer period. Above this height, the discrepancy between both model results decrease with increasing height. During February 2007, the differences between Sim$_{Basic}$ and Sim$_{EC5}$ are smaller compared to the summer case. On average, a discrepancy of -0.07 K d^{-1} is found with its largest difference of -0.16 K d^{-1} near the surface. Smaller differences

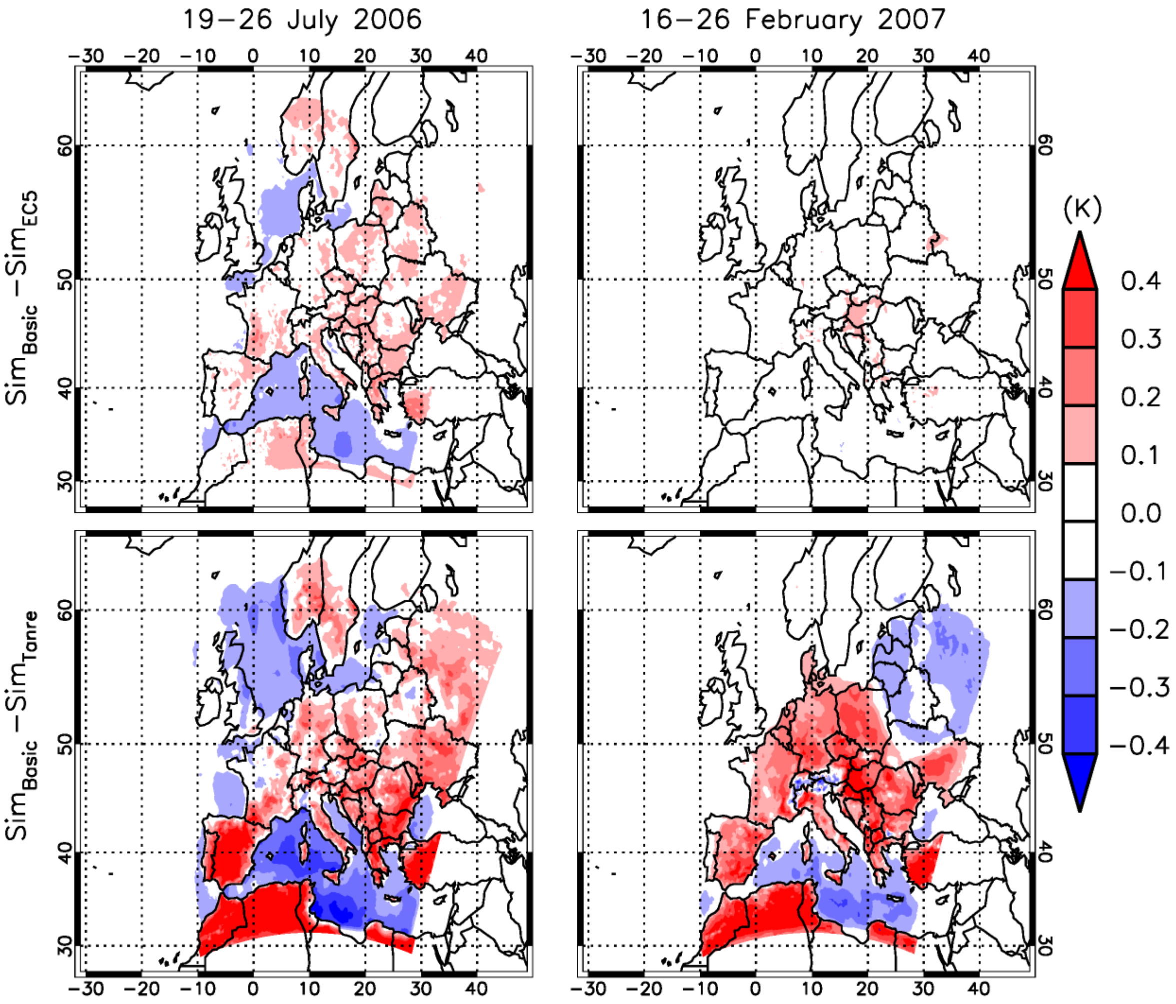

Figure 5.28: Difference of 2 m temperature (K) for the entire simulation periods (left panel: 19 – 26 July 2006; right panel: 16 – 26 February 2007). Differences are determined between Sim_{Basic} and Sim_{EC5} (upper panel) as well as between Sim_{Basic} and Sim_{Tanre} (lower panel).

between Sim_{Basic} and Sim_{EC5} during the winter case (in contrast to the summer case) are due to the higher cloud cover in the winter and lower AODs.

In case of the thermal cooling rate, which is also shown in Figure 5.26, often higher thermal cooling rates are computed for the summer time period by means of Sim_{Basic}. Throughout the entire profile an average difference of 0.02 K d^{-1} is determined between Sim_{Basic} and Sim_{EC5}) during July 2006. In case of the winter simulation period, the differences are low and an average of 0.00 K d^{-1} between Sim_{Basic} and Sim_{EC5} is found. Thermal cooling rates from -1.9 K d^{-1} to -1.8 K d^{-1} (Sim_{Basic}) and from -2.0 K d^{-1} to -1.8 K d^{-1} (Sim_{EC5}) are determined.

The higher fraction of absorbing aerosol and the distinct increase of the solar heating rate, simulated by Sim_{EC5}, leads to a stronger decrease of the total cloud cover fraction compared to Sim_{Basic} (Figure 5.27, Table 5.12). During summer an average difference in cloud cover between Sim_{Basic} and Sim_{EC5} of 0.8% and during winter of 0.4% is found. The existence of more absorbing aerosol, when performing simulations with the Sim_{EC5} model setup, causes the computation of less solar flux at the surface compared to Sim_{Basic} even with the lower cloud cover (Table 5.22). During the summer period, this effect is very distinct with average differences of $7.4\,\mathrm{W\,m^{-2}}$ for the entire period and with $15.4\,\mathrm{W\,m^{-2}}$ when taking only 12 UTC values into account. During the winter period, these values decrease but also represent the decrease of the solar flux at the surface by means ob Sim_{EC5}. Due to the simulation of generally lower total cloud cover fractions by means of Sim_{EC5} and the stronger aerosol absorption, the solar flux at TOA is more positive, compared to Sim_{Basic} simulations. On average, the solar flux at the TOA, computed by Sim_{EC5}, is higher during both summer and winter period (Table 5.12). The differences between Sim_{Basic} and Sim_{EC5} increase when using 12 UTC values only. The lower solar flux, reaching the surface, results in the computation of general lower 2 m temperatures by Sim_{EC5}, compared to Sim_{Basic} (Figure 5.28, upper panel). As presented before, the effect is stronger during summer than during winter. For the entire simulation periods, average discrepancies of 0.09 K (summer) and 0.03 K (winter) are found. These data decrease in case of 00 UTC values and increase when taking 12 UTC values into account (Table 5.12). A lower solar flux reaches the surface when performing the simulations with the Sim_{EC5} model setup, thus, a general lower value of the thermal flux near the surface and at TOA is determined during both time periods (Table 5.12).

Comparison between Sim_{Basic} and Sim_{Tanre}

Higher solar heating rates are computed by Sim_{Tanre} (blue line), compared to Sim_{Basic} and Sim_{EC5}, for both time periods (Figure 5.26). As mentioned before, higher average solar heating rates are determined by Sim_{Tanre} between surface and 1.3 km than for the other ones. Above 1.3 km, solar heating rates, computed by Sim_{Tanre}, are now lower than based on Sim_{EC5} and nevertheless distinct larger compared to Sim_{Basic}. Near the surface, a solar heating rate of $1.9\,\mathrm{K\,d^{-1}}$ is determined by Sim_{Tanre}. During February 2007, the average solar heating rate is always higher than the other ones when using data from Sim_{Tanre} simulations with a maximum value of $0.9\,\mathrm{K\,d^{-1}}$ also near the surface. Whereas Sim_{Basic} and Sim_{EC5} represent a very similar vertical profile of the solar heating rate, the profile, simulated by the Sim_{Tanre} model setup, differs significantly for both simulation periods. These results represent clearly the very different description of the aerosol distribution of the “urban” and “continental” aerosol type by the Tanré

Table 5.12: Differences, calculated between different model setups (Sim$_{Basic}$ - Sim$_{EC5}$ and Sim$_{Basic}$ - Sim$_{Tanre}$), regarding the total cloud cover, 2 m temperature, solar flux (surface and TOA) and thermal flux (surface and TOA) for the two simulation periods. The values are averages for the periods of time and refer to the entire model domain (sea and land surfaces). In case of the 2 m temperature, the values are given for land surface only.

19 – 26 July 2006

Parameter	Period of time	Sim$_{Basic}$ - Sim$_{EC5}$	Sim$_{Basic}$ - Sim$_{Tanre}$
Total cloud cover (%)	entire	0.8	0.5
	00 UTC	0.8	-0.1
	12 UTC	1.2	0.6
2 m temperature (K)	entire	0.09	0.29
	00 UTC	0.04	0.05
	12 UTC	0.12	0.15
Solar flux (surface) (W m^{-2})	entire	7.4	19.1
	12 UTC	15.4	43.6
Solar flux (TOA) (W m^{-2})	entire	-7.7	3.9
	12 UTC	-17.2	8.3
Thermal flux (surface) (W m^{-2})	entire	0.5	-2.7
	00 UTC	0.6	-2.5
	12 UTC	0.6	-3.6
Thermal flux (TOA) (W m^{-2})	entire	0.5	-1.0
	00 UTC	0.4	-0.8
	12 UTC	0.7	-1.5

16 – 26 February 2007

Parameter	Period of time	Sim$_{Basic}$ - Sim$_{EC5}$	Sim$_{Basic}$ - Sim$_{Tanre}$
Total cloud cover (%)	entire	0.4	0.2
	00 UTC	0.3	-0.2
	12 UTC	0.6	0.3
2 m temperature (K)	entire	0.03	0.24
	00 UTC	0.02	0.06
	12 UTC	0.05	0.60
Solar flux (surface) (W m^{-2})	entire	1.1	10.0
	12 UTC	3.2	32.8
Solar flux (TOA) (W m^{-2})	entire	-1.8	0.6
	12 UTC	-6.2	1.8
Thermal flux (surface) (W m^{-2})	entire	0.3	-2.2
	00 UTC	0.3	-2.0
	12 UTC	0.5	-3.0
Thermal flux (TOA) (W m^{-2})	entire	0.1	-0.9
	00 UTC	0.1	-0.8
	12 UTC	0.2	-1.3

scheme (Tanré et al., 1984), compared to the results computed by Sim$_{Basic}$ and Sim$_{EC5}$. For the Sim$_{Basic}$ model setup, an average difference (Sim$_{Basic}$ - Sim$_{Tanre}$) of 0.06 K d^{-1} (summer) and of 0.04 K d^{-1} (winter) is calculated for thermal cooling rates. But in general, Sim$_{Tanre}$ often leads to lower thermal cooling rates, compared to the other three model setups.

Due to the differences of the magnitude of the heating rate, differences concerning the atmospheric dynamics have to be expected as well. Simulations, performed by means of Sim$_{Tanre}$, lead to a general lower total cloud cover fraction compared with Sim$_{Basic}$ (Figure 5.27, lower panel). On average, this discrepancy is not as distinct as between Sim$_{Basic}$ and Sim$_{EC5}$ but in contrast to the other comparisons, negative differences are determined now for night-time data. Here, values of -0.1% (summer) and of -0.2% (winter) indicate that Sim$_{Tanre}$ computes higher total cloud cover fraction during the night in contrast to Sim$_{Basic}$ (Table 5.12). The higher nightly total cloud cover results in a lower 2 m temperature difference when taking 00 UTC values into account. During July 2006, a difference of 0.05 K is determined and during February 2007, the difference is slightly larger (0.06 K). The differences increase in case of the 12 UTC values and in case of the entire period (Table 5.12). The differences in total cloud cover fraction, compared with Sim$_{Basic}$ are relatively low, but significant differences occur related to the solar flux near the surface for both periods due to higher AODs implemented in the Sim$_{Tanre}$ model setup. The Sim$_{Tanre}$ model setup determines solar fluxes which are on average lower by 19.1 W m^{-2} (entire period) and 43.6 W m^{-2} (12 UTC) during July 2006 and by 10.0 W m^{-2} (entire period) and 32.8 W m^{-2} (12 UTC) during February 2007. For the entire simulation periods, an average difference of -1.0 W m^{-2} (summer) and of -0.9 W m^{-2} (winter), compared with Sim$_{Basic}$, is determined (Table 5.12). A distinct contrast to the other comparisons is the tendency of Sim$_{Tanre}$ to simulate lower solar fluxes at the TOA compared to Sim$_{Basic}$. This effect is lower during February 2007 (0.6 W m^{-2}) than during July 2006 (3.9 W m^{-2}).

It is shown, that discrepancies between the individual model setups Sim$_{Basic}$, Sim$_{EC5}$ and Sim$_{Tanre}$ occur, whereas Sim$_{EC5}$ computes a higher fraction of “urban” and therefore of absorbing aerosol than the other ones. Thus, comparisons between Sim$_{Basic}$ and Sim$_{EC5}$ point to the differences which occur when the absorbing properties of the aerosol change, indicated by higher “urban” aerosol concentration in the atmosphere. The comparison with the standard model setup, which is described by the Tanré scheme (Tanré et al., 1984), and Sim$_{Basic}$ also represents distinct discrepancies, caused by the different aerosol distributions.

5.3.3 Conclusion

Model calculations for the summer (19 – 26 July 2006) and winter time period (16 – 26 February 2007) are used to study the radiative forcing which is caused by the existence of the absorbing aerosol within Europe. It is shown that absorbing aerosol influences the solar heating rates, mainly within the PBL. Additionally, the DRF determined at TOA strongly depends on the AOD, on the surface albedo as well as on the cloud cover. A cloud cover decrease (summer: 1.0%, winter: 0.7%) is found, caused by the heating effect of the absorbing aerosol. A lower total cloud cover fraction is the reason for the increase of the solar flux at the surface and the TOA. The absorbing aerosol SRE leads to an increase of the solar flux at the surface whereas the DRF results in a decrease. Determination of the SRE is limited when using models with a coarse resolution as mentioned by Johnson et al. (2004). To obtain details on the SRE, a higher spatial model resolution is required.

Due to the occurrence of the absorbing aerosol and its reduction effect in case of the cloud cover, a decrease of the 2 m temperature is computed by COSMO – MUSCAT. During day-time, a decrease of -0.24 K is determined for the summer and of -0.25 K for the winter period. When using the lower EC limit to distinguish between more absorbing “urban” and less absorbing “continental” aerosol as done by Sim_{EC5}, a further reduction of cloud cover will lead to a higher SRE. Therefore, the results based on model setup with the higher EC limit (20% in case of Sim_{Basic}) represent the lower limit of SRE values.

Comparison of Sim_{Basic} results and those of the original radiation scheme (Sim_{Tanre}) shows significant differences due to the different AOD distributions. Higher solar heating rates are simulated for summer and winter by Sim_{Tanre} than by Sim_{Basic}. Whereas on average lower cloud cover is computed by Sim_{Tanre} during day-time, a higher cloud cover is found during the night which is reflected by the differences in 2 m temperatures.

The indirect effect of the aerosol particles on microphysical cloud properties is not studied here. Further, the results presented here are only meaningful for the two short simulation periods in the frame of this work. Thus, model simulations of longer time periods are necessary to ensure the relevance of these results.

5.4 Sensitivity of model results to grid size and simulation time

Table 5.13: Minimum, maximum and average values of EC, $PM_{2.5}$, “urban” and “continental” aerosol mass for the entire model domain for the summer and winter simulation periods within the near surface model layer.

19 – 26 July 2006				
		Sim_{Basic}	Sim_{long}	Sim_{14km}
EC	Minimum	$4.0\,\mathrm{x}\,10^{-7}$	$4.0\,\mathrm{x}\,10^{-7}$	$3.3\,\mathrm{x}\,10^{-7}$
$(\mathrm{g\,m^{-3}})$	Maximum	$5.2\,\mathrm{x}\,10^{-6}$	$5.0\,\mathrm{x}\,10^{-6}$	$6.7\,\mathrm{x}\,10^{-6}$
	Average	$9.4\,\mathrm{x}\,10^{-7}$	$9.4\,\mathrm{x}\,10^{-7}$	$9.0\,\mathrm{x}\,10^{-7}$
$PM_{2.5}$	Minimum	$2.0\,\mathrm{x}\,10^{-6}$	$2.0\,\mathrm{x}\,10^{-6}$	$2.0\,\mathrm{x}\,10^{-6}$
$(\mathrm{g\,m^{-3}})$	Maximum	$2.6\,\mathrm{x}\,10^{-5}$	$2.9\,\mathrm{x}\,10^{-5}$	$3.1\,\mathrm{x}\,10^{-5}$
	Average	$7.1\,\mathrm{x}\,10^{-6}$	$7.2\,\mathrm{x}\,10^{-6}$	$6.7\,\mathrm{x}\,10^{-6}$
“urban”	Minimum	0.0	0.0	0.0
mass	Maximum	$1.0\,\mathrm{x}\,10^{-3}$	$9.7\,\mathrm{x}\,10^{-4}$	$1.4\,\mathrm{x}\,10^{-3}$
$(\mathrm{g\,m^{-2}})$	Average	$1.1\,\mathrm{x}\,10^{-4}$	$1.0\,\mathrm{x}\,10^{-4}$	$1.1\,\mathrm{x}\,10^{-4}$
“continental”	Minimum	0.0	0.0	0.0
mass	Maximum	$1.7\,\mathrm{x}\,10^{-3}$	$1.9\,\mathrm{x}\,10^{-3}$	$2.0\,\mathrm{x}\,10^{-3}$
$(\mathrm{g\,m^{-2}})$	Average	$4.0\,\mathrm{x}\,10^{-4}$	$3.7\,\mathrm{x}\,10^{-4}$	$3.4\,\mathrm{x}\,10^{-4}$
16 – 26 February 2007				
		Sim_{Basic}	Sim_{long}	Sim_{14km}
EC	Minimum	$1.9\,\mathrm{x}\,10^{-7}$	$1.8\,\mathrm{x}\,10^{-7}$	$1.3\,\mathrm{x}\,10^{-7}$
$(\mathrm{g\,m^{-3}})$	Maximum	$9.1\,\mathrm{x}\,10^{-6}$	$8.9\,\mathrm{x}\,10^{-6}$	$1.1\,\mathrm{x}\,10^{-5}$
	Average	$1.2\,\mathrm{x}\,10^{-6}$	$1.1\,\mathrm{x}\,10^{-6}$	$1.0\,\mathrm{x}\,10^{-6}$
$PM_{2.5}$	Minimum	$1.3\,\mathrm{x}\,10^{-6}$	$1.3\,\mathrm{x}\,10^{-6}$	$7.2\,\mathrm{x}\,10^{-7}$
$(\mathrm{g\,m^{-3}})$	Maximum	$4.9\,\mathrm{x}\,10^{-5}$	$5.0\,\mathrm{x}\,10^{-5}$	$6.6\,\mathrm{x}\,10^{-5}$
	Average	$6.2\,\mathrm{x}\,10^{-6}$	$6.3\,\mathrm{x}\,10^{-6}$	$5.5\,\mathrm{x}\,10^{-6}$
“urban”	Minimum	0.0	0.0	0.0
mass	Maximum	$2.0\,\mathrm{x}\,10^{-3}$	$2.0\,\mathrm{x}\,10^{-3}$	$2.5\,\mathrm{x}\,10^{-3}$
$(\mathrm{g\,m^{-2}})$	Average	$1.7\,\mathrm{x}\,10^{-4}$	$1.5\,\mathrm{x}\,10^{-4}$	$1.6\,\mathrm{x}\,10^{-4}$
“continental”	Minimum	0.0	0.0	0.0
mass	Maximum	$3.3\,\mathrm{x}\,10^{-3}$	$3.3\,\mathrm{x}\,10^{-3}$	$4.4\,\mathrm{x}\,10^{-3}$
$(\mathrm{g\,m^{-2}})$	Average	$1.8\,\mathrm{x}\,10^{-4}$	$2.5\,\mathrm{x}\,10^{-4}$	$2.1\,\mathrm{x}\,10^{-4}$

In this study, model simulations, performed with the Sim_{Basic} model setup, represent a new description of the determination of $PM_{2.5}$, the hygroscopic growth of certain substances, which was not described before within this regional model, and the computation of the radiative effects, which differs from the original setup of the Tanré scheme (Tanré et al., 1984). Different variations of this basic model setup are introduced within Table 2.1. Concerning the Sim_{dry} model setup, comparisons with observation data and the basic model setup Sim_{Basic} are shown in Section 5.2.3. Here, the influence of the hygroscopic growth, which is implemented in the model, is analyzed. Additionally, the different methods to determine "urban" and "continental" aerosol types by means of the EC fraction of $PM_{2.5}$ are also studied, comparing results, computed by Sim_{Basic} and Sim_{EC5} (Section 5.3.2). In case of the radiative effect, the discrepancies, which occur when using a new description as done with Sim_{Basic} and the original setup described by Tanré (Tanré et al., 1984), are also presented here (Section 5.3.2).

In addition to the sensitivity studies described above, the role of the restart conditions (Page 19), especially for relatively short time periods (summer: 8 days, winter: 11 days), must be discussed. Therefore, model calculations without the short restart cycle (Sim_{long}; Table 2.1) are performed as well. Here, COSMO is started on 18 July 2006 and 15 February 2007, respectively, and performs the calculations alone for 24 hours. Afterwards MUSCAT is started and both models run in parallel until the end of the individual simulation periods without restart. The restart conditions tie the modeled meteorological fields to observations. Thus, comparisons between Sim_{Basic} and Sim_{long} can give information regarding the stability of the meteorological fields in case of such relatively short time periods.

Performances of model simulations with a relatively low horizontal resolution are quite fast but certain features are insufficiently resolved. Simulations are performed with a horizontal resolution of 28 km x 28 km lead to satisfying results (Sim_{Basic}). Model computations with a higher horizontal resolution of 14 km x 14 km are performed as well to analyze whether improvements are found for comparison with surface observations (e.g., $PM_{2.5}$, EC and SO_4^{2-}), AOD or vertical backscatter profiles.

Table 5.13 summarizes the information about the minimum, maximum and average values of computed EC, $PM_{2.5}$, "urban" and "continental" aerosol within the near surface model layer for the entire summer and winter simulation periods. The values refer to the simulation results based on Sim_{Basic}, Sim_{long} and Sim_{14km}. In case of EC, Sim_{Basic} and Sim_{long} often lead to similar minimum and maximum values (for both time periods), whereas in case of Sim_{14km}, these values are distinct lower (in case of EC minimum) or higher (in case of EC maximum) compared to the other model setups. Local EC emissions likely cause these distinct differences, which are different due to the different horizontal resolution, while $PM_{2.5}$ emissions are variable in the model emissions. For the average EC values all three model setups are very similar for the summer as well as for the winter period (Table 5.13). The minimum $PM_{2.5}$ concentrations are equal for the summer period ($2.0 \times 10^{-6}\,g\,m^{-3}$) for all three model setups and only small differences are determined in case of the maximum and average $PM_{2.5}$ values. During winter, differences between the individual model computations are slightly larger, whereas Sim_{14km} results are often clearly different from the other

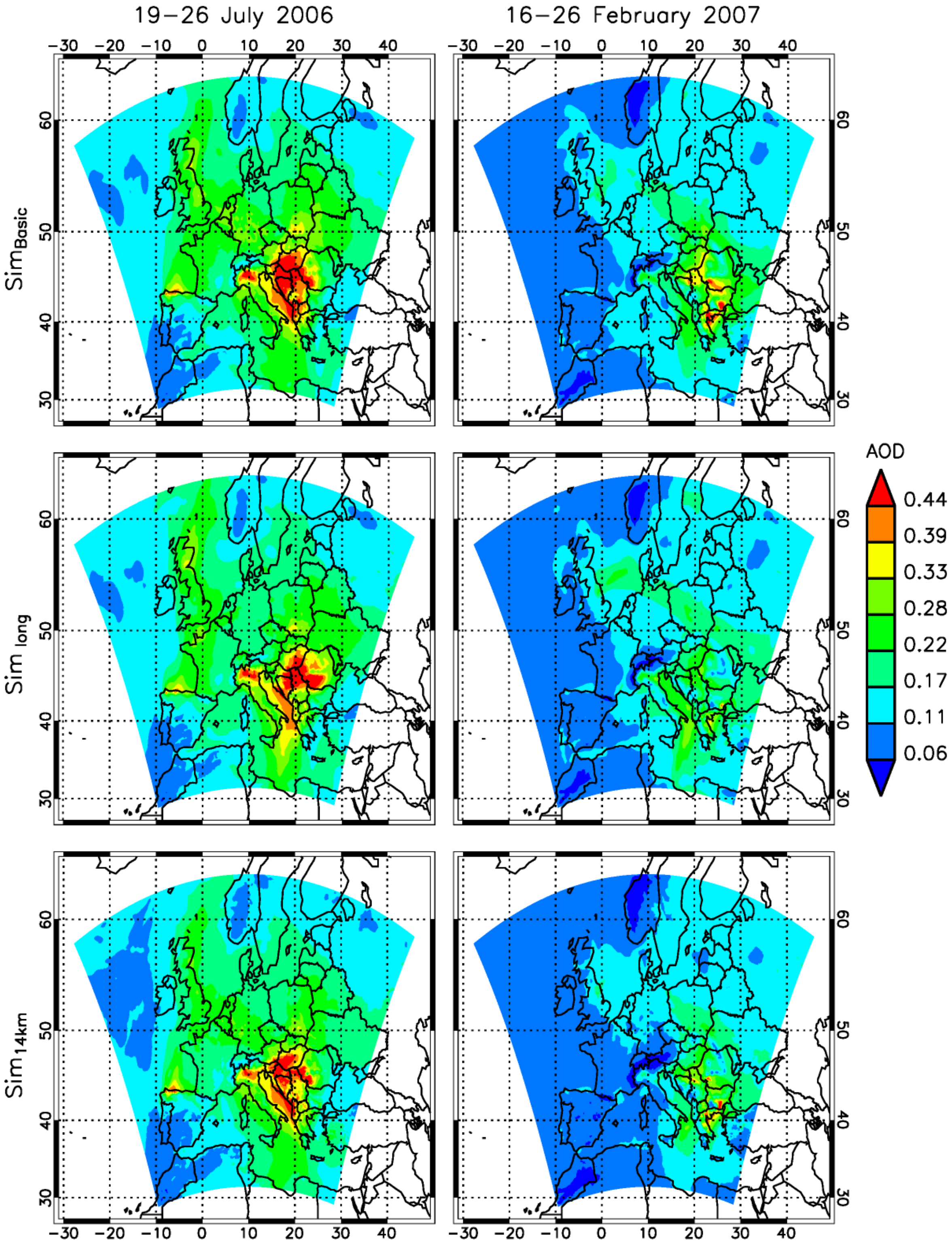

Figure 5.29: Maps of AOD, representing the average distribution based on Sim$_{Basic}$ (upper panel), Sim$_{long}$ (middle panel) and Sim$_{14km}$ (lower panel) simulations for the summer (left panel) and winter period (right panel).

Table 5.14: Minimum (τ_{min}), maximum (τ_{max}) and average (τ_{mean}) AODs, based on simulations performed by Sim$_{Basic}$, Sim$_{long}$ and Sim$_{14km}$ for 19 – 26 July 2006 and 16 – 26 February 2007.

		Sim$_{Basic}$			Sim$_{long}$			Sim$_{14km}$		
		τ_{min}	τ_{max}	τ_{mean}	τ_{min}	τ_{max}	τ_{mean}	τ_{min}	τ_{max}	τ_{mean}
July 2006	19	0.04	0.36	0.11	0.04	0.36	0.11	0.04	0.43	0.11
	20	0.06	0.92	0.15	0.06	1.1	0.16	0.06	2.2	0.14
	21	0.07	0.93	0.18	0.07	1.0	0.18	0.05	1.2	0.17
	22	0.02	0.89	0.20	0.02	0.76	0.20	0.02	0.77	0.19
	23	0.05	1.2	0.21	0.05	0.98	0.20	0.03	1.08	0.19
	24	0.04	1.48	0.21	0.05	2.22	0.21	0.03	1.96	0.20
	25	0.03	1.60	0.23	0.04	2.07	0.23	0.02	1.37	0.22
	26	0.04	1.74	0.25	0.04	2.02	0.24	0.04	2.02	0.23
	19 – 26	0.05	0.63	0.19	0.05	1.10	0.19	0.05	0.96	0.18
February 2007	16	0.03	0.76	0.10	0.03	0.76	0.10	0.02	1.51	0.09
	17	0.01	0.61	0.13	0.01	0.64	0.13	0.01	0.76	0.11
	18	0.02	0.61	0.13	0.00	0.60	0.12	0.01	0.72	0.11
	19	0.02	1.28	0.14	0.02	0.49	0.12	0.02	1.63	0.12
	20	0.01	1.31	0.15	0.01	0.80	0.13	0.01	1.74	0.12
	21	0.01	1.41	0.14	0.02	0.86	0.13	0.01	1.57	0.12
	22	0.02	2.23	0.15	0.02	1.29	0.14	0.01	1.69	0.13
	23	0.01	1.38	0.15	0.02	0.89	0.15	0.01	1.15	0.14
	24	0.02	1.05	0.15	0.03	1.09	0.16	0.02	0.89	0.13
	25	0.02	0.60	0.14	0.02	0.77	0.14	0.01	0.71	0.12
	26	0.02	0.54	0.13	0.01	0.45	0.12	0.01	0.73	0.11
	16 – 26	0.04	0.81	0.14	0.04	0.53	0.13	0.03	1.00	0.12

results (Table 5.13). All three model setups are equal in the description of the vertical distribution of chemical compounds, which influences the transport from outside into the model domain. Nevertheless, discrepancies occur when performing simulations without daily restart (Sim$_{long}$) or with a higher horizontal resolution (Sim$_{14km}$) compared to Sim$_{Basic}$.

The discrepancies between the model results in case of the computation of the "urban" and "continental" aerosol types are not very large. The separation of the "urban" aerosol from the "continental" aerosol by means of an EC fraction of 20% (Section 2.3) is the same for Sim$_{Basic}$, Sim$_{long}$ and Sim$_{14km}$. Lowest average "urban" aerosol mass (summer: $1.0\,\mathrm{x}\,10^{-4}\,\mathrm{g\,m^{-2}}$, winter: $1.5\,\mathrm{x}\,10^{-4}\,\mathrm{g\,m^{-2}}$) is computed by the Sim$_{long}$ setup compared to Sim$_{Basic}$ and Sim$_{14km}$ for July 2006 and February 2007. But discrepancies between the three model results remain small. During February 2007, the differences between Sim$_{Basic}$, Sim$_{long}$ and Sim$_{14km}$ are slightly larger than during 19 – 26 July 2006 in case of the average "urban" and "continental" aerosol mass (Table 5.13).

The AOD is calculated based on the computed chemical compounds. As shown in Figure 5.29, the average AOD distribution for all three model setups is very similar for summer and winter period. This is a quite satisfying result showing a specific stability of the model when comparing model results based on daily restart (Sim_{Basic}) and without daily restart (Sim_{long}) or with a higher horizontal resolution (Sim_{14km}). Nevertheless, small differences in case of the AOD pattern are found. For instance, during the summer case, Sim_{Basic} and Sim_{14km} compute AODs larger than 0.22 for the region of Germany, whereas Sim_{long} simulations lead to lower AODs in that region. Differences are also found for the Balkan region (Figure 5.29). Here, the pattern of the AOD distribution differs among all three model setups during summer. For the entire summer simulation period an average AOD of 0.19 is determined for Sim_{Basic} and Sim_{long}. In contrast, Sim_{14km} produces a slightly lower average AOD (0.18) (Table 5.14).

In Figure 5.30 the number-normalized frequency distribution of the simulated AODs is shown. The distributions as well as the average AODs, based on the three model setups, are very similar for both summer and winter period. Differences between the individual model setups in case of the maximum daily AODs are calculated, but minimum and average AODs of the entire simulation period are similar (Table 5.14). For the AOD range of 0.12 – 0.14, the highest fractions of 0.14 and 0.15 are found for Sim_{Basic} and Sim_{long}. In case of Sim_{14km} the AOD range of the highest fraction (0.15) is slightly lower (0.10 – 0.12).

Small discrepancies occur regarding the simulation of the AOD based on Sim_{Basic}, Sim_{long} and Sim_{14km} during February 2007. Due to the precipitation events (Section 4.2), lower AOD values are computed by all three model setups (Figure 5.29). In the Balkan region, distinct differences of the computed horizontal AOD distributions are found. AOD values larger than 0.44 are mainly computed by Sim_{Basic}, whereas those high AODs occur rarely for Sim_{long} and Sim_{14km}. On average, only small differences are found. Largest average AOD (for the entire winter period) is determined for Sim_{Basic} (0.14) and lower average AODs of 0.13 and 0.12 for Sim_{long} and Sim_{14km} (Table 5.14). As for the summer case, often distinct differences are found for the maximum AOD for each day and the entire period but the average values remain quite constant during winter.

The number-normalized frequency distribution of all three model setups is more narrow than during the summer case (Figure 5.30). A higher fraction of 0.27 (AOD range: 0.08 – 0.10) is determined for Sim_{14km} simulations.

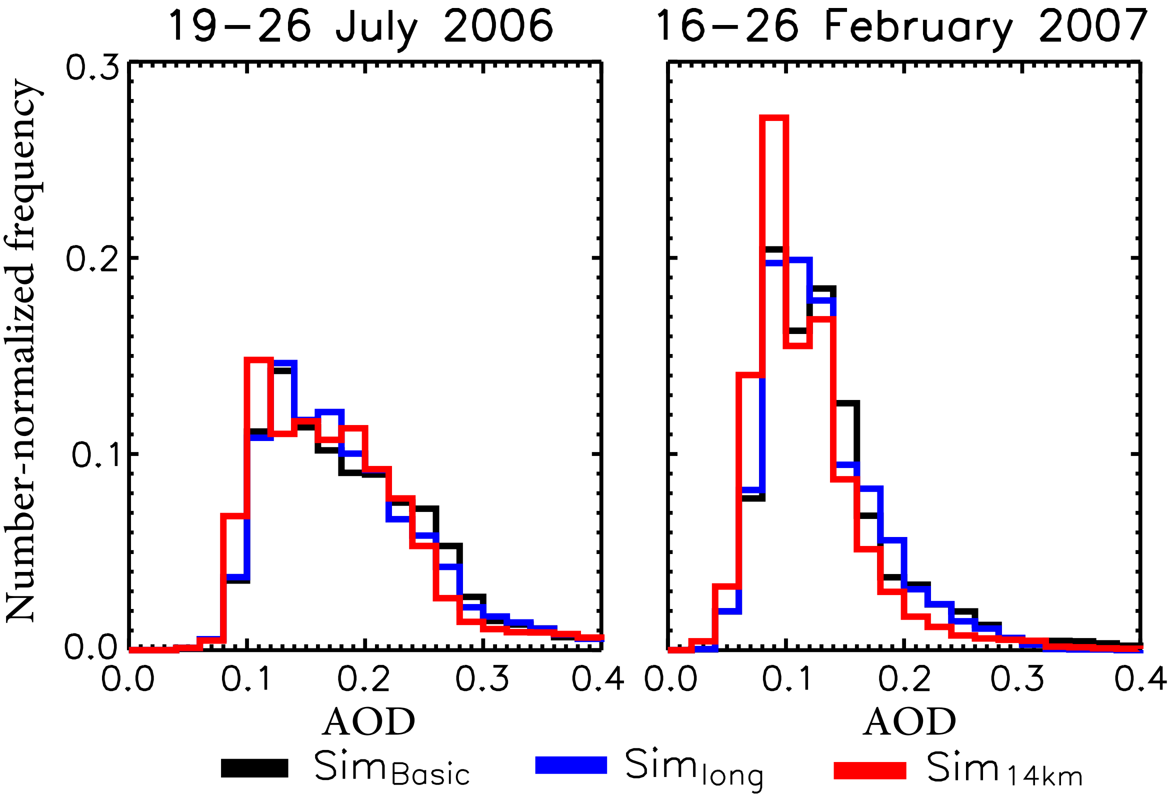

Figure 5.30: Number-normalized frequency distributions of the average AOD representing the entire individual simulation periods and the entire model domain. Blue line: Sim_{Basic}. Green line: Sim_{long}. Red line: Sim_{14km}.

5.4.1 Comparison to observations of vertical backscatter profiles

Vertical backscatter profiles can provide the sensibility regarding certain allocations of the model in different heights (see Section 5.1). The large amount of CALIOP data is therefore used to test the differences in Sim_{Basic}, Sim_{long} and Sim_{14km} setups. In Figure 5.31 average vertical profiles of backscatter coefficients are shown for summer and winter based on data without influence of marine and dust aerosol. The CALIOP profiles are based on $\mathrm{CALIOP}^{data1}_{5km}$ and $\mathrm{CALIOP}^{data4}_{5km}$ data as introduced in Section 3.1.2. Data of $\mathrm{CALIOP}^{data1}_{5km}$ are determined based on loosely restrictions compared to $\mathrm{CALIOP}^{data4}_{5km}$ (see also Figure 3.2). CALIOP backscatter profiles and computed profiles of backscatter values were adjusted for the comparisons (Section 3.1.2). Continuous black lines represent average CALIOP backscatter profiles which refer to a horizontal model grid resolution of 28 km x 28 km which are shown before in Figure 5.3. Thus, this profile is used for comparisons with model results based on Sim_{Basic} (dashed black line; see also Figure 5.3) and Sim_{long} (dashed blue line). Individual CALIOP pro-

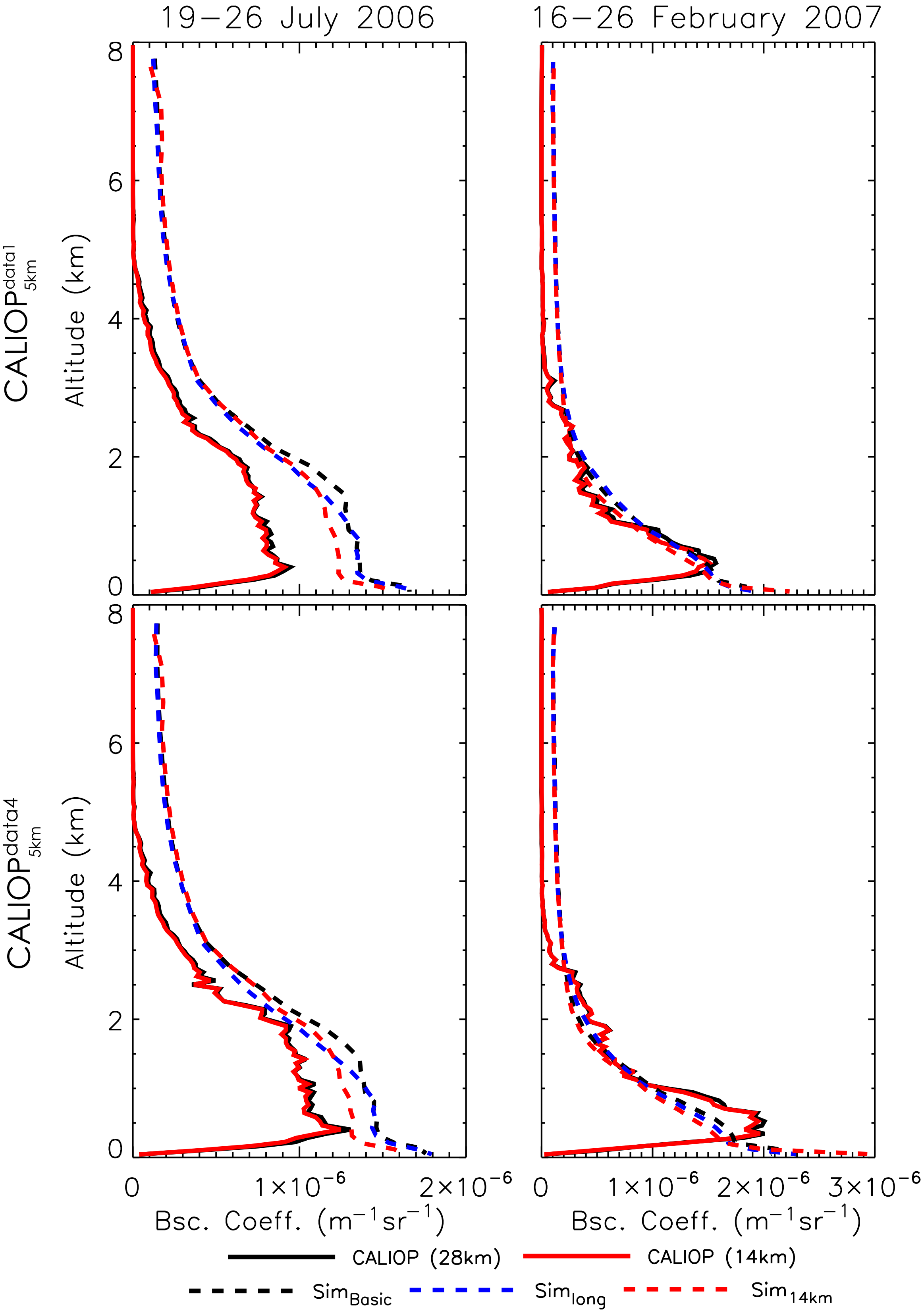

Figure 5.31: Average vertical backscatter profiles without marine and dust influence. Upper panel: CALIOP$^{data1}_{5km}$. Lower panel: CALIOP$^{data4}_{5km}$. Continuous lines: CALIOP backscatter profiles. Dashed lines: Simulated backscatter profiles.

Table 5.15: Values of the absolute (x 10^{-7} m^{-1} sr^{-1}) and relative bias (%), determined for each 500 m height level between surface and 4.5 km altitude for the different data sets without marine and dust aerosol for 19 – 26 July 2006 and 16 – 26 February 2007.

		CALIOP$^{data1}_{5km}$				CALIOP$^{data4}_{5km}$			
		Sim$_{14km}$		Sim$_{long}$		Sim$_{14km}$		Sim$_{long}$	
	Altitude (km)	A$^{md}_{bias}$	R$^{md}_{bias}$	A$^{md}_{bias}$	R$^{md}_{bias}$	A$^{md}_{bias}$	R$^{md}_{bias}$	A$^{md}_{bias}$	R$^{md}_{bias}$
19 – 26 July 2006	0.0 – 0.5	7.2	113	8.1	122	6.2	77	7.3	85
	0.5 – 1.0	4.1	51	5.1	62	2.5	23	3.6	33
	1.0 – 1.5	4.1	55	4.7	62	2.3	24	2.9	29
	1.5 – 2.0	3.5	52	3.1	45	2.0	22	1.2	13
	2.0 – 2.5	2.8	60	2.4	50	1.9	30	1.1	18
	2.5 – 3.0	2.5	90	2.1	70	2.2	61	1.7	43
	3.0 – 3.5	2.3	133	2.0	107	2.2	99	1.8	76
	3.5 – 4.0	2.1	216	1.9	175	2.1	167	1.9	134
	4.0 – 4.5	2.0	398	1.8	294	2.0	322	1.7	235
16 – 26 February 2007	0.0 – 0.5	7.0	72	6.1	60	6.5	51	5.1	39
	0.5 – 1.0	-1.2	-10	-0.9	-7	-4.8	-29	-4.5	-27
	1.0 – 1.5	0.9	17	1.6	27	0.7	-9	-0.2	-3
	1.5 – 2.0	0.3	10	1.2	32	-1.5	-28	-0.5	-10
	2.0 – 2.5	-0.06	-2	0.4	15	-1.3	-33	-0.7	-19
	2.5 – 3.0	0.8	61	0.9	67	0.1	8	0.3	14
	3.0 – 3.5	1.3	296	1.3	262	1.3	281	1.4	283
	3.5 – 4.0	1.4	1050	1.4	905	1.4	1638	1.4	1604
	4.0 – 4.5	1.2	1042	1.2	998	1.3	3656	1.3	4573

files also have to be determined for comparisons with model results based on Sim$_{14km}$ (dashed red line). By means of the algorithm, described in Section 3.1.2 on Page 38, the CALIOP profiles are calculated for a horizontal grid resolution of 14 km x 14 km. Based on these individual backscatter profiles an average CALIOP profile for this fine model grid resolution is available and shown in Figure 5.31 as continuous red line.

Discrepancies between the average CALIOP profiles determined for model grid resolution of 28 km x 28 km (black line) and of 14 km x 14 km (red line) are negligible. Additionally, the shape of the CALIOP profiles is very similar. On the other hand, differences among the individual average simulated backscatter profiles are distinct for both summer and winter period as well as for both CALIOP data sets shown here (Figure 5.31). All model results are identical regarding the occurrence of the maximum backscatter values near the surface during both periods. Differences mainly occur within the PBL and seem to be more distinct during July 2006 (Figure 5.31, left panel). A maximum difference of 1.4 x 10^{-7} m^{-1} sr^{-1} (at 1.6 km) is determined between Sim$_{Basic}$ and Sim$_{long}$ and of 1.8 x 10^{-7} m^{-1} sr^{-1} (at 0.12 km) between Sim$_{Basic}$ and Sim$_{14km}$ in case of CALIOP$^{data1}_{5km}$. These discrepancies increase for CALIOP$^{data4}_{5km}$ data during summer (Sim$_{Basic}$ - Sim$_{long}$: $\Delta\beta_{max} = 1.7$ x 10^{-7} m^{-1} sr^{-1} at 1.6 km; Sim$_{Basic}$ -

Sim$_{14km}$: $\Delta\beta_{max} = 2.1 \,\mathrm{x}\, 10^{-7}\,\mathrm{m}^{-1}\,\mathrm{sr}^{-1}$ at 0.21 km). During this time period, the average backscatter profile, based on Sim$_{14km}$, leads to generally lower backscatter values compared to the other model results between surface and $\sim$ 1.5 km altitude for CALIOP$^{data1}_{5km}$ and CALIOP$^{data4}_{5km}$. Highest backscatter values are often computed by means of Sim$_{Basic}$ within the PBL. In case of the result, based on Sim$_{long}$, a slightly different evaluation of the PBL height which is lower than for Sim$_{Basic}$ and Sim$_{14km}$ is found. This behavior point towards a different vertical mixing by Sim$_{long}$ compared to Sim$_{Basic}$.
The average profiles of backscatter values based on Sim$_{Basic}$ often lead to higher values compared to Sim$_{long}$ and Sim$_{14km}$ results during February 2007. Here, the vertical profile based on Sim$_{14km}$ contains the lowest backscatter values for CALIOP$^{data1}_{5km}$ and CALIOP$^{data4}_{5km}$ (Figure 5.31, right panel). Between Sim$_{Basic}$ and Sim$_{long}$ maximum differences of $1.5 \,\mathrm{x}\, 10^{-7}\,\mathrm{m}^{-1}\,\mathrm{sr}^{-1}$ (at 0.12 km) in case of CALIOP$^{data1}_{5km}$ and of $2.5 \,\mathrm{x}\, 10^{-7}\,\mathrm{m}^{-1}\,\mathrm{sr}^{-1}$ (at 0.12 km) in case of CALIOP$^{data4}_{5km}$ are calculated. Comparisons between Sim$_{Basic}$ and Sim$_{14km}$ lead to similar maximum backscatter differences of $1.5 \,\mathrm{x}\, 10^{-7}\,\mathrm{m}^{-1}\,\mathrm{sr}^{-1}$ (at 0.56 km) in case of CALIOP$^{data1}_{5km}$ and of $2.0 \,\mathrm{x}\, 10^{-7}\,\mathrm{m}^{-1}\,\mathrm{sr}^{-1}$ (at 0.56 km) in case of CALIOP$^{data4}_{5km}$. The evaluation of a different height of the PBL by means of Sim$_{long}$ compared to Sim$_{Basic}$ and Sim$_{14km}$ is not found for February 2007.

Due to the different compilation of the CALIOP data sets (CALIOP$^{data1}_{5km}$, CALIOP$^{data4}_{5km}$) the agreements between CALIOP profiles and the three computed backscatter profiles leads to different results. In Table 5.15, the absolute and relative biases, calculated between the individual CALIOP data sets and simulation results (Sim$_{long}$ and Sim$_{14km}$), are summarized. The biases, determined between CALIOP$^{data1}_{5km}$ and Sim$_{Basic}$ as well as between CALIOP$^{data4}_{5km}$ and Sim$_{Basic}$ for data without influence of marine and dust aerosol, are presented before in Table 5.2. Between surface and 1.5 km altitude, Sim$_{14km}$ computations lead to better agreements with CALIOP$^{data1}_{5km}$ and CALIOP$^{data1}_{5km}$ compared to Sim$_{long}$ and Sim$_{Basic}$. Above 1.5 km altitude, Sim$_{long}$ results are in a better agreement with observed backscatter values than the other ones. Whereas only overestimations of the experimentally observed values by the various model setups are found during summer, cases of over- and underestimations are determined during winter (Figure 5.31, Table 5.15; see also Table 5.2). Simulation results, performed with a finer horizontal resolution (Sim$_{14km}$), result in better agreements with observed backscatter profiles of CALIOP$^{data1}_{5km}$ between 1.0 km and 3.0 km, whereas worse agreements are determined for comparisons with Sim$_{long}$ data. Comparisons with CALIOP$^{data4}_{5km}$ show better agreements with Sim$_{long}$ and Sim$_{Basic}$ results than with Sim$_{14km}$.
Thus, depending on the simulation period (summer, winter) and the CALIOP data sets (CALIOP$^{data1}_{5km}$, CALIOP$^{data4}_{5km}$), the computed values of Sim$_{Basic}$, Sim$_{long}$ and Sim$_{14km}$

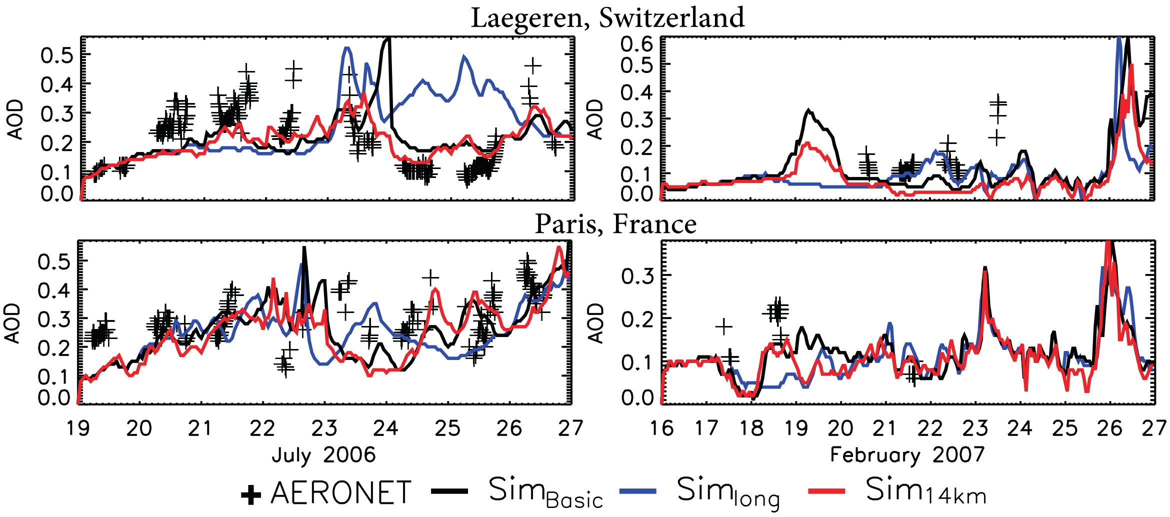

Figure 5.32: Time series of observed (black crosses) and simulated (black line: Sim_{Basic}, blue line: Sim_{long}, red line: Sim_{14km}) AOD during 19 – 26 July 2006 (left panel) and 16 – 26 February 2007 (right panel).

are in a different agreement with the observed values. During summer, the agreement between CALIOP data and Sim_{14km} are in a better agreement compared to the other model setups. Additionally, model results based on Sim_{long} point towards a different description of the vertical mixing within the model during summer. During winter, this behavior was not found, eventually caused by the different meteorological situation. Simulations, performed without daily restart (Sim_{long}) show improvements regarding the representation of experimentally observed backscatter values during February 2007.

5.4.2 Comparison to observations of AOD

In Figure 5.32 the AOD time series at two AERONET stations are shown during 19 – 26 July 2006 and 16 – 26 February 2007, respectively (compare Figure 5.13). In addition to the observed AOD, the simulation results based on Sim_{Basic}, Sim_{long} and Sim_{14km} are presented. In case of the AERONET station in Laegeren (Switzerland) it is shown, that AODs computed by Sim_{14km} in summer are closer to the observed AOD than calculated by Sim_{Basic}. Here, the higher horizontal resolution of the model grid cells improves the agreement between measurement and simulation. It is obvious, that Sim_{long} diverges from the other simulations and from the AERONET data in particular in the summer period. In winter, such deviation can be found in the first simulation week, less obvious later in the simulation period. This shows that the aerosol distribution develops differently and deviates from the observations when no restarts are performed.

For Sim_{Basic} and Sim_{14km}, a mean absolute bias of 0.0 is calculated between simulated and observed AOD (compare Table 5.14), whereas minimum and maximum differences between model setup and AERONET AOD are -0.65 and 0.98 during July 2006. The mean absolute bias, determined for the comparison between observation and Sim_{long} results, is 0.02 (minimum: -0.66, maximum: 0.63) and is therefore not as good as the agreements between AERONET observation and Sim_{Basic} and Sim_{14km} results. During winter time, comparisons between AERONET AOD and AOD computed by Sim_{long} leads to a mean absolute bias of 0.0 and is therefore equal to Sim_{Basic}. A negative mean bias is found for Sim_{14km} ($\text{A}_{bias}^{mean} = \text{-}0.03$). Thus, different results are found during summer and winter simulation period without the possibility to classify a model setup with best descriptions regarding the comparison with AOD observation data.

5.4.3 Comparison to surface concentrations

Due to the simulation of similar $\text{PM}_{2.5}$ and EC concentrations in the atmospheric model layer close to the surface by Sim_{Basic}, Sim_{long} and Sim_{14km}, discrepancies when comparing these results with EMEP (EMEP, 2012) observations are also small. In Figure 5.33, the daily average data of $\text{PM}_{2.5}$ concentrations at five EMEP stations is shown. These data are introduced in Section 5.2.5 in Figures 5.18 – 5.19. In Figure 5.33, open triangles represent results based on EMEP observations and filled triangles results based on Sim_{Basic} (black filled triangles), Sim_{long} (blue filled triangles) and Sim_{14km} (red filled triangles) computations.

Differences between the various model setups of the daily average values are found. In most cases the discrepancies, at the stations shown here, remain small (Figure 5.33). The horizontal resolution of Sim_{14km} is higher compared to Sim_{Basic} but does not lead to better agreements between computed and observed data. Actually, for the data shown in Figure 5.33, results based on Sim_{Basic} are in a better agreement with EMEP than the other model computations during summer. At the station in Iskrba, where all model setups underestimate the observation data, results based on Sim_{14km} are often slightly larger than those of Sim_{Basic} and Sim_{long}. Therefore, agreements between Sim_{14km} and EMEP observation of $\text{PM}_{2.5}$ measurements in Iskrba are better. During February 2007, simulation results based on Sim_{long} lead to better agreements at the EMEP stations shown here, also in Iskrba. It is mentioned in Section 5.2.5, that Illmitz is the lowest point in Austria. Thus, discrepancies between model results and surface observation occur due to the geographical situation. Unfortunately, an improvement is not found

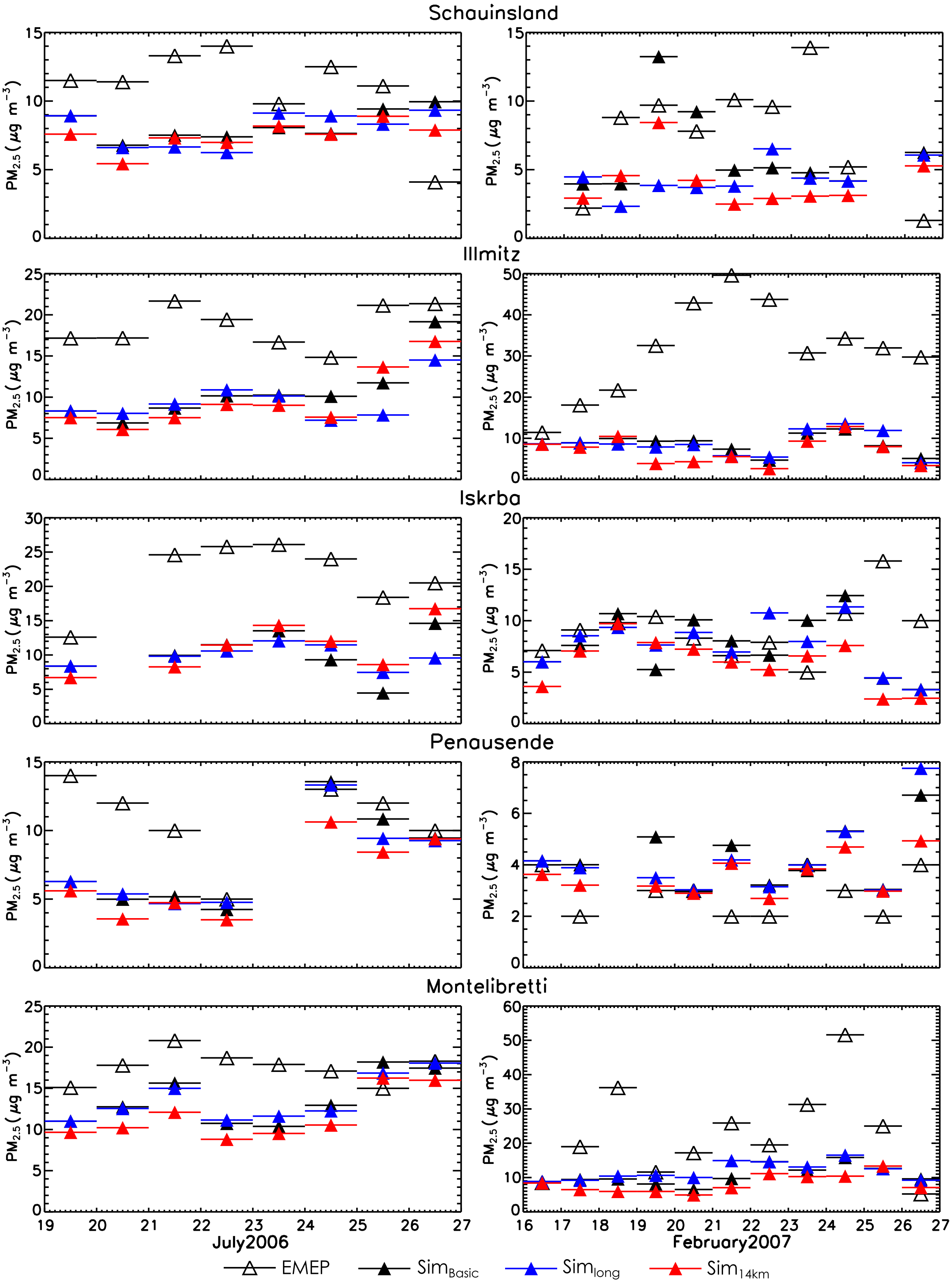

Figure 5.33: Daily average values of observed (black open triangles) and simulated $PM_{2.5}$ (Sim_{Basic}: black filled triangles, Sim_{long}: blue filled triangles, Sim_{14km}: red filled triangles) at five EMEP stations (Schauinsland, Illmitz, Iskrba, Penausende, Montelibretti).

Table 5.16: Minimum, maximum and mean absolute and relative biases for the entire summer and winter period, determined based on EMEP observations and model simulations (Sim_{Basic}, Sim_{long}, Sim_{14km}) of $PM_{2.5}$, EC and SO_4^{2-}.

			19 – 26 July 2006			16 – 26 February 2007		
			Sim_{Basic}	Sim_{long}	Sim_{14km}	Sim_{Basic}	Sim_{long}	Sim_{14km}
$PM_{2.5}$	Absolute bias ($\mathrm{x}\,10^{-6}\mathrm{g\,m^{-3}}$)	Minimum	-34.1	-33.5	-34.1	-75.4	-75.4	-75
		Maximum	5.9	5.3	5.2	5.9	5.0	4.0
		Average	-7.1	-7.1	-7.8	-7.4	-7.7	-8.9
	Relative bias (%)	Minimum	-88	-86	-88	-94	-94	-94
		Maximum	207	207	182	523	565	458
		Average	-41	-40	-46	-7.8	-8.7	-22
EC	Absolute bias ($\mathrm{x}\,10^{-6}\mathrm{g\,m^{-3}}$)	Minimum	-2.1	-2.0	-2.2	-7.5	-7.7	-8.0
		Maximum	1.7	1.7	1.6	1.8	1.8	1.4
		Average	-0.2	-0.2	-0.3	-1.3	-1.4	-1.8
	Relative bias (%)	Minimum	-70	-78	-77	-85	-88	-90
		Maximum	1537	1537	1424	230	230	174
		Average	248	268	183	-20	-25	-43
SO_4^{2-}	Absolute bias ($\mathrm{x}\,10^{-6}\mathrm{g\,m^{-3}}$)	Minimum	-3.1	-1.1	-1.5	-0.9	-0.9	-1.0
		Maximum	7.5	7.1	7.1	5.4	4.2	2.9
		Average	1.2	1.4	1.0	1.0	0.9	0.6
	Relative bias (%)	Minimum	-65	-59	-54	-61	-61	-66
		Maximum	550	511	517	1411	1336	1171
		Average	108	122	85	198	213	146

when using model results with a finer horizontal resolution (Sim_{14km}) for comparisons.

In Table 5.16, the absolute and relative biases, determined between EMEP data (taking all EMEP stations into account) and model results, are summarized. It is shown that simulation results based on Sim_{long} (see also Figure 5.33, blue filled triangles) are quite similar to model results performed with daily restart (Sim_{Basic}) for both summer and winter period. Simulations, performed with a horizontal resolution of 14 km x 14 km (Sim_{14km}) do not lead to a significant improvement of $PM_{2.5}$, EC and SO_4^{2-} computations compared to the other model setups. Nevertheless, results based on Sim_{14km} are often different for summer and winter, as shown in Table 5.16.

The differences between model results and EMEP observations are quite large (Table 5.16). Thus, it is not possible to define the model setup with the best computation results. Better result regarding local effects and emissions may be achieved with a finer grid resolution as with 14 km x 14 km, which remains to be tested.

5.4.4 Radiative and dynamic effects

As summarized in Table 5.13, differences between Sim_{Basic} and Sim_{long} for the "urban" (summer: -0.02 $\mathrm{g\,m^{-1}}$, winter: 0.01 $\mathrm{g\,m^{-1}}$) and "continental" aerosol (summer: -0.05 $\mathrm{g\,m^{-1}}$, winter: -0.02 $\mathrm{g\,m^{-1}}$) mass for both time periods (related to the entire vertical column between surface and 8.0 km altitude) are not very large. Differences between Sim_{Basic} and Sim_{14km} are quite larger for both time periods and aerosol types. A lower average "urban" mass is simulated by Sim_{14km} during July 2006 (0.09 $\mathrm{g\,m^{-1}}$) and during February 2007 (0.303 $\mathrm{g\,m^{-1}}$). For the "continental" aerosol type the average discrepancy between Sim_{Basic} and Sim_{14km} simulation is equal (0.07 $\mathrm{g\,m^{-1}}$) for both time periods. Thus, discrepancies of the computation of radiative and meteorological parameters may occur. Comparisons of radiative and dynamic parameters are also studied based on Sim_{Basic}, Sim_{long} and Sim_{14km} results.

Results of the comparisons between Sim_{Basic} and Sim_{long} as well as between Sim_{Basic} and Sim_{14km} are presented in Figure 5.34 for both time periods. Results for 2 m temperature and total cloud cover are shown as number-normalized frequency distributions based on simulations by Sim_{Basic}, Sim_{long} and Sim_{14km}. 2 m temperature data refer to the land surface. Thus, 6083 data are available for Sim_{Basic} and Sim_{long} and 32709 data for Sim_{14km}. Additional information is summarized in Table 5.17. Here, the differences between Sim_{Basic} and Sim_{long} as well as between Sim_{Basic} and Sim_{14km} are shown for total cloud cover, 2 m temperature and solar flux (surface, TOA). Due to the different horizontal resolution between Sim_{Basic} and Sim_{14km}, Sim_{14km} data are averaged to get the coarser resolution of 28 km x 28 km for comparisons.

The distributions of Sim_{Basic} and Sim_{long} for the summer case seem to be very similar for both 2 m temperature and total cloud cover (Figure 5.34). Simulations based on Sim_{Basic} and Sim_{long} lead to nearly the same minimum (Sim_{Basic}: 283.6 K, Sim_{long}: 284.5 K), maximum (Sim_{Basic}: 313.5 K, Sim_{long}: 313.5 K) and average (Sim_{Basic}: 298.4 K, Sim_{long}: 298.5 K) 2 m temperature for the land surface and the entire summer period. Results based on Sim_{14km} simulations differ regarding the 2 m temperature (T_{min}: 277.9 K, T_{max}: 313.5 K, T_{mean}: 294.5 K). In case of the total cloud cover the number-normalized frequency distributions are very similar for all three model setups, what is also found for the statistical parameters (Sim_{Basic}: $\mathrm{TCC}_{min} = 0.0\%$, $\mathrm{TCC}_{max} = 99.5\%$, $\mathrm{TCC}_{mean} = 34.7\%$; Sim_{long}: $\mathrm{TCC}_{min} = 0.0\%$, $\mathrm{TCC}_{max} = 99.8\%$, $\mathrm{TCC}_{mean} = 32.7\%$; Sim_{14km}: $\mathrm{TCC}_{min} = 0.0\%$, $\mathrm{TCC}_{max} = 99.1\%$, $\mathrm{TCC}_{mean} = 32.3\%$).
Nevertheless, when computing the differences between Sim_{Basic} and Sim_{long} as well as between Sim_{Basic} and Sim_{14km}, distinct differences are found as shown in Table 5.17. In

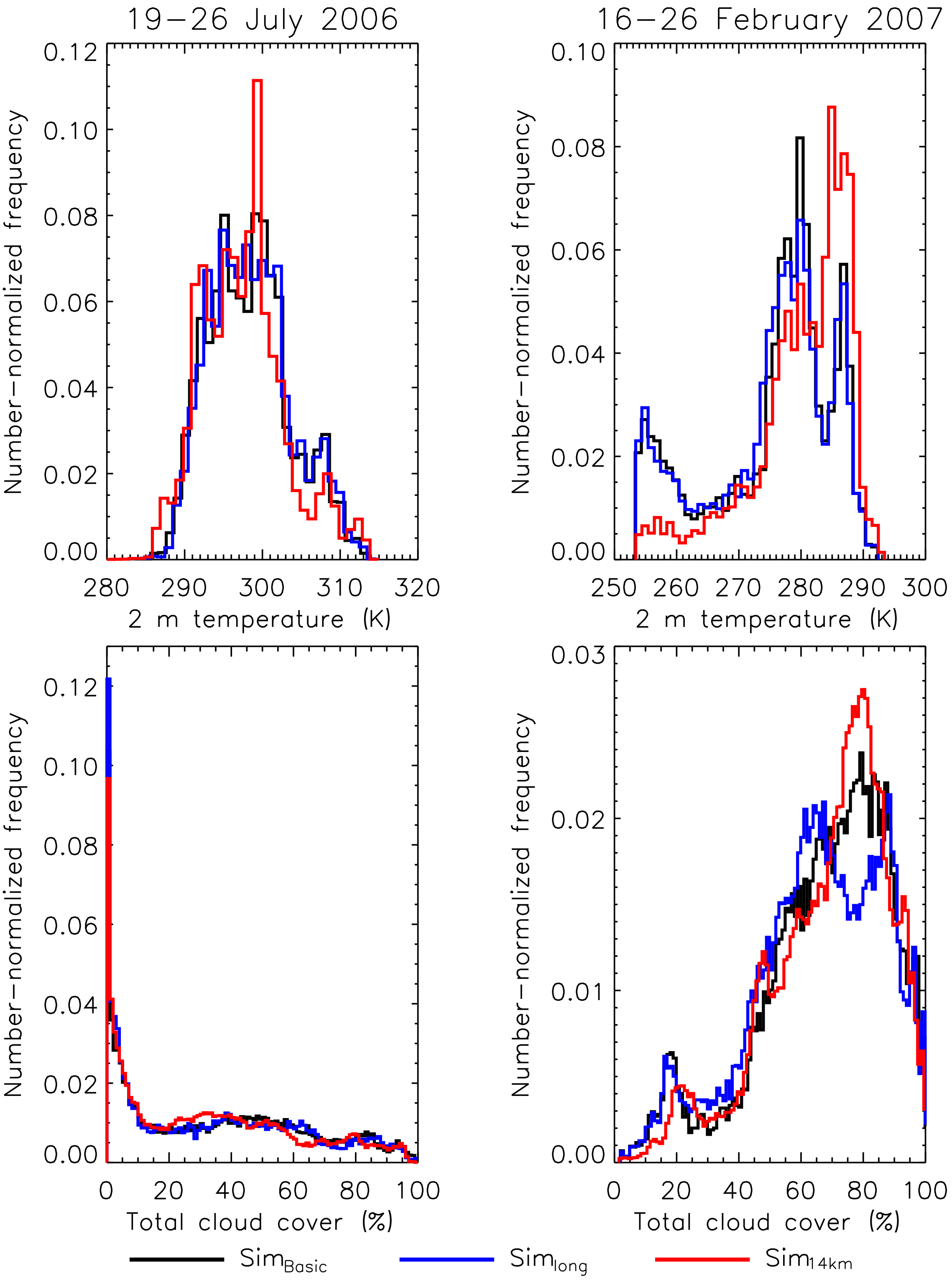

Figure 5.34: Number-normalized frequency distribution of 2 m temperature (upper panel; data refer to land surface) and total cloud cover (lower panel) during 19 − 26 July 2006 and 16 − 26 February 2007. The values represent the average data for the entire simulation periods based on the simulations by Sim$_{Basic}$ (black line), Sim$_{long}$ (blue line) and Sim$_{14km}$ (red line). Binsize: 1 K (2 m temperature), 1% (total cloud cover)

case of the total cloud cover, differences range here from 1.2% (00 UTC) to 1.9% (entire period) during July 2006 for Sim_{Basic} - Sim_{long}. Because of the similarity of the "urban" and "continental" aerosol mass, significant differences are not caused by the description of the aerosol types and their optical properties. The atmospheric situation develops very different when performing model simulation without restart (Sim_{long}) compared to frequent restarts (Sim_{Basic}). Additionally, a higher solar flux is calculated near the surface as well as at TOA (Table 5.17) by means of Sim_{long} in contrast to Sim_{Basic} for both time periods. The lower total cloud cover fraction supports the higher solar flux at TOA (summer: -2.9 W m^{-2}, winter: -2.2 W m^{-2}; Table 5.17). Due to differences according to the solar flux and total cloud cover fraction distinct differences related to the 2 m temperature are found. This is due to the different meteorological situation and not statistically significant.

Concerning the computation of the total cloud cover it is shown, that lower cloud fractions are simulated by the Sim_{14km} model setup compared to Sim_{Basic} during July 2006. Discrepancies larger than 2% are calculated for the entire time period as well as for day- and night-time averages (Table 5.17). Thus, the solar flux near the surface as well as at TOA is distinctly higher by means of Sim_{14km} in contrast to Sim_{Basic}. The discrepancies are larger when comparing Sim_{Basic} and Sim_{long}. In case of the solar flux differences of -6.6 W m^{-2} (surface) and of -5.2 W m^{-2} (TOA) are determined between Sim_{Basic} and Sim_{14km} for the entire period. The values are more distinct during day-time (Table 5.17). That also means, that higher 2 m temperatures are computed over land surface by means of the model setup with the higher horizontal resolution (Sim_{Basic}). Up to 0.72 K difference is calculated here between Sim_{Basic} and Sim_{14km}.
During 16 – 26 February 2007, the distribution of the 2 m temperature differs significantly between Sim_{14km} and the other model setups presented here. A distinct shift into higher values is found for Sim_{14km} (Figure 5.34). But average (Sim_{Basic}: 275.4 K, Sim_{long}: 275.2 K, Sim_{14km}: 274.6 K) and maximum (Sim_{Basic}: 291.8 K, Sim_{long}: 291.9 K, Sim_{14km}: 292.4 K) 2 m temperature values are similar for all three setups. Minimum values are very different in case of Sim_{14km} (261.0 K) compared to Sim_{Basic} (253.3 K) and Sim_{long} (253.4 K). And in case of the total cloud cover, all three model setups differ distinctly for cloud fractions from 60% to 90% for the same period but the statistical parameters remain close together (Sim_{Basic}: $\mathrm{TCC}_{min} = 1.9\%$, $\mathrm{TCC}_{max} = 100\%$, $\mathrm{TCC}_{mean} = 67.5\%$; Sim_{long}: $\mathrm{TCC}_{min} = 1.9\%$, $\mathrm{TCC}_{max} = 100\%$, $\mathrm{TCC}_{mean} = 65.0\%$; Sim_{14km}: $\mathrm{TCC}_{min} = 1.5\%$, $\mathrm{TCC}_{max} = 100\%$, $\mathrm{TCC}_{mean} = 68.7\%$).
The differences of the total cloud cover fraction, determined between Sim_{Basic} and Sim_{long} are distinct during the winter simulation period. This is caused by the development of different meteorological situations locally (Table 5.17).

Table 5.17: Differences, calculated between the both model setups Sim$_{Basic}$ and Sim$_{long}$ of the total cloud cover, 2 m temperature and solar flux (surface and TOA) for the two simulation periods. The values are averages for the named periods of time and refer to the entire model domain (sea and land surfaces). In case of the 2 m temperature, the values are given for land surface.

19 – 26 July 2006

Parameter	Period of time	Sim$_{Basic}$ - Sim$_{long}$	Sim$_{Basic}$ - Sim$_{14km}$
Total cloud cover	entire	1.9	2.3
(%)	00 UTC	1.2	2.9
	12 UTC	1.8	2.5
2 m temperature	entire	-0.16	-0.44
(K)	00 UTC	0.03	-0.27
	12 UTC	-0.47	-0.72
Solar flux	entire	-3.7	-6.6
(surface) (W m^{-2})	12 UTC	-8.7	-16.4
Solar flux	entire	-2.9	-5.2
(TOA) (W m^{-2})	12 UTC	-6.5	-12.5

16 – 26 February 2007

Parameter	Period of time	Sim$_{Basic}$ - Sim$_{long}$	Sim$_{Basic}$ - Sim$_{14km}$
Total cloud cover	entire	2.5	-1.1
(%)	00 UTC	2.1	-1.2
	12 UTC	2.3	-0.8
2 m temperature	entire	0.19	-0.02
(K)	00 UTC	0.18	-0.16
	12 UTC	-0.02	0.31
Solar flux	entire	-9.7	-3.0
(surface) (W m^{-2})	12 UTC	-2.8	-11.3
Solar flux	entire	-2.2	-1.3
(TOA) (W m^{-2})	12 UTC	-7.7	-5.9

During February 2007, a higher cloud cover fraction is simulated by means of Sim$_{14km}$ compared to Sim$_{Basic}$ (Table 5.17). This could be caused by the lower fraction of "urban" aerosol mass which is also computed by the Sim$_{14km}$ model setup. The lower fraction of absorbing aerosol within the atmospheric column, compared to Sim$_{Basic}$, produces a minor heating effect and therefore leads to a higher cloud cover. Due to this isolation by the clouds, a higher 2 m temperature is computed by Sim$_{14km}$ for the entire period (ΔT = -0.02 K) and for the night-time values (ΔT = -0.16 K). During day-time, where the difference of the simulated total cloud cover between Sim$_{Basic}$ and Sim$_{14km}$ is low, Sim$_{Basic}$ computes distinct higher 2 m temperatures over the land surface (Table 5.17). In total, a higher fraction of solar flux is simulated near the surface as well as at TOA but with a weaker effect compared to July 2006 (Table 5.17). Despite the day-time average difference of the solar flux near the surface of -11.3 W m^{-2}, the discrepancies between Sim$_{Basic}$ and Sim$_{14km}$ of the solar flux are lower in contrast to the difference between Sim$_{Basic}$ and Sim$_{long}$.

5.4.5 Conclusion

To test the sensitivity of the basic model (Sim$_{Basic}$) regarding the horizontal resolution and the application of daily restart cycles, two additional model setups, Sim$_{14km}$ and Sim$_{long}$, are used for the two simulation periods. Sim$_{14km}$ simulation is done with a finer horizontal resolution of 14 km x 14 km in contrast to Sim$_{Basic}$ with the resolution of 28 km x 28 km. Whereas the Sim$_{Basic}$ model setup is performed with daily restart, the Sim$_{long}$ setup is done without daily restart. AOD, vertical backscatter profiles, PM$_{2.5}$, EC and SO_4^{2-} as well as the radiative and dynamic effects are analyzed based on the results of Sim$_{Basic}$, Sim$_{long}$ and Sim$_{14km}$ and partially compared to experimental observation data.

On average, the computed horizontal distribution of AOD is often similar for all three model setups during July 2006 and February 2007. This leads to nearly identical average AODs for each day and the entire period, whereas often distinct differences are found for the maximum values of AOD. Comparison to observed AOD at AERONET stations shows similar time series for Sim$_{Basic}$ and Sim$_{14km}$. In case of Sim$_{long}$, the computed AODs differ from Sim$_{Basic}$, Sim$_{14km}$ as well as from observed AERONET AOD at the end of the summer period and in the beginning of the winter period.

Large amount of available CALIOP data allows the detailed comparison to the simulated vertical backscatter profiles. Average backscatter profiles based on Sim$_{Basic}$, Sim$_{14km}$ and Sim$_{long}$ differ slightly in the magnitude and the shape of the profile. During summer period, an indication of a different vertical mixing in simulation based on the Sim$_{long}$ setup is found.

Only a limited comparing of the model results to the surface measurements of PM$_{2.5}$, EC and SO_4^{2-} is possible due to the low amount of available experimental data. Results of the three individual model setups differ, but these discrepancies remain small and do not show a significant improvement in a particular case.

Distinct differences between Sim$_{Basic}$, Sim$_{14km}$ and Sim$_{long}$ results are found for 2 m temperature, total cloud cover and solar flux. The differences between the results of Sim$_{14km}$ and Sim$_{Basic}$ are stronger pronounced for the summer than for the winter period, probably also due to the different meteorological situation. By means of the daily restart in Sim$_{Basic}$ setup the model is kept close to the “real” atmosphere in contrast to Sim$_{long}$ setup. But the deviation between the Sim$_{Basic}$ and the Sim$_{long}$ data are typically of the same order of magnitude as the influence of different horizontal resolutions, thus pointing towards a sufficient stability of the model over the duration of the entire time periods.

While in comparison the 14 km x 14 km resolution gives slightly better results compared to 28 km x 28 km in case of e.g., the reproduction of the vertical backscatter profile, these differences are not sufficient to justify the higher computational effort for the higher resolution in the European domain for many applications. A study of longer time periods with different meteorological situations are not the subject of this work, but are certainly necessary to confirm the findings discussed here.

Chapter 6

Summary and Outlook

6.1 Summary

The regional transport model COSMO – MUSCAT is used to study the aerosol in Europe. The focus is on the “urban” and “continental” aerosol types which are important for the European domain. Descriptions of marine and dust aerosol types are not implemented within this model version. Five different aerosol types are used in general within the radiation scheme of COSMO. This scheme is based on the studies of Tanré (Tanré et al., 1984). The calculation of chemical substances is done by the chemical transport model MUSCAT. Based on H_2SO_4, $(NH_4)_2SO_4$, NH_4NO_3, EC and $PPM_{2.5}$, $PM_{2.5}$ is calculated. Except for EC, the hygroscopic growth for the substances is also considered in this study. An EC fraction larger than 20% of $PM_{2.5}$ classifies the aerosol type as “urban”, otherwise it is classified as “continental”. Both aerosol types differ regarding their optical properties. The mass as well as the information whether “urban” or “continental” aerosol exists within the individual model grid cells is transported to the radiation scheme of COSMO and differs from the Tanré scheme for these both aerosol types. Additionally, the description of the vertical distribution of chemical compounds at the lateral model boundaries is important, but here, information is limited. Observations of the vertical distribution of chemical compounds is often limited to certain time periods and locations. Thus, the model lacks in this kind of description. In COSMO – MUSCAT a standard setup ($\mathrm{Sim}_{Standard}$) is used to describe this vertical distribution at the lateral model boundaries, which is equal for all four lateral model boundaries and seasons. In this study, long-term lidar profiles are used to describe these vertical distributions individually for a summer and a winter period, representing more realistic descriptions of the planetary boundary layer (Sim_{Basic}). Ground-based lidar profiles, close to the simulations period, which are used here, are also used to make a determination of the vertical distribution at the lateral model boundaries (Sim_{Ind}).

Model simulations are performed for two different time periods which last 8 (19 – 26 July 2006) and 11 (16 – 26 February 2007) days. During the summer period, rather constant meteorological conditions occurred. Due to low wind speeds, the transport of atmospheric particles from outside into the model domain was weak and thus the accumulation of particles within the atmosphere occurred. In contrast, the winter simulation period is characterized by several rain- and snowfall events which removed the particles out of the atmosphere and thus also limited the transport of particles into the model domain. Within the model version, used here, marine aerosol as well as dust is not implemented. But during the summer simulation period, Saharan dust is transported into the European model domain which is not computed by the model. Additional, marine aerosol over sea surface and its transport is not described.

Simulation results are compared with surface $\mathrm{PM}_{2.5}$, EC and SO_4^{2-} observations, measured at EMEP stations, AOD, measured at European AERONET stations and ground- (EARLINET) and space-based (CALIOP) lidar profiles.

Based on CALIOP observations, an intensive study is performed, due to the large amount of observation profiles, and thus, a detailed analysis of the model abilities is possible. CALIOP data provide information about the vertical and the horizontal structure of the atmosphere due to a dense global coverage of observations. Information about the existence of specific aerosol types and their backscatter coefficients is provided as well and are a useful tool for model evaluation. CALIOP data with a horizontal resolutions of 5 and 40 km are presented here. Based on these data, five different CALIOP data sets are created for both summer and winter period. The data sets are used to show the difficulties in using CALIOP data correctly. Further, it is shown that the marine aerosol classification lacks. Because marine aerosol is only identified over sea surface and thus is not in coherence with ground-based observations (Putaud et al., 2004). Comparisons with model computation results can therefore lead to discrepancies.
Comparisons between experimentally observed (CALIOP) and computed backscatter profiles lead to quite satisfying results. The model is able to reproduce shape and the general magnitude of the observed backscatter coefficients of all five CALIOP data sets, mainly within the PBL. At higher altitudes, often distinct differences between observation and simulation results occur, caused by the significant decrease of the observed backscatter values compared to simulation data. For the entire average backscatter profile an overestimation by the model of all five CALIOP data sets is found during July

2006. During February 2007, underestimations of the observation profiles also occur. This underestimation can be caused by the occurrence of precipitation events during that time period which result in an effective removal of particles out of the atmosphere. During summer time, best agreements are found when comparing $\mathrm{CALIOP}_{5km}^{data3}$ with model results. On the other hand, quite good results are found in case of CALIOP_{40km} comparisons during February 2007. The focus of this study is the simulation of the anthropogenic aerosol within Europe and thus marine and dust aerosol are not implemented in that model version. Based on CALIOP data it is possible to perform comparisons between CALIOP data and model results also without the influence of marine and dust caused backscatter values. Based on the analysis of some statistical parameters no distinct improvement is found after sorting out backscatter values of both aerosol types. Nevertheless, it was possible to show, that during summer period the backscatter values of the observed average backscatter profiles above the PBL decrease after sorting out. It is assumed, that dust transport mainly occurs at higher height levels. During February 2007, a distinct decrease of the measured backscatter values within the PBL was found, caused by the sorting out of marine aerosol.
Performing comparisons between model and CALIOP backscatter profile depending on day- and night-time, leads to significant results during summer simulation period. During night-time, the agreements are better than during day-time, what was also shown in other studies where ground- and space-based lidar profiles where compared depending on their observation time (e.g., Mamouri et al., 2009). During February 2007, this distinct discrepancies was not as clear as during July 2006. In general, due to the large number of observation data based on CALIOP measurements, a detailed analysis about the model performance, also for specific aerosol types (existence, transport and magnitude), can be done. CALIOP data also have to be checked in detail for such comparisons, however.

Computed optical parameters, like the backscatter coefficient used for comparisons with CALIOP data, are based on the simulation of specific aerosol compounds. Regarding the simulation of $\mathrm{PM}_{2.5}$ distinct structures within Europe for the summer and winter period are computed. For instance, high $\mathrm{PM}_{2.5}$ mass is determined for large cities and their surroundings due to high urban emissions, whereas the average $\mathrm{PM}_{2.5}$ mass is lower during February 2007 than during July 2006. Due to the precipitation events, particles are removed from the atmosphere during winter and therefore cause lower $\mathrm{PM}_{2.5}$ and also lower AODs. But the fraction of EC is higher during the winter period. Here, the formation of the lower PBL and higher emissions due to heating causes these differences compared to July 2006. Regarding the calculation of AODs, local emissions are dominant for both time periods, whereas the transport is limited

for both cases.
By means of the computed AOD comparisons with AODs observed at AERONET stations and located close to the lateral model boundaries are shown here. The ratio between both data sets provides an weighting factor which can be used to adjust the vertical profiles at the lateral model boundaries. Therefore, information about the strength of the transport of particles from outside into the model domain are implemented. Further, by means of this method, each lateral model boundary can be described individually. Comparisons of simulation results based on Sim$_{Basic}$, Sim$_{Standard}$ and Sim$_{Ind}$, without any individual weighting, and the model setups with the individual weighting at the lateral model boundaries (Sim$^{weight}_{Basic}$, Sim$^{weight}_{Standard}$, Sim$^{weight}_{Ind}$) are presented here. In case of PM$_{2.5}$, EC, SO_4^{2-}, AOD and ground-based lidar observations no distinct differences between the model setups are found. No clear distinction whether one model setup provides better agreements with observation data is found. The use of lidar profiles to describe the vertical distribution at the lateral model boundaries instead of a fixed standard profile is recommended here.

Due to the performance of three different model simulations for the summer and winter simulation period, the direct and semi-direct radiative effects are analyzed. The existence of “urban” aerosol, with a high absorbing nature, and “continental” aerosol, influences distinctly solar and thermal fluxes as well dynamical effects. In all cases, the presence of absorbing aerosol reduces cloud cover which increases solar radiation reaching the ground, contracting the reduction of surface radiation by aerosol extinction. These results are only characteristic for these short time periods and can not be used as general assumption for summer and winter times. Thus, the performance of simulations which last longer time periods are necessary.

The sensitivity of the basic model setup (Sim$_{Basic}$) to specific model adjustments is shown. For instance, the influence of the relative humidity on the computation of AOD and vertical backscatter profiles is presented, based on model results performed with dry aerosol. It was shown, that the implementation of aerosol which is able to grow under the influence of the relative humidity leads to good agreements with observation data. For some cases an over- and underestimation of the hygroscopic growth and therefore an misinterpretation of the optical properties was found. The influence of the chosen MEE, which is also characteristic for each compound, is not studied in this context. Here, the classification of the magnitude of the influence on the determination of optical parameters by means of relative humidity and MEE would be meaningful. Regarding the determination of the radiative effects by means of “urban” and “continental” aerosol, studied by using the original setup of the radiation scheme (Sim$_{Tanre}$)

and another limit to separate "urban" from "continental" aerosol (Sim$_{EC5}$) are presented. Distinct differences between Sim$_{Basic}$ and Sim$_{EC5}$ compared to Sim$_{Tanre}$ are determined. The Tanré scheme obviously uses a different description for the aerosol distribution as used for Sim$_{Basic}$ and Sim$_{EC5}$, that is not up-to-date. Differences between Sim$_{Basic}$ and Sim$_{EC5}$ were also mainly regulated by the different amount of "urban" and "continental" aerosol which causes differences in case of the solar heating rate and therefore on the total cloud cover. Comparisons between model results performed with different horizontal resolution represented a slight improvement of the comparison with observation data in some cases when using a higher horizontal model resolution (Sim$_{14km}$). Especially, in case of the development of the vertical backscatter profile it is shown, that the Sim$_{14km}$ result differs from the basic setup Sim$_{Basic}$ due to a different vertical mixing. Differences between model results, performed without daily restart (Sim$_{long}$) compared to Sim$_{Basic}$ are found, mainly in case of simulated AOD.

6.2 Outlook

The results point towards several model issues that should be investigated further. Thus, further studies regarding the description of the hygroscopic growth, which can be described in a regional model like COSMO – MUSCAT, are necessary. Therefore, experimental studies are needed, which cover a wide range of chemical compounds and mixtures as well as environments and relative humidities. Further, comparisons with CALIOP data showed the need to implement mineral and marine aerosol type in the model. Actually, the transport, deposition and the radiative effects of Saharan dust within Europe can be described by COSMO – MUSCAT for specific events. A combination of these aerosol types in model simulations is needed. This is also the case for the implementation of marine aerosol within COSMO – MUSCAT.

A correct description of chemical compounds at the lateral model boundaries is necessary to describe the transport of atmospheric particles from outside into the model domain correctly. Only small differences between three different descriptions (Sim$_{Basic}$, Sim$_{Standard}$, Sim$_{Ind}$) are shown here. Nevertheless, the usage of a Standard Profile (Sim$_{Standard}$) at the lateral model boundaries can not be recommended, because this profile does not represents the different seasonal formation of the PBL or any local characteristics, like the typical westerly flows in Europe. The use of a climatological lidar profile as done for the Sim$_{Basic}$ model simulations should be preferred. This prescription of observed profiles at the boundaries would be even more important for smaller model domains, that are more strongly controlled by inflow from the boundaries. Using lidar profiles, obtained close to the simulation period (Sim_{Ind}) makes only sense in case of a large number of available profiles, for relatively short time periods and when observation data are representative for the entire model domain. Even with shortcomings, CALIOP observation data offer the best possibility to describe the vertical resolution of chemical compounds. It is suggested to use the long-term observation CALIOP profiles to determine climatological profiles. These profiles could be determined for each season and also for some specific regions or meteorological situations. In general, longer simulation periods will be performed, because statements regarding the radiative effects due to specific aerosol types or substances are only possible when simulations are done representing a season or longer periods.

Appendix A

Appendix

A.1 Selection of equivalent model grid cell

The observation data, performed at EMEP, AERONET and EARLINET stations and by the CALIPSO satellite include information of the geographical coordinates (latitude, longitude). Due to the spacial discretization of the model, it is necessary to determine an equivalent model grid cell to compare the experimental data with the results of the simulation. The model domain is described by a two-dimensional field for latitude(I,J) and longitude(I,J). The grid cell index in the x-y-plane is represented by I and J. Because of the non equidistant distribution of the model grid, the equivalent grid cell, containing the experiment coordinates, is determined by means of the Jordan curve theorem (Wikipedia, 2012). The model grid cell can be described as a polygon, where a coordinate is located within such a polygon if a test axis crosses an odd number of edges of this polygon (independent from the direction) or outside of the polygon else. This principle is used to find the model grid cells for each available observation point from the experiment.

A.2 Statistical parameters

Mean absolute bias (Kondragunta et al., 2008):

$$A_{bias}^{mean} = \frac{1}{N}\sum_{i=1}^{N}(S_i - O_i). \tag{A.1}$$

Mean relative bias:

$$R_{bias}^{mean} = \frac{1}{N}\sum_{i=1}^{N}(\frac{S_i - O_i}{O_i}) \cdot 100\%. \tag{A.2}$$

N represents the number of all individual values i. S_i and O_i represents simulated and observed data.

A.3 Optical parameters

Single scattering albedo (SSA). The SSA is determined based on the ratio of scattering to scattering plus absorption (Dubovik et al., 2002) and ranges between zero and one. A SSA of one implies that the extinction is due to scattering, whereas a SSA of zero implies an extinction due to absorption.

Asymmetry parameter (g). By means of the asymmetry parameter the angular distribution of the scattered light can be described. As summarized by Ogren et al. (2006) the asymmetry parameter is the cosine-weighted average of the phase function (phase function is the probability of radiation being scattered in a given direction). The values range from -1 (backward scattering) to +1 (forward scattering).

Volume depolarization ratio (δ_V). The volume depolarization ratio is defined as the ratio between the perpendicular ($\beta_{\perp}$) and the parallel (β_{II}) backscatter coefficient (Omar et al., 2009) and is a potential parameter to distinguish between spherical particles and non-spherical particles.

Color ratio (χ). The color ratio is determined based on the ratio of backscatter coefficients at the wavelengths of e.g., 1064 nm and 532 nm:

$$\chi = \frac{\beta_{1064\,nm}}{\beta_{532\,nm}}. \tag{A.3}$$

By means of the color ratio it is possible to describe the spectral variabilities of the optical properties of a scattering medium (Bi et al., 2009). Related to the CALIOP data, the color ratio is used to distinguish cloud particles from aerosols (Liu et al., 2004).

A.4 List of abbreviations

AeroCom	Aerosol Comparisons between Observations and Models
AERONET	Aerosol Robotic Network
AOD	Aerosol Optical Depth
ASDC	Atmospheric Science Data Center
asl	above sea level
AVD	Atmospheric Volume Description
BC	Black Carbon
CAD	Cloud-Aerosol Discrimination
CALIOP	Cloud-Aerosol Lidar with Orthogonal Polarization
CALIPSO	Cloud-Aerosol Lidar and Infrared Pathfinder Satellite Observation
CAM3	Community Atmosphere Model version 3
CARBOSOL	Carbonaceous Aerosols over Europe
CORINAIR	Co-ordinated Information on the Environment in the European Community-AIR
COSMO	Consortium for Small-scale Modeling
CTM	Chemistry Transport Model
DREAM	Dust REgional Atmospheric Modeling
DRF	Direct Radiative Forcing
DWD	*Deutscher Wetterdienst* (German Weather Service)
EARLINET	European Aerosol Research Lidar Network
EC	Elemental Carbon
EMEP	European Monitoring and Evaluation Programme
FT	Free Troposphere
GF	Growth Factor
GME	Global Model Europe
GOCART	Goddard Chemistry Aerosol Radiation Transport
HSRL	High Spectral Resolution Lidar

IIR	Imaging Infrared Radiometer
IPCC	Intergovernmental Panel on Climate Change
lidar	light detection and ranging
LM	*Lokal Modell* (Local Model)
LR	Lidar (Extinction-to-Backscatter) Ratio
MEE	Mass Extinction Efficiency ($m^2\,g^{-1}$)
MODIS	Moderate Resolution Imaging Spectroradiometer
MUSCAT	MultiScale Atmospheric Transport Model
OM	Organic Matter
PBL	Planetary Boundary Layer
PC	Pearson Correlation
PDF	Probability Distribution Function
PM	Particulate Matter
PM_{10}	Particulate Matter up to $10\,\mu m$
$PM_{2.5}$	Particulate Matter up to $2.5\,\mu m$
POLDER	Polarization and Directionality of the Earth's Reflectances
$PPM_{2.5}$	Primary Particulate Matter up to $2.5\,\mu m$
$PPM^*_{2.5}$	Primary Particulate Matter up to $2.5\,\mu m$ without EC
PPM_{10}	Primary Particulate Matter up to $10\,\mu m$
POM	Particulate Organic Matter
Q-AMS	Quadrupole Aerosol Mass Spectrometer
RACM	Regional Atmospheric Chemistry Mechanism
RE	Radiative Effect
RH	Relative Humidity
SCA	Scene Classification Algorithm
SDF	Semi-Direct Forcing
Sim_{14km}	Model setup with a horizontal resolution of 14 km x 14 km (Table 2.1)
$Sim_{AerosolNoFB}$	Model setup where "urban" and "continental" aerosol types influence the radiation only (Table 2.1)

Sim_{Basic}	Basic model setup (details are summarized in Table 2.1)
$\mathrm{Sim}_{Basic}^{weight}$	Basic model setup with individual weighting factors, used at the lateral model boundaries (Table 2.1)
Sim_{dry}	Model setup without hygroscopic growth (Table 2.1)
Sim_{EC5}	Model setup with a threshold of 5% for EC fraction to separate between "urban" and "continental" aerosol types (Table 2.1)
Sim_{Ind}	Model setup with individual lidar profiles (Table 2.1)
$\mathrm{Sim}_{Ind}^{weight}$	Model setup with individual lidar profiles with individual weighting factors, used at the lateral model boundaries (Table 2.1)
Sim_{long}	Model setup without daily restart (Table 2.1)
$\mathrm{Sim}_{NoAerosol}$	Model setup without impact of "urban" and "continental" aerosol on the solar radiation in COSMO – MUSCAT (Table 2.1)
Sim_{noEmi}	Model setup without local emissions (Table 2.1)
$\mathrm{Sim}_{noTrans}$	Model setup without transport of substances from outside into the model domain (Table 2.1)
$\mathrm{Sim}_{Standard}$	Model setup with Standard Profile (Table 2.1)
$\mathrm{Sim}_{Standard}^{weight}$	Model setup with Standard Profile and with individual weighting factors, used at the lateral model boundaries (Table 2.1)
Sim_{Tanre}	Model setup with the Tanré scheme (Table 2.1)
SPM	Suspended Particulate Matter
SRE	Semi-Radiative Effect
SSA	Single Scattering Albedo
SST	Sea Surface Temperature
TC	Total Carbon
TCC	Total Cloud Cover
TCC_{min}	Minimum of Total Cloud Cover
TCC_{max}	Maximum of Total Cloud Cover
TCC_{mean}	Average of Total Cloud Cover
TOA	Top of Atmosphere
WFC	Wide Field Camera
WRF	Weather Research and Forecasting

A.5 List of symbols

å	Ångström Exponent
A_{bias}	Absolute Bias
A_{bias}^{mean}	Mean Absolute Bias
c_p	Specific Heat Capacity for Dry Air (1005 $\mathrm{J\,K^{-1}\,kg^{-1}}$)
F	Radiant flux density ($\mathrm{W\,m^{2}}$)
g	Asymmetry Parameter
G	Geometric Factor
i	Individual Substance
I	Grid Cell Index (x-direction)
J	Grid Cell Index (y-direction)
K	Performance
l	Atmospheric Layer
m	Mass
N	Number
O	Observation
P	Power
R	Distance
R_{bias}	Relative Bias
R_{bias}^{mean}	Mean Relative Bias
S	Lidar Ratio
t	Time
T	Transmission / Temperature
V	Volume
z	Altitude

α	Extinction Coefficient ($\mathrm{m^{-1}}$)
β	Backscatter Coefficient ($\mathrm{m^{-1}\,sr^{-1}}$)
β_{min}	Minimum Backscatter Coefficient ($\mathrm{m^{-1}\,sr^{-1}}$)
β_{max}	Maximum Backscatter Coefficient ($\mathrm{m^{-1}\,sr^{-1}}$)
β_{mean}	Average Backscatter Coefficient ($\mathrm{m^{-1}\,sr^{-1}}$)
β_{median}	Median Backscatter Coefficient ($\mathrm{m^{-1}\,sr^{-1}}$)
β_{stddev}	Standard Deviation of Backscatter Coefficient ($\mathrm{m^{-1}\,sr^{-1}}$)
β_O	Observed Backscatter Coefficient ($\mathrm{m^{-1}\,sr^{-1}}$)
β_S	Simulated Backscatter Coefficient ($\mathrm{m^{-1}\,sr^{-1}}$)
β'	Attenuated Backscatter Coefficient ($\mathrm{m^{-1}\,sr^{-1}}$)

$\beta_{\perp}$	Perpendicular Backscatter Coefficient ($\mathrm{m^{-1}\,sr^{-1}}$)
β_{II}	Parallel Backscatter Coefficient ($\mathrm{m^{-1}\,sr^{-1}}$)
δ_V	Volume Depolarization Ratio
λ	Wavelength (μm, nm)
ρ	Density ($\mathrm{g\,m^{-3}}$)
τ	Aerosol Optical Depth
τ_{min}	Minimum of Aerosol Optical Depth
τ_{max}	Maximum of Aerosol Optical Depth
τ_{mean}	Average of Aerosol Optical Depth
$\tau_{relDiff}$	Relative Difference of Aerosol Optical Depth
χ	Color Ratio

List of Figures

List of Tables

Bibliography

Ackerman, A. S., Toon, O. B., Stevens, D. E., Heymsfield, A. J., Ramanathan, V., and Welton, E. J. (2000). Reduction of tropical cloudiness by soot. *Science*, 288:1042–1047.

AeroCom (last visit: July 2012). Aerosol Comparisons between Observations and Models. *http://aerocom.met.no/aerocomhome.html.*

AERONET (last visit: May 2012). AErosol RObotic NETwork. *http://aeronet.gsfc.nasa.gov/.*

Allen, R. J. and Sherwood, S. C. (2010). Aerosol-cloud semi-direct effect and land-sea temperature contrast in a GCM. *Geophysical Research Letters*, 37.

Ansmann, A., Bösenberg, J., Chaikovsky, A., Comerón, A., Eckhardt, S., Eixmann, R., Freudenthaler, V., Ginoux, P., Komguem, L., Linné, H., Márquez, M. A. L., Matthias, V., Mattis, I., Mitev, V., Müller, D., Music, S., Nickovic, S., Pelon, J., Sauvage, L., Sobolewsky, P., Srivastava, M. K., Stohl, A., Torres, O., Vaughan, G., Wandinger, U., and Wiegner, M. (2003). Long-range transport of Saharan dust to northern Europe: The 11-16 October 2001 outbreak observed with EARLINET. *Journal of Geophysical Research*, 108.

Ansmann, A., Tesche, M., Gross, S., Freudenthaler, V., Seifert, P., Hiebsch, A., Schmidt, J., Wandinger, U., Mattis, I., Müller, D., and Wiegner, M. (2010). The 16 April 2010 major volcanic ash plume over central Europe: EARLINET lidar and AERONET photometer observations at Leipzig and Munich, Germany. *Geophysical Research Letters*, 37.

ASDC (last visit: May 2012). Atmospheric Science Data Center, CALIPSO Data and Information. *http://eosweb.larc.nasa.gov/PRODOCS/calipso/table_calipso.html.*

Aurela, M., Sillanpää, M., Pennanen, A., Mäkelä, T., Laakia, J., Tolonen-Kivimäki, O., Saarnio, K., Yli-Tuomi, T., Aalto, P., Salonen, I., Pakkanen, T., Salonen, R. O., and Hillamo, R. (2010). Characterization of urban particulate matter for a health-related study in southern Finland. *Boreal Environment Research*, 15:513–532.

Bagtasa, G., Takeuchi, N., Fukagawa, S., Kuze, H., Shina, T., Naito, S., Sone, A., and Kan, H., editors (2006). *Mass Extinction Efficiency for tropospheric aerosols from Portable Automated Lidar and β-ray SPM counter*, volume 3P-30, pp.499-502 of *Proceedings of 23rd International Laser Radar Conference.*

Bauer, S. E. and Menon, S. (2012). Aerosol direct, indirect, semidirect, and surface albedo effects from sector contributions based on the IPCC AR5 emissions for preindustrial and present-day conditions. *Journal of Geophysical Research*, 117.

Bi, L., Yang, P., Kattawar, G. W., Baum, B. A., Hu, Y. X., Winker, D. M., Brock, R. S., and Lu, J. Q. (2009). Simulation of the color ratio associated with the backscattering of radiation by ice particles at the wavelengths of 0.532 and 1.064 μm. *Journal of Geophysical Research*, 114:D00H08.

Bösenberg, J., Matthias, V., Amodeo, A., Amoiridis, V., Ansmann, A., Baldasano, J. M., Balin, I., Balis, D., Böckmann, C., Boselli, A., Carlsson, G., Chaikovsky, A., Chourdakis, G., Comerón, A., De Tomasi, F., Eixmann, R., Freudenthaler, V., Giehl, H., Grigorov, I., Hågård, A., Iarlori, M., Kirsche, A., Kolarov, G., Komguem, L., Kreipl, S., Kumpf, W., Larcheveque, G., Linné, H., Matthey, R., Mattis, I., Mekler, A., Mironova, I., Mitev, V., Mona, L., Müller, D., Music, S., Nickovic, S., Pandolfi, M., Papayannis, A., Pappalardo, G., Pelon, J., Pérez, C., Perrone, R. M., Persson, R., Resendes, D. P., Rizi, V., Rocadenbosch, F., Rodrigues, A., Sauvage, L., Schneidenbach, L., Schumacher, R., Shcherbakov, V., Simeonov, V., Sobolewski, P., Spinelli, N., Stachlewska, I., Stoyanov, D., Trickl, T., Tsaknakis, G., Vaughan, G., Wandinger, U., Wang, X., Wiegner, M., Zavrtanik, M., and Zerefos, C. (2003). EARLINET: A European Aerosol Research Lidar Network to Establish an Aerosol Climatology. *Max-Planck-Institut Report*, 348.

CALIPSO L1B (last visit: May 2012). CALIPSO Level 1B, Atmospheric Science Data Center. *http://eosweb.larc.nasa.gov/PRODOCS/calipso/Quality_Summaries/ CALIOP_L1ProfileProducts_3.01.html.*

CALIPSO L2 V2.01 (last visit: May 2012). CALIPSO Level 2, Version 2.01, Atmospheric Science Data Center. *http://eosweb.larc.nasa.gov/PRODOCS/calipso/Quality_Summaries/ CALIOP_L2ProfileProducts_2.01.html.*

CALIPSO L2 V3.01 (last visit: May 2012). Calipso Level 2 Version 3.01, Atmospheric Science Data Center. *http://eosweb.larc.nasa.gov/PRODOCS/calipso/Quality_Summaries/ CALIOP_L2ProfileProducts_3.01.html.*

Chand, D., Wood, R., Anderson, T. L., Satheesh, S. K., and Charlson, R. J. (2009). Satellite-derived direct radiative effect of aerosols dependent on cloud cover. *Nature Geoscience*, 2:181–184.

Chandra, S., Satheesh, S. K., and Srinivasan, J. (2004). Can the state of mixing of black carbon aerosols explain the mystery of 'excess' atmospheric absorption? *Geophysical Research Letters*, 31.

Chazette, P., Raut, J. C., Dulac, F., Berthier, S., Kim, S. W., Royer, P., Sanak, J., Loaec, S., and Grigaut-Desbrosses, H. (2010). Simultaneous observations of lower tropospheric continental aerosols with a ground-based, an airborne, and the spaceborne CALIOP lidar system. *Journal of Geophysical Research*, 115.

Chin, M., Rood, R. B., Lin, S. J., Müller, J. F., and Thompson, A. M. (2000). Atmospheric sulfur cycle simulated in the global model GOCART: Model description and global properties. *Journal of Geophysical Research*, 105:24,671–24,687.

Cook, J. and Highwood, E. J. (2004). Climate response to tropospheric absorbing aerosols in an intermediate general-circulation model. *Quarterly Journal of the Royal Meteorological Society*, 130:175–191.

de la Campa, A. M. S., Pio, C., de la Rosa, J. D., Querol, X., Alastuey, A., and González-Castanedo, Y. (2009). Characterization and origin of EC and OC particulate matter near the Donana National Park (SW Spain). *Environmental Research*, 109:671–681.

Deschamps, P.-Y., Breon, F. M., Leroy, M., Podaire, A., Bricaud, A., Buriez, J. C., and Seze, G. (1994). The POLDER mission: instrument characteristics and scientific objectives. *IEEE Transactions on Geoscience and Remote Sensing*, 32:598–615.

DREAM (last visit: February 2012). Barcelona Supercomputing Center-Centro Nacional de Supercomputación, Surface concentration of BSC-DREAM8b lowest model level dust (μg m^{-3}). *http://www.bsc.es/projects/earthscience/DREAM/.*

Dubovik, O., Holben, B., Eck, T. F., Smirnov, A., Kaufman, Y. J., King, M. D., Tanré, D., and Slutsker, I. (2002). Variability of absorption and optical properties of key aerosol types observed in worldwide locations. *Journal of the Atmospheric Sciences*, 59:590–608.

EARLINET (last visit: May 2012). A European Aerosol Research Lidar Network to Establish an Aerosol Climatology. *http://earlinet.org/.*

Eck, T. F., Holben, B. N., Reid, J. S., Dubovik, O., Smirnov, A., O'Neill, N. T., Slutsker, I., and Kinne, S. (1999). Wavelength dependence of the optical depth of biomass burning, urban, and desert dust aerosols. *Journal of Geophysical Research*, 104:31333–31349.

Eichler, H., Cheng, Y. F., Birmili, W., Nowak, A., Wiedensohler, A., Brüggemann, E., Gnauk, T., Herrmann, H., Althausen, D., Ansmann, A., Engelmann, R., Tesche, M., Wendisch, M., Zhang, Y. H., Hu, M., Liu, S., and Zeng, L. M. (2008). Hygroscopic properties and extinction of aerosol particles at ambient relative humidity in South-Eastern China. *Atmospheric Environment*, 42:6321–6334.

EMEP (last visit: May 2012). Co-operative programme for monitoring and evaluation of the long-range transmissions of air pollutants in Europe. *http://emep.int/.*

EMEP/CORINAIR (last visit: May 2012). European Environment Agency. *http://www.eea.europa.eu/publications/EMEPCORINAIR3.*

Fan, J., Zhang, R., Tao, W.-K., and Mohr, K. I. (2008). Effects of aerosol optical properties on deep convective clouds and radiative forcing. *Journal of Geophysical Research*, 113.

Giglio, L., Descloitres, J., Justice, C. O., and Kaufman, Y. J. (2003). An enhanced contextual fire detection algorithm for MODIS. *Remote Sensing of Environment*, 87:273–282.

Ginoux, P., Chin, M., Tegen, I., Prospero, J. M., Holben, B., Dubovik, O., and Lin, S.-J. (2001). Sources and distributions of dust aerosols simulated with the GOCART model. *Journal of Geophysical Research*, 106:20,255–20,273.

Guibert, S., Matthias, V., Schulz, M., Bösenberg, J., Eixmann, R., Mattis, I., Pappalardo, G., Perrone, M. R., Spinelli, N., and Vaughan, G. (2005). The vertical distribution of aerosol over Europe - synthesis of one year of EARLINET aerosol lidar measurements and aerosol transport modeling with LMDzT-INCA. *Atmospheric Environment*, 39:2933–2943.

Hair, J. W., Hostetler, C. A., Cook, A. L., Harper, D. B., Ferrare, R. A., Mack, T. L., Welch, W., Izquierdo, L. R., and Hovis, F. E. (2008). Airborne High Spectral Resolution Lidar for profiling aerosol optical properties. *Applied Optics*, 47:6734–6752.

Helmert, J., Heinold, B., Tegen, I., Hellmuth, O., and Wendisch, M. (2007). On the direct and semidirect effects of Saharan dust over Europe: A modeling study. *Journal of Geophysical Research*, 112.

Hitzenberger, R., Petzold, A., Bauer, H., Ctyroky, P., Pouresmaeil, P., Laskus, L., and Puxbaum, H. (2006). Intercomparison of thermal and optical measurement methods for elemental carbon and black carbon at an urban location. *Environmental Science & Technology*, 40:6377–6383.

Hodzic, A., Bessagnet, B., and Vautard, R. (2006). A model evaluation of coarse-mode nitrate heterogeneous formation on dust particles. *Atmospheric Environment*, 40:4158–4171.

Hodzic, A., Chepfer, H., Vautard, R., Chazette, P., Beekmann, M., Bessagnet, B., Chatenet, B., Cuesta, J., Drobinski, P., Goloub, P., Haeffelin, M., and Morille, Y. (2004). Comparison of aerosol chemistry transport model simulations with lidar and Sun photometer observations at a site near Paris. *Journal of Geophysical Research*, 109.

Hohenegger, C. and Vidale, P. L. (2005). Sensitivity of the European climate to aerosol forcing as simulated with a regional climate model. *Journal of Geophysical Research*, 110.

Holben, B. N., Eck, T. F., Slutsker, I., Tanré, D., Buis, J. P., Setzer, A., Vermote, E., Reagan, J. A., Kaufman, Y. J., Nakajima, T., Lavenu, F., Jankowiak, I., and Smirnov, A. (1998). AERONET - A federated instrument network and data archive for aerosol characterization. *Remote Sensing of Environment*, 66:1–16.

Holben, B. N., Tanré, D., Smirnov, A., Eck, T. F., Slutsker, I., Abuhassan, N., Newcomb, W. W., Schafer, J. S., Chatenet, B., Lavenu, F., Kaufman, Y. J., Castle, J. V., Setzer, A., Markham, B., Clark, D., Frouin, R., Halthore, R., Karneli, A., O'Neill,

N. T., Pietras, C., Pinker, R. T., Voss, K., and Zibordi, G. (2001). An emerging ground-based aerosol climatology: Aerosol optical depth from AERONET. *Journal of Geophysical Research*, 106:12067–12097.

Horvath, H. (1993). Atmospheric light absorption–A review. *Atmospheric Environment*, 27:293–317.

Horvath, H., Alados Arboledas, L., Olmo, F. J., Jovanović, O., Gangl, M., Kaller, W., Sánchez, C., Sauerzopf, H., and Seidl, S. (2002). Optical characteristics of the aerosol in Spain and Austria and its effect on radiative forcing. *Journal of Geophysical Research*, 107.

Hu, Y. X., Rodier, S., Xu, K. M., Sun, W. B., Huang, J. P., Lin, B., Zhai, P. W., and Josset, D. (2010). Occurrence, liquid water content, and fraction of supercooled water clouds from combined CALIOP/IIR/MODIS measurements. *Journal of Geophysical Research*, 115.

Iorga, G., Hitzenberger, R., Kasper-Giebl, A., and Puxbaum, H. (2007). Direct radiative effect modeled for regional aerosols in central Europe including the effect of relative humidity. *Journal of Geophysical Research*, 112.

IPCC (2007). Intergovernmental Panel on Climate Change. *Climate Change 2007: The Physical Science Basis*, pages 996 pp., S. Solomon et al., Cambridge University Press, Cambridge, U. K.

Johnson, B. T., Shine, K. P., and Forster, P. M. (2004). The semi-direct aerosol effect: Impact of absorbing aerosols on marine stratocumulus. *Quarterly Journal of the Royal Meteorological Society*, 130:1407–1422.

Kacenelenbogen, M., Vaughan, M. A., Redemann, J., Hoff, R. M., Rogers, R. R., Ferrare, R. A., Russell, P. B., Hostetler, C. A., Hair, J. W., and Holben, B. N. (2011). An accuracy assessment of the CALIOP/CALIPSO version 2/version 3 daytime aerosol extinction product based on a detailed multi-sensor, multi-platform case study. *Atmospheric Chemistry and Physics*, 11:3981–4000.

Kaskaoutis, D. G. and Kambezidis, H. D. (2006). Investigation into the wavelength dependence of the aerosol optical depth in the Athens area. *Quarterly Journal of the Royal Meteorological Society*, 132:2217–2234.

Kiehl, J. T. and Rohde, H. (1995). *Aerosol forcing of climate*, chapter 15, page 281. John Wiley & Sons Ltd.

Kim, D., Wang, C., Ekman, A. M. L., Barth, M. C., and Rasch, P. J. (2008). Distribution and direct radiative forcing of carbonaceous and sulfate aerosols in an interactive size-resolving aerosol-climate model. *Journal of Geophysical Research*, 113.

King, M. D., Kaufman, Y. J., and Menzel, W. P. Tanré, D. (1992). Remote-sensing of cloud, aerosol, and water-vapor properties from the Moderate Resolution Imaging Spectrometer (MODIS). *IEEE Transactions on Geoscience and Remote Sensing*, 30:2–27.

Kinne, S., Schulz, M., Textor, C., Guibert, S., Balkanski, Y., Bauer, S. E., Berntsen, T., Berglen, T. F., Boucher, O., Chin, M., Collins, W., Dentener, F., Diehl, T., Easter, R., Feichter, J., Fillmore, D., Ghan, S., Ginoux, P., Gong, S., Grini, A., Hendricks, J. E., Herzog, M., Horowitz, L., Isaksen, L., Iversen, T., Kirkavåg, A., Kloster, S., Koch, D., Kristjansson, J. E., Krol, M., Lauer, A., Lamarque, J. F., Lesins, G., iu, X., Lohmann, U., Montanaro, V., Myhre, G., Penner, J. E., Pitari, G., Reddy, S., Seland, O., Stier, P., Takemura, T., and Tie, X. (2006). An AeroCom initial assessment optical properties in aerosol component modules of global models. *Atmospheric Chemistry and Physics*, 6:1815–1834.

Koch, D. and Del Genio, A. D. (2010). Black carbon semi-direct effects on cloud cover: review and synthesis. *Atmospheric Chemistry and Physics*, 10:7685–7696.

Koffi, B., Schulz, M., Bréon, F.-M., Griesfeller, J., Winker, D., Balkanski, Y., Bauer, S., Berntsen, T., Chin, M., Collins, W. D., Dentener, F., Diehl, T., Easter, R., Ghan, S., Ginoux, P., Gong, S., Horowitz, L. W., Iversen, T., Kirkevåg, A., Koch, D., Krol, M., Myhre, G., Stier, P., and Takemura, T. (2012). Application of the CALIOP layer product to evaluate the vertical distribution of aerosols estimated by global models: AeroCom phase I results. *Journal of Geophysical Research*, 117.

Köhler, H. (1921). Zur Kondensation des Wasserdampfes in der Atmosphäre. *Meteorologische Zeitschrift*, 38:168–171.

Kondragunta, S., Lee, P., McQueen, J., Kittaka, C., Prados, A. I., Ciren, P., Laszlo, I., Pierce, R. B., Hoff, R., and Szykman, J. J. (2008). Air quality forecast verification using satellite data. *Journal of Applied Meteorology and Climatology*, 47:425–442.

Lagrosas, N., Kuze, H., Takeuchi, N., Fukagawa, S., Bagtasa, G., Yoshii, Y., and Yabuki, M. (2005). Correlation study between suspended particulate matter and portable automated lidar data. *Aerosol Science*, 36:439–454.

Laurent, B., Tegen, I., Heinold, B., Schepanski, K., Weinzierl, B., and Esselborn, M. (2010). A model study of Saharan dust emissions and distributions during the SAMUM-1 campaign. *Journal of Geophysical Research*, 115.

Liu, D., Wang, Z., Liu, Z. Y., Winker, D., and Trepte, C. (2008). A height resolved global view of dust aerosols from the first year CALIPSO lidar measurements. *Journal of Geophysical Research*, 113.

Liu, Z. Y., Vaughan, M., Winker, D., Kittaka, C., Getzewich, B., Kuehn, R., Omar, A., Powell, K., Trepte, C., and Hostetler, C. (2009). The CALIPSO Lidar Cloud and Aerosol Discrimination: Version 2 Algorithm and Initial Assessment of Performance. *Journal of Atmospheric and Oceanic Technology*, 26:1198–1213.

Liu, Z. Y., Vaughan, M. A., Winker, D. M., Hostetler, C. A., Poole, L. R., Hlavka, D., Hart, W., and McGill, M. (2004). Use of probability distribution functions for discriminating between cloud and aerosol in lidar backscatter data. *Journal of Geophysical Research*, 109.

Lohmann, U. and Feichter, J. (2001). Can the direct and semi-direct aerosol effect compete with the indirect effect on a global scale? *Geophysical Research Letters*, 28:159–161.

Majewski, D., Liermann, D., Prohl, P., Ritter, B., Buchhold, M., Hanisch, T., Paul, G., Wergen, W., and Baumgardner, J. (2002). The operational global icosahedral-hexagonal gridpoint model GME: Description and high-resolution tests. *Monthly Weather Review*, 130:319–338.

Mallet, M., Roger, J. C., Despiau, S., Dubovik, O., and Putaud, J.-P. (2003). Microphysical and optical properties of aerosol particles in urban zone during ESCOMPTE. *Atmospheric Research*, 69:73–97.

Mamouri, R. E., Amiridis, V., Papayannis, A., Giannakaki, E., Tsaknakis, G., and Balis, D. S. (2009). Validation of CALIPSO space-borne-derived attenuated backscatter coefficient profiles using a ground-based lidar in Athens, Greece. *Atmospheric Measurement Techniques*, 2:513–522.

Marmer, E. and Langmann, B. (2007). Aerosol modeling over Europe: 1. Interannual variability of aerosol distribution. *Journal of Geophysical Research*, 112.

Massling, A., Stock, M., and Wiedensohler, A. (2005). Diurnal, weekly, and seasonal variation of hygroscopic properties of submicrometer urban aerosol particles. *Atmospheric Environment*, 39:3911–3922.

Matthias, V. (2008). The aerosol distribution in Europe derived with the Community Multiscale Air Quality (CMAQ) model: comparison to near surface in situ and sunphotometer measurements. *Atmospheric Chemistry and Physics*, 8:5077–5097.

Mattis, I., Ansmann, A., Wandinger, U., and Müller, D. (2003). Unexpectedly high aerosol load in the free troposphere over central Europe in spring/summer 2003. *Geophysical Research Letters*, 30.

Mattis, I., Müller, D., Ansmann, A., Wandinger, U., Preißler, J., Seifert, P., and Tesche, M. (2008). Ten years of multiwavelength Raman lidar observations of free-tropospheric aerosol layers over central Europe: Geometrical properties and annual cycle. *Journal of Geophysical Research*, 113.

Meier, J., Tegen, I., Heinold, B., and Wolke, R. (2012a). Direct and semi-direct radiative effects of absorbing aerosols in Europe: Results from a regional model. *Geophysical Research Letters*, 39.

Meier, J., Tegen, I., Mattis, I., Wolke, R., Alados Arboledas, L., Apituley, A., Balis, D., Barnaba, F., Chaikovsky, A., Sicard, M., Pappalardo, G., Pietruczuk, A., Stoyanov, D., Ravetta, F., and Rizi, V. (2012b). A regional model of European aerosol transport: Evaluation with sun photometer, lidar and air quality data. *Atmospheric Environment*, 47:519–532.

Meier, J., Wehner, B., Massling, A., Birmili, W., Nowak, A., Gnauk, T., Brüggemann, E., Herrmann, H., Min, H., and Wiedensohler, A. (2009). Hygroscopic growth of urban aerosol particles in Beijing (China) during wintertime: a comparison of three experimental methods. *Atmospheric Chemistry and Physics*, 9:6865–6880.

Meloni, D., di Sarra, A., DeLuisi, J., Di Iorio, T., Fiocco, G., Junkermann, W., and Pace, G. (2003). Tropospheric aerosols in the Mediterranean: 2. Radiative effects through model simulations and measurements. *Journal of Geophysical Research*, 108.

Morgan, W. T., Allan, J. D., Bower, K. N., Capes, G., Crosier, J., Williams, P. I., and Coe, H. (2009). Vertical distribution of sub-micron aerosol chemical composition from North-Western Europe and the North-East Atlantic. *Atmospheric Chemistry and Physics*, 9:5389–5401.

Morgan, W. T., Allan, J. D., Bower, K. N., Esselborn, M., Harris, B., Henzing, J. S., Highwood, E. J., Kiendler-Scharr, A., McMeeking, G. R., Mensah, A. A., Northway, M. J., Osborne, S., Williams, P. I., Krejci, R., and Coe, H. (2010). Enhancement of the aerosol direct radiative effect by semi-volatile aerosol components: airborne measurements in North-Western Europe. *Atmospheric Chemistry and Physics*, 10:8151–8171.

Müller, D., Ansmann, A., Mattis, I., Tesche, M., Wandinger, U., Althausen, D., and Pisani, G. (2007). Aerosol-type-dependent lidar ratios observed with Raman lidar. *Journal of Geophysical Research*, 112:1–11.

Müller, D., Kolgotin, A., Mattis, I., Petzold, A., and Stohl, A. (2011). Vertical profiles of microphysical particle properties derived from inversion with two-dimensional regularization of multiwavelength Raman lidar data: experiment. *Applied Optics*, 50:2069–2079.

Müller, D., Mattis, I., Wandinger, U., Ansmann, A., Althausen, D., Dubovik, O., Eckhardt, S., and Stohl, A. (2003). Saharan dust over a central European EARLINET-AERONET site: Combined observations with Raman lidar and Sun photometer. *Journal of Geophysical Research*, 108.

NASA/GSFC (last visit: February 2012). Global Fire Maps. *http://rapidfire.sci.gsfc.nasa.gov/firemaps/*.

Nickovic, S., Kallos, G., Papadopoulos, A., and Kakaliagou, O. (2001). A model for prediction of desert dust cycle in the atmosphere. *Journal of Geophysical Research*, 106:18,113–18,129.

Nowak, A. (2005). *Das feuchte Partikelgrößenspektrometer: Eine neue Messmethode zur Bestimmung von Partikelgrößenverteilung (<1µm) und großaufgelösten hygroskopischen Wachstumsfaktoren bei definierten Luftfeuchten*. PhD thesis, University of Leipzig.

Ogren, J. A., Andrews, E., McComiskey, A., Sheridan, P., Jefferson, A., and Fiebig, M. (2006). New Insights into Aerosol Asymmetry Parameter. *Sixteenth ARM Science Team Meeting Proceedings*, Albuquerque, NM, March 27-31.

Omar, A. H., Winker, D. M., Kittaka, C., Vaughan, M. A., Liu, Z. Y., Hu, Y. X., Trepte, C. R., Rogers, R. R., Ferrare, R. A., Lee, K. P., Kuehn, R. E., and Hostetler, C. A. (2009). The CALIPSO Automated Aerosol Classification and Lidar Ratio Selection Algorithm. *Journal of Atmospheric and Oceanic Technology*, 26:1994–2014.

Omar, A. H., Won, J. G., Winker, D. M., Yoon, S. C., Dubovik, O., and McCormick, M. P. (2005). Development of global aerosol models using cluster analysis of Aerosol Robotic Network (AERONET) measurements. *Journal of Geophysical Research*, 110.

Pappalardo, G., Amodeo, A., Pandolfi, M., Wandinger, U., Ansmann, A., Bsenberg, J., Matthias, V., Amiridis, V., De Tomasi, F., Frioud, M., Iarlori, M., Komguem, L., Papayannis, A., Rocadenbosch, F., and Wang, X. (2004). Aerosol lidar intercomparison in the framework of the EARLINET project. 3. Raman lidar algorithm for aerosol extinction, backscatter, and lidar ratio. *Applied Optics*, 43:5370–5385.

Pappalardo, G., Wandinger, U., Mona, L., Hiebsch, A., Mattis, I., Amodeo, A., Ansmann, A., Seifert, P., Linné, H., Apituley, A., Arboledas, L. A., Balis, D., Chaikovsky, A., D'Amico, G., De Tomasi, F., Freudenthaler, V., Giannakaki, E., Giunta, A., Grigorov, I., Iarlori, M., Madonna, F., Mamouri, R. E., Nasti, L., Papayannis, A., Pietruczuk, A., Pujadas, M., Rizi, V., Rocadenbosch, F., Russo, F., Schnell, F., Spinelli, N., Wang, X., and Wiegner, M. (2010). EARLINET correlative measurements for CALIPSO: First intercomparison results. *Journal of Geophysical Research*, 115.

Penner, J. E., Zhang, S. Y., Chin, M., Chuang, C. C., Feichter, J., Feng, Y., Geogdzhayev, I. V., Ginoux, P., Herzog, M., Higurashi, A., Koch, D., Land, C., Lohmann, U., Mishchenko, M., Nakajima, T., Pitari, G., Soden, B., Tegen, I., and Stowe, L. (2002). A Comparison of Model- and Satellite-Derived Aerosol Optical Depth and Reflectivity. *Journal of the Atmospheric Sciences*, 59:441–460.

Péré, J. C., Mallet, M., Pont, V., and Bessagnet, B. (2010). Evaluation of an aerosol optical scheme in the chemistry-transport model CHIMERE. *Atmospheric Environment*, 44:3688–3699.

Péré, J. C., Mallet, M., Pont, V., and Bessagnet, B. (2011). Impact of aerosol direct radiative forcing on the radiative budget, surface heat fluxes, and atmospheric dynamics during the heat wave of summer 2003 over western Europe: A modeling study. *Journal of Geophysical Research*, 116.

Powell, K. A., Hostetler, C. A., Liu, Z., Vaughan, M. A., Kuehn, R. E., Hunt, W. H., Lee, K.-P., Trepte, C. R., Rogers, R. R., Young, S. A., and Winker, D. M. (2009). CALIPSO Lidar Calibration Algorithms. Part I: Nighttime 532-nm Parallel Channel and 532-nm Perpendicular Channel. *Journal of Atmospheric and Oceanic Technology*, 26:2015–2033.

Powell, K. A., Vaughan, M. A., Kuehn, R., Hunt, W. H., and Lee, K.-P. (2008). Revised calibration strategy for the CALIOP 532-nm channel: Part II–Daytime. In *24th International Laser Radar Conference*.

Putaud, J. P., Raes, F., Van Dingenen, R., Brüggemann, E., Facchini, M. C., Decesari, S., Fuzzi, S., Gehrig, R., Hüglin, C., Laj, P., Lorbeer, G., Maenhaut, W., Mihalopoulos, N., Müllller, K., Querol, X., Rodriguez, S., Schneider, J., Spindler, G., ten Brink, H., Tørseth, K., and Wiedensohler, A. (2004). European aerosol phenomenology-2: chemical characteristics of particulate matter at kerbside, urban, rural and background sites in Europe. *Atmospheric Environment*, 38:2579–2595.

Putaud, J. P., Van Dingenen, R., Alastuey, A., Bauer, H., Birmili, W., Cyrys, J., Flentje, H., Fuzzi, S., Gehrig, R., Hansson, H. C., Harrison, R. M., Herrmann, H., Hitzenberger, R., Hüglin, C., Jones, A. M., Kasper-Giebl, A., Kiss, G., Kousa, A., Kuhlbusch, T. A. J., Löschau, G., Maenhaut, W., Molnar, A., Moreno, T., Pekkanen, J., Perrino, C., Pitz, M., Puxbaum, H., Querol, X., Rodriguez, S., Salma, I., Schwarz, J., Smolik, J., Schneider, J., Spindler, G., ten Brink, H., Tursic, J., Viana, M., Wiedensohler, A., and Raes, F. (2010). A European aerosol phenomenology-3: Physical and chemical characteristics of particulate matter from 60 rural, urban, and kerbside sites across Europe. *Atmospheric Environment*, 44:1308–1320.

Quaas, J., Boucher, O., Jones, A., Weedon, G. P., Kieser, J., and Joos, H. (2009). Exploiting the weekly cycle as observed over Europe to analyse aerosol indirect effects in two climate models. *Atmospheric Chemistry and Physics*, 9:8493–8501.

Redemann, J., Turco, R. P., Liou, K. N., Hobbs, P. V., Hartley, W. S., Bergstrom, R. W., Browell, E. V., and Russell, P. B. (2000). Case studies of the vertical structure of the direct shortwave aerosol radiative forcing during TARFOX. *Journal of Geophysical Research*, 105:9971–9979.

Renner, E. and Wolke, R. (2010). Modelling the formation and athmospheric transport of secondary inorganic aerosols with special attention to regions with high ammonia emissions. *Atmospheric Environment*, 44:1904–1912.

Ritter, B. and Geleyn, J. F. (1992). A comprehensive radiation scheme for numerical weather prediction models with potential applications in climate simulations. *Monthly Weather Review*, 120:303–325.

Rossow, W. B. and Zhang, Y. C. (2010). Evaluation of a Statistical Model of Cloud Vertical Structure Using Combined CloudSat and CALIPSO Cloud Layer Profiles. *Journal of Climate*, 23:6641–6653.

Sakaeda, N., Wood, R., and Rasch, P. (2011). Direct and semidirect aerosol effects of southern African biomass burning aerosol. *Journal of Geophysical Research*, 116.

Sato, M., Hansen, J., Koch, D., Lacis, A., Ruedy, R., Dubovik, O., Holben, B., Chin, M., and Novakov, T. (2003). Global atmospheric black carbon inferred from AERONET. *Proceedings of the National Academy of Sciences of the United States of America*, 100:6319–6324.

Schmid, H., Laskus, L., Abraham, H. J., Baltensperger, U., Lavanchy, V., Bizjak, M., Burba, P., Cachier, H., Crow, D., Chow, J., Gnauk, T., Even, A., ten Brink, H. M., Giesen, K., Hitzenberger, R., Hueglin, C., Maenhaut, W., Pio, C., Carvalho, A., Putaud, J.-P., Toom-Sauntry, D., and Puxbaum, H. (2001). Results of the "carbon conference" international aerosol carbon round robin test stage I. *Atmospheric Environment*, 35:2111–2121.

Schulz, J.-P. and Schättler, U. (2009). Kurze Beschreibung des Lokal-Modells Europa COSMO-EU (LME) und seiner Datenbanken auf dem Datenserver des DWD. `http://www.dwd.de/bvbw/generator/DWDWWW/Content/Forschung/FE1/Veroeffentlichungen/Download/LME__DBbeschr__0901,templateId=raw,property=publicationFile.pdf/LME_DBbeschr_0901.pdf`.

Sievers, O. (2004). *Bestimmung von strahlungsbedingten, atmosphärischen Erwärmungsraten aus MSG-Daten.* PhD thesis, Universität Hamburg.

Simpson, D., Fagerli, H., Jonson, J. E., Tsyro, S., Wind, P., and Tuovinen, J.-P. (2003). Transboundary Acidification, Eutrophication and Ground Level Ozone in Europe, PART I, Unified EMEP Model Description. *EMEP MSC-W Report 1/2003.*

Smirnov, A., Holben, B. N., Eck, T. F., Dubovik, O., and Slutsker, I. (2000). Cloud-screening and quality control algorithms for the AERONET database. *Remote Sensing of Environment*, 73:337–349.

Solmon, F., Giorgi, F., and Liousse, C. (2006). Aerosol modelling for regional climate studies: application to anthropogenic particles and evaluation over a European/African domain. *Tellus*, 58B:51–72.

Spindler, G., Brüggemann, E., Gnauk, T., Grüner, A., Müller, K., and Herrmann, H. (2010). A four-year size-segregated characterization study of particles PM$_{10}$, PM$_{2.5}$ and PM$_{1}$ depending on air mass origin at Melpitz. *Atmospheric Environment*, 44:164–173.

Stephens, G. L., Vane, D. G., Boain, R. J., Mace, G. G., Sassen, K., Wang, Z. E., Illingworth, A. J., O'Connor, E. J., Rossow, W. B., Durden, S. L., Miller, S. D., Austin, R. T., Benedetti, A., Mitrescu, C., and CloudSat Sci, T. (2002). The cloudsat mission and the A-train - A new dimension of space-based observations of clouds and precipitation. *Bulletin of the American Meteorological Society*, 83:1771–1790.

Steppeler, J., Doms, G., Schättler, U., Bitzer, H. W., Gassmann, A., Damrath, U., and Gregoric, G. (2003). Meso-gamma scale forecasts using the nonhydrostatic model LM. *Meteorology and Atmospheric Physics*, 82:75–96.

Stern, R., Builtjes, P., Schaap, M., Timmermans, R., Vautard, R., Hodzic, A., Memmesheimer, M., Feldmann, H., Renner, E., Wolke, R., and Kerschbaumer, A. (2008). A model inter-comparison study focussing on episodes with elevated PM10 concentrations. *Atmospheric Environment*, 42:4567–4588.

Stockwell, W. R., Kirchner, F., and Kuhn, M. (1997). A new mechanism for regional atmospheric chemistry modeling. *Journal of Geophysical Research*, 102:25,847–25,879.

Su, L. and Toon, O. B. (2011). Saharan and Asian dust: similarities and differences determined by CALIPSO, AERONET, and a coupled climate-aerosol microphysical model. *Atmospheric Chemistry and Physics*, 11:3263–3280.

Takemura, T., Nakajima, T., Dubovik, O., Holben, B. N., and Kinne, S. (2002). Single-scattering albedo and radiative forcing of various species with a global three-dimensional model. *Journal of Climate*, 15:333–352.

Tang, I., Wong, W., and Munkelwitz, H. R. (1981). The relative importance of atmospheric sulfates and nitrates in visibility reduction. *Atmospheric Environment*, 15:2463–2471.

Tang, I. N. (1996). Chemical and size effects of hygroscopic aerosols on light scattering coefficients. *Journal of Geophysical Research*, 101:19,245–19,250.

Tanré, D., Geleyn, J. F., and Slingo, J. (1984). First results of the introduction of an advanced aerosol-radiation interaction in the ECMWF low resolution global model. In Gerber, H. E., editor, *Aerosols and their Climate Effects*. Deepak, A.

Textor, C., Schulz, M., Guibert, S., Kinne, S., Balkanski, Y., Bauer, S., Berntsen, T., Berglen, T., Boucher, O., Chin, M., Dentener, F., Diehl, T., Easter, R., Feichter, H., Fillmore, D., Ghan, S., Ginoux, P., Gong, S., Grini, A., Hendricks, J., Horowitz, L., Huang, P., Isaksen, I., Iversen, T., Kloster, S., Koch, D., Kirkevåg, A., Kristjansson, J. E., Krol, M., Lauer, A., Lamarque, J. F., Liu, X., Montanaro, V., Myhre, G., Penner, J., Pitari, G., Reddy, S., Seland, O., Stier, P., Takemura, T., and Tie, X. (2006). Analysis and quantification of the diversities of aerosol life cycles within AeroCom. *Atmospheric Chemistry and Physics*, 6:1777–1813.

Tiedtke, M. (1989). A Comprehensive Mass Flux Scheme for Cumulus Parametrization in Large-Scale Models. *Monthly Weather Review*, 117:1779–1800.

Tombette, M., Chazette, P., Sportisse, B., and Roustan, Y. (2008). Simulation of aerosol optical properties over Europe with a 3-D size-resolved aerosol model: comparisons with AERONET data. *Atmospheric Chemistry and Physics*, 8:7115–7132.

Tsyro, S., Simpson, D., Tarrasón, L., Klimont, Z., Kupiainen, K., Pio, C., and Yttri, K. E. (2007). Modeling of elemental carbon over Europe. *Journal of Geophysical Research*, 112.

Twomey, S. (1977). The influence of pollution on the shortwave albedo of clouds. *Journal of Atmospheric Sciences*, 34:1149–1152.

University of Wyoming (last visit: February 2012). College of Engineering, Department of Atmospheric Sciences, Soundings. *http://weather.uwyo.edu/upperair/sounding.html*.

Van Dingenen, R., Raes, F., Putaud, J.-P., Baltensperger, U., Charron, A., Facchini, M.-C., Decesari, S., Fuzzi, S., Gehrig, R., Hansson, H.-C., Harrison, R. M., Hüglin, C., Jones, A. M., Laj, P., Lorbeer, G., Maenhaut, W., Palmgren, F., Querol, X., Rodriguez, S., Schneider, J., ten Brink, H., Tunved, P., Tørseth, K., Wehner, B., Weingartner, E., Wiedensohler, A., and Wåhlin, P. (2004). A European aerosol phenomenology-1: physical characteristics of particulate matter at kerbside, urban, rural and background sites in Europe. *Atmospheric Environment*, 38:2561–2577.

Vaughan, M. A., Powell, K. A., Kuehn, R. E., Young, S. A., Winker, D. M., Hostetler, C. A., Hunt, W. H., Liu, Z. Y., McGill, M. J., and Getzewich, B. J. (2009). Fully Automated Detection of Cloud and Aerosol Layers in the CALIPSO Lidar Measurements. *Journal of Atmospheric and Oceanic Technology*, 26:2034–2050.

Vogel, B., Vogel, H., Bäumer, D., Bangert, M., Lundgren, K., Rinke, R., and Stanelle, T. (2009). The comprehensive model system COSMO-ART Radiative impact of aerosol on the state of the atmosphere on the regional scale. *Atmospheric Chemistry and Physics*, 9:8661–8680.

Wandinger, U., Mattis, I., Tesche, M., Ansmann, A., Bösenberg, J., Chaikovski, A., Freudenthaler, V., Komguem, L., Linné, H., Matthias, V., Pelon, J., Sauvage, L., Sobolewski, P., Vaughan, G., and Wiegner, M. (2004). Air mass modification over Europe: EARLINET aerosol observations from Wales to Belarus. *Journal of Geophysical Research*, 109.

Wandinger, U., Tesche, M., Seifert, P., Ansmann, A., Müller, D., and Althausen, D. (2010). Size matters: Influence of multiple scattering on CALIPSO light-extinction profiling in desert dust. *Geophysical Research Letters*, 37.

Weijers, E. P., Schaap, M., Nguyen, L., Matthijsen, J., van der Gon, H. A. C. D., ten Brink, H. M., and Hoogerbrugge, R. (2011). Anthropogenic and natural constituents in particulate matter in the Netherlands. *Atmospheric Chemistry and Physics*, 11:2281–2294.

Weingartner, E., Burtscher, H., and Baltensperger, U. (1997). Hygroscopic properties of carbon and diesel soot particles. *Atmospheric Environment*, 31:2311–2327.

Weitkamp, C., editor (2005). *Lidar: Range-Resolved Optical Remote Sensing of the Atmosphere*. Springer.

Wendisch, M., Hellmuth, O., Ansmann, A., Heintzenberg, J., Engelmann, R., Althausen, D., Eichler, H., Müller, D., Hu, M., Zhang, Y., and Mao, J. (2008). Radiative and dynamic effects of absorbing aerosol particles over the Pearl River Delta, China. *Atmospheric Environment*, 42:6405–6416.

Wendisch, M., Müller, D., Mattis, I., and Ansmann, A. (2006). Potential of lidar backscatter data to estimate solar aerosol radiative forcing. *Applied Optics*, 45:770–783.

Wex, H., Kiselev, A., Stratmann, F., and Zoboki, J. (2005). Measured and modeled equilibrium sizes of NaCl and $(NH_4)_2SO_4$ particles at relative humidities up to 99.1%. *Journal of Geophysical Research*, 110.

Wex, H., Kiselev, A., Ziese, M., and Stratmann, F. (2006). Calibration of LACIS as a CCN detector and its use in measuring activation and hygroscopic growth of atmospheric aerosol particles. *Atmospheric Chemistry and Physics*, 6:4519–4527.

Wikipedia (last visit: May 2012). Jordan curve theorem. *http://en.wikipedia.org/wiki/Jordan_curve_theorem*.

Winker, D. M., Hostetler, C. A., Vaughan, M. A., and Omar, A. H. (2006). CALIOP Algorithm Theoretical Basic Document, Part I: CALIOP Instrument, and Algorithms Overview. *Rep. PC-SCI-202 Part I, Release 2.0 (available at: http://www-calipso.larc.nasa.gov/resources/pdfs/PC-SCI-202.Part1_v2-Overview.pdf)*.

Winker, D. M., Vaughan, M. A., Omar, A., Hu, Y. X., Powell, K. A., Liu, Z. Y., Hunt, W. H., and Young, S. A. (2009). Overview of the CALIPSO Mission and CALIOP Data Processing Algorithms. *Journal of Atmospheric and Oceanic Technology*, 26:2310–2323.

Wolke, R. and Knoth, O. (2000). Implicit-explicit Runge-Kutta methods applied to atmospheric chemistry-transport modelling. *Environmental Modelling & Software*, 15:711–719.

Wolke, R., Knoth, O., Hellmuth, O., Schröder, W., and Renner, E. (2004). The Parallel Model System LM-MUSCAT for Chemistry-Transport Simulations: Coupling Scheme, Parallelization and Applications. *Parallel Computing*, 13:363–369.

Wolke, R., Schröder, W., Schrödner, R., and Renner, E. (2012). Influence of grid resolution and meteorological forcing on simulated European air quality: A sensitivity study with the modeling system COSMO-MUSCAT. *Atmospheric Environment*, 53:110–130.

Wu, D. L., Chae, J. H., Lambert, A., and Zhang, F. F. (2011). Characteristics of CALIOP attenuated backscatter noise: implication for cloud/aerosol detection. *Atmospheric Chemistry and Physics*, 11:2641–2654.

Yoshida, R., Okamoto, H., Hagihara, Y., and Ishimoto, H. (2010). Global analysis of cloud phase and ice crystal orientation from Cloud-Aerosol Lidar and Infrared Pathfinder Satellite Observation (CALIPSO) data using attenuated backscattering and depolarization ratio. *Journal of Geophysical Research*, 115.

Young, S. A. and Vaughan, M. A. (2009). The Retrieval of Profiles of Particulate Extinction from Cloud-Aerosol Lidar Infrared Pathfinder Satellite Observations (CALIPSO) Data: Algorithm Description. *Journal of Atmospheric and Oceanic Technology*, 26:1105–1119.

Yu, H., Chin, M., Winker, D. M., Omar, A. H., Liu, Z., Kittaka, C., and Diehl, T. (2010). Global view of aerosol vertical distributions from CALIPSO lidar measurements and GOCART simulations: Regional and seasonal variations. *Journal of Geophysical Research*, 115.

Zhang, Y., Klein, S. A., Boyle, J., and Mace, G. G. (2010). Evaluation of tropical cloud and precipitation statistics of Community Atmosphere Model version 3 using CloudSat and CALIPSO data. *Journal of Geophysical Research*, 115.

Acknowledgements

By submitting this thesis I want to take the chance to thank some persons who guided me on my way so far due to their knowledge and personal support.

Prof. Dr. Ina Tegen, I wish to thank for the introduction into the interesting and intensive work of science. Her comprehension about things in addition to the work at the Leibniz Institute for Tropospheric Research and her always existing cheerfulness often made things easier and will be an ideal for my future way.

Further, I am deeply grateful to Dr. Ina Mattis und Dr. Ulla Wandinger. Their competent guidance helped me to cross the barriers of lidar observations. They have been holding me to a high standard and enforcing strict validations for each research result.

I have been amazingly fortunate to have thus excellent working environment.

I started my work at the Modeling Department of em. Prof. Dr. Eberhard Renner, who always impressed me due to his confidence and support for the members of his department.

I also wish to thank Dr. Ralf Wolke and Dr. Bernd Heinold for the discussions that helped me sorting out the details of my work, especially to get behind the regional model COSMO – MUSCAT.

In the lectures of em. Prof. Dr. Jost Heintzenberg and Prof. Dr. Alfred Wiedensohler my interest in aerosol science during my student time was sparked.

I owe my gratitude to all those people from Prof. Dr. Tegen's group who have made this dissertation possible and because of whom my graduate experience has been one that I will cherish forever. Especially I shall thank Dr. Kerstin Schepanski for her high scientific level stimulating me to stay tuned and Birgit Heinrich and Kerstin Müller for making things just simple.

I would like to thank the steady support of knowledge and technical material by Thomas Jagemann, Katja Schmieder and Marcus Naschke, which was the basis for this work.

Many friends have helped me stay sane through these years. I'm greatly thankful for havening friends who helped when too many things happened at once and who know when its not the time to ask for the progress of my thesis. Primarily there is a big need to thank my very best friend Sergej, the one who spend so much time with me for looking after the "big blue box" and never lost his confidence in me.

Most importantly, I wish to thank my mother any brother. They are the ones who taught me the basic principles and always to keep going. The gratitude for my family cannot be put into words.

List of Publications

Journal Publications

- Meier, J., Mattis, I., Müller, D., Tegen, I. (2008/2009). Model initialization and validation with ground- and space-based lidar measurements and sun photometer measurements, *2-Jahresbericht des Leibniz-Institut für Troposphärenforschung*, 96 – 98.

- Meier, J., Wehner, B., Massling, A., Birmili, W., Nowak, A., Gnauk, T., Brüggemann, E., Herrmann, H., Hu, M., Wiedensohler, A. (2009). Hygroscopic growth of urban aerosol particles in Beijing (China) during wintertime: A comparison of three experimental methods, *Atmospheric Chemistry and Physics*, 9: 6865 – 6880.

- Meier, J., Tegen, I., Mattis, I., Wolke, R., Alados Arboledas L., Apituley, A., Balis, D., Barnaba, F., Chaikovsky, A., Sicard, M., Pappalardo, G., Pietruczuk, A., Stoyanov, D., Ravetta, F., Rizi, V. (2012). A regional model of European aerosol transport: Evaluation with sun photometer, lidar and air quality data, *Atmospheric Environment*, 47: 519 – 532.

- Meier, J., Tegen, I., Heinold, B., Wolke, R. (2012). Direct and semi-direct radiative effects of absorbing aerosols in Europe: Results from a regional model, *Geophysical Research Letters*, 39: L09802.

Oral Presentations

- Conference of the Leibniz-Institute for Tropospheric Research (2008). Characterization of the European aerosol by means of regional modelling and lidar measurements, Nimbschen, Germany.

- 8th International Symposium on Tropospheric Profiling: Integration of Needs (2009). Model initialization and validation with ground- and space-based lidar measurements, Delft, The Netherlands.

- COSMO User Seminar (2010). Initialization and validation of COSMO – MUSCAT with ground- and space-based lidar measurements and sun photometer measurements, Langen, Germany.

- COSMO User Seminar (2011). COSMO – MUSCAT case studies of the direct radiative effects of absorbing aerosols in Europe, Langen, Germany.
- Interim evaluation of the Leibniz-Institute for Tropospheric Research (2012). *Direkte und semi-direkte Aerosoleffekte in Europe: Modellresultate*, Leipzig, Germany.

Poster Presentations

- European Geosciences Union EGU (2010). Model initialization and validation with ground- and space-based lidar measurements and sun photometer measurements, Vienna, Austria.

Curriculum Vitae

Personal information

Family name	Meier
First name	Jessica
Date of birth	08.03.1981
Place of birth	Berlin (Germany)
Nationality	German
Address	Kiebitzweg 18, 38518 Gifhorn
Telephone	+49 151 280 789 67
E-Mail	jessica.meier@tropos.de

Education

1987 - 1990	Primary school, Gablenz, Germany
1993 - 1999	Lew-Landau secondary school, Weißwasser, Germany
1999 - 2000	Schooling as radiologic technologist, University hospital Dresden, Germany
2000 - 2006	Study of meteorology, Leipzig University, Germany
2005 - 2006	Topic of diploma thesis: " *Untersuchung des hygroskopischen Partikelwachstums des urbanen Aerosols in Peking (China) und die Simulation der Sichtweite*"
June 2006	Research assistant at the Leibniz Institute for Tropospheric Research, Leipzig, Germany
July 2006 - May 2007	Research assistant at the Helmholtz Centre for Environmental Research, Leipzig, Germany
July 2007 - September 2012	Ph.D. student in the Modeling Department at the Leibniz Institute for Tropospheric Research, Leipzig, Germany

Selbständigkeitserklärung

Hiermit erkläre ich, dass ich die vorliegende Arbeit selbständig und ohne unzulässige Hilfe oder Benutzung anderer als der angegebenen Hilfsmittel angefertigt habe. Ich versichere, dass Dritte von mir weder unmittelbar noch mittelbar geldwerte Leistungen für Arbeiten erhalten haben, die im Zusammenhang mit dem Inhalt der vorliegenden Dissertation stehen, und dass die vorgelegte Arbeit weder im Inland noch im Ausland in gleicher oder ähnlicher Form einer anderen Prüfungsbehörde zum Zwecke einer Dissertation oder eines anderen Prüfungsverfahrens vorgelegt und in ihrer Gesamtheit noch nicht veröffentlicht wurde. Alles aus anderen Quellen oder von anderen Personen übernommene Material, das in der Arbeit verwendet wurde oder auf das direkt Bezug genommen wird, wurde als solches kenntlich gemacht. Insbesondere wurden alle Personen genannt, die direkt an der Entstehung der vorliegenden Arbeit beteiligt waren.
Es haben keine erfolglosen Promotionsversuche stattgefunden.
Die Promotionsordnung vom 23. März 2010 wird anerkannt.

Leipzig, den 19.12.2012

Jessica Meier